STRUCTURAL STABILITY OF HIGHWAY EMBANKMENTS IN THE ARCTIC CORRIDOR

by

Earl Marvin B. De Guzman

A Thesis
Submitted to the Faculty of Graduate Studies
in Partial Fulfilment of the Requirements
for the Degree of

DOCTOR OF PHILOSOPHY

Department of Civil Engineering
University of Manitoba
Winnipeg, Manitoba

Marolo C. Alfaro, Ph.D., P.Eng.
Professor - University of Manitoba

Guy Doré, Ph.D., ing.
Professeur titulaire - Université Laval
and
Adjunct Professor - University of Manitoba

Lukas U. Arenson, Dr.Sc.Techn.ETH, P.Eng.
Principal Geotechnical Engineer
BGC Engineering Inc.
and
Adjunct Professor - University of Manitoba

Kristopher J. Dick, Ph.D., P.Eng.
Senior Scholar - University of Manitoba

Jocelyn L. Hayley, Ph.D, P.Eng.
Professor - University of Calgary

ABSTRACT

There are uncertainties related to the mechanical behaviour of highway embankments where frozen soil is used as fill material and experience natural thawing and settlements during the first thawing season following construction. Side slope sloughing, fill cracking, and development of localized thaw settlements underneath the embankment shoulders and side slopes typically occur due to thawing of the frozen soil and permafrost foundation. Test sections were constructed and instrumented with temperature and displacement sensors along the Inuvik-Tuktoyaktuk Highway in the Northwest Territories, Canada to assess the thermal and mechanical performance of frozen fill embankments. One of the test sections was reinforced with layers of wicking woven geotextiles at its side slopes to provide reinforcement against lateral movements and instabilities during the thawing season. This is the first research where woven geotextiles were used for slope reinforcement of initially frozen fill in Arctic regions. Significant lateral displacements occurred in the summer following end-of-construction for the control (unreinforced) and reinforced test sections, with the reinforced section showing reduced lateral movements. Temperatures in the embankment and permafrost foundation have also been increasing due to warming air temperatures, leading to additional displacements as the previously compacted frozen fill thaws.

Large-scale direct shear and pullout tests were conducted on the soil and woven geotextiles, respectively, under different moisture contents and environmental conditions to quantify their influence on embankment performance. The most critical condition, based on the tests conducted, occurs during the onset of the first thawing when the ice bonding in the soil matrix melts. The interface properties obtained from the pullout tests showed that the wicking geotextile has higher interface friction properties compared to a non-wicking geotextile at comparable strain levels.

Thermal modelling and coupled thermal-mechanical modelling were carried out using commercially-available finite element software TEMP/W and ABAQUS, respectively, and were calibrated with recorded field data. Climate modelling scenarios were also used to evaluate performance under near-term and long-term conditions. The coupled models confirmed the benefit of using woven geotextiles in reducing displacements when used as reinforcement in thawing slopes. With confidence on model results for the test sections, parametric studies were conducted to investigate the influence of embankment thickness, slope inclination, reinforcement length, and reinforcement spacing on the thermal and mechanical performance of these embankments. The monitored field performance, use of woven geotextiles as slope reinforcement, and numerical modelling considering the effects of climate change presented in this thesis will help improve the existing design guidelines for highway embankments in Arctic regions.

Keywords: highway embankments, winter construction, permafrost, frozen fill compaction, reinforced slopes, wicking geotextiles, interface resistance, shear strength, large-scale direct shear test, pullout test, numerical modelling, climate change

ACKNOWLEDGEMENTS

The research work presented was funded by the Department of Infrastructure of the Government of Northwest Territories (DOI-GNWT) and Transport Canada. I would like to acknowledge the support and encouragement from my advisors Dr. Marolo Alfaro, Dr. Guy Doré, and Dr. Lukas Arenson in completing this research. Their insightful comments over the years of collaboration are deeply appreciated. Special thanks to Dr. Alfaro for providing valuable guidance since I started my graduate program, and the opportunity to grow as a respectable researcher. I extend my gratitude to Dr. Kris Dick for serving in my advisory committee and examination panel, and Dr. Jocelyn Hayley as the external examiner. Their comments and suggestions provided guidance in adding clarity to the contents of this work.

I would like to thank the engineers of DOI-GNWT: Mohammad Hossain, Patrice Ndiangang, and Dean Ahmet, for their assistance and field support during the construction of the test embankments. E. Gruben's Transport Ltd provided logistical support with DOI personnel at the construction site and formed a critical part to the successful construction of the test sections. The contribution of TenCate Geosynthetics through René Laprade and Andrew Lister for supplying the wicking and non-wicking woven geotextiles for this research is also appreciated.

I would like to acknowledge the contribution of the following laboratory technicians in support of the large-scale direct shear and pullout tests: Kerry Lynch, Brendan Pachal, Chad Klowak, Grant Whiteside, and Scott Sparrow. Our geotechnical laboratory technician Kerry Lynch provided valuable support in setting up the instrumentation program in the field as well as logistical aid for my winter and summer site visits. The assistance of Chantal Lemieux from Université Laval in coordinating their test program is also appreciated.

I would like to acknowledge the following graduate students: Aron Piamsalee for his assistance in installing instrumentation in April 2015, Samuel Kaluzny for his assistance with my field work in installing the local weather station, camera traps, drilling, and coring of frozen core samples from the foundation at the research site in March 2017, and Dylan Stafford for his assistance with the field work on using aerial drones and terrestrial laser scanning. The friendship of Samuel and Dylan through the course of our work has been remarkable and deeply cherished.

Finally, I would like to thank my family for continuously supporting me through my endeavours in this research program, providing the courage to take on the challenges, and always being there as a source of strength in troubling times. I offer the success and the completion of this work to them.

Earl Marvin B. De Guzman, M.Sc., P.Eng.
Winnipeg, Manitoba (September 2020)

TABLE OF CONTENTS

Chapter 3 Shear Strength of Embankment Fill

Chapter 4 Soil-Geotextile Interface Properties

Chapter 5 Numerical Modelling: Thermal Performance

Chapter 6 Numerical Modelling: Mechanical Performance

LIST OF TABLES

Chapter 6 Numerical Modelling: Mechanical Performance

LIST OF FIGURES

Chapter 1 Introduction

Chapter 2 Field Performance of Highway Embankments in the Arctic

Chapter 3 Shear Strength of Embankment Fill

Chapter 4 Soil-Geotextile Interface Properties

Chapter 5 Numerical Modelling: Thermal Performance

Chapter 6 Numerical Modelling: Mechanical Performance

LIST OF NOTATIONS AND ACRONYMS

Chapter 2 Field Performance of Highway Embankments in the Arctic

AWS	Automatic weather station
DAQ	Data acquisition system
ECCC	Environment and Climate Change Canada
EOC	End-of-construction
EOY	End-of-year
GT	Geotextile layer
MDAT	Mean daily air temperatures
NASA	National Aeronautics and Space Administration
SAA	ShapeAccelArrays
ST	Spring thawing
TS	Thermistor string
WF	Winter freezing

Chapter 3 Shear Strength of Embankment Fill

CM	Composite mix
EC	Environmental chamber
EGS	Grab samples from embankment fill
G	Shear modulus (kPa)
H	Height (mm)
K	Bulk modulus (kPa)
L	Length (mm)
LVDT	Linear Variable Differential Transformers
SAA	ShapeAccelArray
T	Temperature (°C)
USCS	Unified Soil Classification System
W	Width (mm)
γ_d	Dry density (kN/m^3)
$\gamma_{d\,max}$	Maximum dry density (kN/m^3)
δ_v	Vertical displacement (mm)
δ_h	Horizontal displacement (mm)
ε_{xy}	Shear strain
ν	Poisson's ratio
ρ	Density (kg/m^3)
σ_n	Normal stress (kPa)

τ	Shear stress (kPa)
ϕ'_{cs}	Critical state friction angle (°)
ϕ'_{p}	Peak friction angle (°)
ψ	Dilation angle (°)

Chapter 4 Soil-Geotextile Interface Properties

a	Hyperbolic intercept parameter
B	Width of the geotextile (mm)
b	Hyperbolic slope parameter
c_p	Apparent cohesion (kPa)
EC	Environmental chamber
EOT	End-of-test
F_{max}	Maximum pullout force (kN)
F_{min}	Minimum pullout force (kN)
H	Height (mm)
HMC	High moisture content
L	Length (mm)
L_e	Distance where displacements were recorded (mm)
LVDT	Linear Variable Differential Transformers
OMC	Optimum moisture content
P_C	Calibration pullout force (kN)
P_G	Gross pullout force (kN)
P_N	Net pullout force (kN)
T	Temperature (°C)
TT	Telltale
w	Moisture content (%)
W	Width (mm)
δ_{gross}	Global displacement (mm)
δ_p	Interface friction angle (°)
ε	Strain on the geotextile
σ_n	Normal stress (kPa)
τ_p	Total shear stress on the geotextile fabric (kPa)

Chapter 5 Numerical Modelling: Thermal Performance

-3yrAct	Three-year actual air temperatures
-3yrAve	Three-year average sinusoidal air temperatures
CanCM4	Fourth Generation Coupled Global Climate Model
CanESM2	Second Generation Earth System Model

CCCma	Canadian Centre for Climate Modelling and Analysis
CGCM	Coupled General Circulation Model
CM	Climate Model
CMIP5	Coupled Model Intercomparison Project Phase 5
c_{vf}	Frozen volumetric heat capacity (kJ/m^3·°C)
c_{vu}	Unfrozen volumetric heat capacity (kJ/m^3·°C)
c_{vw}	Volumetric heat capacity of water (MJ/m^3·°C)
ESM	Earth System Model
h	heat transfer coefficient at 2 m
IPCC	Intergovernmental Panel on Climate Change
k_{frozen}	Frozen thermal conductivity (kJ/days·m·°C)
k_{snow}	Snow thermal conductivity
$k_{unfrozen}$	Unfrozen thermal conductivity (kJ/days·m·°C)
$n_{freezing}$	Freezing n-factor
$n_{thawing}$	Thawing n-factor
q_g	Ground heat flux
q_{lat}	Latent heat flux
q_{nl}	Net terrestrial (longwave) radiation
q_{ns}	Net solar (shortwave) radiation
q_s	Downwelling shortwave radiation
q_{sens}	Sensible heat flux
q_{snow}	Snow heat flux
RCP	Representation Concentration Path
SEB	Surface energy balance approach
T_a	Air temperature
T_g	Absolute temperature of the ground surface
TM	Thermal modifier approach
T_{snow}	Temperature of snow at the ground surface
VWC	Volumetric water content (m^3/m^3)
w	Water content (%)
w_u	Unfrozen water content (%)
α	Albedo
ε_a	Air emissivity
ε_s	Surface emissivity
ρ_d	Dry density (kg/m^3)
ρ_w	Water density (kg/m^3)
σ	Stefan-Boltzmann constant

Chapter 6 Numerical Modelling: Mechanical Performance

-3yrAct	Three-year actual air temperatures
-3yrAve	Three-year average sinusoidal air temperatures
-d05i1	Boundary condition using d2005i1 near-term climate change model
-d05i2	Boundary condition using d2005i2 near-term climate change model
-d15	Boundary condition using d2015 near-term climate change model
-O	Parametric reinforced models using original geotextile properties
-HE	Parametric reinforced models using higher elastic modulus for the geotextile
-HI	Parametric reinforced models using higher soil-geotextile interface properties
-rcp26	Boundary condition using RCP 2.6 long-term climate change model
-rcp45	Boundary condition using RCP 4.5 long-term climate change model
-rcp85	Boundary condition using RCP 8.5 long-term climate change model
A	sine function amplitude
CCCma	Canadian Centre for Climate Modelling and Analysis
CP	Fully-coupled approach for deformation analysis
CCP	Control test section model using CP
CHT	Control test section model for heat transfer analysis
CSQ	Control test section model using SQ
c	Cohesion (kPa)
d	Material cohesion for plasticity model in Abaqus
E	Elastic modulus (Pa)
E_f	Soil-geotextile interface efficiency factor
e_o	Void ratio
FWC	Forced warming conditions
GL#	Geotextile layer number
L	Length of geotextile (m)
$n_{freezing}$	Freezing n-factor
$n_{thawing}$	Thawing n-factor
p'	Mean effective stress (Pa)
p'_b	Hydrostatic compression yield stress (Pa)
RHT	Reinforced test section model for heat transfer analysis
RSQ	Reinforced test section model using SQ
SQ	Sequentially-coupled approach for deformation analysis
s	Vertical spacing between geotextile layers (m)
THES	Thawed horizontal extent from slope (m)
TM	Thermal modifier approach
UCP	Unreinforced model using CP
UHT	Unreinforced model for heat transfer analysis

USQ	Unreinforced model using SQ
u_x, u_y, u_z	displacement degrees of freedom
x_c	Sine function phase shift
y_o	Sine function offset
β	Angle of friction for plasticity model in Abaqus
Δ_{max}	Maximum displacement (mm)
ε_{vol}^{pl}	Plastic volumetric strain
θ	Friction angle of the soil (°)
κ	Kappa (recompression index)
λ	Lambda (compression index)
ν	Poisson's ratio
tan δ	Equivalent soil-geotextile interface friction angle
tan ϕ	Equivalent soil friction angle
ω	Sine function period

CHAPTER 1

INTRODUCTION

1.1. Research Background

There are numerous challenges associated with constructing highways in the Arctic. Embankments are typically constructed during the winter months to preserve the permafrost foundation and minimize environmental impacts. Placement of embankment fill material is easier when the frozen natural ground surface makes movements of construction equipment most effective (Savage 1965). Fill material is placed by end dumping, and construction vehicles are prohibited from traveling on or damaging the vegetation mat beyond the limit of the fill footprint itself (McHattie and Esch 1983). In their studies on the influence of vegetation cover on permafrost, Yi et al. (2007) reported that even a thin presence of peat greatly retards ground thaw. Peat has higher porosity than mineral soil which allows larger storage for water (De Guzman and Alfaro 2018). Peat provides insulation to the underlying permafrost because it requires more latent heat to achieve the same depth of thaw compared to mineral soil. Removal of the active layer and replacing it with either coarse-grained or fine-grained soil will only accelerate permafrost degradation (Yu et al. 2012, Sengupta et al. 1990).

Non-frost-susceptible materials (e.g., gravel) suitable for embankment construction are not always available in construction sites in the Arctic (Berg and Esch 1983, Saboundjian 2008). Construction is only done in the winter with locally-available frozen soil from nearby borrow sources. Frozen soil when used as fill material is very difficult to compact at sub-zero temperatures. They are relatively strong while they remain frozen but become soft and compressible upon

thawing. For a comparable compactive effort, a frozen soil will have a lower dry density at a given water content than a soil in the unfrozen state. The maximum dry density at an optimum water content typically observed for unfrozen soil cannot be achieved in frozen conditions (Burwash and Clark 1981, De Guzman et al. 2018[*]). When the water content of the frozen soil increases, the dry density and workability of compacting the frozen soil decreases. In addition to the potential for development of settlements once the soil thaws there is also a significant reduction in shear strength (De Guzman et al. 2018). Alkire et al. (1976) also noted that a potential problem related to construction of embankments using frozen fill is the relatively slow rate of thawing and associated development of settlements following the construction.

Embankment thickness (fill height) varies along a project site due to terrain conditions. They are typically designed to provide adequate ground insulation and minimize permafrost degradation (Argue et al. 1981) under known climatic conditions. The construction of embankments inevitably results to thermal disturbance of the underlying permafrost. The permafrost will degrade if the insulating effect provided by the embankment fill is less than the insulating effect of the original active layer. On the other hand, the permafrost can rise into the embankment if the insulating effect of the embankment fill is greater than the insulating effect of the original active layer. The thermal regime in the active layer and the underlying permafrost mainly depends on the thermal properties of the foundation soil and the interaction between the atmosphere and the ground (Gold 1967, Yu et al. 2012, Wu and Niu 2013).

Thick embankments (also called high-fill sections) act as a wind break favouring significant snow accumulation on the embankment shoulders and toes, which insulates the ground surface, decreases heat loss in the winter, and prevents further ground freezing (Fortier et al. 2011). Snow

[*] Chapter 3 of this manuscript.

accumulation on the side slopes of an embankment can either be naturally-driven (precipitation, snow drifting due to wind gusts) or mechanically-driven (snow ploughing from road surface). Progressively deeper thawing generally occurs beneath snow-covered roadway side slopes (Esch 1983) and can cause problems of side slope sloughing and spreading as the side slopes subside into the thaw channel that forms below the toe of the slope (McGregor et al. 2010). This results to longitudinal embankment cracking in addition to thawing of compacted frozen fill in the summer months. Frequent snow removal from the side slopes helps minimize the insulating effect of snow cover during the winter months (McHattie and Esch 1983, Malenfant-Lepage and Doré 2010) but may not always be economical for an entire highway system and at thick embankment sections with steeper slopes where equipment mobility is restricted.

Climate change has been a global driving force in recent years as a design consideration in assessing how structures built now will perform in the future. Linear infrastructure such as embankments built in Arctic regions are especially vulnerable to climate change as global warming will affect the seasonal active layer; that is, the active layer will grow deeper and thawing of the permafrost will lead to increased deformations in the embankment. Smith et al. (2010) reported that permafrost across North America has been generally been warming. This warming trend in the permafrost due to increasing ambient air temperatures may lead to the embankment instabilities mentioned earlier (Jørgensen and Ingeman-Nielsen 2012).

There are uncertainties related to the mechanical behaviour of embankments that were initially compacted with frozen fill and then experienced natural thawing and settlements during the first thawing season following construction. Settlements and lateral spreading can lead to serviceability problems impacting overall embankment performance which may lead to embankment failure (Saboundjian 2008) and ultimately affect economic productivity and safety (Regehr et al. 2013).

With these knowledge gaps and performance issues of embankments constructed under winter conditions, this research aims to investigate the operating mechanisms causing instabilities and deformations of these embankments and contribute in improving overall embankment performance.

1.2. Inuvik-Tuktoyaktuk Highway: First and Only Canadian Highway to the Arctic Coast

The completion of the Inuvik to Tuktoyaktuk Highway (ITH) has been a long standing goal of the Town of Inuvik, the Hamlet of Tuktoyaktuk, and the residents of the Inuvialuit Settlement Region (Environmental Impact Review Board 2011). The construction of the ITH helps address the goals of Northern economic development, supporting future natural resource exploration, development, and production (such as the natural gas and oil reserves in the Mackenzie Delta and Basin), and reinforcing Canadian sovereignty objectives (Infrastructure Canada 2015).

Detailed road alignment, environmental data gathering, and engineering design were conducted in the 1960s and 70s and had been continuously revised to address the concerns of local communities and other stakeholders during an extensive environmental review process, leading to the development of the route alignment alternatives in 2009. The highway has been identified as a priority development by the Government of Canada and Government of the Northwest Territories (GNWT). The ITH, which extends the Dempster Highway past the Inuvik to the Arctic Coast, is an all-weather transportation link and completes Canada's road network from the Pacific, to Atlantic, and to Arctic coasts. Fig. 1.1 shows the designed alignment of the highway. Typical 'cut and fill' techniques that are often employed in the southern areas of the Northwest Territories were not used along the ITH in order to protect the permafrost terrain along the highway alignment (Environmental Impact Review Board 2011) and to minimize, if not completely eliminate, the possible instabilities. To comply with vertical geometry requirements, embankment fill thickness

ranged from 1.5 to 12 m. The recorded warming trend in air temperatures due to climate change in the Northwest Territories is expected to render stability problems to be more prevalent when the frozen fill thaws (McGregor et al. 2010, Intergovernmental Panel on Climate Change 2014). A partnership was developed between the University of Manitoba, Université Laval, and the Department of Infrastructure of the GNWT in constructing and instrumenting tests sections along the ITH to investigate and address the issues presented earlier. One of these test sections was reinforced with layers of woven geotextiles at its slope to reduce side slope sloughing and fill cracking. To the author's knowledge, this is the first research program that used woven geotextiles as slope reinforcement of initially frozen fill in Arctic regions.

1.3. Problem Statement

The problems associated with embankments in the Arctic that this research aims to address are summarized in the following unknowns:

1. Effects of using frozen soil in embankment performance;
2. Length of time the frozen soil used to construct the embankment will remain frozen;
3. If taliks[†] will form, if there are instabilities associated with its development, and if it will affect embankment performance;
4. How woven geotextiles contribute in reducing embankment instabilities; and,
5. Impact of climate change on the performance of unreinforced and reinforced embankments.

[†] Talik – a layer or body of unfrozen ground in a permafrost area

1.4. Research Hypotheses

1. Short-term stability of highway embankments in the Arctic is governed by thawing of frozen soil and corresponding decrease in shear strength at the slopes where significant lateral displacements and settlements occur during the subsequent summer after winter construction;
2. Long-term stability is governed by climate change conditions where the depth of thaw penetration in the embankment fill and foundation soil increases over time contributing to additional displacements and the formation of taliks can lead to instabilities which may compromise performance; and
3. Geotextiles with wicking function when used as slope reinforcement reduce lateral displacements and improve the short-term and long-term stability of embankments.

1.5. Research Objectives

The following objectives of this research are as follows:

1. Understand how the use of frozen soil during winter construction affects embankment performance during the subsequent summer following construction, at service, and under climate change conditions;
2. Quantify the benefit of using woven geotextiles (wicking and non-wicking) as slope reinforcement in reducing lateral displacements for embankments constructed with frozen soil;
3. Determine the effect of thin and thick embankments on the thermal regime of the permafrost foundation and how this impacts embankment stability;
4. Investigate the instabilities associated with the change of temperature and strength in the embankment fill and foundation soil; and

5. Based on the findings of objectives 1-4, recommend design and construction guidelines for new linear infrastructure built on continuous permafrost regions.

1.6. Thesis Organization

This chapter (Chapter 1) presented the background, hypotheses, and objectives of this research. Chapter 2 presents the construction and field performance of the embankment test sections. A comprehensive analysis of the field data (temperature, displacements) are discussed in this chapter.

Chapter 3 and Chapter 4 presents the laboratory testing program conducted on the soil and the woven geotextile (wicking and non-wicking), respectively, under different moisture contents (wet and optimum) and environmental conditions (frozen, thawed, and cyclic freeze-thaw). Chapter 3 focuses on the shear strength of the soil using a large scale direct shear test. Chapter 4 focuses on the interface strength between the woven geotextiles and the soil from pullout tests.

Thermal numerical modelling was conducted on the thin and thick embankments using (1) thermal modifiers and (2) surface energy balance model calibrated with field data from Chapter 2 and the results are comprehensively presented in Chapter 5. A series of near-term (modelled to year 2025 and year 2035) and long-term (modelled to year 2100) climate change models were applied on the thick embankment sections. Parametric studies were performed on different embankment geometries and boundary conditions to study their influence on the thermal regime of embankments and underlying permafrost.

To quantify the mechanical performance of the embankments in Chapter 2, soil and geotextile properties obtained from Chapters 3 and 4, respectively, were used in sequentially-coupled and fully-coupled thermal-mechanical models and the results are presented in Chapter 6. Only the thermal modifier approach was used in the coupled modelling. Parametric studies were also

conducted to investigate the influence of embankment thickness, slope inclination, reinforcement length, and reinforcement spacing on the thermal and mechanical performance of these embankments. A summary of the research work done is presented in Chapter 7. The hypotheses and objectives are also revisited to provide overall conclusions. Areas of future research are provided as recommendations in this chapter.

During the course of this research, several publications have been prepared for technical journals and conference proceedings. These submissions and publications have been identified at the beginning of each chapter as a footnote. There are sections and discussions that are overlapping in between chapters and care was exercised to clearly identify these in each chapter. Except for Chapter 1 and Chapter 7, and the material provided in the research background, each chapter has at least one technical journal paper associated with it. Relevant review of literature are presented in each chapter as part of the technical journal publishing procedures. Tables, figures, and notations and acronyms are found at the end of each chapter.

1.7. Original Contributions

By understanding the operating mechanisms causing instabilities and excessive displacements in highway embankments constructed under winter conditions, improvements on the guidelines for the design, construction, and their maintenance can be made for future linear infrastructure development in Arctic regions. The following original contributions of this research program are as follows:

1. This is the first research program that used woven geotextiles as slope reinforcement using initially frozen fill in the Arctic. By understanding the contribution of geotextiles in reducing lateral displacements, critical embankment heights can be supported adequately without

compromising stability and steeper slopes can be achieved without sacrificing the thermal integrity of the embankment and the foundation soil.

2. The large-scale direct shear tests investigated the shear strength of the embankment soil. Most studies in the literature account for the shear strength of the permafrost foundation and how it affects the stability of the overlying embankment. However, limited study has been made on the mechanical strength of coarse-grained frozen soil from locally-available borrow sources used for embankment construction. The results from this study showed how different environmental conditions reduces the shear strength of the embankment material and should be taken into account in the preliminary stages of design and developing long-term maintenance strategies of these embankments.

3. The thermal modelling of the test sections provided a baseline thermal condition after winter construction. Field data supports evidence that climate change is affecting the thermal performance of these embankments even though the embankments are still providing adequate insulation to the permafrost. Near-term and long-term conditions were assessed using climate models available for the region. Adequate design can be made prior to construction for new infrastructure while mitigation strategies can be optimized for existing ones for continued thermal performance.

4. Both sequentially-coupled and fully-coupled analyses were conducted to determine the thermal and mechanical effects on embankment performance. These models were calibrated against field data. Parametric models considering the influence of embankment thickness, slope inclination, reinforcement length, and reinforcement spacing were investigated and results provide reasonable estimates of performance with improved confidence.

Fig. 1.1. Alignment of ITH in Northwest Territories, Canada and location of research embankment test section (map courtesy of DOT-GNWT).

CHAPTER 2

FIELD PERFORMANCE OF HIGHWAY EMBANKMENTS IN THE ARCTIC[1,2]

2.1. Introduction

The research background in Chapter 1 presented the difficulties associated with embankments in Arctic regions. The literature (for example, Sun et al. 2005, Qi et al. 2007, Saboundjian 2008, Ma et al. 2008, Wu et al. 2010, Ma et al. 2012, Jørgensen and Ingeman-Nielsen 2012, Yu et al. 2013, Batenipour et al. 2014) has provided a wealth of information on embankment performance attributed to permafrost degradation. However, limited work has been done on the thawing of the frozen soil used in the construction of the embankment fill and how this influences embankment performance. As mentioned previously, there are uncertainties related to the mechanical behaviour of embankments that were initially compacted with frozen fill and then experienced natural thawing and settlements during the first thawing season following construction. In this chapter,

[1] This chapter has been submitted, accepted, and/or published in peer-reviewed journals and/or conference proceedings as follows:
De Guzman, E.M.B., Alfaro, M., Doré, G., Arenson, L.U., and Piamsalee, A. 2020. Performance of highway embankments in the Arctic constructed under winter conditions. Canadian Geotechnical Journal (accepted).

De Guzman, E.M.B., Kaluzny, S.W., Stafford, D.M.J., Alfaro, M., Arenson, L.U., and Doré, G. 2020. Four-year monitored performance of a geotextile-reinforced fill slope along a highway to Canada's Arctic coast. 4th Pan-American Conference on Geosynthetics. Rio de Janeiro, Brazil.

Parent, M., Doré, G., Lemieux, C., **De Guzman, E.M.B.**, and Alfaro, M. 2019. Relative Importance of Mechanical Degradation of Permafrost Embankment. 18th International Conference on Cold Regions Engineering. Quebec, QC.

De Guzman, E.M.B., Alfaro, M., Doré, G. and Arenson, L. 2017. Performance of instrumented sections along a highway in the Canadian arctic. 19th International Conference on Soil Mechanics and Geotechnical Engineering. Seoul, South Korea. pp. 1979-1982.

De Guzman, E.M.B., Piamsalee, A., Alfaro, M., Arenson, L., and Doré, G. 2016. Performance of a Reinforced Highway Embankment along the Inuvik-Tuktoyaktuk Highway, Northwest Territories, Canada. 11th International Conference on Permafrost, Potsdam, Germany. pp. 1115.

De Guzman, E.M.B., Piamsalee, A., Alfaro, M., Arenson, L., and Doré, G. 2015. Geotextile-Reinforced Fill Slope Along a Highway to Canada's Arctic Coast. 3rd Pan-American Conference on Geosynthetics. Florida, USA. pp. 1614-1626.

De Guzman, E.M.B., Piamsalee, A., Alfaro, M., Arenson, L., Doré, G., and Hayley, D. 2015. Initial Monitoring of Instrumented Test Sections along the Inuvik-Tuktoyaktuk Highway. 68th Canadian Geotechnical Conference. Quebec, QC.

[2] A list of notations and acronyms used in this chapter are found in page 62.

the monitored field data are used to describe the thermal and mechanical behaviour of the thick embankments as well as the thermal behaviour of the thin embankment to assess embankment performance.

2.2. Embankment Construction

Two test sections, each 20 m long, were constructed along ITH in April 2015. The completed test sections, which lengths were constrained by local conditions, are shown in Fig. 2.1a. The first test section (STA 82+380 to STA 82+400) was constructed and instrumented to serve as the control section. The second test section (STA 82+400 to STA 82+420), referenced hereafter as the reinforced section, was similarly instrumented as the control section but its side slopes were reinforced with wicking woven geotextiles. Both embankment test sections are 5.3 m thick with embankment slopes 3H:1V (Fig. 2.2a shows the cross-section of the instrumented embankment). Non-woven geotextiles 6 m in length were placed at the toe towards the interior of the embankment as a separator between the natural ground surface and the embankment fill material along the whole stretch of the highway. Frozen fill material as shown in Fig. 2.3 taken from the nearest borrow pit source (Pit 174) was used to construct the embankment tests sections with an average moisture content of 16%. In Chapter 3, the physical properties of this soil as well as its shear strength properties using a large-scale direct shear box at different environmental conditions were determined. The soil has fines content ranging from 11% to 13%, an average plastic limit of 16.4%, an average liquid limit of 24.6%, and a plasticity index of 6.6%. About 72% passing the 0.075 mm (No. 200) sieve was of silt fraction based on the results of the hydrometer test. The soil is classified as well-graded sand with silt and gravel to silty sand with gravel based on the Unified Soil Classification System (USCS). The foundation soil is predominantly organic (peat) based on frozen soil cores obtained in March 2017 from the centreline and at an offset from the embankment

toe. The organic mat is approximately 7 m thick. This is underlain by highly plastic clay with some presence of cobbles based on visual inspection of the grab samples. A third test section was instrumented at its midslope (Fig. 2.1a) in April 2017 to determine the influence of thin embankments (designed thickness for permafrost insulation) on permafrost temperatures. The thickness of this embankment is 1.8 m. Unlike the two thick embankment sections constructed in April 2015, the thin embankment is purely monitoring temperatures. This thin embankment section was already built during the 2015 construction season.

The woven geotextiles installed at the side slopes of the reinforced section have drainage capabilities (wicking) in addition to their reinforcement function. It was conceptualized they will provide drainage paths for the melt water during spring and summer seasons when the embankment undergoes thawing. The wicking yarns are hydrophilic and hygroscopic, which means that they attract water molecules and transport water, respectively. In the past, wicking geotextiles have been used in the following applications: (1) mitigating differential frost heaves, (2) minimizing the effect of swelling and shrinkage of expansive subgrades, (3) enhancing lateral drainage in areas with high water tables, and (4) minimizing moisture accumulation within the base course and/or subgrade. Some properties of the geotextile in the cross-direction are summarized in Table 2.1. This type of geotextile has been successfully used in the Dalton Highway Beaver Slide Area in Alaska to act as a capillary barrier and prevent the occurrence of frost boils (Zhang et al. 2014). A similar successful application was used in the Pioneer Scenic Byway in Montana to prevent the occurrence of frost heaves along the highway (Sikkema and Carpita 2016). For these studies the wicking geotextile were only used for its drainage and separation functions. Here, the geotextiles were laid out on the side slopes during construction as shown in Fig. 2.4a to provide reinforcement. These geotextiles have an overhang of 0.5 m (Fig. 2.4b) to allow water to

flow out of the embankment. The length of the geotextile installed in the embankment is 8.4 m to intercept the potential failure surface when the embankment thaws and if sloughing occurs. The geotextiles were spaced at every 900 mm of elevation. In the author's knowledge, this is the first application of using a wicking geotextile fabric with reinforcement as the primary function and in-plane drainage as secondary and using geotextiles as slope reinforcement for embankments in Arctic regions. Geogrids have previously been used as basal reinforcements for embankments in permafrost regions (Kinney and Connor 1987, Kinney and Connor 1990). However, they were used in polygonal grounds to bridge the development of voids when ice wedges thaw underneath the embankments. The interface strength properties between the woven geotextiles and the soil at different environmental conditions are presented in Chapter 4.

2.3. Field Instrumentation and Installation

Installation of instrumentations for the thick embankments commenced on April 14, 2015 and was completed on April 20, 2015. The temperature on site during construction ranged from -35°C to -2°C, with an average temperature of -18°C during fill material end dumping and compaction. Construction was halted when air temperatures were above -10°C. The road surface became wet closer to -5°C with ruts developing due to construction traffic. Prior to construction of the thick embankment test sections and installation of instrumentation, an initial lift of 600 mm was placed on the research site. Only snow along the road right-of-way and at the toe of the embankment where the data acquisition system was installed were removed during construction. Great care was taken to avoid stripping of the natural ground surface to protect the underlying permafrost. The control and reinforced embankment test sections were both instrumented with thermistor strings for temperature monitoring and ShapeAccelArrays (SAAs) to measure lateral displacements and settlements. These instrumentations were connected to a data acquisition system (DAQ) at an

offset from the toe of the embankment (Fig. 2.1a, b) which can be remotely accessed through satellite connection. Remote monitoring was done continuously from mid-February to mid-November when the solar panels can charge the batteries supplying power to the DAQ. Data from the DAQ were manually downloaded from mid-November to mid-February of the following year depending on site access conditions when the batteries have to be manually recharged. Additional instrumentations were installed at the research site in April 2017 to monitor the temperature in a thin embankment section (Fig. 2.1a) and the displacements occurring at the toe of the thick embankment sections (Fig. 2.1d). Although not presented here, Fredlund thermal conductivity sensors were installed in the field to measure suction in the embankment to establish a correlation with the unfrozen water content as the embankment undergoes thawing. Unfortunately, the sensors were embedded in the frozen core and no meaningful results were recorded during the monitoring period. Some of the cable sensors had also been inadvertently damaged during snow clearing operations.

2.3.1. Thermistor Strings

Thermistor strings were installed at different locations in the embankments and underlying foundation soil (Table 2.2). Thermistor strings in the control section are labelled as TS-C and are labelled TS-R for the reinforced section. Two thermistor strings were laid out horizontally at the top (TS-C1, TS-R1) and along the base (TS-C2, TS-R2) of the embankments, and another two vertically installed through the foundation at the centreline (TS-C3, TS-R3) and at the toe (TS-C4, TS-R4) for each test section. A schematic diagram showing the locations of these thermistor strings and their nodes are shown in Fig. 2.2a. The base thermistor is 600 mm above the natural ground surface, while the top thermistor is 500 mm below the road surface. The additional vertical thermistor strings installed in April 2017 at the foundation soil (TS-C5, TS-R5) are also shown in

Fig. 2.2a. The thermistor string installed at the midslope (TS-S) of the thin embankment section is shown in Fig. 2.2c.

2.3.2. ShapeAccelArrays

Vertical and horizontal ShapeAccelArrays (SAAs) were installed at midslope and midheight of both thick embankment sections to monitor lateral displacements and settlements, respectively, as shown in Fig. 2.2a and summarized in Table 2.2. SAAs in the control section are labelled as SAA-C and SAA-R in the reinforced section. The vertical SAAs (SAA-CV, SAA-RV) are located at an offset of 12 m from the embankment centreline, with its first node 400 mm below the slope surface. The vertical SAAs were anchored at the frozen foundation soil. Similarly, the horizontal SAA (SAA-CH, SAA-RH) were anchored inside the embankment either sitting on top of compacted frozen soil at the core of the embankment or below the 0°C isotherm. The outer ends of the horizontal SAAs are 12 m away from the embankment centreline. The first nodes of the horizontal SAAs are 400 mm below the slope surface. Additional SAAs were installed at the foundation close to the toe of the thick embankments in April 2017. One vertical SAA (SAA-CVT) was installed 3.5 m away from the toe of the control section, and two vertical SAAs were installed at 0.5 m (SAA-RVT1) and 3.5 m (SAA-RVT2) away from the toe of the reinforced section. These vertical SAAs have their first nodes above ground and were encased with PVC pipes to prevent damage. A 12 m long horizontal SAA (SAA-CHT) was installed 0.5 m away from the toe of the control section to a depth of 0.5 m below the ground surface. In addition to displacements, the SAA nodes also provide temperature measurements which can supplement the thermistor readings.

2.3.3. Strain Gauges

Strain gauges were installed on geotextile strips 4.2 m in width (Fig. 2.2b) parallel to the direction of wicking to measure the development of reinforcement strains as the embankment undergoes

thawing. The strain gauges can provide an insight to the effectiveness of the geotextiles in reducing lateral displacements at the slope. The strain gauges were attached to the geotextiles following the recommendations by Warren et al. (2010).

The wicking geotextiles were installed in the field along the 20 m long reinforced test section. Fig. 2.5 shows the installation of the strain gauge on geotextiles using an adhesive in between the wicking strands (Fig. 2.5a), the installation of connection terminals to the strain gauge (Fig. 2.5b), silicone rubber applied to the strain gauge (Fig. 2.5c) to protect it and the connection terminal from installation damage, and placement of the instrumented geotextile strip in the field (Fig. 2.5d). The geotextile strip was instrumented in the laboratory prior to installation in the field because of the workability and setting time for the adhesive used with the strain gauges is achieved in a more controlled environment (e.g., temperature, dust, moisture) compared to that at the site. Only a narrow strip of geotextile was instrumented instead of the whole geotextile width to make the transportation of the fabric from the laboratory to the field practical and decrease the risk of damaging the strain gauges. There is a 1.0 m overlap between the non-instrumented geotextile and the instrumented one as recommended by the geotextile supplier.

The wicking geotextile layers were laid out horizontally at every 900 mm from initial placement of fill material on both sides of the embankment. Only half of the embankment was instrumented with strain gauges and the instrumented geotextile layers installed at Els. 22.564 m (GT-E1.8), 23.464 m (GT-E2.7), and 25.264 m (GT-E4.5). A total of nine strain gauges were installed per geotextile layer (Fig. 2.2b): seven at the top and two at the bottom. The strain gauges at the top of the fabric were installed every 1.0 m with the first strain gauge installed 1.5 m away from the edge of the slope. The letters on Fig. 2.2b indicate the ID of the strain gauge and are different from the letters used on Fig. 2.2a. The strain gauges at the bottom of the fabric were

spaced by 3.0 m with the first strain gauge installed 3.5 m away from the edge of the slope. The two strain gauges at the bottom of the fabric were installed directly underneath the strain gauges at the top of the fabric to account for possible effects of bending on the geotextile strains.

2.4. Monitored Results and Field Performance

2.4.1. Air Temperatures

Fig. 2.6 shows the mean daily air temperatures recorded by Environment and Climate Change Canada (ECCC) weather stations for Inuvik and Tuktoyaktuk, and from National Aeronautics and Space Administration (NASA) satellite data for the research site from January 1, 2015 to July 31, 2018. An automatic weather station (AWS) was installed at the research site in March 2017 (Fig. 2.1c) and monitored temperatures since installation are also shown in Fig. 2.6 (solid line). Table 2.3 summarizes the locations of the ECCC weather stations and at the research site. Fig. 2.7 shows a comparison of the mean daily air temperature at one location compared to another from the period of March 17, 2017 to July 31, 2018. The fits showed good correlation with the slope of the fitted line (B in Fig. 2.7a to Fig. 2.7d) almost or equal to 1.0. The intercepts (A in Fig. 2.7a to Fig. 2.7d) indicate the temperature difference between stations. The temperature in Inuvik is 3.2°C (Fig. 2.7a) and 2.0°C (Fig. 2.7b) warmer than Tuktoyaktuk and the research site, respectively. Tuktoyaktuk is 1.2°C colder than the research site (Fig. 2.7c). Satellite data obtained from NASA for the research site was also compared with the local weather station (Fig. 2.7d) and showed that using satellite data for this site is reliable in determining local conditions in the absence of local data. Ten-year historical data (2006 - 2016) from ECCC weather stations in Inuvik and Tuktoyaktuk show there is an average warming of 0.26°C/year.

2.4.2. Observations after Construction

Fig. 2.8 shows photographs of observations at the start of the first thawing period. Fig. 2.8a shows longitudinal cracks that had developed at the crest of the control section in July 2015. The reinforced section only showed thin cracks during the same period. Water draining from the embankment slopes during the first thawing ponded at the toe of both sections in October 2015 (Fig. 2.8b). Fig. 2.8c shows a photo of the west side of the embankment (upstream side) when the culvert close to the research site got clogged during spring thawing on May 18, 2016. Two key issues were noted with the clogged culvert and the water ponding at the toe of the embankment: (1) accelerated thawing of the frozen foundation soil; and (2) water seeping into the embankment towards the frozen core of the embankment. During previous site visits in April 2016 and April 2017, the depth of snow cover was approximately measured using a survey rod with 20 mm at the crest of the embankment, 450 mm at the mid-slope, 705 mm at the toe, and 610 mm at the natural ground surface 10 m away from the toe.

2.4.3. Temperature Readings

2.4.3.1. Phase 1: Thick Embankments

The temperature readings recorded by the thermistor strings and SAAs for both control and reinforced sections were similar with measured temperature difference between them ranging from 0.05°C to 0.4°C; therefore, only the recorded readings from the control section are presented. The temperatures recorded for the reinforced section are presented in Appendix A (Fig. A1). Fig. 2.9 shows the temperature readings from the horizontally-laid thermistor strings at the top (Fig. 2.9a) and base (Fig. 2.9b) as well as the vertically-laid thermistor strings at foundation centreline (Fig. 2.9c) and toe (Fig. 2.9d) of the embankment. They are plotted at different times. The top thermistor (TS-C1) shows that there is uniform warming and cooling across the road surface in response to

the ambient air temperatures. The warmest temperatures recorded by TS-C1 were between the months of July and August. It can be seen that the temperatures for August 2017 were warmer than in August 2015 and 2016. The base thermistor (TS-C2) shows that from the embankment centreline to about 11.5 m towards the toe, the core of the embankment has remained frozen since end-of-construction, while beyond this distance the seasonal temperature fluctuations occur on the embankment slopes. TS-C2-C was below 0°C in August 2015. It has since been experiencing warming and the extent of the frozen core decreasing.

The temperature readings (TS-C3) show that the foundation at the centreline remained below -3°C for the three-year monitoring period. The month of December for each year was when TS-C3 recorded the warmest temperatures due to seasonal lag. Warming in the foundation was observed in December but the thickness of the fill material for the test sections provided adequate insulation preventing permafrost thaw from the centreline to the shoulder.

The thermistor string at the toe (TS-C4) recorded the same warming trend for the months of August. It should be noted that the seasonal thaw depth at the toe is ranging between 0.5 and 1.5 m from the natural ground surface and not where the line crosses the 0°C ordinate. TS-C4-A and TS-C4-B are 1.0 m apart which only provides temperature at these depths and not in between the nodes. This warm temperature at the toe during the winter months may be attributed to the reduced extraction of heat as snow accumulated near the toe. It was observed during installation of an additional sensor at the test site in late August 2017, that the frozen ground at the toe of the embankment was approximately at 0.53 m below ground surface.

Fig. 2.10 shows the temperature readings from the vertical (Fig. 2.10a) and horizontal (Fig. 2.10b) SAAs installed mid-slope and mid-height of the control section, respectively. Similar to TS-C1 and TS-C2, the SAAs recorded the warmest temperatures in August of each year close to

the slope surface. The seasonal temperature fluctuation has reached to 1.7 m for SAA-CV from the slope ground surface in August 2017, compared to the 1.2 m depth in August 2015. The temperatures recorded by SAA-CV confirm that the foundation soil is still frozen at this offset from the embankment centreline and that the SAAs are properly anchored at this depth. In Fig. 2.10b, SAA-CH showed that until October 2016 the core of the embankment fill has remained frozen up to a height of 2.7 m from the base of the embankment and 5.0 m away from its centreline towards the slope. For the third monitoring year, the nodes that used to be below 0°C (SAA-CV-P5, SAA-CH-P10) have experienced warming as high as 2.5°C in August 2017. This contributed to the decrease in the thickness and extent of the frozen core as was observed with the temperature readings from TS-C2. The temperatures recorded from SAA-RV and SAA-RH in the reinforced section are also shown in Appendix A (Fig. A2).

Fig. 2.11 shows the comparison of temperature nodes close to the embankment surface (Fig. 2.11a) and in the foundation soil (Fig. 2.11b) with the mean daily air temperature at the research site using NASA satellite data. In Fig. 2.11a, the temperature nodes closest to the embankment surface respond quickly to the ambient air temperature during the spring (transition) and summer months, but exhibit a seasonal lag during the winter months for the SAA nodes. The SAA nodes closest to the slope ground surface (SAA-CV-P1, SAA-RV-P1) are slightly cooler than the thermistor nodes close to the road surface because of the insulation provided by the snow cover on the slopes resulting from both snow clearing to maintain accessibility as well as natural snow drifting. There are data gaps in December of each year due to issues with power supply. Fig. 2.11b shows temperature nodes in the foundation soil 1.5 m below the natural ground surface. TS-C3-B has reached a maximum temperature of -3.6°C throughout the three-year monitoring period. SAA-CV-P15 warmed as high as -2.5°C. These two nodes are at the same depth in the foundation.

The thermistor node at the centreline has the full thickness of the embankment at 5.3 m, compared to the mid-slope SAA node which only has 3.1 m. TS-C4-B (1.5 m below the natural ground surface at the toe) has its maximum temperature at -1.2°C for the first and third year but warmed as high as -0.8°C in the second year, possibly due to remnant effects of water ponding due to the clogged culvert on the west side of the embankment in May 2016.

The warming trends observed in the temperature nodes (thermistors, SAAs) in the embankment fill and foundation soil are attributed to two factors: (a) warmer and longer summer months recorded from the AWS led to deeper thaw penetration in the slopes and foundation soil, and (b) heat extraction during the winter months was attenuated because of the snow accumulation at the embankment slopes. Wu and Niu (2013) had similar observations indicating that there is an overlapping influence of warming air temperatures and thermal disturbance on the permafrost underneath the embankment. In later chapters, pure heat transfer (Chapter 5) and coupled thermal-mechanical (Chapter 6) numerical modelling were conducted to further investigate how changes in ground temperatures impact the long-term performance of embankments in Arctic regions.

With warming air temperatures, the depth of thaw penetration will increase and the maximum depth of refreezing will be shallower since snow cover minimizes heat extraction during the winter months. With this thermal condition, talik growth may occur as has been reported in the literature (McHattie and Esch 1983, Yu et al. 2012). Once taliks form, additional heat source in the ground causes further thawing of the permafrost and an unending cycle of thawing will be initiated, eventually leading to embankment failure (Esch 1988).

The frozen core of the embankment is by definition permafrost as the soil has remained continuously below 0°C for at least 2 years. It should be pointed out that the embankment is an engineered structure using frozen soil. The environment (winter conditions) when the embankment

was constructed with frozen soil means the thermal regime was below 0°C. Under these conditions, the permafrost table aggraded into the embankment fill. The frozen core of the embankment, however, has been shrinking since completion of the test sections based on the measured ground temperatures. The shrinking of the frozen core is an important consideration in the context of climate change as will be presented in Chapter 5.

2.4.3.2. Phase 2: Thin Embankment and Additional Foundation Thermistors

Fig. 2.12 shows the temperature distribution at the midslope of the thin embankment section at different times. In comparison to the thick embankments, the fill material has completely thawed following the embankment construction at this location. There was a slight decrease in the thickness of the active layer from 0.5 m to 0.3 m, which confirms that the embankment is providing some insulation to the permafrost foundation. The warming trend presented earlier were also observed in the thin embankment section. Preliminary thermal numerical models by De Guzman et al. (2019)[3] reflected that the permafrost table is at the natural ground surface at the centreline of the embankment. The original design objective of preserving the permafrost was achieved for both embankment thicknesses at the research location.

Fig. 2.13 shows the temperatures recorded by TS-C5 installed at a 3.5 m offset from the embankment toe of the control section. Similar to the observations made at TS-C4, the depth of the permafrost table is somewhere in between the 0.1 m and 1.1 m depths from the natural ground surface. The SAA nodal temperatures in SAA-CVT are compared with TS-C5 (Fig. 2.14) at different time steps in October 2017. The temperatures recorded by the SAA are showing similar trends throughout its depth compared to the thermistor string. This indicates temperatures from

[3] Chapter 5 of this manuscript

SAAs can be relied upon in the absence of thermistor strings. SAAs provide displacement measurements that are unavailable from thermistor strings. From Fig. 2.14a, it shows that the extent of the seasonal thaw depth is near at the 0.5 m depth. There are no thermistor strings installed beside the SAAs installed at the midslope of the thick embankments (SAA-CV, SAA-RV), but the lateral displacements recorded that will be discussed in the following section support that movements occur close to 0°C.

2.4.4. Lateral and Vertical Displacements

2.4.4.1. Phase 1: Embankment Fill (SAAs installed in April 2015)

Recorded lateral displacements for both control and reinforced sections are shown in Fig. 2.15. The lateral displacements recorded in the reinforced section (Fig. 2.15b) are less than that of the control section (Fig. 2.15a). The largest displacements occurred at the SAA node closest to the slope surface during the first thawing season after construction. The lateral displacements in the reinforced section are consistently less than that of the control section. The mobilization of tensile forces in the geotextile reinforcements reduced the lateral movements of the embankment slope as expected. Although the temperature of the SAA nodes P6 and P7 were recorded to be between -1°C and 0°C (Fig. 2.10a), there have been movements observed in the three-year monitoring period, particularly larger for the control section. The thickness of the soil from the base of the embankment that has not moved in the control section is approximately 0.62 m and 0.75 m for the reinforced section based on the SAA readings where the temperatures are less than -2°C. As will be presented and discussed in Chapter 3, large-scale direct shear tests of compacted frozen and unfrozen soils from the test site showed that there is a significant reduction in shear strength and shear stiffness after the first cycle of thawing (e.g., thawing following embankment construction) and thus leading to lateral displacements.

In the following discussion, three nodes at both test sections were selected along the length of the vertical SAA (Fig. 2.15). Fig. 2.16a shows the lateral displacements of P1 and P3 during the first spring thawing, following embankment construction. The lateral displacements are similar for both test sections until displacements at P1x and P3x were reached. For P1x, about 30 mm of displacements were mobilized before the force in the geotextile was mobilized. As air temperatures were warming, the seasonal depth of fluctuation increased and thus started displacing at deeper nodes. For both P1x and P3x, initial displacements were required before the geotextile fabric can provide resistance against lateral movements. Fig. 2.16b shows the lateral displacements over the three-year monitoring period for three different nodes at different elevations (P1, P3, and P5) for both test sections. The geotextiles provided the most resistance against lateral movements during the first thawing after construction. There are minimal to almost no displacements during the winter months until the spring season of the following year. Since end-of-construction of the test sections, the embankment was able to consolidate for three thawing seasons before the highway was officially opened to traffic in November 2017.

Table 2.4 summarizes the lateral displacements for the control and reinforced sections from spring thawing (ST) to winter freezing (WF) at different elevations. The largest lateral displacements occurred during the first spring thawing and, as expected, were recorded at the top of the vertical SAAs. Contrary to initial expectation that the lateral displacements would decrease over time, the increased displacements during the third year (ST3 to WF3) were slightly larger than the second year, except for P3 of the reinforced section. This is attributed to the warmer temperatures recorded in the mid-slope of the embankment for the third year (Fig. 2.10a). Frozen soil provides anchor support to the vertical SAAs. In the case of P5, the once frozen soil during ST1 and ST2 experienced warmer temperatures above 0°C in ST3 and additional lateral

displacements were mobilized, propagating to the slope surface. The displacement at P5 in the reinforced section is significantly less than that of the control section during ST1, but has gradually increased during the monitoring period due to warming air temperatures. Although these displacements are increasing due to thawing at the slopes, the cumulative displacements of the reinforced section at different elevations are considerably less than that of the control section, confirming that the geotextiles are providing reinforcement to the high fill section. From the summer site visits conducted by the author, there are other high fill sections along the ITH that have shown distress in the form of side slope sloughing and shoulder cracking, especially at locations where air temperatures are warmer. Different design configurations (slope inclination, reinforcement length, reinforcement spacing) are investigated in Chapter 6 using numerical modelling to study the use of geotextiles as slope reinforcement in Arctic regions.

Table 2.5 summarizes the difference between the lateral displacements of the control and reinforced sections for each year of the monitoring period. The average lateral displacement recorded in the control section during the winter freezing and spring thawing (e.g., WF1 to ST2) is subtracted from the average lateral displacement of the reinforced section during the same period. The largest difference between the two sections occurred during the third year where thawing of the previously frozen soil contributed to additional displacements. Both test sections are still displacing due to thawing at the slopes, but the addition of woven geotextiles helped in mitigating slope movements. The rate of lateral displacements with respect to time during spring thawing are summarized in Table 2.6 for both test sections. P3 and P5 of the control section have rates increasing from ST2 to ST3, and similarly for P1 and P5 of the reinforced section. Based on these observations, there are two possible scenarios: (1) the development of lateral displacements will eventually decrease over time, or (2) the development of these lateral displacements will

increase over time due to the effects of warming where previous compacted frozen soil begins to thaw in the embankment and possible loss of toe support as the seasonal thaw depth in foundation soil increases. The deformation of the embankment is closely related to the thermal changes in the embankment fill and foundation soil. The embankment fill affects the thermal behaviour of the foundation, and any increase in the foundation temperature can lead to compression of the native soil, which affects embankment stability. Proactive maintenance operations (e.g., snow clearing during the winter months) should be planned accordingly to reduce the heat trapped in the winter.

Fig. 2.17 shows the vertical settlements of the control (Fig. 2.17a) and reinforced (Fig. 2.17b) sections. Most of the settlements occurred during the first year of thawing. At the end of the first year of monitoring, both horizontal SAAs at the outermost node recorded 275 mm of vertical settlement. The range of settlements in the third year of monitoring is between 225 and 325 mm in the control section, and between 275 mm and 325 mm in the reinforced section. Unfortunately, the temperature recorded at the anchor point (SAA-CH-P17, SAA-RH-P17) has experienced above 0°C temperatures (Fig. 2.10b) in the third year which could have slightly affected the settlement readings.

2.4.4.2. Phase 2: Foundation Soil (SAAs installed in April 2017)

Fig. 2.18 shows the lateral displacements at the foundation soil from SAA-CVT (Fig. 2.18a) and SAA-CHT (Fig. 2.18b). The displacements are occurring to a depth of 4 m for SAA-CVT in between 15 mm and 20 mm. Although these are not significant, it indicates that movements on the permafrost are occurring. Compared to SAA-RVT2, there is a natural channel close to SAA-CVT (Fig. 2.1d) which may be influencing its behaviour. In Fig. 2.18b, an average of 240 mm of lateral displacement was recorded. The movement at this location is influenced by the possible movements happening at the toe of the embankment as well as the seasonal freezing and thawing

at the active layer. The non-uniform displacements indicate that heterogeneous nature of the native soil and the backfill used for the sensor.

Fig. 2.19 shows the lateral displacements at the foundation soil from SAA-RVT1 (Fig. 2.19a) and SAA-RVT2 (Fig. 2.19b). The first node of these SAAs are close to the ground surface. The top of the SAA and its communication cables are protected by a PVC pipe cap. These pipe caps are free to move because the bentonite backfill used to hold it in place become wet from the snowmelt. The PVC pipe cap has been moved in previous site visits to keep the pipe in the vertical. It is practical to evaluate the movements of the SAA at a location where pipe movement due to alignment can be isolated from the movements of the foundation due to the embankment loading. The displacements at SAA-RVT2 are negligible compared to the slight movements happening at 0.5 m from the toe (SAA-RVT1). The influence of embankment loading on the permafrost foundation is somewhere between 0.5 m and 3.0 m.

2.4.5. Strain Gauge Readings

Fig. 2.20 shows the strain gauge readings for the three layers of geotextile at Els. 22.564 m (GT-E1.8, Fig. 2.20a), 23.464 m (GT-E2.7, Fig. 2.20b), and 25.264 m (GT-E4.5, Fig. 2.20c). All wire connections of the strain gauges on GT-E1.8 stopped working after February 2016 as they were damaged due to accidental snow clearing. Similar to the observations with the vertical SAAs, the largest strains (mobilization of forces) in the reinforcements occurred during the first thawing season. There were also minimal to no straining recorded during the winter months. From the latest recorded readings (April 20, 2018), the strain gauges were reading between 0.0005 to 0.0023% elongation. Although these are not significant strains, these plots confirm the relative mobilization of tensile forces that reduced lateral displacements at the slopes. As indicated, the design of the embankment was not modified for the reinforced section. The slopes were graded (3H:1V) to

minimize the potential of slope instabilities and provide adequate thermal insulation to the permafrost foundation. The use of geotextiles can provide reinforcement to build steeper slopes and minimize required fill material to construct the embankment. It has been observed however in the literature that steeper slopes are detrimental to the thermal stability underneath the embankment shoulder (McGregor et al. 2010). The economic benefit of using geotextiles to build steeper slopes and using geotextiles to reinforce slopes that protect the underlying permafrost are investigated in Chapter 6.

2.5. Chapter Summary and Conclusions

Three instrumented test sections were constructed along the ITH to monitor the performance of highway embankments constructed during the winter season. One of the test sections was reinforced with wicking woven geotextiles at its side slopes. The general thermal behaviour of the embankments provided new insight into the thawing of frozen fills placed in the winter and the deformation behaviour revealed some interesting effects.

1. The temperature sensors have shown a warming trend in the embankment fill and foundation soil for both thick (5.3 m) and thin (1.8 m) embankments. This is attributed to warming air temperatures and the heat trapped in the embankment during the winter months when the embankment slopes are covered in snow. The core of the thick embankments has remained frozen in the monitoring period but has reduced in size since end-of-construction. The thaw-depth at the embankment toes have also increased during this period. Thawing of the previously compacted frozen soil may lead to reduction in shear strength available to resist traffic loading and development of larger lateral displacements and settlements. The increasing seasonal thaw depth at the toe might also lead to loss of support and cause instability in the embankment slopes. The thin embankment shows that there is a slight aggradation of the

original permafrost table at the midslope location indicating that the embankment is providing insulation.

2. Largest lateral displacements were recorded in the summer following construction of the thick embankments and attributed to the thawing of the frozen soil at the slopes. The embankments were allowed to drain for three years to overcome the development of lateral displacements, which can otherwise affect performance if the highway was opened to traffic right after its construction. Although lateral displacements that occurred on the second and third year of thawing were less than that at end-of-construction, the seasonal thaw depth at the slopes have gone deeper and led to additional displacements.

3. The addition of the woven geotextiles with wicking as secondary function to its primary purpose of reinforcement has reduced the lateral displacements as the embankment slope experiences seasonal freezing and thawing. The control section remains stable even without slope reinforcement, but development of longitudinal cracks and settlements can eventually lead to serviceability problems as the depth of thaw penetration increases due to climate change.

The monitored field results for these test sections, together with the results of the laboratory tests conducted on the soil (Chapter 3) and the geotextile (Chapter 4), will be used in Chapter 6 to calibrate a coupled thermal-mechanical model and investigate the operating mechanisms contributing to the performance of the embankment test sections. The potential behaviour of these embankments under climate change conditions is also being investigated via thermal numerical modelling, which will be presented in Chapter 5.

Table 2.1. Properties of the wicking woven geotextile fabric (provided by TenCate).

Mechanical Properties	Units	Minimum Average Roll Value
Tensile Strength (at ultimate)	kN/m	78.7
Tensile Strength (at 2% strain)	kN/m	13.1
Tensile Strength (at 5% strain)	kN/m	56.9
CBR Puncture Strength	N	10235
Permittivity	sec^{-1}	0.24
Apparent Opening Size	mm	0.43
Wet Front Movement (vertical)	inches	6.0
Wet Front Movement (horizontal)	inches	73.3

Table 2.2. Summary of nodes and spacing for thermistor strings and SAAs.

Instrumentation	Label	Location	Orientation	Description
Thermistor Strings	TS-C1/TS-R1	Top	Horizontal	4 nodes spaced @ 2.0 m
	TS-C2/TS-R2	Base	Horizontal	7 nodes spaced @ 3.0 m
	TS-C3/TS-R3	Foundation	Vertical	4 nodes spaced @ 1.0 m
	TS-C4/TS-R4	Toe	Vertical	4 nodes spaced @ 1.0 m
	TS-C5/TS-R5	Toe	Vertical	7 nodes spaced @ 1.0 m
	TS-S*	Midslope	Vertical	13 nodes spaced @ 0.5 m
SAAs	SAA-CV/SAA-RV	Midslope	Vertical	16 nodes spaced @ 0.305 m
	SAA-CH/SAA-RH	Midheight	Horizontal	16 nodes spaced @ 0.500 m
	SAA-CVT SAA-RVT1 SAA-RVT2	Toe	Vertical	11 nodes spaced @ 0.500 m
	SAA-CHT	Toe	Horizontal	25 nodes spaced @ 0.500 m

* All instrumentations are in the vicinity of the thick embankment sections, except for TS-S installed at the midslope of the thin section

Table 2.3. Location of the research site and weather stations in Inuvik and Tuktoyaktuk.

Location	Classification	Latitude	Longitude
Inuvik	ECCC Weather Station	68°18’14” N	133°28’59”W
Research Site	AWS and NASA Satellite	69°01’06” N	133°16’16” W
Tuktoyaktuk	ECCC Weather Station	69°26’00” N	133°01’00” W

Table 2.4. Lateral displacements at different elevations for control and reinforced sections at different seasonal stages.

Section	Elevation (m)	Lateral Displacements (mm)			
		ST1 to WF1	ST2 to WF2	ST3 to WF3	Cumulative
Control	23.464 (P1)	190.4	57.5	63.0	310.9
	22.854 (P3)	124.5	42.4	49.7	216.6
	22.244 (P5)	54.8	28.7	36.4	119.9
Reinforced	23.464 (P1)	147.0	45.3	47.9	240.2
	22.854 (P3)	73.9	35.6	25.2	134.7
	22.244 (P5)	6.1	15.0	32.4	53.5

Table 2.5. Difference between lateral displacements of control and reinforced sections.

Elevation (m)	Lateral displacements (mm)		
	Year 1 March 02, 2016	Year 2 March 06, 2017	Year 3 February 16, 2018
23.464 (P1)	44.9	57.1	75.3
22.854 (P3)	51.7	58.5	86.2
22.244 (P5)	49.8	63.7	70.4

Table 2.6. Rate of lateral displacements with respect to time during spring thawing for control and reinforced sections.

Season	Rate of lateral displacements (mm/day)					
	Control Section			Reinforced Section		
	23.464 m (P1)	22.854 m (P3)	22.244 m (P5)	23.464 m (P1)	22.854 m (P3)	22.244 m (P5)
ST1	2.46642	1.66029	0.76302	1.88587	0.85729	0.10196
ST2	1.04318	0.68625	0.45298	0.70630	0.54902	0.16035
ST3	0.99781	0.79191	0.66251	0.97060	0.49394	0.59466

Fig. 2.1. Site photos: (a) aerial view of the completed test sections along the highway, (b) satellite and DAQ at the toe of the embankment, (c) weather station close to the research site, and (d) locations of additional instrumentations installed in April 2017.

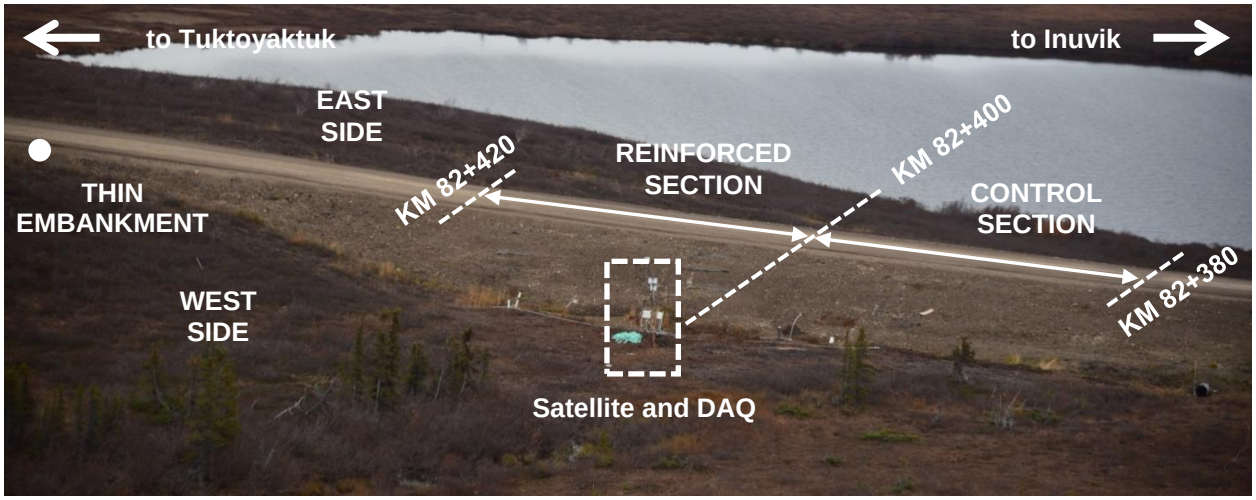

(a)

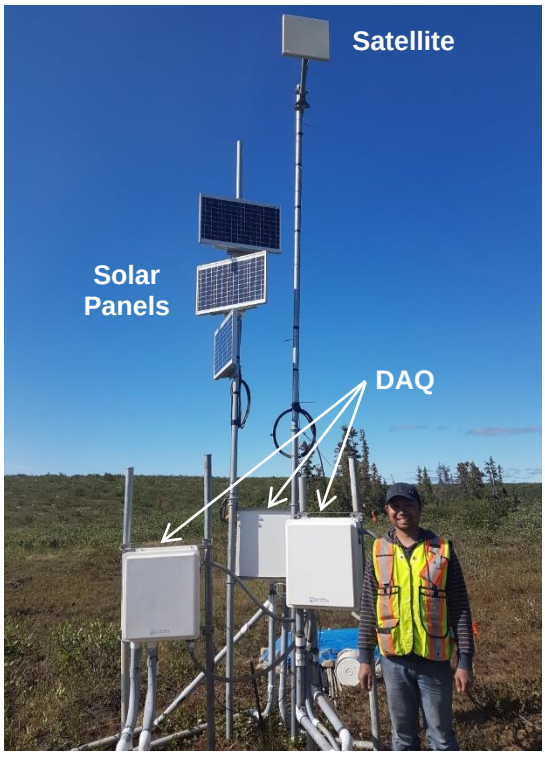

(b)

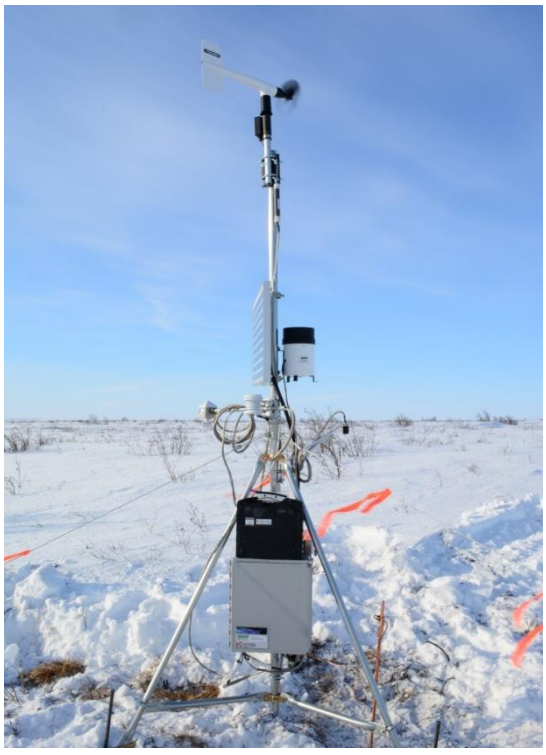

(c)

Fig. 2.1 (continued)

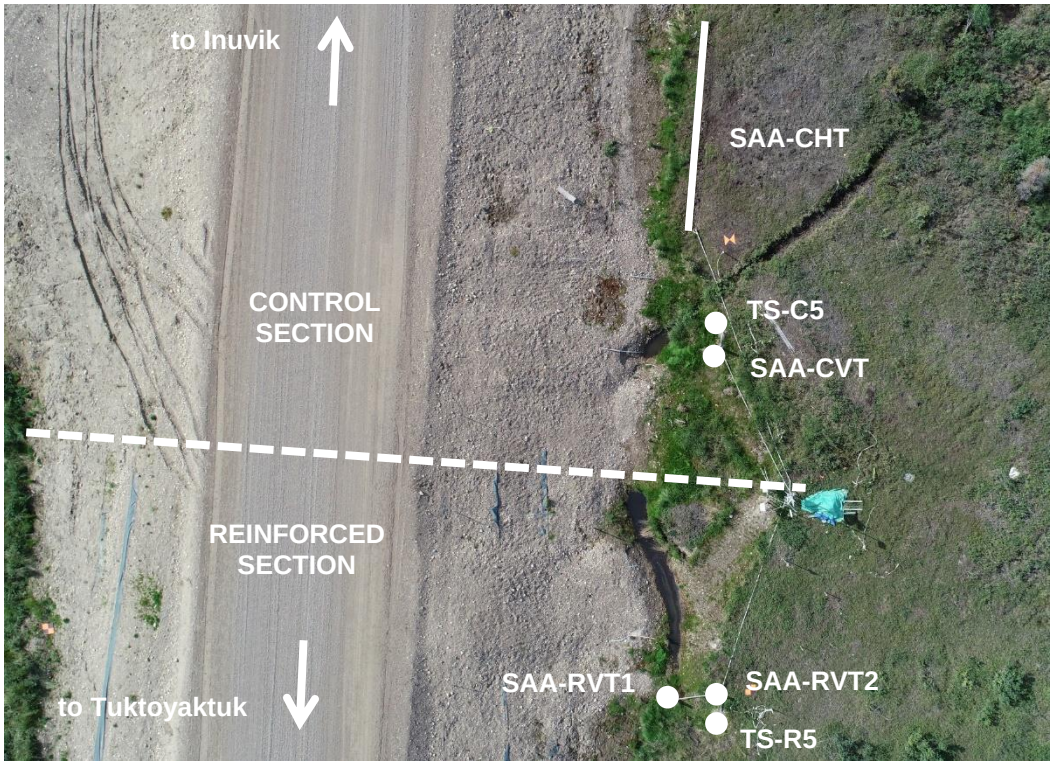

(d)

Fig. 2.2. Instrumentation installed in the embankments: (a) cross-section of thick embankment section with wicking geotextiles installed, (b) strain gauge layout in geotextile fabric, and (c) cross-section of thin embankment section. All units in metres.

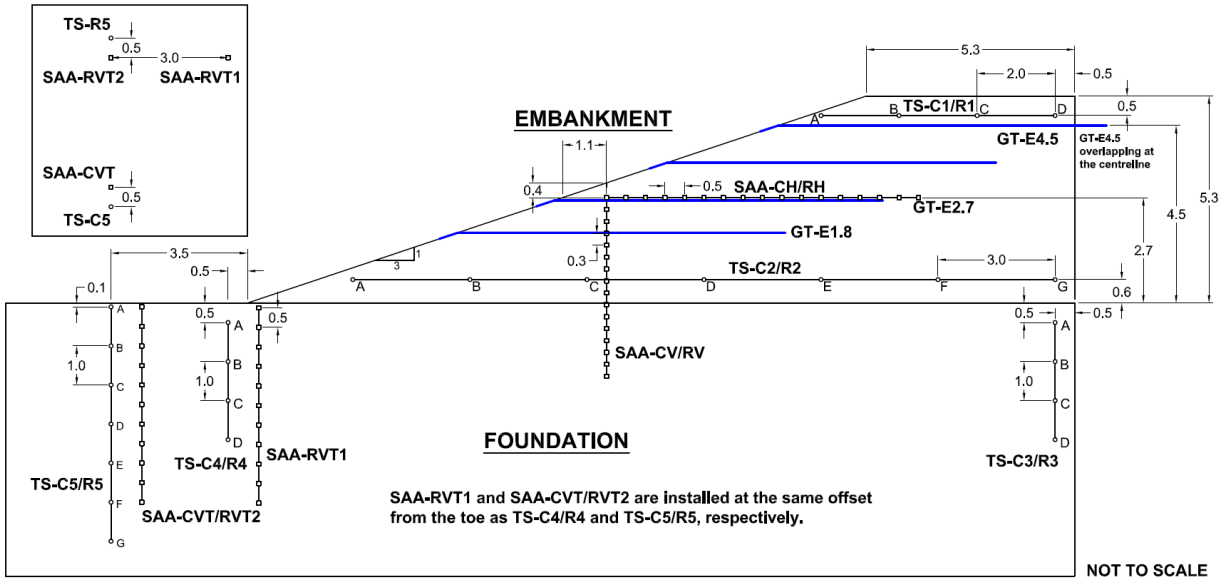

(a)

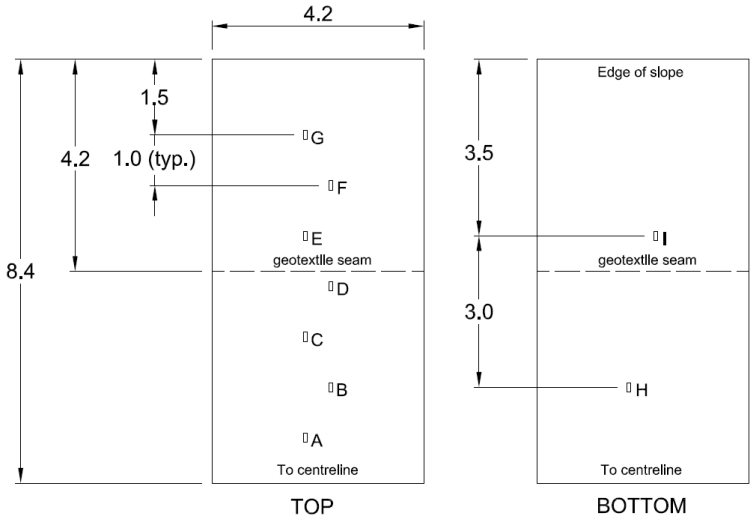

(b)

Fig. 2.2 (continued)

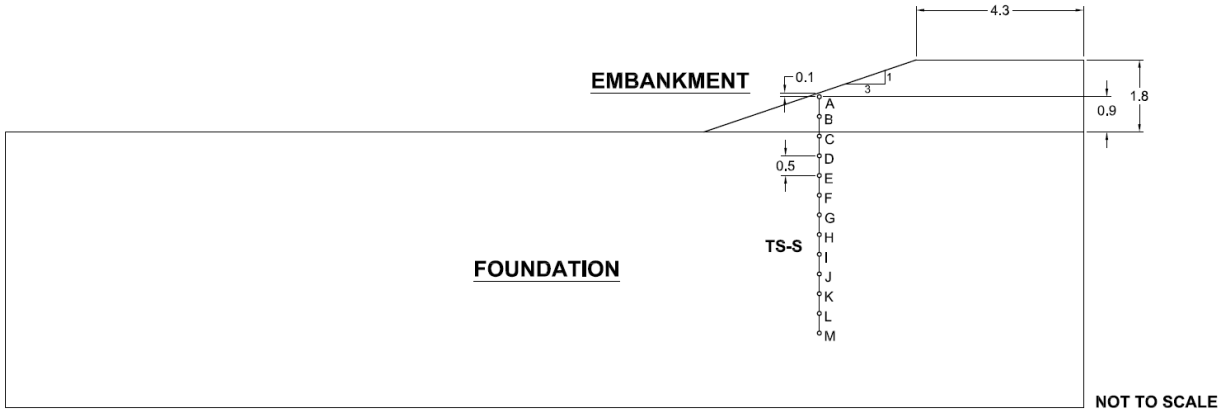

(c)

Fig. 2.3. Frozen soil used from borrow source pit (Pit 174) during embankment construction at KM 82+380.

Fig. 2.4. Wicking geotextiles in the reinforced embankment section: (a) installation of wicking geotextiles and (b) geotextile overhang for wicking function.

(a)

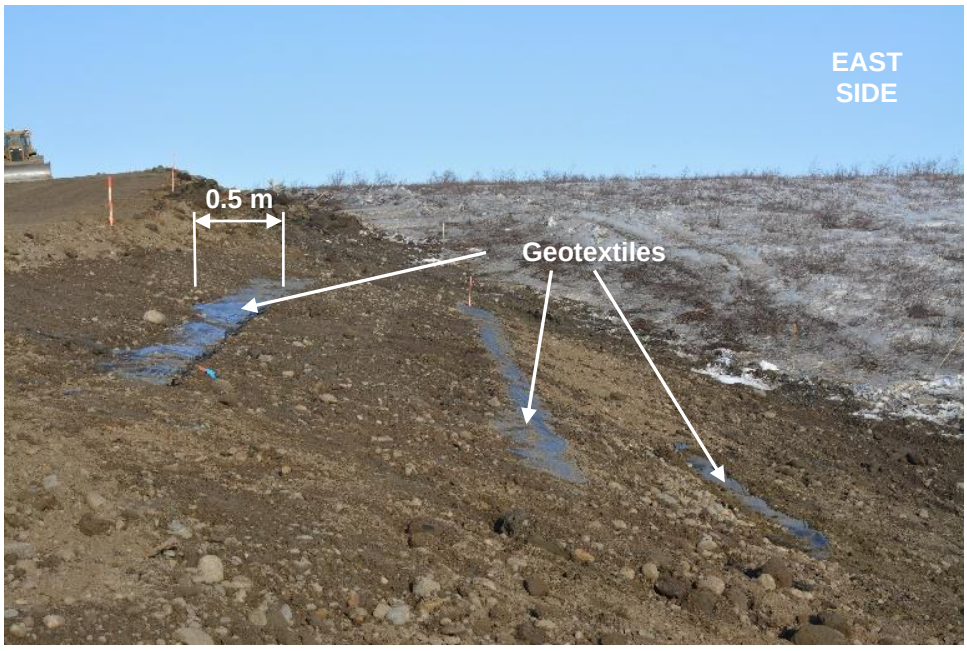

(b)

Fig. 2.5. Strain gauge attachment on wicking geotextile: (a) resin placement on the underside of strain gauge, (b) soldering of connections to communication cables, (c) epoxy coating added for strain gauge protection, and (d) geotextile installation in the field.

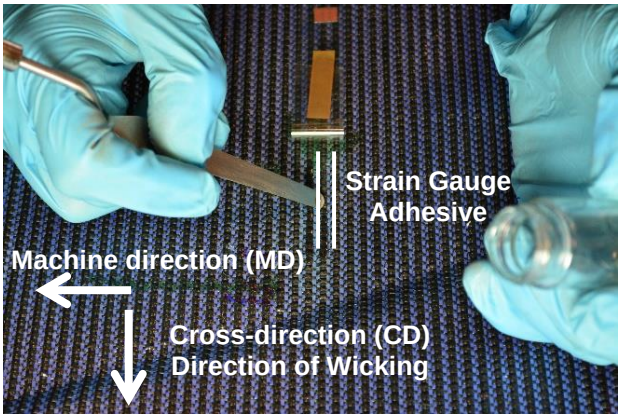

(a)

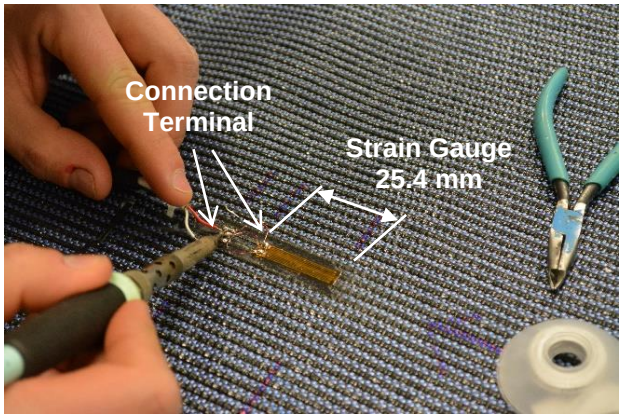

(b)

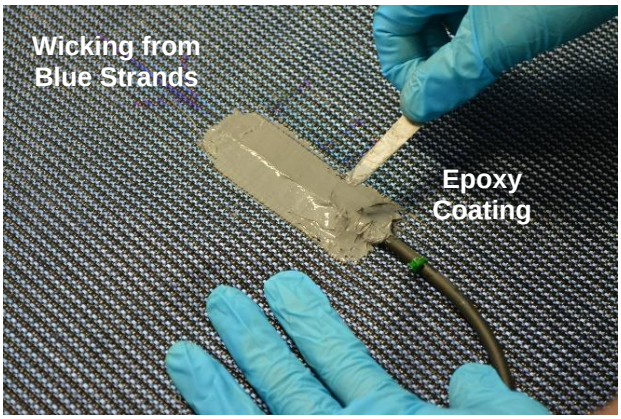

(c)

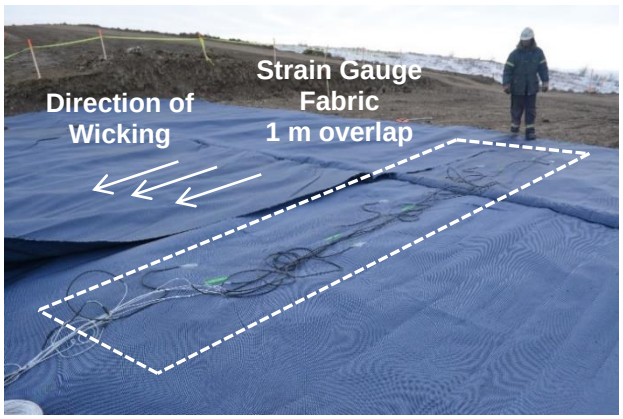

(d)

Fig. 2.6. Mean daily air temperatures recorded at different locations along ITH.

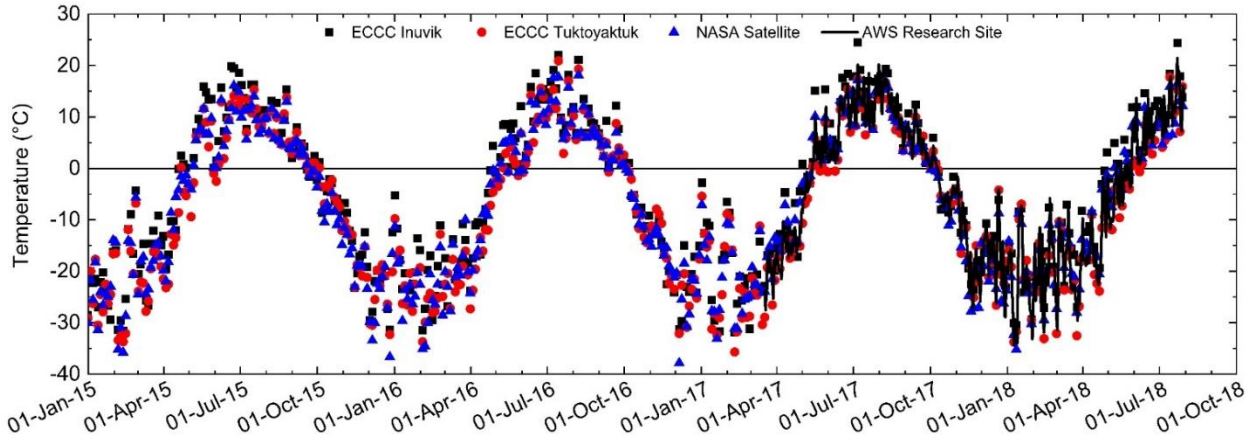

Fig. 2.7. Comparison of recorded mean daily air temperatures (MDAT) from March 17, 2017 to July 31, 2018: (a) ECCC Inuvik vs. ECCC Tuktoyaktuk, (b) ECCC Inuvik vs. AWS Research Site, (c) ECCC Tuktoyaktuk vs. AWS Research Site, and (d) NASA Satellite vs. AWS Research Site.

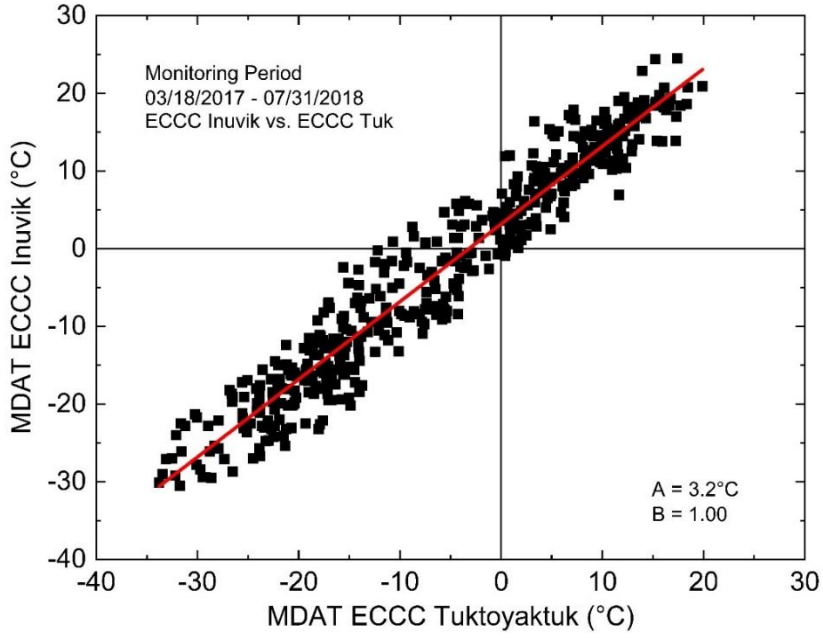

(a)

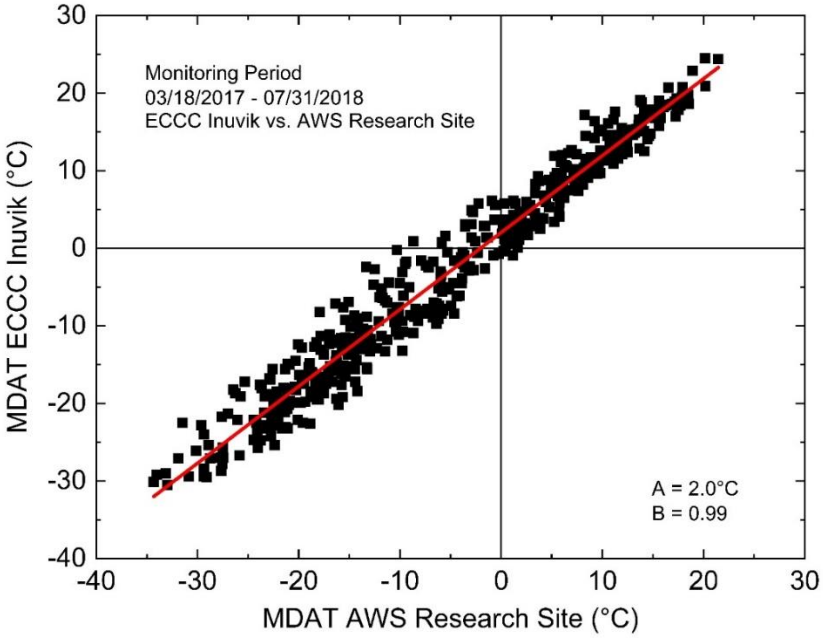

(b)

Fig. 2.7 (continued)

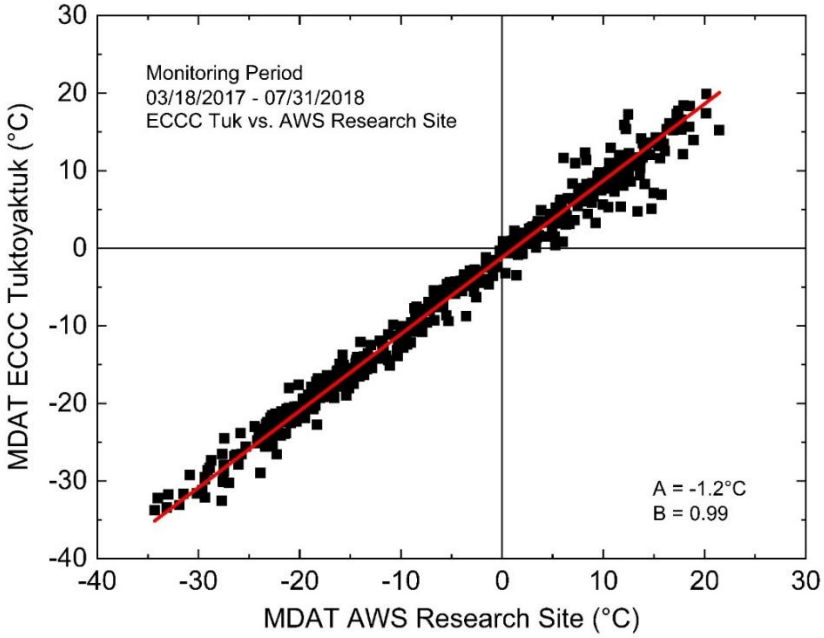

(c)

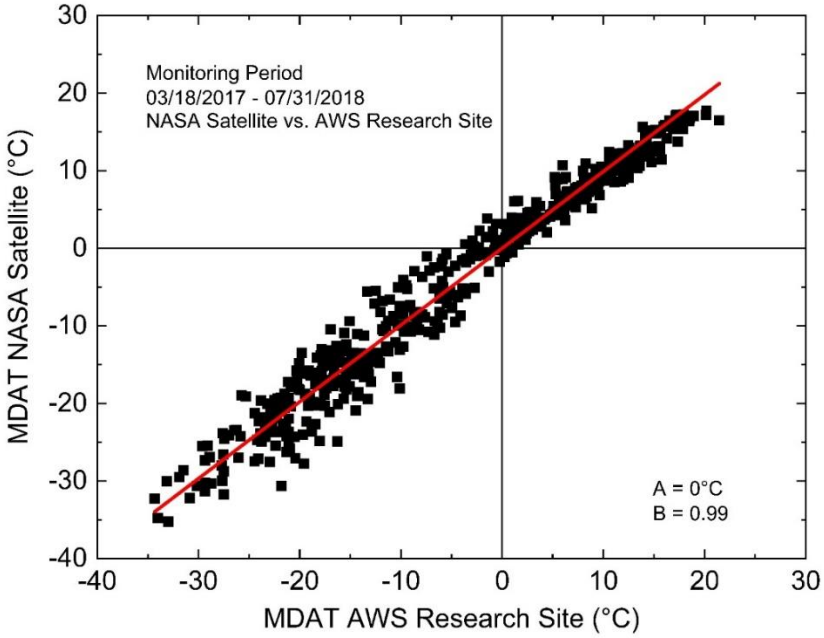

(d)

Fig. 2.8. Field observations after construction: (a) longitudinal cracks along the crest of control section in July 2015, (b) ponding at the toe of the embankment section in October 2015, and (c) flooding on the west of embankment section in May 2016. Photo in (a) courtesy by L. Arenson. Photos in (b) and (c) courtesy by DOT-GNWT.

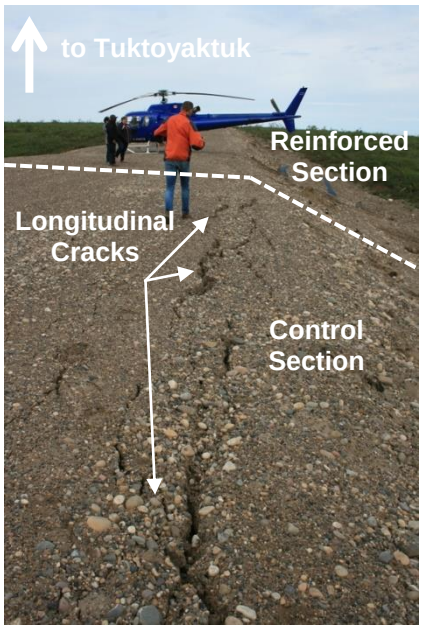

(a)

(b)

(c)

Fig. 2.9. Temperature readings at different time steps at different locations in the control embankment section: (a) top, (b) base, (c) centreline, and (d) toe. EOC: end-of-construction and EOY: end-of-year.

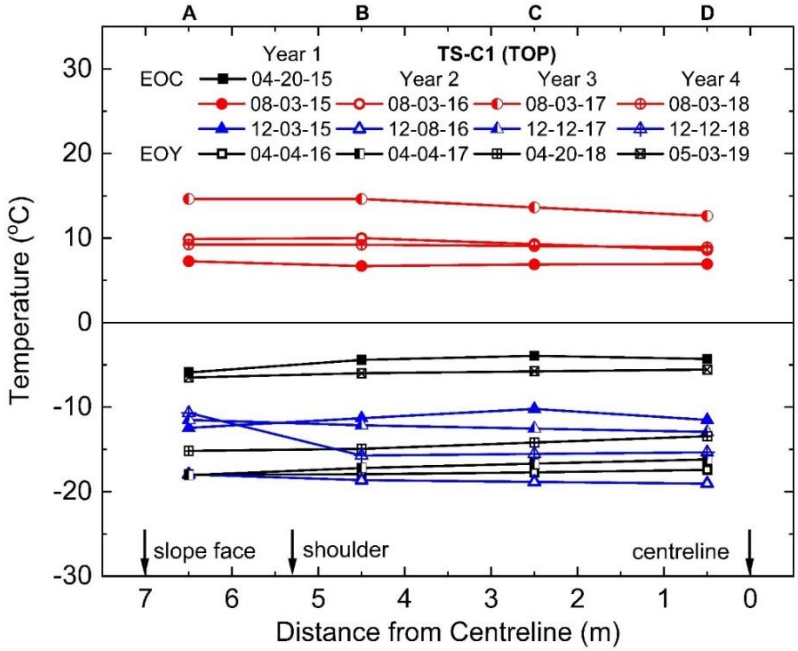

(a)

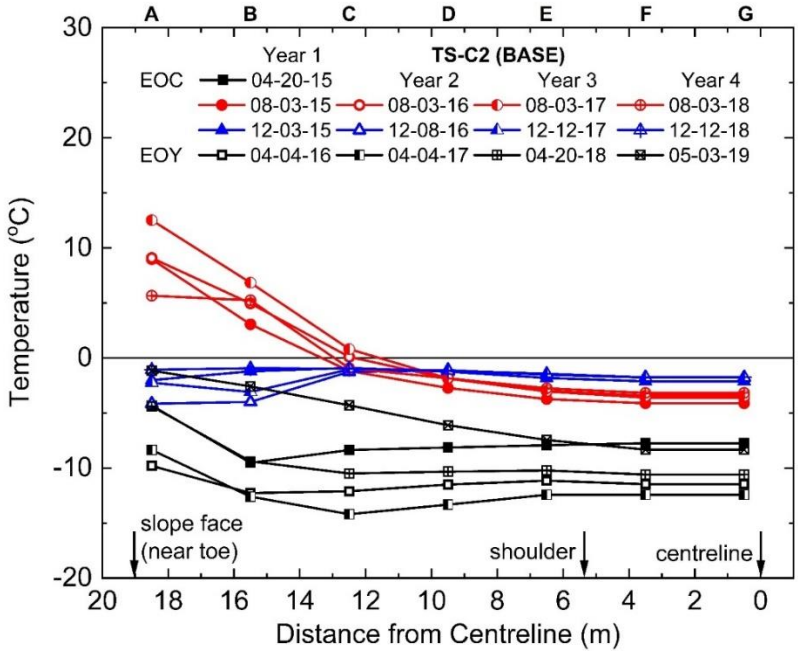

(b)

Fig. 2.9 (continued)

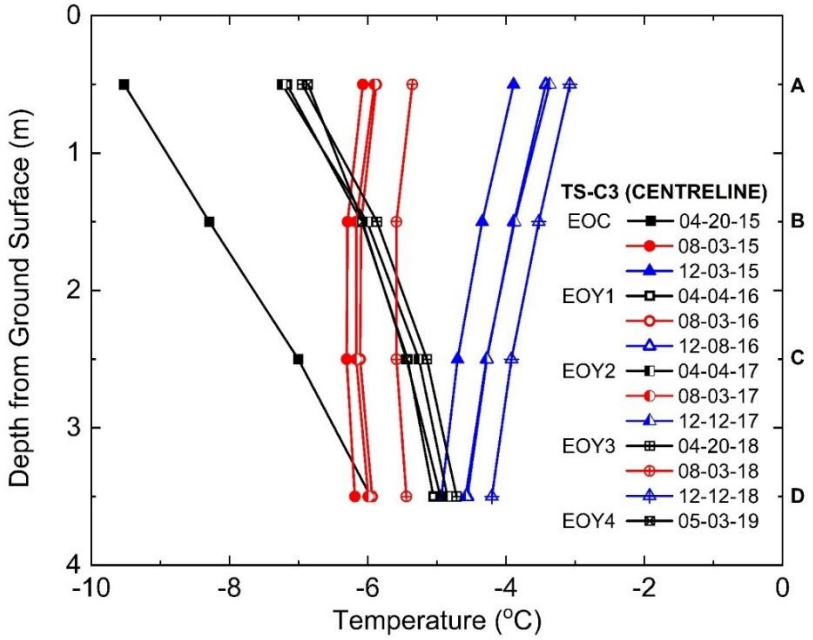

(c)

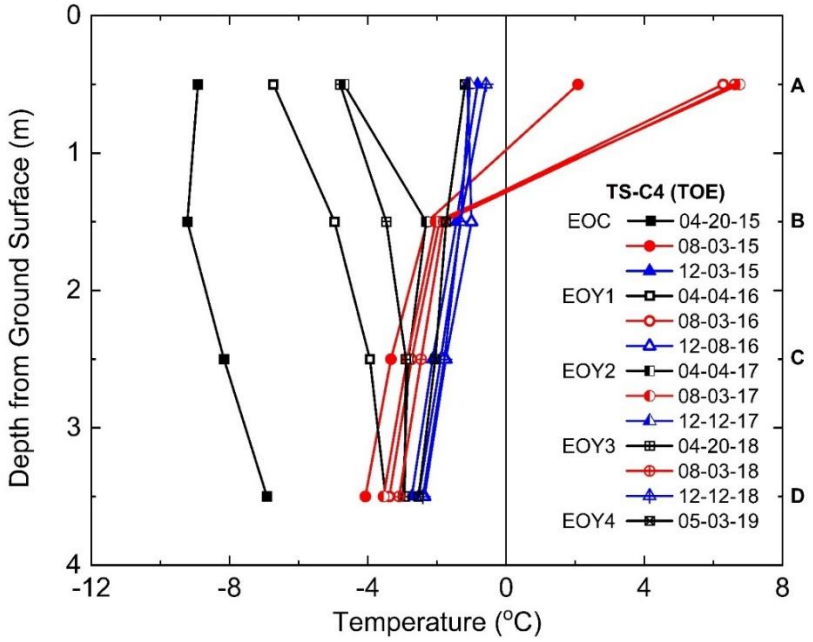

(d)

Fig. 2.10. Temperature readings from (a) vertical and (b) horizontal ShapeAccelArrays at different time steps at different locations in the control embankment section. EOC: end-of-construction and EOY: end-of-year.

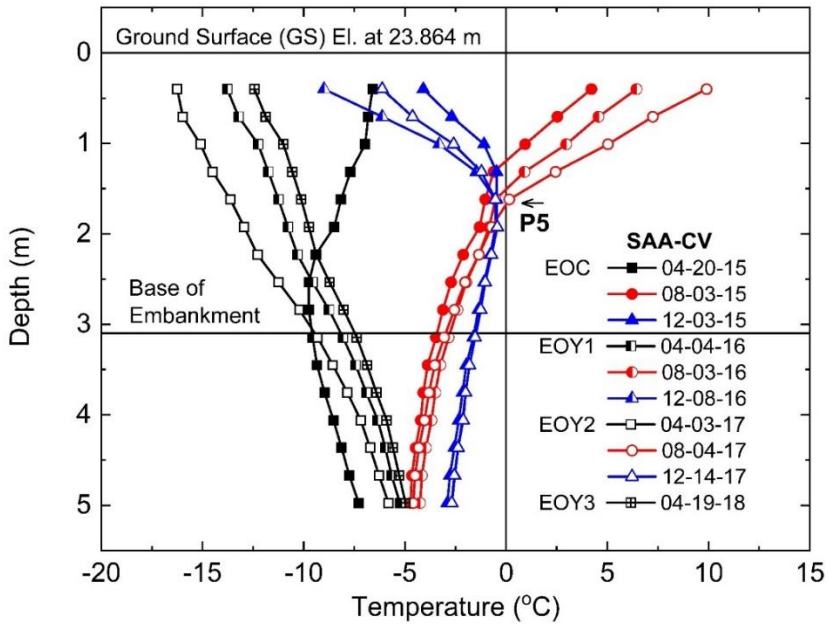

(a)

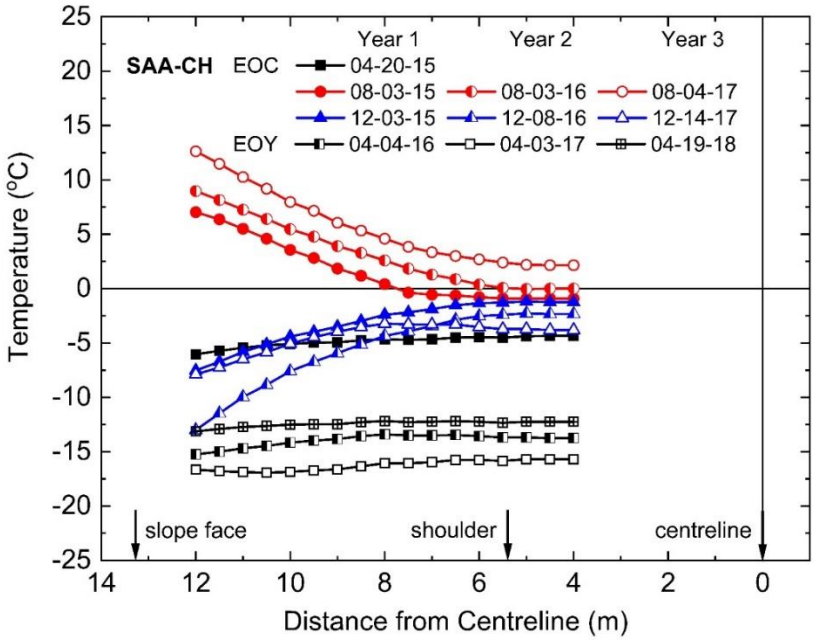

(b)

Fig. 2.11. Comparison of temperature nodes (a) close to embankment surface and (b) in foundation soil with air temperature.

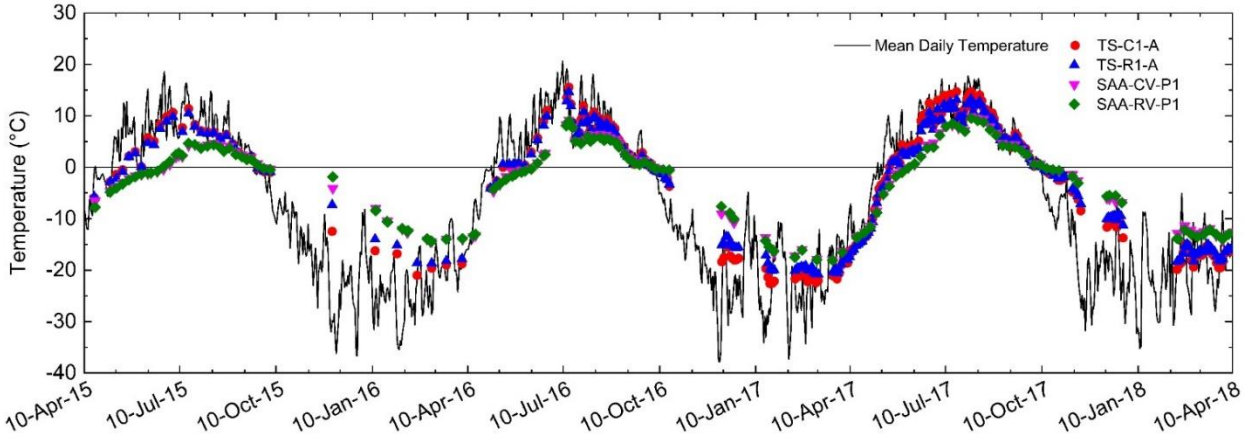

(a)

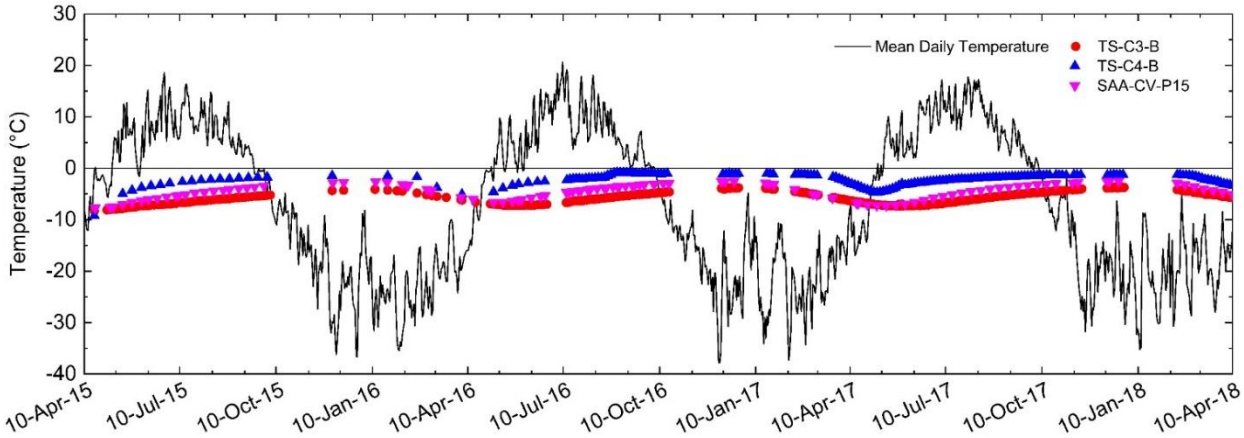

(b)

Fig. 2.12. Temperature readings at different time steps in the thin embankment section.

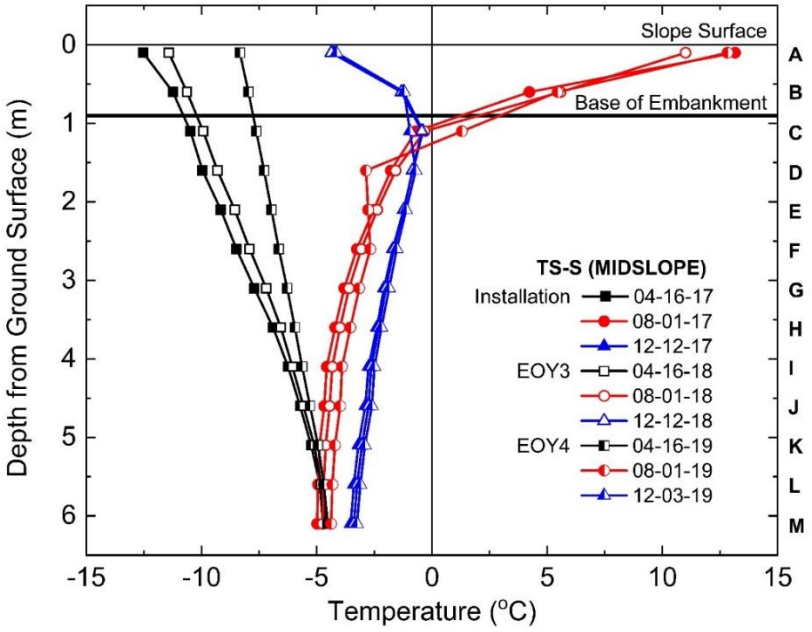

Fig. 2.13. Temperature readings at different time steps in the foundation soil at 3.5 m away from the toe of the control section.

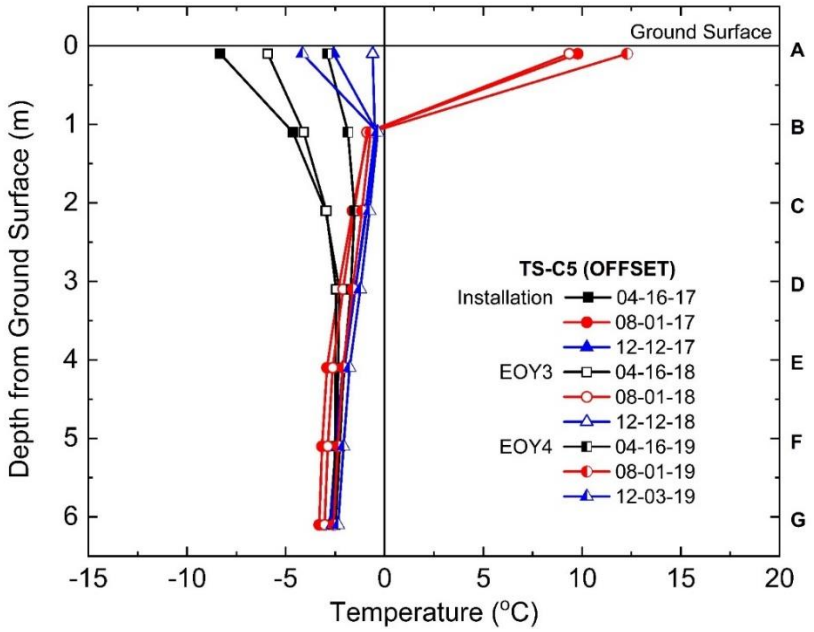

Fig. 2.14. Comparison of temperatures recorded by SAA and the thermistor string with depth at different time steps.

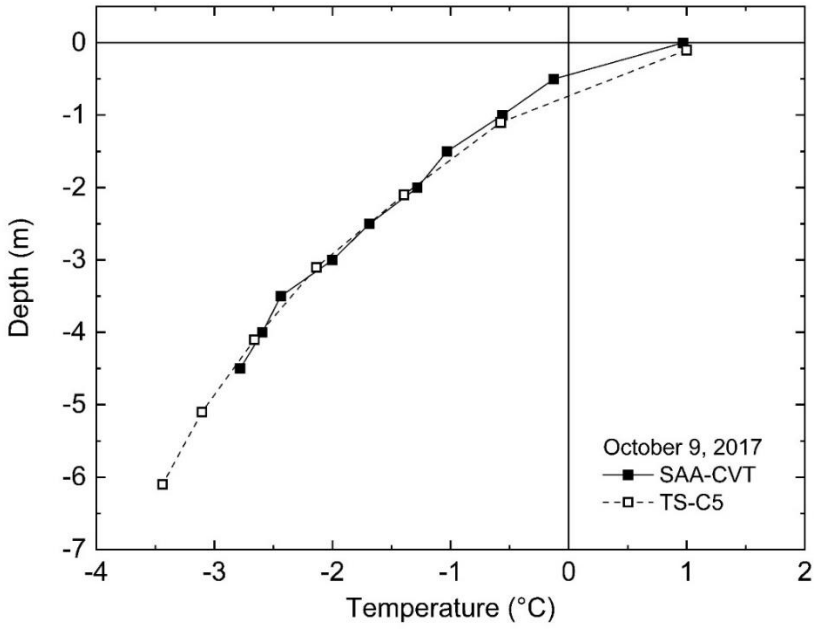

(a)

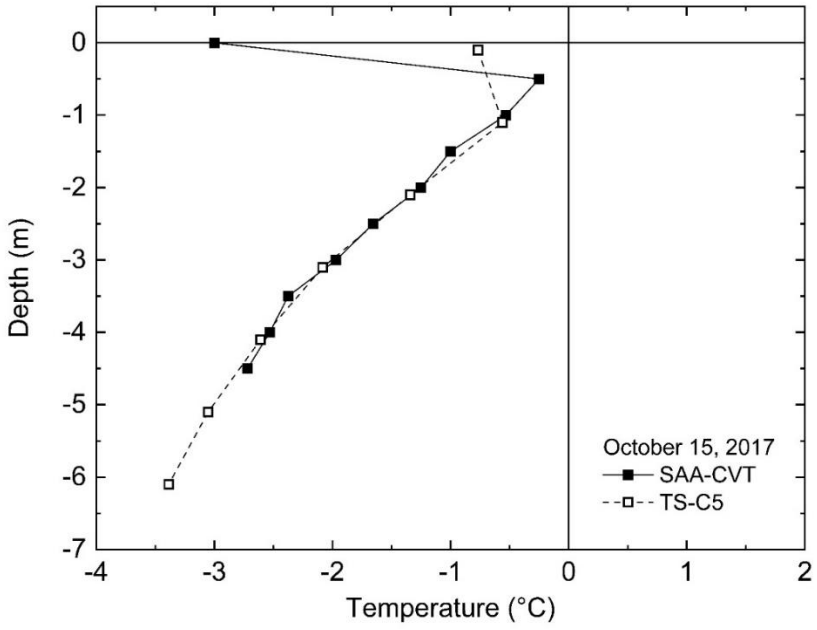

(b)

Fig. 2.15. Lateral displacements at different time steps at midslope: (a) control and (b) reinforced sections. EOC: end-of-construction and EOY: end-of-year.

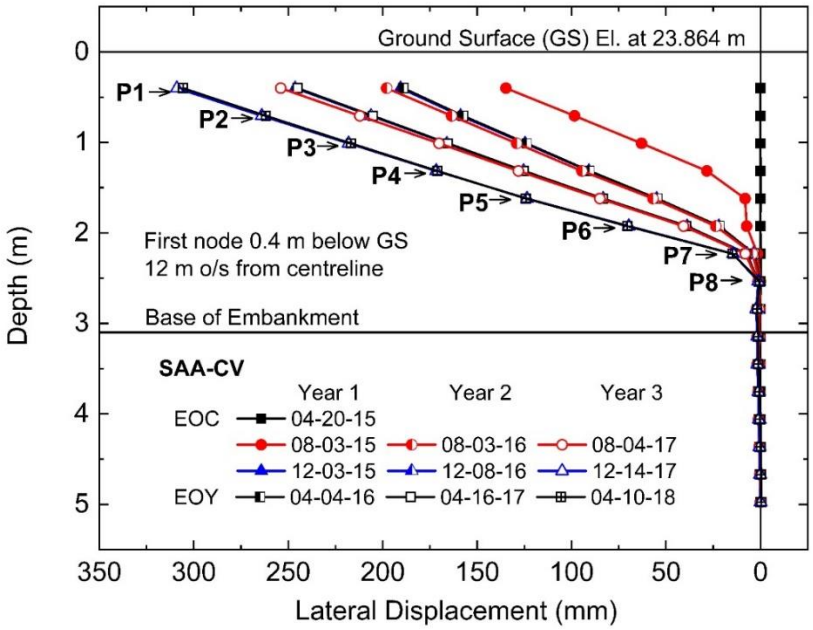

(a)

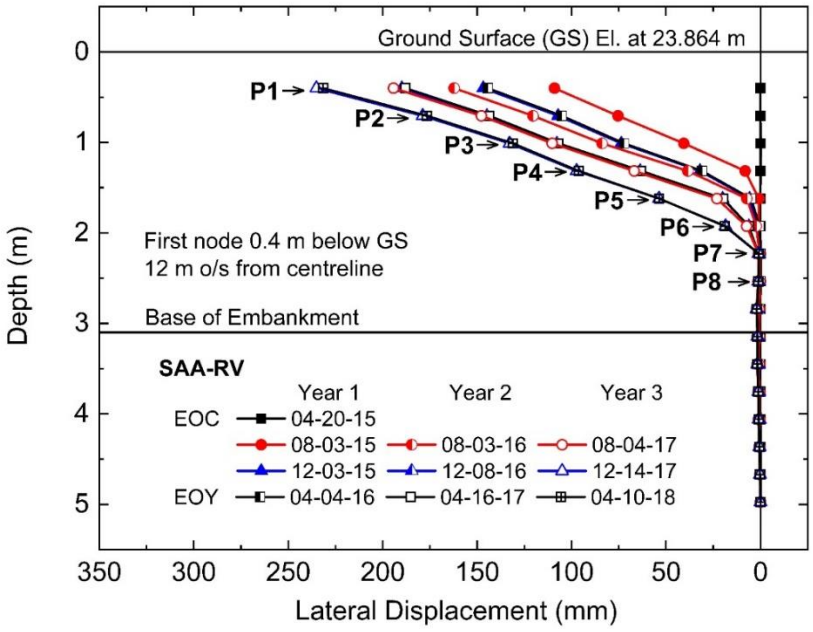

(b)

Fig. 2.16. Lateral displacements with time at different elevations: (a) first spring thawing season after construction and (b) monitoring period.

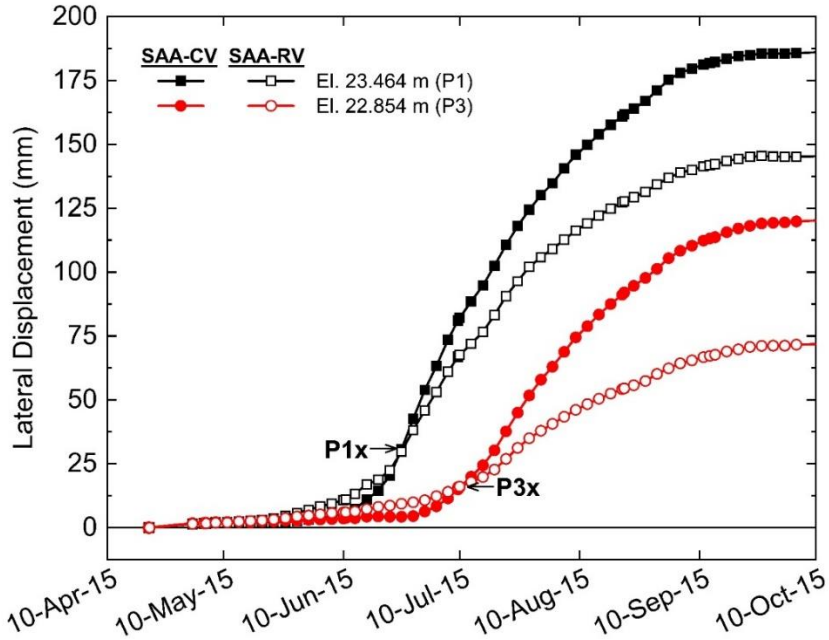

(a)

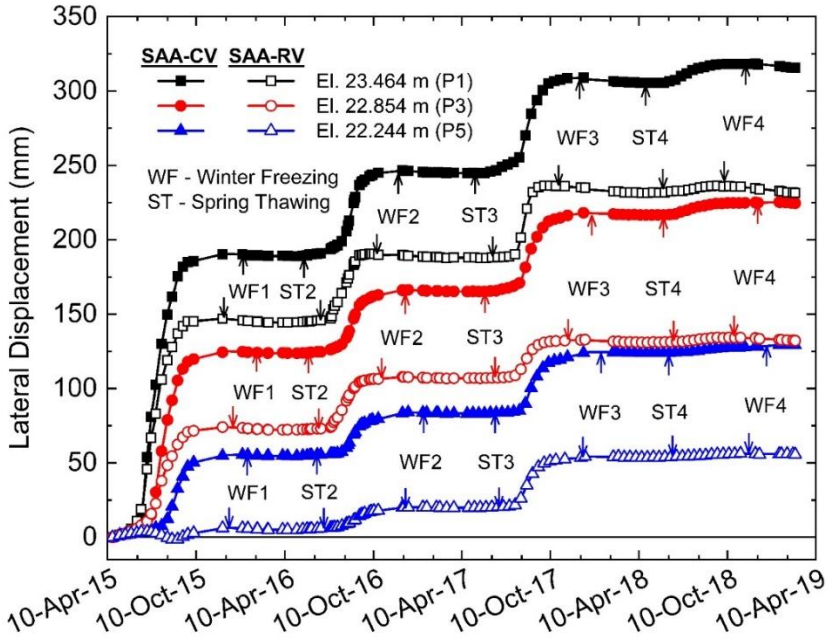

(b)

Fig. 2.17. Vertical displacements at different time steps at midslope: (a) control and (b) reinforced sections. EOC: end-of-construction and EOY: end-of-year.

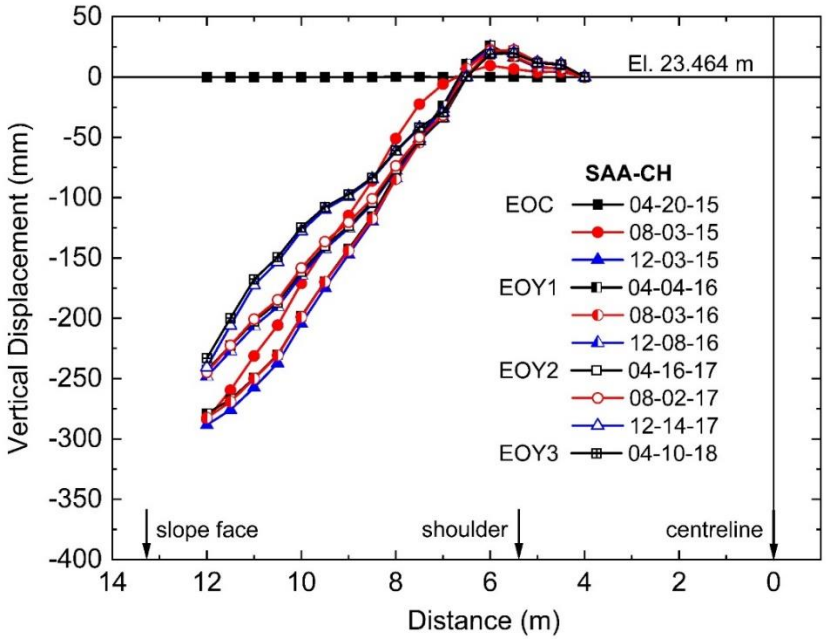

(a)

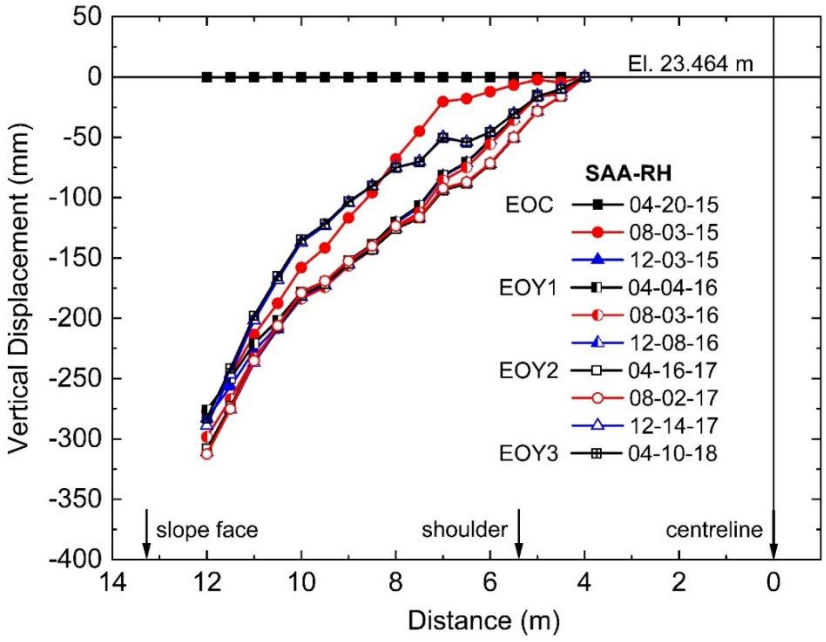

(b)

Fig. 2.18. Lateral displacements at different time steps at toe of the control section: (a) vertical SAA-CVT at 3.5 m offset and (b) horizontal SAA-CHT at 0.5 m offset.

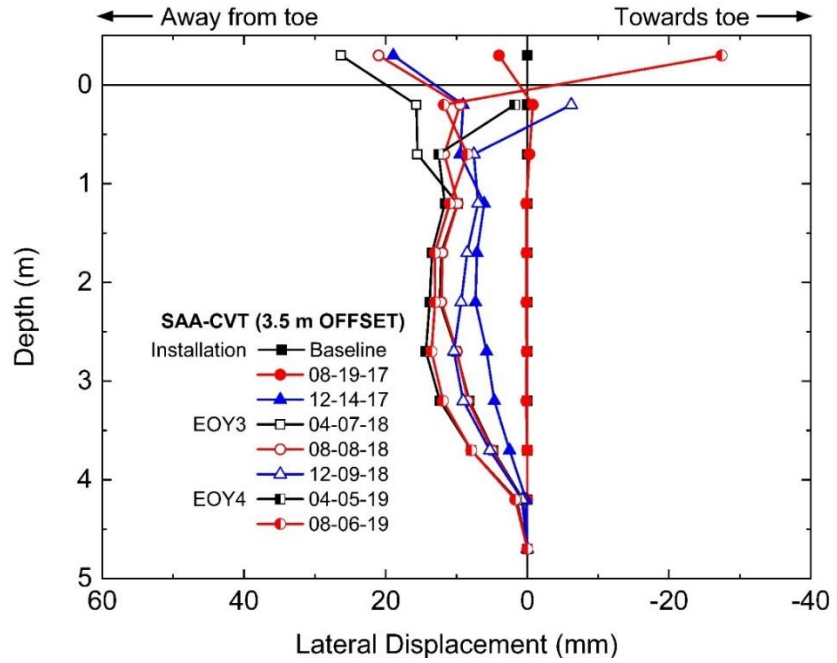

(a)

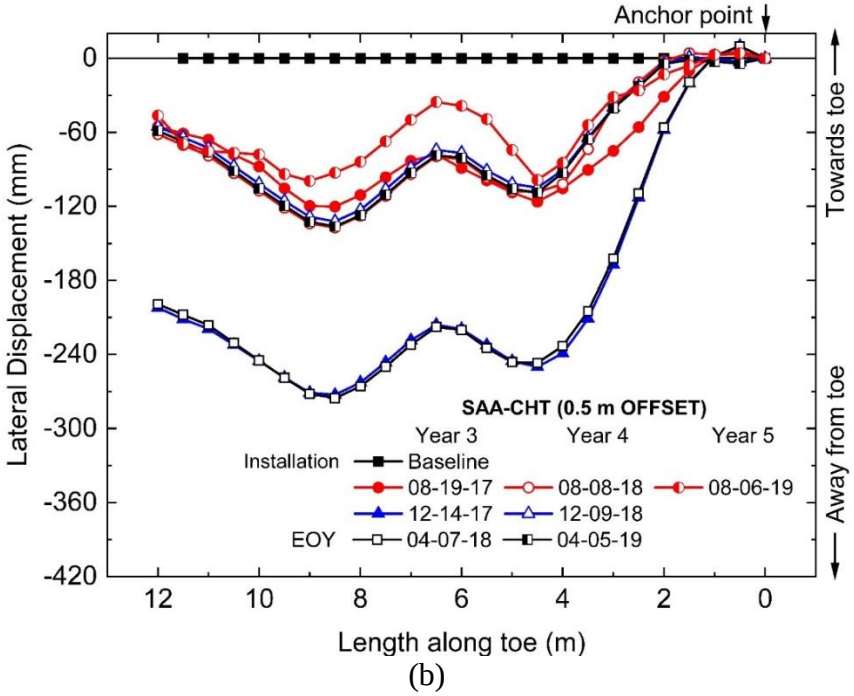

(b)

Fig. 2.19. Lateral displacements at different time steps at toe of the reinforced section: (a) vertical SAA-RVT1 at 0.5 m offset and (b) vertical SAA-RVT2 at 3.5 m offset.

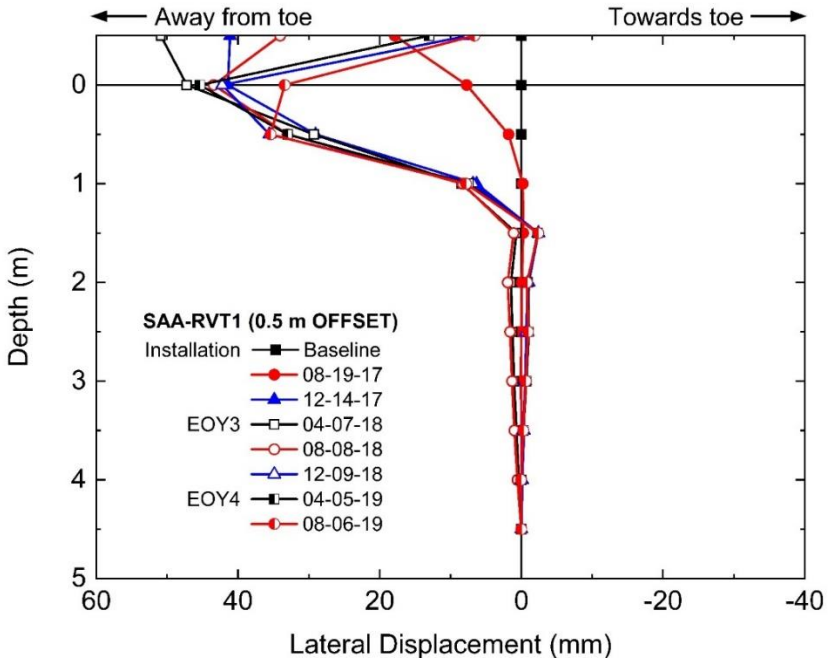

(a)

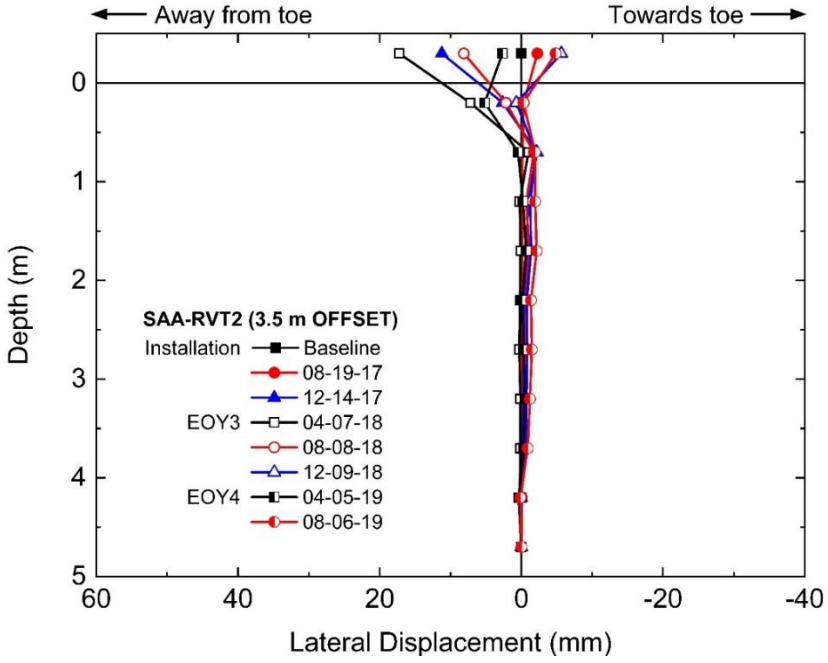

(b)

Fig. 2.20. Strain gauge readings with time at different locations: (a) 1.8 m, (b) 2.7 m, and (c) 4.5 m from embankment base.

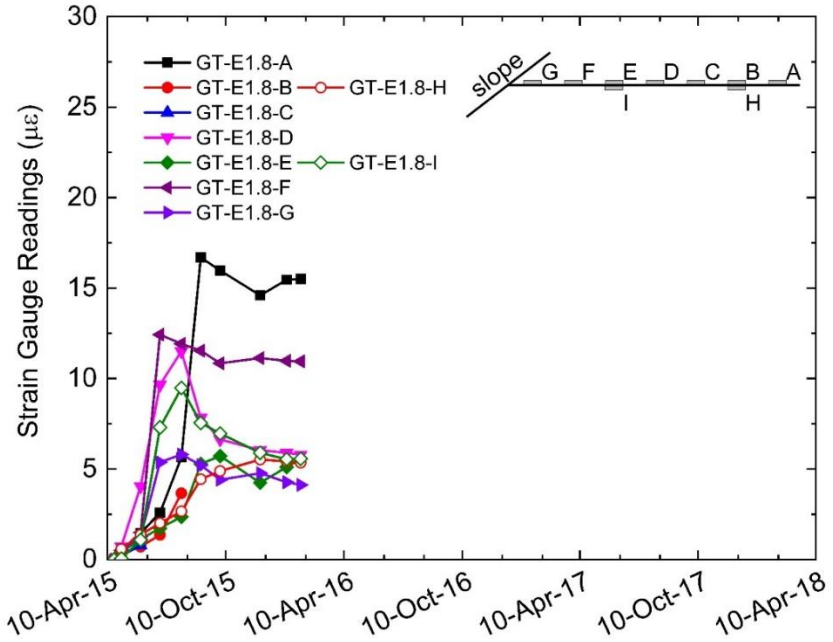

(a)

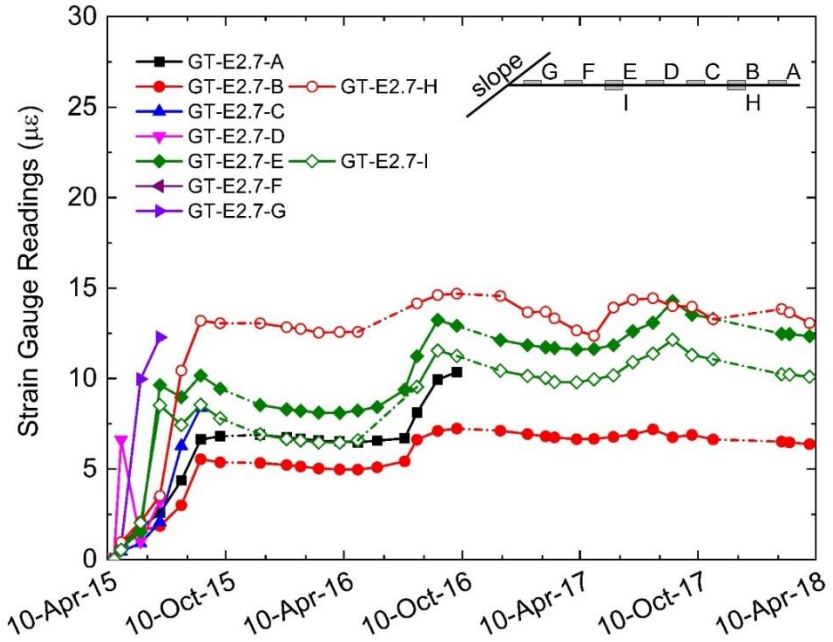

(b)

Fig. 2.20 (continued)

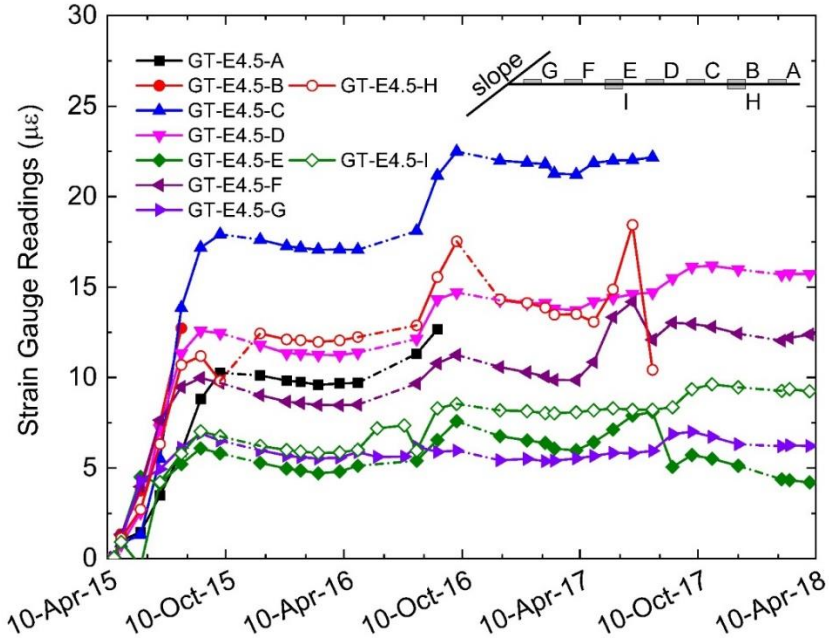

(c)

List of Notations and Acronyms in this Chapter

AWS	Automatic weather station
DAQ	Data acquisition system
ECCC	Environment and Climate Change Canada
EOC	End-of-construction
EOY	End-of-year
GT	Geotextile layer
MDAT	Mean daily air temperatures
NASA	National Aeronautics and Space Administration
SAA	ShapeAccelArrays
ST	Spring thawing
TS	Thermistor string
WF	Winter freezing

CHAPTER 3

SHEAR STRENGTH OF EMBANKMENT FILL[1,2]

3.1. Introduction

As the frozen soil in the embankment warms up, the shear strength of the soil decreases significantly until it reaches its minimum just above 0°C after which it remains constant with increasing temperature (Ladanyi 1996). For fine-grained frozen soil, a major contributor to its mechanical strength is ice cementation, i.e. cohesion. An increase in temperature increases the unfrozen water content in such soils and decreases the ice cohesion (Ladanyi 1996, Arenson and Springman 2015). Ladanyi (1996) also indicated that the frozen soil will steadily weaken and eventually, on complete thawing, lose all additional strength from ice cementation. However, there is limited study on the mechanical strength of naturally occurring coarse-grained frozen soil (soil mixture ranging from well-graded sand with silt and gravel to silty sand with gravel) used for road or railway embankment construction.

The shear strength of the soil used to construct the embankments presented in Chapter 2 varies throughout the year as the embankment is subjected to seasonal temperature and moisture changes and freeze-thaw cycles, especially for the soil on the slopes exposed to ambient air temperature and high solar radiation (Barker and Thomas 2013). Shear strength is therefore an important

---

[1] This chapter has been published in peer-reviewed journals and conference proceedings as follows:
De Guzman, E.M.B., Stafford, D., Alfaro, M., Doré, G., and Arenson, L.U. 2018. Large-Scale Direct Shear Testing of Compacted Frozen Soil under Freezing and Thawing Conditions. Cold Regions Science and Technology. 151:138-147.

Stafford, D., **De Guzman, E.M.B.**, Alfaro, M.C., Doré, G., and Arenson, L.U. 2017. Shear Strength of Soils under Frozen and Thawed Conditions using a Large Direct Shear Box. 70th Canadian Geotechnical Conference. Ottawa, ON.

De Guzman, E.M.B., Alfaro, M., Arenson, L., and Doré, G. 2016. Large-scale Direct Shear Testing of Compacted Frozen Soil under Freezing Conditions. 11th International Conference on Permafrost, Potsdam, Germany. pp. 1077.

[2] A list of notations and acronyms used in this chapter are found in page 96.

parameter in assessing the long-term stability of embankment slopes constructed in the winter using frozen soil. Aside from slope failures due to the reduction in shear strength of the embankment slopes, base failures can also occur because of permafrost degradation in the foundation in response to construction induced changes in the ground thermal regime (Andersland and Ladanyi 2004).

Shear strength of compacted frozen soil during winter construction and subsequent natural thawing in the spring and summer is an important consideration for the Inuvik-Tuktoyaktuk Highway (ITH). Most researchers account for the shear strength of the permafrost foundation and how it affects the stability of the overlying embankment (Crory 1973, Yang et al. 2015, Loria et al. 2017). However, only limited research is available on the strength of embankments due to winter construction. In order to describe what effects the changing shear strength of the fill material may have on the embankment stability, a series of large-scale direct shear tests was performed under different environmental conditions.

3.2. Methodology

A series of direct shear tests was carried out on remolded frozen soil to determine its shear strength under frozen, thawed (upon phase change), and cyclic freeze-thaw conditions using the University of Manitoba large-scale direct shear equipment. The sample preparation and temperature conditioning as well as details of the set-up and the test procedure are discussed below. Testing was initially carried out to determine the time to reach thermal equilibrium in the environmental chamber for each phase of the test; that is, temperature at the shear plane during each test condition and the change in temperature in the shear plane during compaction, phase change, and freeze-thaw stages.

3.2.1. Soil Preparation and Conditioning

The material used for testing was from an actual borrow source used for the ITH embankment construction. Grab samples, consisting of small volumes of disturbed soil, were taken from the fill and from the nearest borrow source (called: Pit 174) during a site visit on March 31, 2015. Additional grab samples were collected during construction of the embankment (April 14 - 20, 2015). Grab samples were transported to the university laboratory where moisture contents were determined on the thawed samples. The average measured moisture content obtained during the construction of the embankments is 16%. Fig. 3.1 presents the grain-size distribution curves of the fill material obtained from Pit 174 and the grab samples (EGS) during embankment construction. The field variability required that a representative mixture be selected for the direct shear tests for consistency. A series of composite mixtures was prepared from Pit 174 material and the average grain size distribution (CM-4 in Fig. 3.1) was chosen for testing. All laboratory samples were prepared with this mixture at a moisture content of 16% that had a fines content ranging from 11% to 13%, an average plastic limit of 16.4%, an average liquid limit of 24.6%, and a plasticity index of 6.6%. About 72% passing the 0.075 mm (No. 200) sieve was of silt fraction based on the results of the hydrometer test. The mixture ranged from well-graded sand with silt and gravel to silty sand with gravel based on the Unified Soil Classification System (USCS).

Dry soil for the composite mixture was prepared from material passing the 19.0 mm (3/4") sieve and screened to achieve a grain size distribution close to the CM-4 distribution (Fig. 3.1). Soil mixtures at different moisture contents were prepared in a series of pans and frozen at -20°C. The frozen mixtures were crushed afterwards with an ordinary hammer and screened passing the 22.5 mm (7/8”) sieve. Compaction testing was completed on the frozen chunks in a 152.4 mm (6”) diameter Proctor mold following Method C of ASTM D698-12 (2012). Frozen soil chunks were

compacted at -10°C. The compaction temperature of -10°C was selected because this is the minimum operable temperature of the large-scale direct shear equipment. Although the frozen soil chunks were prepared larger than the maximum aggregate size allowed for the method, it was intended that this would best mimic the winter embankment construction conditions.

As shown in Fig. 3.2, the dry density linearly decreased with increasing moisture content. The results confirm observations by Burwash and Clark (1981) who completed standard Proctor tests for sand, silt, and clay soils below 0°C. The optimum dry density observed for unfrozen soils was not observed below freezing (-10°C for the testing program).

Johnson and Sallberg (1962) noted that for a comparable compaction effort, a frozen soil will have a lower dry density at a given moisture content than a soil in the unfrozen state. The workability during compaction also decreased as the moisture content of the frozen soil increased. It was noted that up to a moisture content of about 16%, the frozen soil chunks could be compacted and densified. However, at moisture content greater than 20%, the individual chunks were only displaced when the hammer was dropped and compaction was poorly achieved. In consequence no optimum moisture content exists (Fig. 3.2). The moisture content of 16% was selected with the dry density of 13.75 kN/m^3 because this corresponds to the average moisture content in the field. Fig. 3.2 also demonstrates that the dry density below -10°C is significantly lower than that at room temperature.

3.2.2. Large-scale Direct Shear Box

Alfaro et al. (2009) provide a schematic of the large-scale direct shear box used in this research. The box has inner dimensions of 1200 x 600 x 400 mm (L x W x H). The bottom half of the box is 250 mm deep and the upper half is 150 mm. A circular cross-section with a diameter of 590 mm was used for this testing program. The upper half of the box is connected to a load cell to measure

the horizontal (shear) load, and a servomotor to move the upper half of the box at a specified shear rate. The displacement rate was selected to be 0.35 mm/min (strain rate of 5.9 x 10-4 s-1) as this rate is the lowest speed the motor can be set to under -10°C conditions. The displacement rate derived from the SAA installed midslope of the control section in Chapter 2 showed slower rates during the thawing season ranging from 0.4 to 0.9 mm/day (2.7 x 10-4 to 6.25 x 10-4 mm/min). The displacement rate was checked manually at different time steps to ensure the rate remained constant throughout the duration of the test. A horizontal strain pot was attached to the front and back end of the direct shear box, with the front end being measured from the movement of the load cell.

Three linear variable differential transformers (LVDTs) were installed on top of the box to measure vertical displacements during the test. An air pressure gauge installed on the top cap measured the normal stress applied. Normal stresses of 25, 50, and 100 kPa were selected corresponding to the vertical stresses expected in the field.

Details of the preparation of the soil and the direct shear box for testing inside the environmental chamber are shown in Fig. 3.3. The frozen chunks were first sized passing the 22.5 mm sieve and weighed to determine the equivalent weight required to achieve a desired compaction height (Fig. 3.3a). Material was added in 50 mm lifts, except for the shear plane where a 100 mm lift was placed. The final lift was 20 mm. A 30 mm thick sand buffer was placed on top to prevent possible punching of the membrane (Fig. 3.3d).

A hammer drill was used (Fig. 3.3b) to compact the frozen chunks to specific heights. Each lift was scarified to ensure a proper bond with the previously compacted lift. The full height of the compacted frozen soil is shown in Fig. 3.3c. A polyethylene plastic membrane was used to separate the soil material from the sand buffer. The sand buffer was intentionally humped in the middle

anticipating settlements expected during the phase change and freeze-thaw tests. The rubber gasket (Fig. 3.3e) was greased with high-vacuum seal to prevent air leakage during application of the normal stress. Rubber matting was then rolled over its top. The top cap was added to seal the upper half of the box (Fig. 3.3f). The brass rods were pushed in on top of the rubber matting for contact and the LVDTs placed afterwards. Finally, the normal stress was applied through the air valve and the direct shear box was checked for air leakages. All sensors were connected to a data acquisition system outside the environmental chamber.

3.2.3. Thermal Equilibrium Testing

One of the key issues in conducting the direct shear tests was to determine how long it took for the shear box temperature to equilibrate to steady state temperatures. Temperature sensors could not be embedded in the soil during the shearing phase as this would have damaged the communication cables. Separate thermal equilibration testing therefore was conducted during the consolidation phase to determine the variation of temperature along the shear plane during compaction, phase change, and freeze-thaw stages. The results were used to determine when to conduct the shearing phases of a test after the consolidation phase. Thermocouples were installed 50 mm above and below the shear plane at the centreline of the direct shear box. Fig. 3.4 shows typical thermal equilibration test data during compaction, phase change, and freeze-thaw stages (Summary see Table 3.1). All tests were compacted frozen and equilibrated first to -10°C. The environmental chamber temperature at the top and bottom of the direct shear box was also recorded. The compaction of frozen chunks to full test height (370 mm) required an average of 2 hours. The normal stress for the test was applied during equilibration. The compacted frozen soil achieved thermal equilibrium (labelled “chamber conditioning” in Fig. 3.4) in 22 hours. The frozen condition tests (C1 in Fig. 3.5) were performed at -10°C at this stage (point A). The observed

fluctuation in the chamber temperature (~1.5°C) during conditioning was attributed to the defrosting of the environmental chamber fan.

Transitional (phase change) tests (C2) followed the same conditioning path as C1. However, once in equilibrium (point A in Fig. 3.4), the environmental chamber was turned off and the soil was allowed to thaw. Shear tests were conducted when both thermocouples read temperatures close to -0.5°C (point B). The temperature during this test condition was constant for 5 hours. The duration of the shearing phase was about 5 hours to reach a displacement of 100 mm at a shearing rate of 0.35 mm/min. Note that the thermocouple 50 mm below the shear plane remained below 0°C for another 6 hours even though the other thermocouple was already above 0°C.

Freeze-thaw condition tests (C3) were set up the same as C1. However, once equilibrium was achieved the environmental chamber was turned off and the soil could thaw and warm to 18°C (point C in Fig. 3.4). After thawing for 2 days, the environmental chamber was turned on again to reach -10°C. A delay of about 3 hours was observed before the temperature in the soil started to drop whereas the environmental chamber is already at -10°C. As shown in Fig. 3.4 it took another 2 days of freezing for the soil to reach -10°C. The last thawing could reach close to -0.5°C (point D in Fig. 3.4) before the shearing phase was initiated for this condition.

Tests were conducted close to -0.5°C for both C2 and C3 conditions to quantify the shear strength near the interface of the frozen and unfrozen soil at critical field temperature conditions. It was conceptualized at the start of the testing program that embankment instability would happen at the interface of the frozen soil core of the embankment and the soil exposed to the seasonal freezing and thawing cycles. From temperatures measured from the SAAs in the control and reinforced sections, lateral displacements occurred at temperatures ranging from -0.5 to -0.8°C. No movements were observed below these temperatures which further support the selection of the

-0.5°C test temperature for C2 and C3. Finally, room conditions tests (C4) were conducted at a temperature of 18°C with moisture content of 16% to determine the shear strength of unaltered, unfrozen soil.

The measurement of soil suction will help in establishing correlation with the unfrozen water content as the frozen soil undergoes thawing. Fredlund thermal conductivity sensors used in the field to measure soil suction were also installed in the direct shear box in contact with the frozen soil during thermal equilibration for C1, but unfortunately the ceramic part of the sensor was damaged during compaction of the frozen soil. However, this does not influence the interpretation of the shear strength properties presented in the following section.

3.2.4. Peak and Critical States

The shear strength of each condition tested was analysed using the method provided by Atkison (2007). Unfrozen dense soils tend to exhibit a rapid increase in shear stress at low shear strains followed by strain-softening with increasing shear strain until reaching critical state shear stress (Budhu 2011). Dense soils will initially compress until they reach a point of no change in volumetric strain, followed by dilation. The dilation is an increase in soil volume as the soil is sheared and causes the shear strength to increase due to the additional stress required to increase volumetric strain of the soil under the applied normal stress.

In a typical shear strength analysis, using the traditional Mohr-Coulomb failure criterion, the failure shear strength (critical state) is determined and plotted against the normal stress. Under different normal stresses, the failure shear strength is recorded and a line is fitted across these points to determine the critical state friction angle. However, the critical state is only achieved at large strains. In Atkinson's method, the critical state friction angle is determined from a point where the soil is shearing at constant volume where the dilation angle is zero degrees. There is a

point during the initial stage of the test where the soil is neither compressing nor dilating; thus, the stress required to shear the soil at that instant is equal to the stress required to shear the soil at critical state. The peak friction angle is determined when the slope of the vertical displacement to the horizontal displacement is maximum, corresponding to the maximum stress ratio. The dilation angle is taken as the difference between the peak friction angle and the critical state friction angle based on Atkinson's method.

3.3. Results and Discussion

Results of the large-scale direct shear tests conducted under different test conditions and normal stresses are presented below. Results of the frozen tests (-10°C) are first discussed, followed by the tests under transitional (phase change) conditions (-0.5°C) then freeze-thaw (-0.5°C) conditions, and finally tests under room conditions.

3.3.1. Case 1 (C1): Frozen Conditions

Fig. 3.5a shows the plot of the stress ratio vs. the horizontal displacement for the frozen tests at -10°C (C1). The stress ratio for C1-25 kPa is higher compared to the other two normal stresses as expected. A peak state can be identified in C1-25 kPa (Fig. 3.5a) corresponding to the maximum slope of the curve of the same test in Fig. 3.5b (the slope tangent to the curve between 7.5 and 12.5 mm in vertical displacement, and between 20 and 25 mm in the horizontal displacement, projected to Fig. 3.5a between the same horizontal displacement), but this slope decreases as the applied normal stress increases. It can also be seen that strain-softening was noticeable at lower pressures. Fig. 3.6a plots stress ratio against the logarithm of normal stress. A line was fitted for both peak and critical state stress ratios. From these fittings, an average value of $\tan\phi'_{cs}$ was determined to be 1.28 (ϕ'_{cs} = 52.1°). The large difference between the peak and critical state stress ratios is caused

by the large dilation that the soil experienced during the tests. This is attributed to the angularity of the frozen soil chunks during the test.

Swiderski (1976) reported that the shear strength of a cohesionless material increases with the degree of angularity. The high degree of angularity in the frozen soil chunks may be responsible for the high shear strength of the soil that developed under frozen conditions. Fig. 3.7 shows the shear plane after a test when the soil was removed and the upper half of the box returned to its original position. About 10 mm below the shear plane, the angularity of the material was noted post-test. It can be hypothesized that during the shearing process, the shear force being recorded is for a block of interlocking frozen chunks of soil, rather than a shear plane being created by the upper and lower boxes. This rigid movement resulting in higher shear stresses supports the idea that frozen soil derives its strength mainly from mineral bonds and internal friction of the frozen soil chunks (Ladanyi 1996). In terms of embankment slopes, the high critical state friction angle does not necessarily mean that steeper slopes can be achieved. The limitations related to compaction at sub-freezing temperatures still exist. Flatter slopes are typically preferred for thermal protection of the permafrost foundation or for practical reasons, allowing equipment to compact and grade the slope.

3.3.2. Case 2 (C2): Transitional (Phase Change) Conditions

Fig. 3.8a shows the stress ratio vs. the horizontal displacement for the transitional (phase change) tests at -0.5°C (C2). The stress ratios and vertical displacements are considerably lower than that of C1. This confirms that a significant amount of shear strength is lost during the thawing process. The initial response of the soil is also less stiff compared to that of C1. The point where the soil is neither dilating nor compressing based on Atkinson's method occurred between 2 and 8 mm in C1. In C2 this is reached between 20 and 40 mm (Fig. 3.8b). Unlike C1, where noticeable peak

strengths were observed, the stress ratios for each normal stress were still increasing at a horizontal displacement of 100 mm. The stress ratios at 100 mm were selected for $\tan\phi'_p$. A line was fitted for both peak and critical state stress ratios in Fig. 3.6b. An average value of $\tan\phi'_{cs}$ is determined to be 0.67 (ϕ'_{cs} = 33.6°) which is 18.5° less than the critical state friction angle for C1. Although the tests were performed at -0.5°C, the reduction in shear strength is attributed to the thawing and softening of the frozen soil chunks, reducing the angularity during shearing, and the presence of unfrozen water during the thawing process. Unfrozen water also influences the shear response at warmer temperatures, further reducing the shear strength (Yasufuku et al. 2003). After the initial thawing of the embankment following winter construction, this considerable loss in shear strength is important to be accounted for as slope failures may occur if not sufficient shear strength can be mobilized to maintain stability.

3.3.3. Case 3 (C3): Freeze-Thaw Conditions

Fig. 3.9a shows the stress ratio vs. the horizontal displacement for the freeze-thaw tests at -0.5°C (C3). Peaks are noticeable for all normal stresses. Similar to C1, the point where the soil is neither dilating nor compressing occurred between 2 to 15 mm. The dilation angle observed for C3 is higher than that of C2. This may be attributed to the fact that C3 was allowed to fully thaw, drain, and consolidate for an entire cycle before being subjected to freezing temperatures again and then thawed afterwards to the transitional temperature. It is also possible, that as the test was progressing into C2 conditions, the frozen soil chunks at the transitional temperature were breaking down and compressing under the applied normal stress. The unfrozen water content in C2 reduced its dilative behaviour. However, the unfrozen water in C3 was allowed to drain from the shear plane, leaving a denser structure at the shear plane before shearing.

A line was fitted for both peak and critical state stress ratios (Figure 6b). An average value of $\tan \phi'_{cs}$ is determined to be 0.51 (ϕ'_{cs} = 27.0°) which is 6.6° less than that of C2. Although the critical state friction angle is lower in C3, the stiffer behaviour of the soil provides stability after cycled conditions and provides additional shear strength.

3.3.4. Case 4 (C4): Room Temperature at Wet Conditions

Fig. 3.10a shows the stress ratio vs. the horizontal displacement for the test carried out at room temperature (C4). It is noticeable that the behaviour of the C4 was comparable to the initial response of C2, but for all cases C4 has a lower stress ratio. This can be attributed to the fact that the soil was very wet and the effect of consolidation was therefore only small. C4 still exhibited some dilation during the first 30 mm of testing (Fig. 3.10b). A line was fitted for both peak and critical state stress ratios in Fig. 3.6b. An average value of $\tan \phi'_{cs}$ is determined to be 0.36 (ϕ'_{cs} = 20.0°) which is 13.6° and 7.0° less compared to those for C2 and C3, respectively.

The conditions as to which C4 were compacted are unlikely to be implemented in southern regions as embankments are normally built at 95% of the optimum moisture content, which in this case is at 9.4%. C4 was rather difficult to compact because of its high moisture content. As indicated earlier, embankments in cold regions are often constructed during the winter to minimize the thermal disturbance to the foundation. The test conditions in C4 are still valuable in this study because it provides comparisons with shear strengths of the soil when not subjected to any freezing, thawing, or cyclic freeze-thaw conditions, but under similar moisture content.

A summary of the stress ratios and corresponding dilation angles is provided in Table 3.2. As the normal stress increases (Fig. 3.6), the fitted lines for the peak stress ratio will eventually

intersect the critical state stress ratio. The corresponding normal stress at the intersection of the two lines will envelope where the peak stress ratios are no longer present at higher normal stresses.

3.4. Numerical Modelling

It is recognized that direct shear tests have limitations and have been criticized for non-uniform distribution of stresses and strains, and for the progressive failure within the sample (Dounias and Potts 1993). However, most geotechnical engineers prefer conducting direct shear tests because it provides a quick estimation of the average ratio of shear to normal stress acting in the shear band providing a direct measure of the angle of internal friction (Zhang and Thornton 2007). The numerical models in this study provide an overview of how the strength values obtained from the testing program can be used during preliminary design (e.g. stability analyses) and discuss the limitations and cautions that must be exercised in interpreting the results. A commercially-available finite difference program FLAC 8.0 (2016) was used as the modelling platform. The construction of the numerical model and the assumptions made are discussed first, followed by a comparison of the numerical modelling results with the experimental results under different boundary conditions. No attempt was made to simulate the freezing and thawing process during the consolidation phase of the test as this is currently not possible. The model is manually adjusted to accommodate these effects by using the shear strength obtained from the experimental results with respect to these conditions.

3.4.1. Model Parameters

The numerical model has a mesh size of 12 x 16 elements with a fixed x-direction boundary condition applied from the base of the model to a height of 0.25 m on both sides and a fixed xy boundary condition at the base. A velocity boundary condition in y-direction was applied from 0.25 m to 0.40 m on both sides of the model to simulate the movement of the upper half of the box

during shearing. This velocity was equivalent to the average rate of shearing: 0.35 mm/s (5.9x10-4 s-1).

A summary of the properties used in FLAC 8.0 to run a direct shear test using an elasto-plastic constitutive model (Mohr-Coulomb model) is provided in Table 3.3. The densities used in the model were derived from the height of the soil inside the box before shearing, following consolidation, the equivalent dry soil mass before frozen compaction, and the average moisture content recorded after the test above and below the shear plane. The shear modulus (G) was selected as the secant modulus at a shear strain (ε_{xy}) corresponding to linear response of the curve in the τ vs. ε_{xy} plot for each test. Davis and Selvadurai (1996) suggested that the shear strain can be approximated by dividing the horizontal displacement (Δx) with the height of the direct shear box. However, because of the nonuniformity of both stress and strain fields, Davis and Selvadurai (1996) recommended caution when using this approximation. A Poisson's ratio (ν) of 0.3 is assumed. There is little to no difference in model results when the Poisson's ratio was changed to 0.2 or 0.25. The bulk modulus (K) was derived from the relationship with known G and ν as follows:

$$K = \frac{2G(1+\nu)}{3(1-2\nu)} \qquad \text{Eq. 3.1}$$

The critical state friction angle (ϕ'_{cs}) and dilation angle (ψ) were determined from the results of the large-scale direct shear tests for each condition presented earlier. The dilation angle is the difference between the peak (ϕ'_{p}) and critical state (ϕ'_{cs}) friction angles for each stress and test condition.

3.4.2. Experimental vs. Numerical Results

The comparison of the experimental results with the numerical simulations is shown in Fig. 3.11. It can be noted that the shear stress response of the numerical simulation using the properties obtained from the tests is considerably lower than that of the experimental results, although the initial response is reasonably modelled. The difference can be attributed to the constitutive model used. The Mohr-Coulomb failure (yield) criterion treats the relationship between shear stress and normal stress as linear, related by the friction angle. Once the soil reaches its yield condition, the soil behaves perfectly plastic, thus showing a constant shear stress (horizontal lines in Fig. 3.6).

The discrepancy between the simulated and measured mobilization of shear resistance may also be attributed to the test setup where the shear plane has a circular cross-section that behaves three-dimensionally while the simulation assumed plane strain conditions. Because of the circular geometry of the shear plane, the middle portion already experiences significant shearing and therefore dilation, while the edges experience little or no shear deformation. The consequence of a 3D condition in shearing is the effect of restrained dilatancy that can mobilize dilatant stresses on and near the edge of the plane of shearing (Kim 2007).

The ‘non-sheared area’ is the non-dilating zone that acts as a restraint against dilatancy in the restraining zone. This generates shear stresses at the interface between the dilating and non-dilating zones and results in an increase in normal stresses at both edges. A 3D condition develops at the edges while the middle section experiences a 2D behaviour. Restrained dilatancy near the edge results in an increase in normal stress (dilatant stress) on the shear plane (Alfaro and Pathak 2005). Essentially, the normal stress in the numerical model needs to be increased to match the experimental results (Kim 2007). This does not, however, invalidate the selection of the critical

state friction angle used in the model as the value is constant even at higher normal stresses (Fig. 3.6).

Table 3.4 summarizes the increased normal stresses due to restrained dilatancy inputted in FLAC to match the behaviour of the experimental results (also shown in Fig. 3.11 and labelled as RD, dotted lines). Now the increased normal stress due to restrained dilatancy shows better agreement with the experimental results versus the original simulation using normal stresses. The effect of restrained dilatancy is greatest at lower normal stresses, especially for C3, given that it is the most dilative test condition.

3.5. Chapter Summary and Conclusions

The shear strength of soils is an essential material property when assessing the stability of road embankments. In Arctic regions, embankments are often constructed during winter when the soil is frozen to minimize environmental impacts and for the ease of access. The shear strength of a fill placed frozen changes as the embankment thaws and then refreezes seasonally. This can affect the stability of the embankment. To quantify this behaviour, large-scale direct shear tests were conducted on remolded frozen soil samples at frozen, transition (phase change), and freeze-thaw conditions. Tests were also conducted on unfrozen soils under room temperature at similar moisture content. The following conclusions can be drawn from the testing:

1. The frozen soil samples exhibited significant shear strength as long as they remained frozen, but upon thawing close to phase change and upon freeze-thaw cycling the shear strength is reduced by up to 50%. The most critical condition, based on the tests conducted, is during the onset of the first thawing when the ice bonding in the soil matrix melts.

2. Compaction in the field during embankment construction plays an important role because there is no optimum condition as to which frozen soils should be compacted. The higher the moisture content of the frozen soil matrix the more challenging the compaction. Although fill material for embankment construction is taken from locally-available sources and thus have high variability both in composition and moisture content, it is practical to keep the moisture content below 20% to benefit from higher compaction densities and to minimize thaw settlements during the onset of the first thawing following winter construction.

3. The experimental results were simulated using a finite difference program and it is demonstrated that restrained dilatancy affects the results of the numerical model, but maintains the critical state friction angle for increased normal stresses. This confirms the validity of the critical state friction angles obtained via laboratory tests for each test condition by assuming that the critical state stress ratio at the initial stages of the test corresponding to a no change in volume is approximately the same at larger displacements (Atkinson's method).

The shear strength properties obtained will be used in Chapter 6 in calibrating coupled thermal-mechanical models to simulate the embankment behaviour presented in Chapter 2.

Table 3.1. Summary of test conditions for direct shear tests.

Test Label	Test temperature at shear plane	Environmental Condition/ Test Description
Frozen (C1)	-10°C	Compacted frozen, tested at constant freezing temperature.
Transitional (C2)	-0.5°C	Compacted frozen, allowed to thaw and consolidate close to -0.5°C, and tested at that temperature.
Freeze-Thaw (C3)	-0.5°C	Compacted frozen, allowed to fully thaw and consolidate close to 18°C, subjected to freezing at -10°C until equilibration, allowed to thaw and consolidate again close to -0.5°C, and tested at that temperature.
Room (C4)	18°C	Room compaction and testing.

Table 3.2. Summary of stress ratios and dilation angles at different test conditions.

Environmental Condition	$\tan\phi'_{cs}$	$\tan\phi'_{p}$	ψ (°)
C1-25 kPa		6.11	28.6
C1-50 kPa	1.28	3.70	22.8
C1-100 kPa		2.58	16.8
C2-25 kPa		1.19	16.2
C2-50 kPa	0.67	1.11	14.4
C2-100 kPa		0.94	9.5
C3-25 kPa		1.88	35.1
C3-50 kPa	0.51	1.52	29.7
C3-100 kPa		1.00	18.0
C4-25 kPa		0.70	14.9
C4-50 kPa	0.36	0.59	10.6
C4-100 kPa		0.54	8.5

Table 3.3. Summary of properties used in the numerical model at different test conditions.

Environmental Condition	Stress (kPa)	ρ (kg/m^3)	G (kPa)	K (kPa)	ϕ'_{cs} (°)	ϕ'_p (°)	ψ (°)
C1-25 kPa	26.4	1625.0	7635.3	16543.2		80.7	28.6
C1-50 kPa	52.7	1625.0	8864.6	19206.6	52.1	74.9	22.8
C1-100 kPa	102.4	1625.0	11410.2	24722.1		68.8	16.8
C2-25 kPa	30.2	1631.1	559.8	1212.9		49.8	16.2
C2-50 kPa	58.7	1723.9	909.3	1970.2	33.6	48.1	14.4
C2-100 kPa	107.7	1679.3	1576.0	3414.7		43.1	9.5
C3-25 kPa	29.2	1822.6	1172.1	2539.6		62.0	35.1
C3-50 kPa	57.3	1831.4	1704.5	3693.1	27.0	56.7	29.7
C3-100 kPa	103.6	1834.5	2242.6	4859.0		45.0	18.0
C4-25 kPa	27.8	2269.6	1167.9	2530.5		34.9	14.9
C4-50 kPa	57.8	2299.4	1486.2	3220.1	20.0	30.6	10.6
C4-100 kPa	104.7	2313.7	1725.3	3738.2		28.5	8.5

Table 3.4. Summary of increased normal stresses due to restrained dilatancy.

Environmental Condition	Actual Normal Stress (kPa)	Restrained Normal Stress (kPa)	Ratio
C1-25 kPa	26.4	47.5	1.8
C1-50 kPa	52.7	79.1	1.5
C1-100 kPa	102.4	133.1	1.3
C2-25 kPa	30.2	39.3	1.3
C2-50 kPa	58.7	70.4	1.2
C2-100 kPa	107.7	118.5	1.1
C3-25 kPa	29.2	64.2	2.2
C3-50 kPa	57.3	97.4	1.7
C3-100 kPa	103.6	145.0	1.4
C4-25 kPa	27.8	50.0	1.8
C4-50 kPa	57.8	98.3	1.7
C4-100 kPa	104.7	167.5	1.6

Fig. 3.1. Grain-size distribution curve of borrow source material (Pit 174-x) and embankment grab samples (EGS-x) used during highway embankment construction, and composite mix (CM-4) used in direct shear tests.

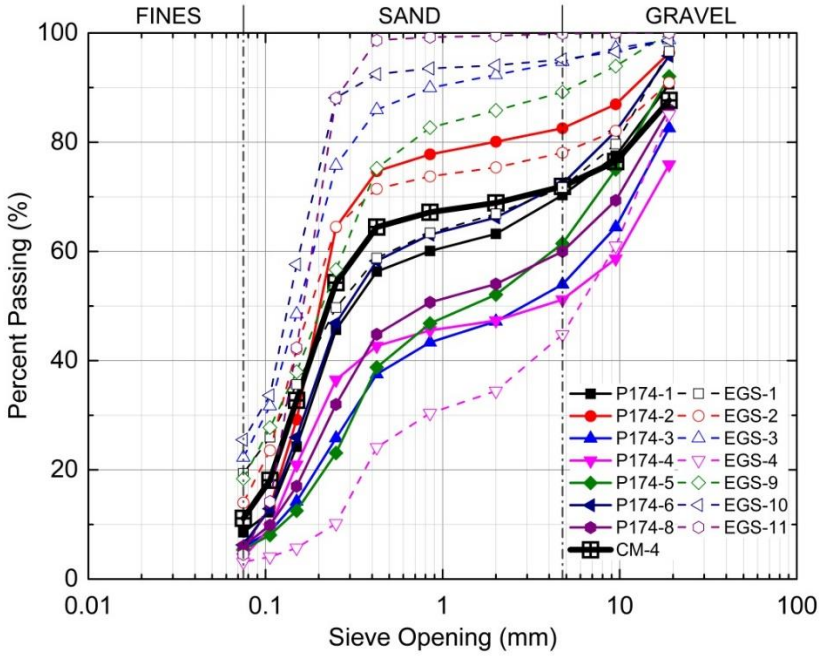

Fig. 3.2. Compaction curve of composite mix (CM-4) at room and below 0°C.

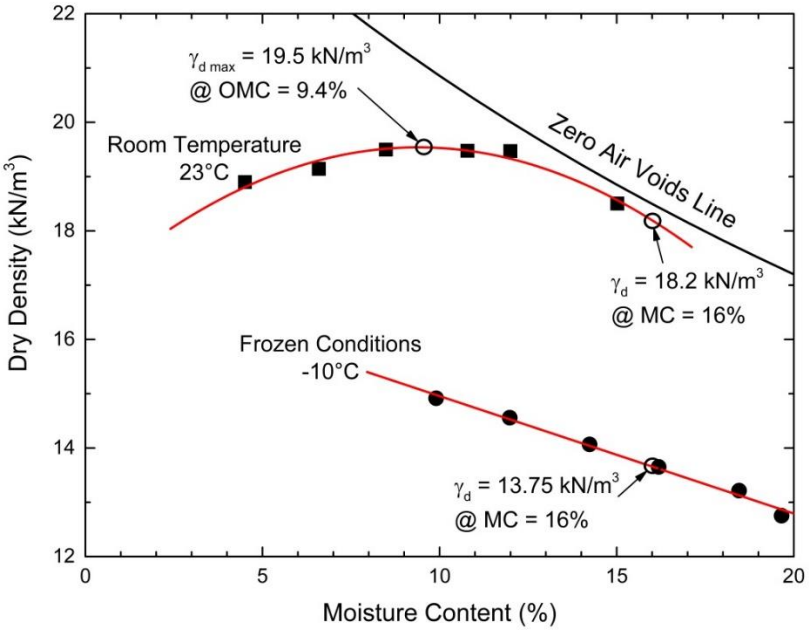

Fig. 3.3. Large-scale direct shear preparation and testing: (a) placement of frozen soil chunks in the direct shear box, (b) compaction of frozen soil chunks to specified density using a hammer drill, (c) finished compacted frozen soil to test height, (d) placement of sand layer on top of polyethylene plastic, (e) placement of rubber matting on top of gasket, (f) complete test set-up before shearing.

Fig. 3.4. Recorded temperature in the soil and environmental chamber (EC) during compaction, thawing, and freeze-thaw stages.

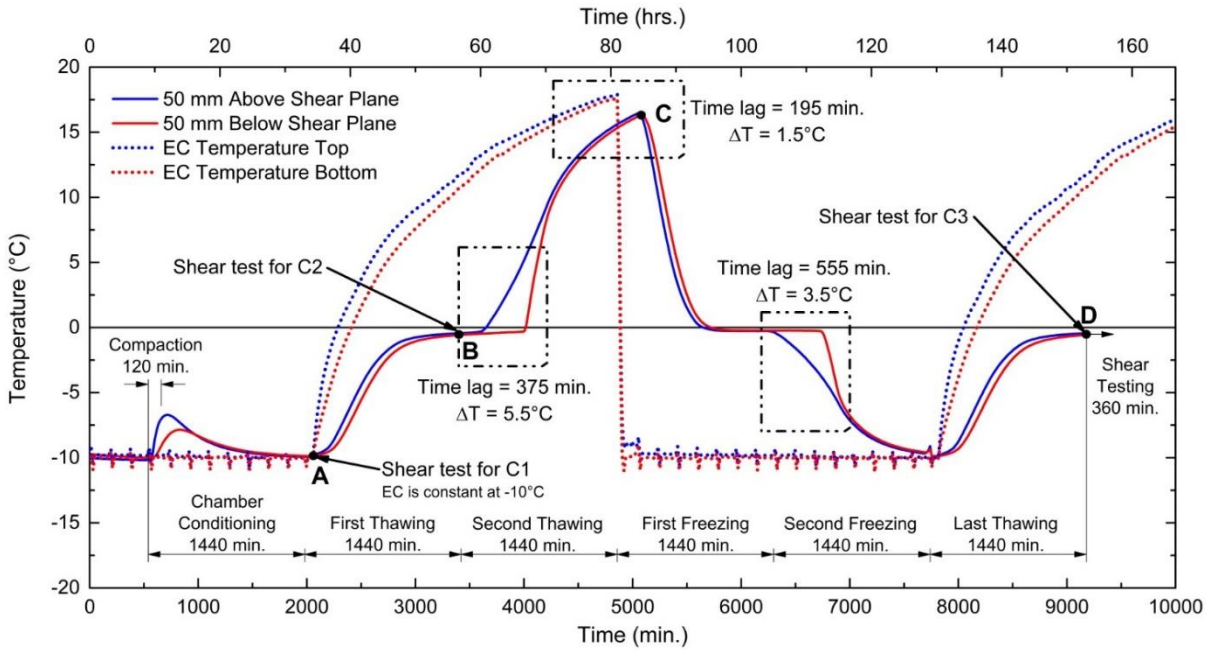

Fig. 3.5. Shearing and dilation under frozen conditions (C1).

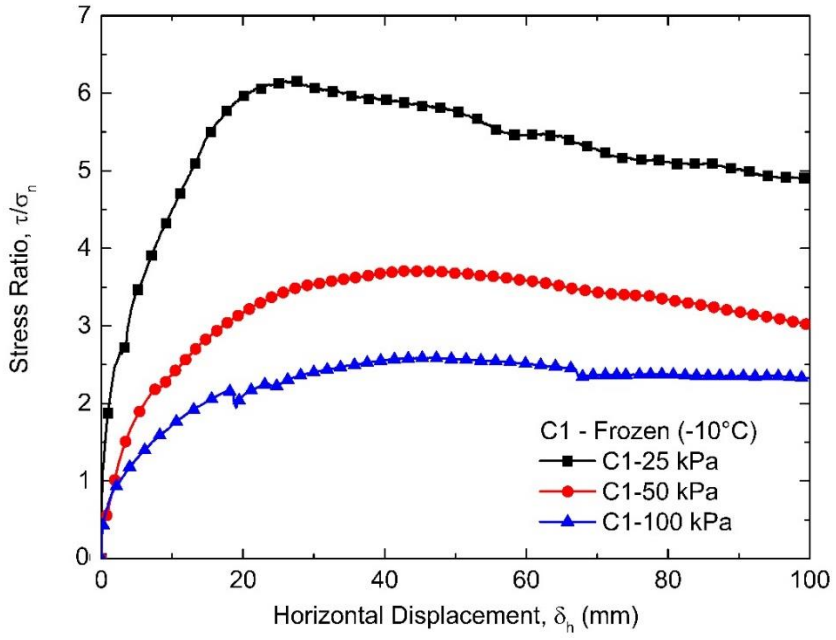

(a)

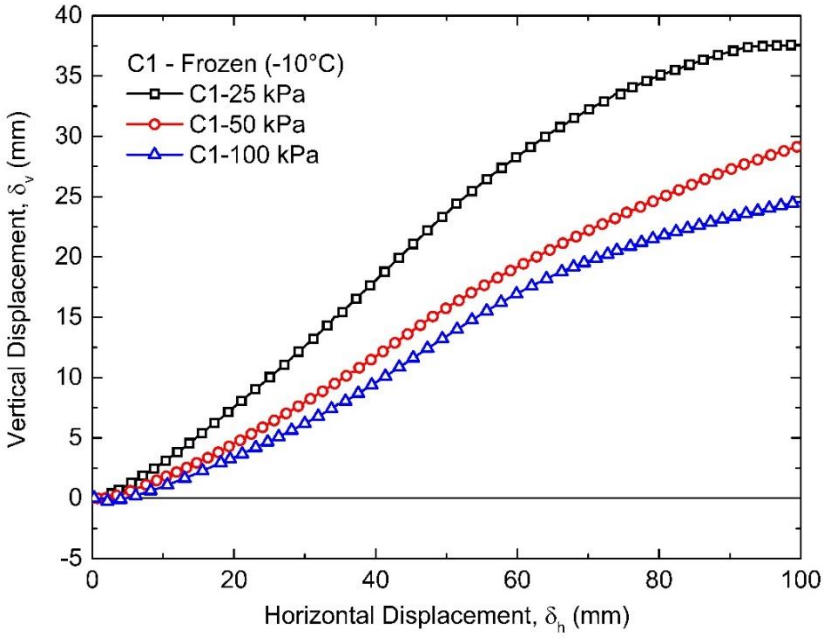

(b)

Fig. 3.6. τ/σ_n vs. log σ_n for peak and critical states for (a) frozen and (b) phase change, freeze-thaw, and room conditions.

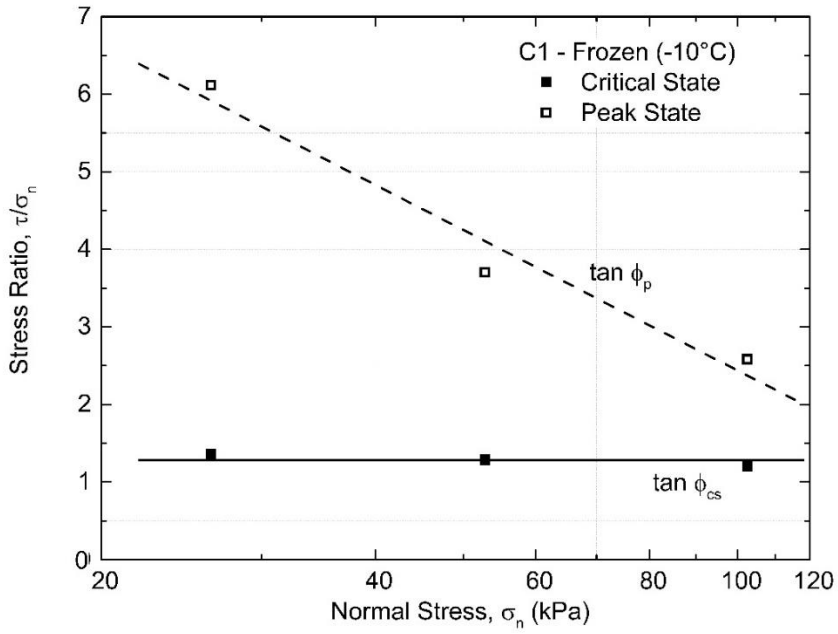

(a)

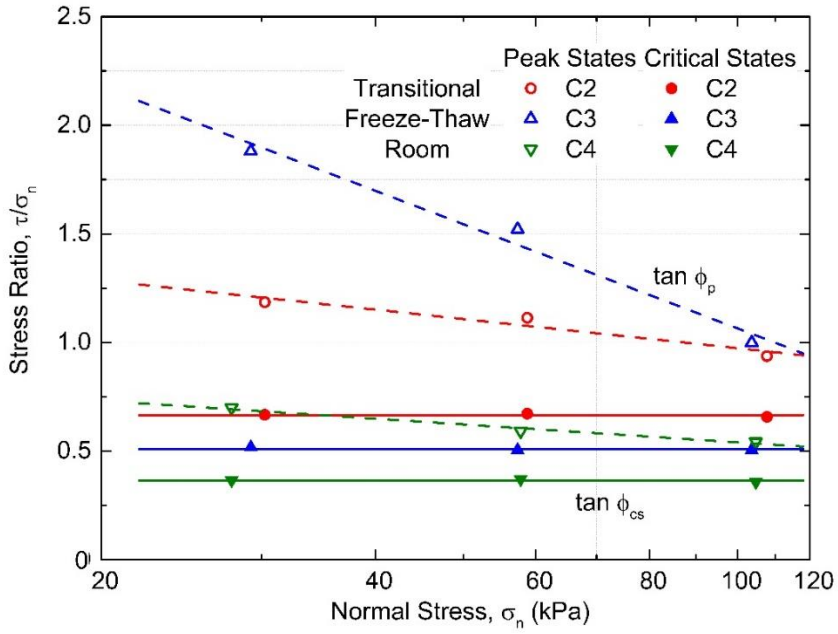

(b)

Fig. 3.7. Observed chunks within shear plane after frozen direct shear tests.

Fig. 3.8. Shearing and dilation under transitional (phase change) conditions (C2).

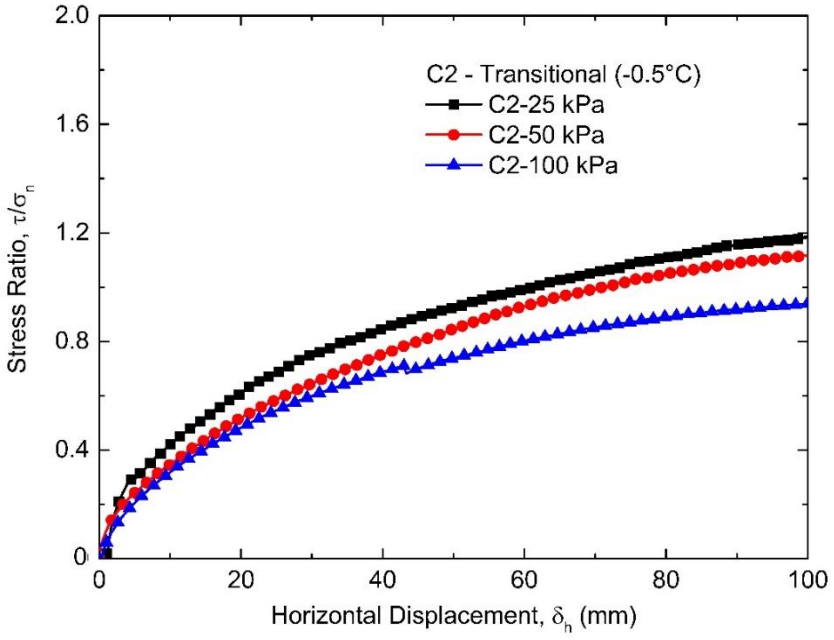

(a)

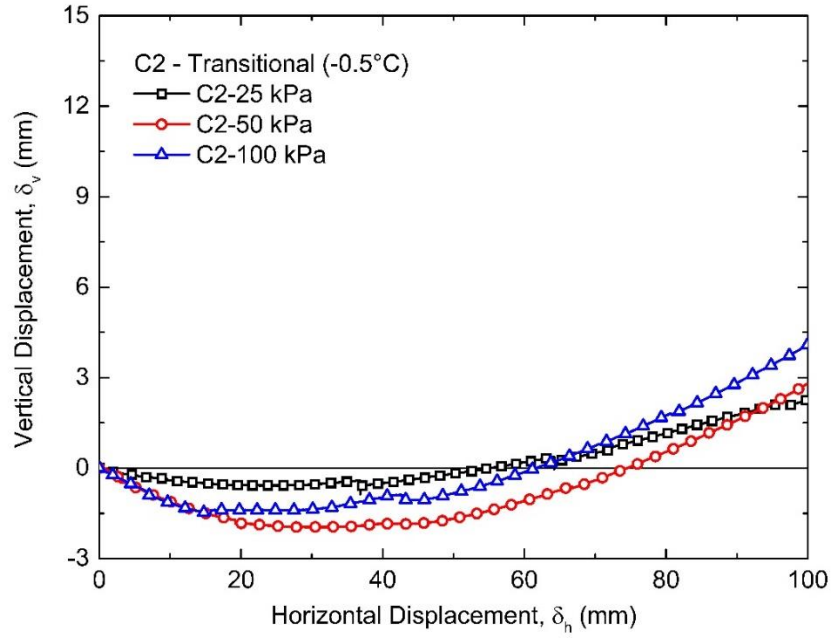

(b)

Fig. 3.9. Shearing and dilation under freeze-thaw conditions (C3).

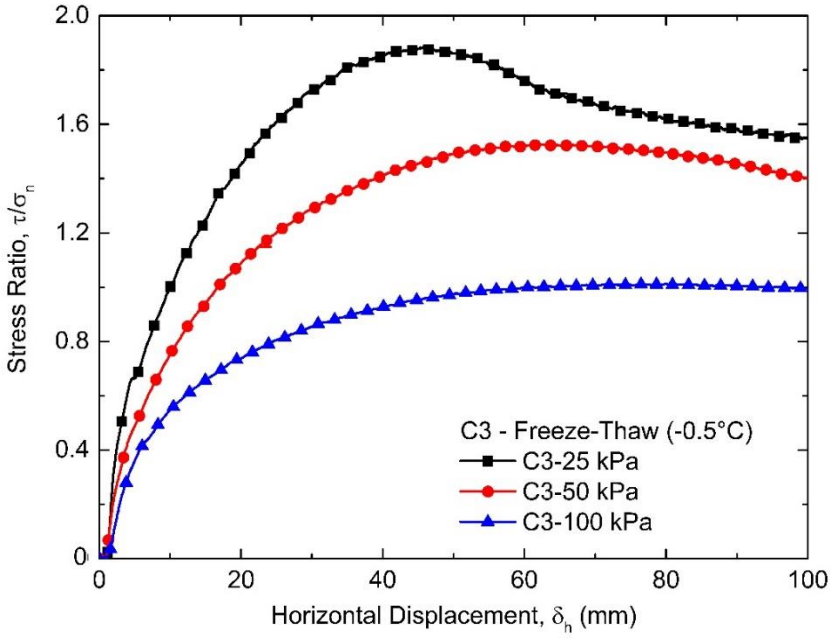

(a)

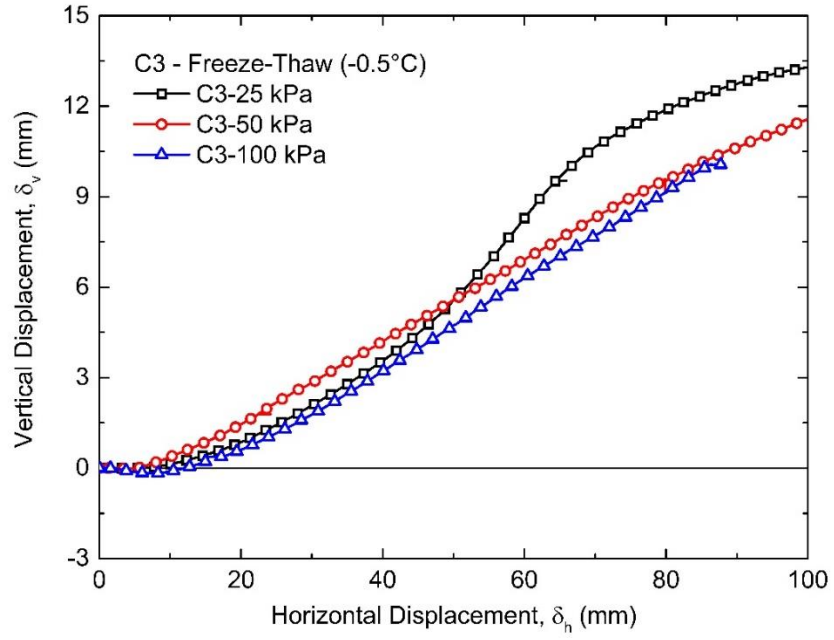

(b)

Fig. 3.10. Shearing and dilation under room conditions (C4).

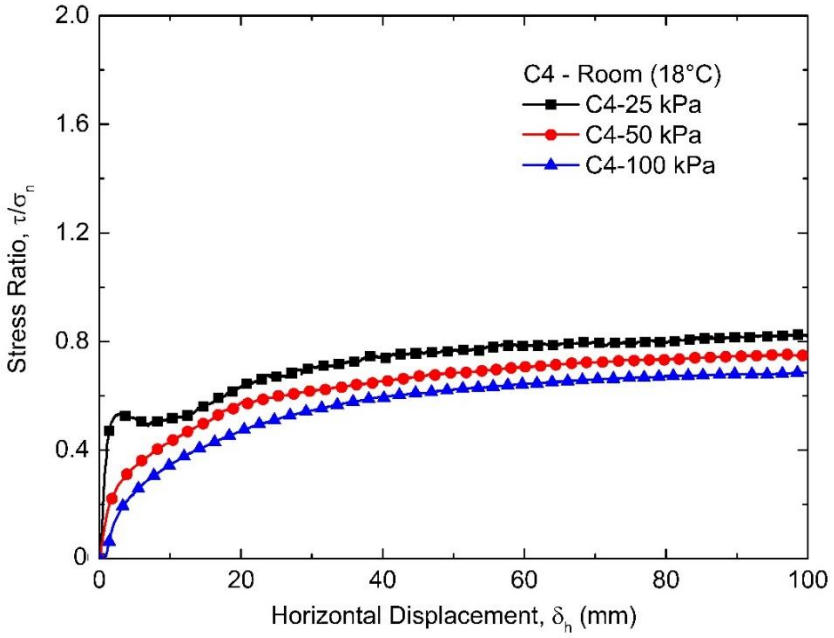

(a)

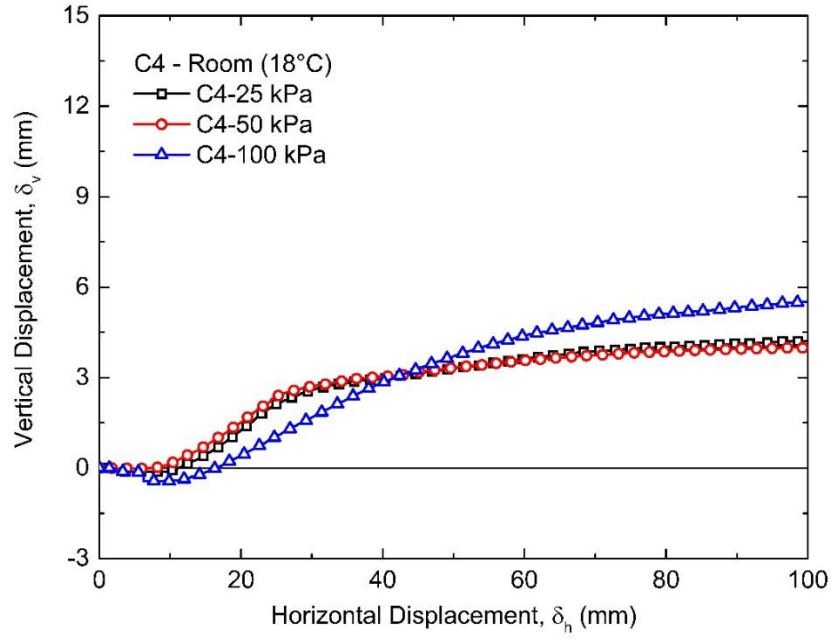

(b)

Fig. 3.11. Comparison of laboratory results with numerical simulations for (a) frozen, (b) transitional (phase change), (c) freeze-thaw, and (d) room conditions. DS: direct shear laboratory tests; FLAC: regular plane strain numerical FLAC 2D model; RD: numerical model using FLAC 2D using restrained dilatancy.

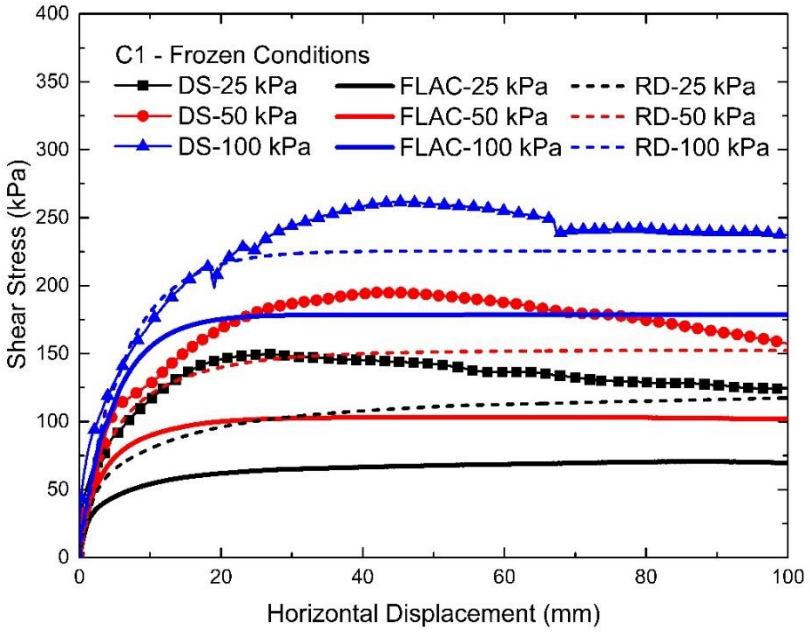

(a)

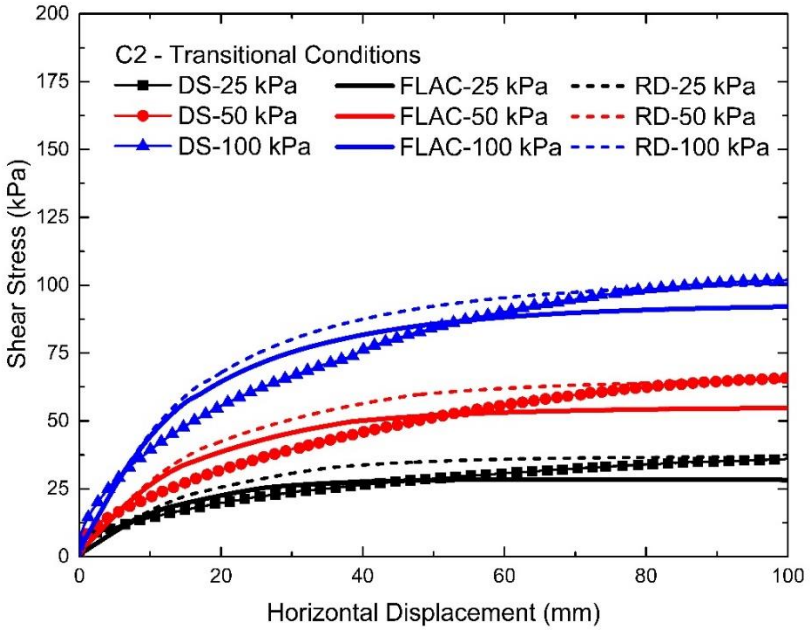

(b)

Fig. 3.11 (continued)

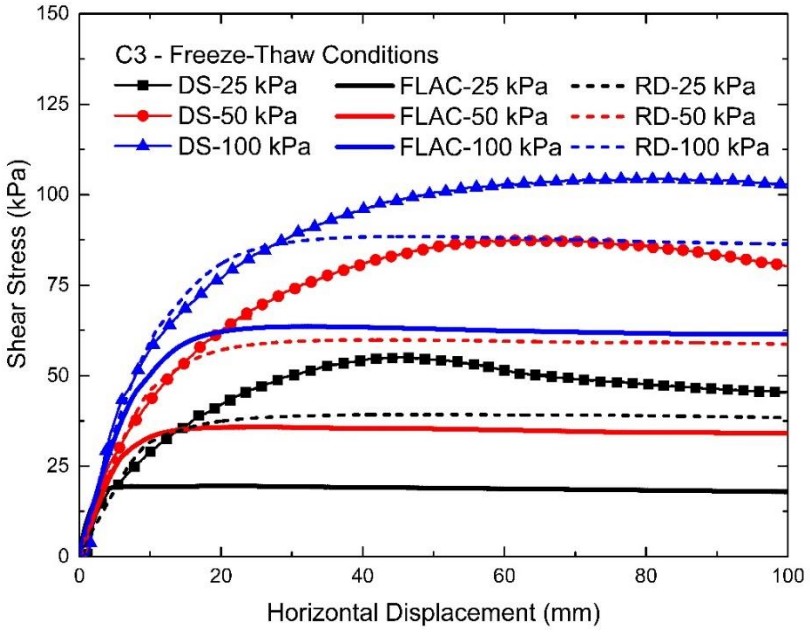

(c)

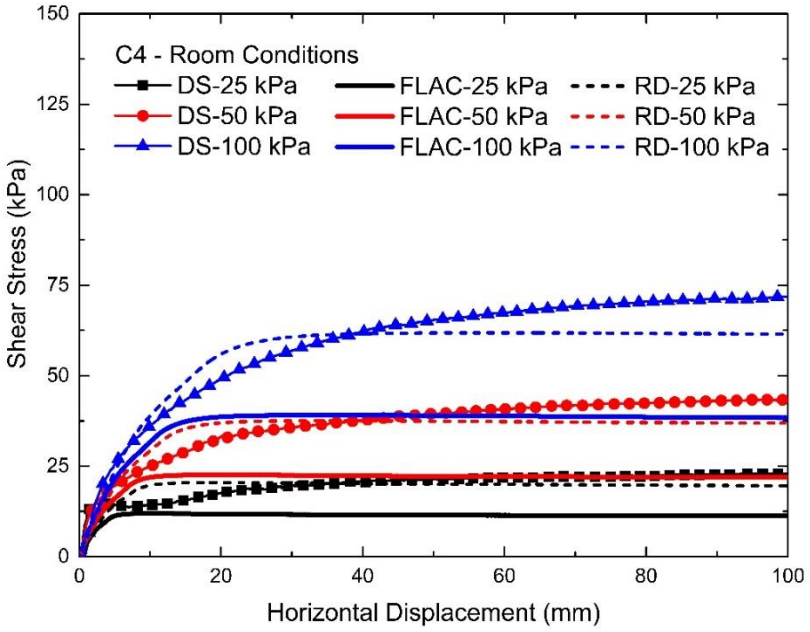

(d)

List of Notations and Acronyms in this Chapter

CM	Composite mix
EC	Environmental chamber
EGS	Grab samples from embankment fill
G	Shear modulus (kPa)
H	Height (mm)
K	Bulk modulus (kPa)
L	Length (mm)
LVDT	Linear Variable Differential Transformers
SAA	ShapeAccelArray
T	Temperature (°C)
USCS	Unified Soil Classification System
W	Width (mm)
γ_d	Dry density (kN/m^3)
$\gamma_{d\,max}$	Maximum dry density (kN/m^3)
δ_v	Vertical displacement (mm)
δ_h	Horizontal displacement (mm)
ε_{xy}	Shear strain
ν	Poisson's ratio
ρ	Density (kg/m^3)
σ_n	Normal stress (kPa)
τ	Shear stress (kPa)
ϕ'_{cs}	Critical state friction angle (°)
ϕ'_p	Peak friction angle (°)
ψ	Dilation angle (°)

CHAPTER 4

SOIL-GEOTEXTILE INTERFACE PROPERTIES[1,2]

4.1. Introduction

Geosynthetics have been extensively used in various geotechnical structures such as mechanically-stabilized earth walls, embankments slopes, and basal foundations. With the use of geosynthetics as a construction material, it has allowed a cost-effective and rapid approach to soil structures construction while satisfying design standards for routine applications. The most common types of geosynthetics used in construction are non-woven and woven geotextiles. Non-woven geotextiles are commonly used as a separation layer between the native and backfill soil. Woven geotextiles on the other hand are commonly used as reinforcement and are installed in one or multiple layers to improve the stability of embankment slopes. The additional strength derived from the use of these woven geotextiles at the slopes enables engineers to design for steeper slopes. With steeper slopes, the costs associated with hauling soil material and embankment footprint are reduced and translate to construction cost savings.

Coarse-grained, free-draining soils (e.g. gravel) suitable for embankment fill material are not always available at project sites and transporting them to remote locations might be cost prohibitive. The use of geotextiles to reinforce locally-available marginal soils (e.g. poorly-

[1] Parts of this chapter were previously published in conference proceedings. This chapter is being prepared for submission in a peer-reviewed journal.
De Guzman, E.M.B., Kaluzny, S.W., Stafford, D.M.J., and Alfaro. M. 2020. Freeze-thaw effects on the interface shear strength of a wicking geotextile. Geosynthetics International (in preparation).

De Guzman, E.M.B., Kaluzny, S.W., and Alfaro, M. 2018. Numerical Analysis in Pullout of a Geotextile With and Without Wicking Function. 11th International Conference on Geosynthetics. Seoul, South Korea.

Kaluzny, S., **De Guzman, E.M.B.**, and Alfaro, M. 2016. Pullout Resistance of Geotextiles With and Without Wicking Function. 69th Canadian Geotechnical Conference. Vancouver, BC.

[2] A list of notations and acronyms used in this chapter are found in page 141.

draining soils with fines content greater than 30%) is an economical and practical alternative to overcome these concerns (Abu-Farsakh et al. 2007, Pathak and Alfaro 2010, Hatami et al. 2011, Esmaili et al. 2014). Reinforced soils are governed by the tensile and pullout capacities of the geotextile. Tensile capacity is made available by manufacturers in their product technical data sheets, but the interface friction angle derived from pullout tests (Alfaro et al 1995a, Alfaro et al. 1995b) is not always available. The pullout test replicates the behaviour of the reinforcement in a soil structure, and the resistance generated at the interface of the soil and the geotextile allows the soil to transmit tensile stresses to the reinforcement (Weerasekara and Wijewickreme 2010). Several factors play a key role in the determination of the soil-reinforcement interaction mechanism such as soil properties (e.g. particle size distribution, density) and the mechanical properties of the geotextile (Lopes 2002) to name a few. Researchers (Khoury et al. 2011, Hatami and Esmaili 2015) found that unsaturated conditions at the soil-geotextile interface heavily influences the overall behaviour of the reinforced structure, where increase in moisture content at the interface reduces the effectiveness of the reinforcement due to the decrease in soil suction. Moisture contents and dry densities of most backfills are likely to be different from the as-compacted values over their service lives due to seasonal wetting and drying cycles (Abu-Farsakh et al. 2007) which also influences the interface resistance. Wetting of the soil-geotextile interface during construction or service life of the reinforced structure could result in considerably lower pullout capacity and interface shear strength (Wang et al. 2017). Wicking geotextiles have been recently introduced in the market to overcome this issue as it provides in-plane drainage (wicking) when water infiltrates through the soil (Zhang et al. 2014). The wicking function of the geotextile allows for wicking of the water even in unsaturated soil conditions (Han et al. 2016). The reinforced embankment along ITH presented in Chapter 2 is the first application of wicking

geotextiles as slope reinforcement in Arctic regions. To the author's knowledge no work has been done to quantify implications of the wicking function will have on the interface resistance of woven geotextiles. It is hypothesized that the interface resistance will be greater when a wicking geotextile is used under saturated conditions compared to an alternative geotextile without the drainage function (non-wicking). In this chapter, the interface shear strength of wicking and non-wicking woven geotextiles were determined from a series of pullout tests under different moisture contents and environmental conditions. In addition, the interface properties are needed in the thermal-mechanical modelling of the reinforced embankment test section in Chapter 6 to investigate how geotextiles influence the behaviour of thawing slopes.

4.2. Methodology

4.2.1. Soil Properties

As presented in Chapter 3, the grain size distribution curve of the soil used in the pullout tests is shown in Fig. 3.1. This mixture on average had a fines content ranging from 11% to 13%, plastic limit of 16.4%, liquid limit of 24.6%, and plasticity index of 6.6%. About 72% passing the 0.075 mm (No. 200) sieve was of silt fraction based on the results of hydrometer tests. The mixture ranged from well-graded sand with silt and gravel to silty sand with gravel based on the Unified Soil Classification System (USCS). The same compaction curves for room and frozen temperature conditions in Fig. 3.2 were used to prepare the soil for the pullout tests. Four conditions were investigated in the testing program: (1) at room conditions with soil at high moisture content (HMC), (2) at room conditions with soil at optimum moisture content (OMC), (3) at thawed conditions using frozen soil at HMC, and (4) at thawed conditions with soil at OMC. For room condition tests, HMC (interchangeably labelled as wet) was taken at w = 16%, while OMC was at w = 9.4%. For the thawed condition tests with soil at HMC, the frozen soil chunks were prepared

at w = 16% and compacted in the pullout box at -10°C similar to the procedure done in the direct shear tests (Section 3.2). The soil was then thawed to room temperature before the pullout testing commenced. This was similarly done for thawed conditions with soil at OMC, except that the soil was compacted first at OMC before it was frozen. The HMC tests simulates a condition for water to flow through the wicking geotextile, while the OMC serves as a control state. The moisture content selected for the HMC tests is almost the same as the plastic limit of the soil. Using soil at HMC is not typical of construction practice in warm climates but was done in order to understand the benefit of wicking once slopes become saturated such as thawing of ice in frozen soil found in cold climates.

4.2.2. Geotextile Properties

Two geotextiles (Fig. 4.1) were investigated: (1) wicking (blue-coloured) and (2) non-wicking (red-coloured) woven geotextiles. Both geotextiles are comparable as both reinforcements exhibit the same tensile strength at 2% strain, are composed of the same polypropylene filament, and are weaved in the same manner during manufacturing. The only difference between the two fabrics is the presence of the wicking filaments (blue strands) along the cross-direction as shown in Fig. 4.1. Relevant properties of the geotextiles based on manufacturer's specifications are summarized in Table 4.1.

4.2.3. Testing Equipment

The same testing box was used for both tensile and pullout tests. The testing box has inner dimensions of 1200 x 600 x 400 mm (L x W x H). The bottom half of the box is 250 mm thick and the upper half is 150 mm. These halves were locked during the pullout tests. The testing box was designed and successfully used for pullout tests of geogrids (Alfaro et al. 1995a; Alfaro et al. 1995b, Mosallanezhad et al. 2016). Some modifications to the testing box (e.g. addition of steel

sleeves) were done since the pullout clamp was buried with the soil following recommendations by Farrag and Morvant (2000). Communication cables of the strain pots, LVDT's, and the load cell for tensile tests, and additionally the air pressure gauge for the pullout tests were connected to a data acquisition system during testing. The testing box is the same one used for the direct shear tests in Chapter 3, except that there were circular inserts installed in the box and the two halves were allowed to slide to simulate shearing. The servomotor was attached to the upper half of the testing box for direct shear tests, but for tensile and pullout tests it was directly attached to the pullout clamp.

4.2.3.1. Tensile Test Set-up and Implementation

Fig. 4.2 shows a typical set-up of a tensile test in the testing box. The set-up of the pullout clamp and telltales for the tensile tests are the same as with the pullout test set-up (Section 4.2.3.2). The geotextile was anchored at the front end (pullout clamp) and back end of the pullout box. On the pullout clamp side, the geotextile was wrapped around an aluminum rod and marine epoxy was used to provide bonding between two geotextile surfaces before screwing a metal bar to the pullout clamp. Once the marine epoxy was placed, the crease was left to cure for a minimum of 12 hours in compression to ensure bonding. The aluminum rod was conceptualized to provide additional bearing resistance against the pullout force on the metal bar and prevent slippage. Earlier trial tests by the author had shown that creasing the geotextile and applying the marine epoxy alone will induce slippage at about 20 mm of displacement. The back end of the geotextile fabric was restrained with an angle bar which was screwed in the testing box. Similar to the pullout clamp at the front end, an aluminum rod was used inside the crease that goes against the angle bar to resist larger tensile forces. A marine epoxy was also used to provide resistance against slippage.

There were five telltales installed on the geotextile fabric (TT#1 to TT#5), and one telltale attached to the pullout clamp (TT#6). The locations of each telltale are also shown in Fig. 4.2. A 50 lb (23 kg) tension cable was used for these telltales. The telltales were tied around a filament on the geotextile and a plastic bonder epoxy was used at the tied connection. The telltales were spaced 100 mm perpendicular to the direction of loading and 200 mm between TT#1 to TT#4. TT#5 was 90 mm from the edge of the pullout clamp. The telltales were connected to the strain pots at the back of the testing box to measure displacements.

The geotextile was 840 mm long and 530 mm wide from the back end of the box to a distance of 750 mm. From 750 mm to 840 mm from the back end of the box, the sides were tapered from 530 mm to 580 mm. The angle bar that comes with the box is 530 mm wide. During trial tests, constant width of 580 mm generated stress concentrations at the corners of the back of the box, while constant width of 530mm caused significant slipping and shearing at the front end. With the tapering of the geotextile towards the pullout clamp, the stress concentrations were significantly reduced by observing the perpendicularly drawn lines on the geotextile fabric (Fig. 4.2).

The pullout clamp was attached to a load cell connected to a servomotor. The servomotor allows the manual adjustment of the position of the pullout clamp as well as controlling the displacement rate once testing commences. A displacement rate of 1 mm/min was applied during the tensile tests. The geotextile was pre-tensioned before the actual test to ensure that the whole fabric was carrying the load.

4.2.3.2. Pullout Test Set-up and Implementation

Details of the preparation of the soil and testing box for room condition tests are shown in Fig. 4.3. All four sides of the box were greased and lined with two layers of polyethylene plastic to minimize side friction and prevent the development of restrained dilatancy (Alfaro et al. 1995b, Hayashi et

al. 1996, Ghionna et al. 2001). A base layer of soil was compacted to a height of 150 mm from the bottom of the box (Fig. 4.3a) using a hammer drill. This was done to minimize the amount of material to be compacted for the testing program. A polyethylene plastic was placed on top of this base layer to prevent moisture migration from the soil interacting with the geotextiles. Below the geotextile only 100 mm was remixed to achieve the target moisture content for both wet and optimum conditions. At the front of the box, a 150 mm steel plate was installed at the top and bottom of the opening and a non-woven geotextile fabric was placed around it to prevent soil material from spilling out once the pullout test commenced. A slit was made on this non-woven geotextile fabric for the pullout clamp.

The soil described in Section 4.2.1 was compacted in two, 50 mm thick layers above the base layer. This layer was compacted with a tamping plate across the entire plane three times for HMC tests while a hammer drill was used for OMC tests. Once the soil below the geotextile fabric has been compacted to elevation matching the level of the horizontal load cell, the pullout clamp with the geotextile fabric was set on top of this surface (Fig. 4.3b), with the pullout clamp connected to the load cell. Unlike the tensile test, the geotextile fabrics in the pullout test span the entire length of the pullout clamp (580 mm) but the telltale locations were at the same locations as shown in Fig. 4.2. The length of the geotextile inside the pullout box is still 840 mm at the start of the test, with a 360 mm overhang at the back of the testing box to facilitate wicking. The telltales were protected with conduits to keep it aligned during the compaction of the soil above the geotextile fabric. These were also connected to the strain pots (Fig. 4.3c) to minimize distortion during the set-up. The top half of the box was then filled with 125 mm of soil in two layers (75 mm and 50 mm) and following the compaction effort described earlier. Fig. 4.3d shows the end of the pullout clamp connected to the load cell and geotextile buried in soil.

A 25 mm thick sand buffer was placed on top of this layer separated by a polyethylene plastic (Fig. 4.3e) to prevent possible punching of the rubber membrane that seals the pullout box. The sand buffer was intentionally humped to account for settlement that would occur after application of the specified normal stress. This sand buffer acts as a flexible layer for uniform application of normal stress on the soil (Leshchinsky and Marcozzi 1990, Alfaro et al. 1995b, Rahmaninezhad et al. 2016). The rubber gasket was greased with high-vacuum seal to prevent air leakage during application of normal stress and the rubber membrane was then rolled over its top afterwards. The top cap was placed to seal the upper half of the box as shown in Fig. 4.3f. The brass rods on the top cap were pushed in on top of the rubber membrane for contact and the linear variable differential transducers (LVDTs) placed afterwards to measure any settlement or dilation that may occur during testing. Once all data cables were connected to the data acquisition system, air pressure was introduced and the testing box was checked for air leakages. Prior to pullout testing, the soil with the geotextile was consolidated at the specified test normal stress for 30 mins. After the consolidation phase was completed, the pullout test was initiated. The displacement rate for the pullout test was the same as the tensile test at 1 mm/min and was maintained constant throughout the duration of the test.

The set-up for the thawed pullout tests are the same as the procedure presented above except that frozen soil was used and the testing was done inside an environmental chamber similar to the direct shear tests in Chapter 3. It should be noted that HMC tests for thawed conditions used frozen soil chunks with w = 16%, while OMC tests were compacted at w = 9.4% before the set-up was frozen in the environmental chamber. Fig. 4.4a shows the pullout clamp and the geotextile fabric inside the pullout box on top of the compacted frozen soil. The telltales (Fig. 4.4b) were connected to the strain pots during compaction. Fig. 4.4b was taken during the thawing cycle and some streaks

of water are seen on the geotextile fabric. Frozen soil was compacted in a series of layers until the test height was achieved at 25 mm below the rim of the pullout box (Fig. 4.4c). The complete set-up of the pullout test inside the environmental chamber is shown in Fig. 4.4d. Heat is generated in the frozen soil chunks during compaction as seen in Fig. 4.5 similar to what was observed in the direct shear tests in Section 3.2.3. The soil was equilibrated with the environmental chamber temperature of -10°C for 1440 min (24 hrs) for both HMC and OMC before the fan was turned off (Point A) to allow the soil to fully thaw. The normal stress was applied for each test while the soil was under temperature equilibration and thawing. It takes about 2880 min (48 hrs) before both temperature sensors reach 15°C at Point C, at which point the thawed pullout tests were started.

4.2.4. Calibration Testing

For all pullout tests conducted, the pullout clamp was confined inside the testing box. By confining the pullout clamp during testing, a constant confined specimen length throughout the duration of the test can be maintained (Alfaro et al. 1995a, Farrag and Morvant 2000). Another advantage of confining the clamp mechanism is that it allows distribution of stress along the reinforcement more effectively in comparison to having the clamp outside of the pullout box. To account for the resistance of the clamp in the pullout test, a calibration test was performed at different normal stresses corresponding to the pullout test with geotextiles. The calibration test is a pullout test without any geotextile attached to the clamp. The method of preparation for the calibration is the same as those carried out in the pullout test with the geotextile for both room and thawed conditions, except the geotextile was cut out from the pullout clamp (Fig. 4.6). The overburden soil was removed and the geotextile was cut at the interface of the clamp. For room condition tests, the overburden soil and soil underneath the expected travel stroke of the pullout clamp were remixed to reach the target moisture conditions and were likewise compacted as presented earlier.

For thawed condition tests, the thawed soil within 450 mm from the front end of the testing box was removed. The environmental chamber and the remainder of the soil inside the testing box were brought to -10°C, after which layers of frozen of soil were compacted underneath the location of the pullout clamp, as well as the layers above the pullout clamp after its reinstallation. The same normal stresses and displacement rate were used for the calibration test. For clarity, gross results are test results that has both the geotextile and the pullout clamp together during the pullout test. Calibration results are test results based on pullout tests with the pullout clamp alone. Net results are test results with the calibration results subtracted from the gross results.

4.2.5. Interpretation of Test Results

Results of the pullout tests were interpreted following the method described in Alfaro et al. (1995a, b). The method is extensively discussed in their paper and only a brief summary is provided in this section. Before this method can be employed, the effect of the pullout clamp must first be removed. The gross pullout force, calibration pullout force, and the net pullout force are denoted as P_G, P_C, and P_N, respectively. A hyperbolic function was used as a fitting function to ensure that the P_C being subtracted from P_G corresponded to the same global displacements at TT#6 (δ_{gross}). Eq. 4.1 shows the formula of the hyperbolic function and the procedure to utilize the formula is briefly presented.

$$P_C = \frac{\delta_{gross} + \sigma_n}{a + b\delta_{gross}} \qquad \text{Eq. 4.1}$$

In Eq. 4.1, a and b are the hyperbolic intercept and slope parameters, respectively, obtained from the normalized $\delta_{calibration}/(P_C/\sigma_n)$ vs. δ_{gross}. The $\delta_{calibration}$ were obtained directly from the calibration pullout tests, which do not necessarily correspond to the displacements recorded during the pullout tests with the geotextile attached. The term P_C/σ_n is the recorded pullout calibration

force normalized by the normal stress applied at the top of the pullout box. Plotting $\delta_{calibration}/(P/\sigma_n)$ vs. δ_{gross} yielded an approximate straight line from which the hyperbolic parameters can be determined. These parameters are used in Eq. 4.1 to determine the P_C corresponding to δ_{gross}. P_C is then subtracted from P_G at the corresponding displacement to obtain P_N. P_N is divided by the width of the geotextile, in this case 580 mm, to obtain the net pullout force expressed in force per metre. It should be noted however that the load being carried by the fabric as well as the strains developing along its length are not solely the results recorded by the load cell and TT#6.

Fig. 4.7a shows the locations of the telltales along the geotextile fabric, while Fig. 4.7b shows the conceptual displacements recorded at each telltale. In Alfaro et al. (1995b), the tensile force per unit width acting along the reinforcement length (Fig. 4.7d) is determined from the average strains calculated based on Fig. 4.7c. Based on the displacements recorded from the telltales along the geotextile fabric, the average strains are derived by subtracting the displacements between two telltales and dividing it by the original distance between the two telltales in consideration. This gives the average strain between the two telltales and will be used to determine the pullout force carried by the geotextile at the mid-point between two adjacent telltale locations.

After the equivalent strains have been determined, the pullout force carried by the geotextile is determined from the results of the tensile test. The pullout capacity of the geotextile is based on the soil-interface resistance available depending on the soil properties, the stiffness of the geotextile fabric, the coarseness of the geotextile fabric surface, and the normal stress applied to it, among other factors. The strain experienced by the geotextile corresponds directly to the tensile load, in this case the pullout force, to cause that strain. Once the equivalent forces along the geotextile have been determined, the shear stress along the fabric can be obtained using the following equation:

$$\tau_p = \frac{F_{max} - F_{min}}{2L_eB} \quad \text{Eq. 4.2}$$

where τ_p is the total shear stress on the geotextile fabric, F_{max} and F_{min} are the maximum and minimum pullout forces, respectively, for a given normal stress, L_e is the distance where displacements were recorded, and B is the width of the geotextile (580 mm). Eq. 4.2 takes into account the top and bottom surface of the geotextile fabric. The interface resistance can be obtained afterwards by plotting τ_p with σ_n with respect to the test condition. Eq. 4.2 explicitly takes into account the length of interface mobilization through L_e.

4.2.6. Interface Test Using Clean Sand

The two geotextile fabrics have similar surface texture according to the manufacturer and that the difference in pullout interface resistance is expected to be attributed mostly to the wicking function. To confirm this, both geotextiles (250 mm in length) were tested in pullout using dry clean sand as backfill material. The same procedure from pullout tests presented earlier and the calibration procedure was done after the test to subtract the interface resistance due to the presence of the pullout clamp.

4.3. Results and Discussion

4.3.1. Tensile Test Results

Fig. 4.8 shows the tensile load vs. strain for the two geotextiles tested. The strain in the horizontal axis was taken as the strain between the clamp and the fixed point at the back-end of the testing box. A repeat test for both geotextiles were done for confirmation (denoted by -R in Fig. 4.8). The tensile load between the two geotextiles are comparable between 1.5% and 2%. The tensile load of the wicking geotextile at 2% is 13.3 kN/m, and 12.4 kN/m for the non-wicking geotextile. Table 4.1 shows the summary of the reported manufacturer tensile loads at 2% axial strain. Interestingly,

the difference between the tensile load of the two geotextiles reported by the manufacturer and the results obtained from the tensile tests in this study are the same (0.9 kN/m). The geotextiles were recommended by the manufacturer as they were manufactured in the same manner except the presence of the wicking strands of the wicking geotextile and have relatively similar tensile force values at 2%. The results of the tensile test conducted are slightly lower than the one reported by the manufacturer due to the difference in testing equipment used to determine this value. Soil structures typically experience considerable deformation at a strain of 2% (Budhu 2011), and thus the interface resistance for both geotextile fabrics were compared at this strain value. The tensile test set-up mimics how the geotextile is being pulled out of the soil except that there is no soil overburden or frictional resistance that needs to be overridden. It is expected that beyond the 2% strain, the tensile loads will diverge as evidenced by the rupture values reported by the manufacturer and as confirmed by the testing conducted in this study. Using the method of interpretation described earlier in Section 4.2.5, larger strains for the non-wicking geotextile will result to lower tensile loads and therefore lower shear stresses at an applied normal stress. This will ultimately result in lower interface resistance for the non-wicking geotextile. The average force on the geotextile from the pullout tests are determined from this plot based on the average strains calculated in between telltales corresponding to the horizontal axis of Fig. 4.8.

4.3.2. Pullout Test Results

4.3.2.1. Room Condition Tests

The gross, calibration, and net pullout loads vs. global displacement for both geotextiles under room HMC conditions are shown in Fig. 4.9a to Fig. 4.9c, respectively. The net pullout load vs. global displacement under room OMC conditions is shown in Fig. 4.10. The gross and calibration pullout loads for the room OMC are provided in Appendix B. For both test conditions, the net

pullout loads of the wicking geotextile at 67 and 117 kPa tests are higher compared to the non-wicking one, while they are relatively the same for the 37 kPa tests. In Fig. 4.9c, the same net pullout load can be achieved at a lower global displacement for the wicking geotextile under the same normal stress. For example, at a normal stress of 117 kPa, a 30 kN/m net pullout load can be achieved at a global displacement of 15 mm for the wicking geotextile, but would require 22 mm for the non-wicking geotextile. Significant displacements need to be mobilized to achieve a higher pullout load for the non-wicking geotextile. Larger net pullout loads were recorded for the wicking geotextiles, which means that the interface resistance for this geotextile will also be larger than the non-wicking geotextile.

Fig. 4.11 and Fig. 4.12 show the horizontal displacements at different telltale locations along the length of wicking (Fig. 4.11a, Fig. 4.12a) and non-wicking (Fig. 4.11b, Fig. 4.12b) geotextiles under HMC and OMC conditions, respectively. In Fig. 4.11 and Fig. 4.12, the displacements recorded are higher closer to the clamp, and are less close to the back-end of the pullout box. The elongation of the geotextile is not uniform, and thus the pullout force along the reinforcement length. As discussed in the previous section, beyond the strain of 2% the tensile resistance of the two geotextile fabrics diverge and will affect the calculated interface resistance. Large horizontal displacements were recorded between TT#4 and TT#6 which resulted to larger strains just in front of the clamp. Horizontal displacements were therefore selected when ε_B (Fig. 4.7c) reached a 2% strain. The strains beyond this point (ε_C, ε_D) will vary accordingly as the load transferred to each telltale will be different. The end-of-test (EOT) horizontal displacements are also superimposed in Fig. 4.11 and Fig. 4.12 to show that at larger pullout loads the displacements recorded will correspondingly be larger. Larger displacements were observed from the 37 kPa tests at EOT and are reduced as the normal stress was increased. It can be seen that TT#1 and TT#2 are less

susceptible to displacements at larger normal stresses. The increase in normal stress applied to the pullout test also reduces the effective length mobilized.

Fig. 4.13 and Fig. 4.14 show the average pullout load in between telltale locations along the length of wicking (Fig. 4.13a, Fig. 4.14a) and non-wicking (Fig. 4.13b, Fig. 4.14b) geotextiles under HMC and OMC conditions, respectively. The net pullout loads between TT#3 and TT#4 are the same in these figures because of the 2% strain limit discussed earlier. The EOT net pullout loads are also superimposed in these figures. These loads are largest in between TT#3 and TT#4 and decrease towards the back-end of the testing box, which indicate that there is non-uniformity of load mobilized along the geotextile. The pullout load has no significant effect beyond the effective length of the geotextile, similar to the embedment depth of geotextiles on reinforced slopes where longer reinforcement does not necessarily indicate a more stable slope.

4.3.2.2. Thawed Condition Tests

Fig. 4.15 shows the net pullout load vs. global displacement for both geotextiles under thawed HMC conditions. Similarly, Fig. 4.16 shows the net pullout load vs. global displacement for both geotextiles under thawed OMC conditions. The gross and calibration pullout loads for both moisture conditions at the thawed state are provided in Appendix B. The pullout loads recorded for thawed OMC tests are slightly larger than the thawed HMC tests as expected. The peak loads for the thawed HMC tests were achieved at larger displacements compared to the thawed OMC tests. The net pullout loads were larger in the thawed OMC tests compared to the thawed HMC tests at global displacements less than 30 mm. The results of the room condition tests are larger than the thawed tests confirming that thawing of soil, in addition to its moisture condition, influences the pullout behaviour and therefore its interface resistance. The horizontal displacements and average pullout loads for the thawed HMC and thawed OMC tests are

summarized in Appendix B. These plots are similar to the ones presented for the room condition tests and were used to determine the interface shear strength for thawed conditions for both geotextiles.

4.3.3. Interface Properties

The interface properties between the soil and the geotextile fabric for both test conditions were obtained by plotting the shear stress against the normal stress for both wicking and non-wicking geotextiles. A line is fitted across these data points where the slope of the line is the interface friction angle (δ_p) between the soil and the geotextile and the intercept in the vertical axis is the apparent cohesion (c_p).

4.3.3.1. Room Condition Tests

Fig. 4.17a shows the interface properties calculated at 2% strain and Fig. 4.17b at EOT. Table 4.2 summarizes the interface properties for the two geotextiles. At low strain levels with comparable soil conditions the wicking geotextile provided interface resistance greater than a non-wicking geotextile. The presence of wicking at wet state of the soil allowed some of the water to be drained out and led to some additional consolidation at the interface. Under OMC condition tests, the difference between the two interface properties is more recognizable that HMC condition. Although the manufacturer indicated that the two geotextiles were constructed in the same manner and material and have relatively close tensile capacity at 2% strain, there is a slight ridge (2 mm) where the wicking yarns were weaved and may have also contributed to an additional surface area during pullout. The wet condition is not typical in construction practice in warm climate but may be representative in cold climates as in the case of ITH. The results presented here provide an understanding how the wicking influenced the interface resistance. Esmaili et al. (2014) noted that the wet condition properties may be conservative but it is not ideal to design with properties that

do not realistically represent field conditions. The interaction of the non-wicking geotextile with the soil close to its plastic limit resulted to the least interface resistance. At the optimum condition the wicking geotextile provided an additional 6.4° to the interface resistance available to the non-wicking geotextile, which was attributed to the suction forces being developed at the interface of the soil and the geotextile (Khoury et al. 2011).

The shear stresses at EOT plotted against the normal stress are shown in Fig. 4.17b. The difference in interface friction angle is to be expected given that the tensile load that can be carried by the geotextile fabric is higher for the wicking geotextile. The comparison that can be made is limited to the test condition for each geotextile since beyond the 2% strain the tensile capacity diverges. Consistent with the observations presented earlier, the OMC condition tests resulted to larger interface resistance. There is an increase of at least 40% from HMC to OMC condition for both geotextiles.

Although not as excessive as the HMC condition, there was still some water flowing out of the wicking geotextile at OMC because of the hydrophilic nature of the wicking yarns. Wang et al. (2017) also reported the same observations. No attempt was made to test the geotextile fabrics with higher fines content passing No. 200, but based on the results presented the use of a wicking geotextile may be most beneficial for poorly-draining backfill material where the interface resistance is improved when water is drawn out of the backfill.

4.3.3.2. Thawed Condition Tests

As mentioned earlier, the room HMC tests are not typical of construction practice but was done to understand the benefit of wicking. The properties calculated from the thawed HMC tests for the wicking geotextile are more appropriate as it simulates the construction condition (i.e. compaction of frozen soil as fill material) and thawing following winter construction for the reinforced

embankment test section along ITH. Fig. 4.18a shows the interface properties calculated at 2% strain and Fig. 4.18b at EOT. Table 4.3 summarizes the interface properties for the two geotextiles. The interface friction angles are relatively the same for both room and thawed conditions at 2% strain, with the thawed properties slightly larger than the room properties calculated. There is a reduction in apparent cohesion for the thawed OMC tests for both geotextiles and thawed HMC test for the non-woven geotextile, but a slight increase for the thawed HMC wicking geotextile. The apparent cohesion calculated is not significant but otherwise provide additional resistance to pullout loads.

Based on these results, frozen soil with moisture contents less than the HMC tests will have interface strength properties greater than the ones calculated in this study at 2% strain under similar testing conditions and soil properties. The thawed OMC results are not the upper limit of strength in this case because the soil was compacted at room condition, frozen to -10°C, and thawed afterwards before pullout testing. In other words, soil compacted at optimum condition without the influence of freezing and thawing will result in the largest interface strength. The slight increase in interface friction angle for the wicking geotextile at OMC also led to a decrease in apparent cohesion. Even though the soil was prepared at OMC, there were still some water flowing through the wicking geotextile as was observed for room condition tests. The thawed OMC tests had more time to allow wicking and consolidation throughout the freezing and thawing stages before pullout testing compared to the room OMC tests. While the thawed properties calculated from the thawed HMC tests are applicable for winter construction where frozen soil was used as fill material, the thawed OMC properties are applicable to southern regions that experience seasonal freezing and thawing where summer construction is permissible. Similar to the room conditions tests, the wicking geotextile resulted to larger interface strength properties compared to its non-wicking

alternative. The difference in interface properties for these geotextiles are more evident under OMC conditions at 2% strain.

The thawed interface properties at EOT (Fig. 4.18b) slightly increased from the 2% strain in Fig. 4.18a. The thawed OMC values for both geotextiles are less than the room OMC values, confirming that freezing and thawing of the backfill soil influences the interface shear strength. There is no direct comparison between the wicking and non-wicking geotextile at EOT given that the tensile properties beyond 2% are different and comparisons are limited to the moisture conditions with respect to the geotextile. The slope of the thawed OMC for the non-wicking geotextile is almost parallel to the thawed HMC for the wicking geotextile similar to the observations with the room condition tests.

4.3.4. Clean Sand Tests

Test results for the sand interface tests under 50 kPa normal stress are summarized in Fig. 4.19 for both geotextiles. The gross pullout loads are shown in Fig. 4.19a where the sand calibration tests (Fig. 4.19b) were subtracted from, with the net pullout load summarized in Fig. 4.19c. Clearly, there is no significant difference between the two types of geotextiles with its pullout load vs. displacement response. As mentioned earlier the sand interface tests were done to confirm that the texture of both geotextile fabrics exhibit the same resistance under dry conditions.

4.4. Summary and Conclusions

The results presented in this chapter focused on reinforcement as the primary function of a wicking geotextile through tensile and pullout testing which provided an insight to its interface strength properties. The tensile tests conducted mimic the mechanism as to how the geotextile is mobilized in the soil in a pullout test. The room HMC tests conducted in this study are not typical in construction practice, but it provided an environment where the benefit of the wicking function

can be realized as confirmed by the thawed HMC tests where frozen soil was used. In both room and thawed environmental conditions, the wicking improved the interface properties at the soil-geotextile interface compared to a non-wicking geotextile. The OMC condition tests where unsaturated soil interacts with the wicking geotextile showed the interface properties are significantly increased compared to a non-wicking geotextile and this is expected to improve the reinforcement function. Although both geotextiles provide reinforcement function, the wicking geotextiles have the added benefit in Arctic regions application.

The properties obtained will be used in Chapter 6 in calibrating coupled thermal-mechanical models to simulate the reinforced embankment behaviour presented in Chapter 2 as well as conducting parametric studies for embankments with different geometries and reinforcement configurations.

Table 4.1. Summary of manufacturer's geotextile properties

Mechanical Properties	Units	Minimum Average Roll Value	
		Wicking Geotextile	Non-wicking Geotextile
Tensile Strength (at 2% strain)	kN/m	15.8	14.9
Permittivity	sec^{-1}	0.24	0.9
Apparent Opening Size	mm	0.43	0.425
Pore Size O_{50}	microns	85	185
Pore Size O_{95}	microns	195	365
Wet Front Movement (vertical)	inches	6.0	---
Wet Front Movement (horizontal)	inches	73.3	---

Table 4.2. Summary of interface friction angle (δ_p) and adhesion (c_p) for wicking and non-wicking geotextiles at 2% strain and EOT under room conditions.

	Geotextile	Test Condition	δ_p (°)	c_p (kPa)
2% strain	Non-wicking	HMC	4.2	5.1
		OMC	5.7	8.7
	Wicking	HMC	5.7	4.8
		OMC	12.1	8.5
EOT	Non-wicking	HMC	8.6	6.6
		OMC	12.7	3.5
	Wicking	HMC	12.7	6.5
		OMC	17.1	3.4

Table 4.3. Summary of interface friction angle (δ_p) and adhesion (c_p) for wicking and non-wicking geotextiles at 2% strain and EOT under thawed conditions.

	Geotextile	Test Condition	δ_p (°)	c_p (kPa)
2% strain	Non-wicking	HMC	4.3	1.2
		OMC	5.7	5.6
	Wicking	HMC	5.8	5.4
		OMC	12.9	5.7
EOT	Non-wicking	HMC	6.3	2.4
		OMC	7.9	2.1
	Wicking	HMC	7.7	7.3
		OMC	14.8	2.7

Fig. 4.1. Geotextile used in the testing program.

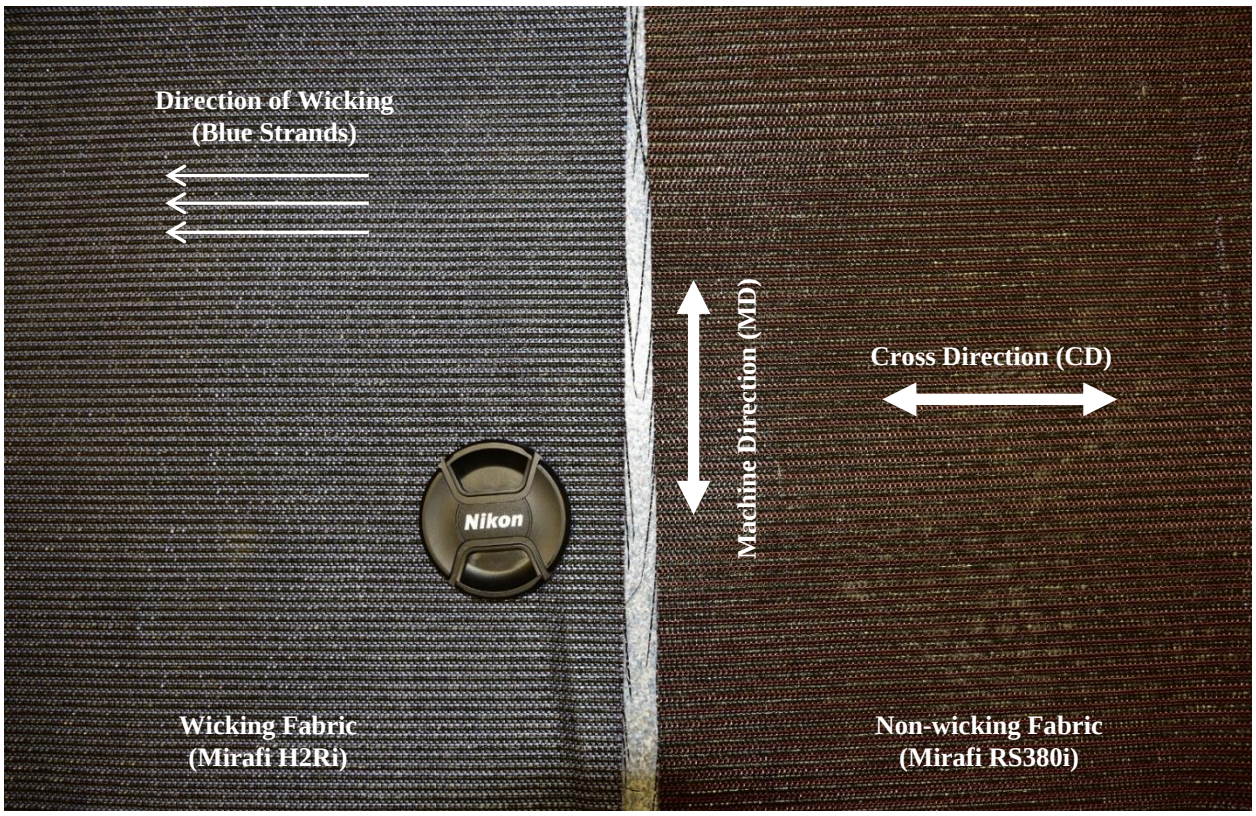

Fig. 4.2. Tensile test set-up (all dimensions in mm).

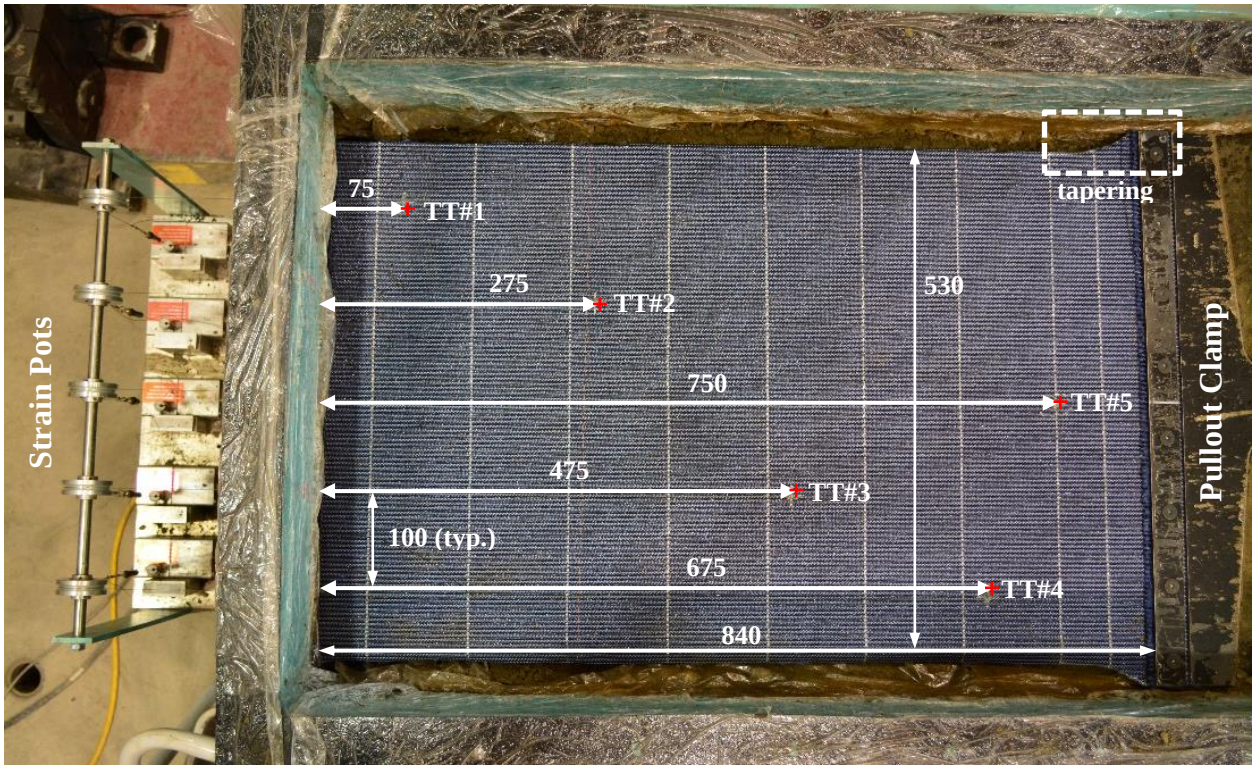

Fig. 4.3. Pullout test set-up for room conditions: (a) compaction of base material, (b) placement of clamp with geotextile at pullout level, (c) telltale connections to strain pots, (d) filling and compaction of soil above geotextile, (e) placement of sand layer on top of polyethylene plastic and wrapped afterwards, and (g) complete test set-up before pullout test.

(a)

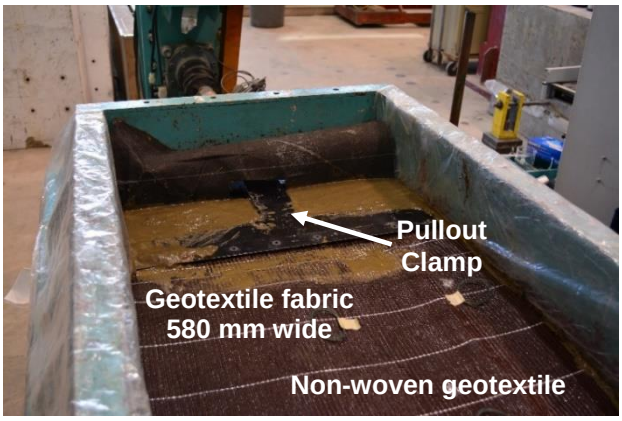

(b)

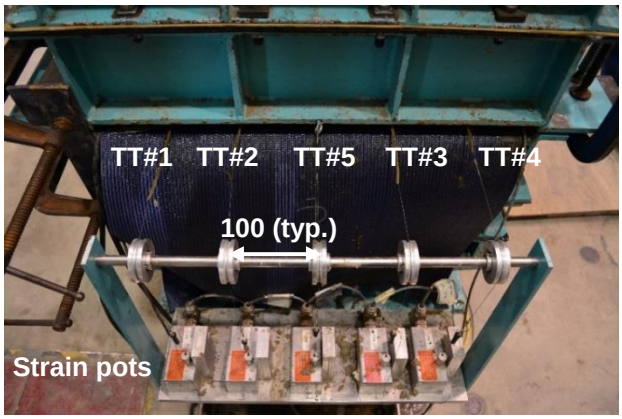

(c)

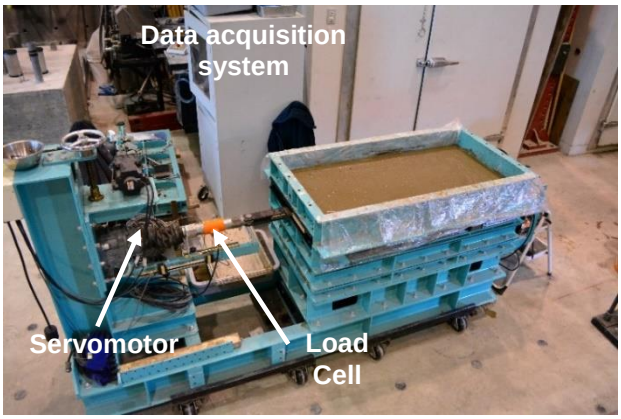

(d)

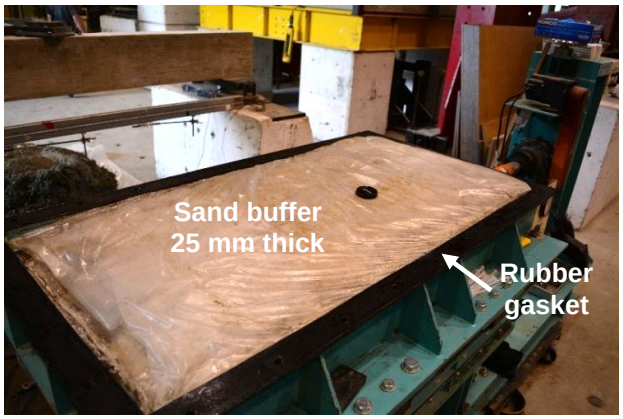

(e)

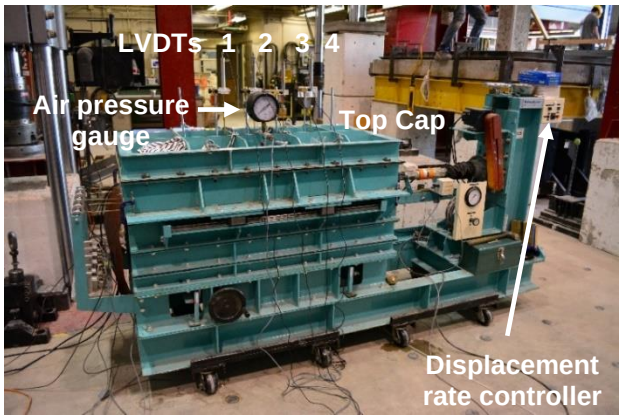

(f)

Fig. 4.4. Pullout test set-up inside environmental cold chamber for thawed tests: (a) placement of clamp with geotextile at pullout level, (b) telltale connection to strain pots, (c) compacted frozen layer to test height, (d) complete test set-up before thawing and pullout.

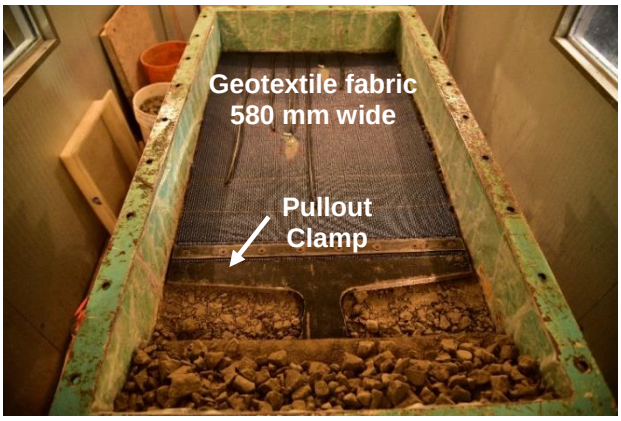

(a)

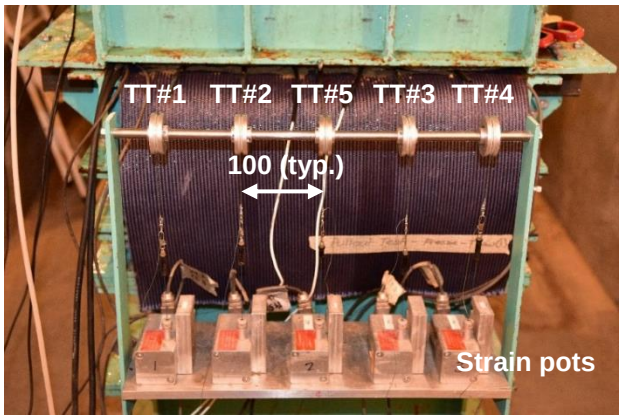

(b)

(c)

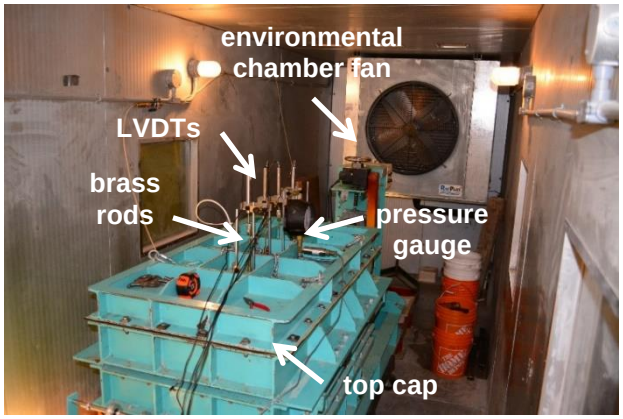

(d)

Fig. 4.5. Recorded temperature in the soil and environmental chamber (EC) during compaction and thawing stages.

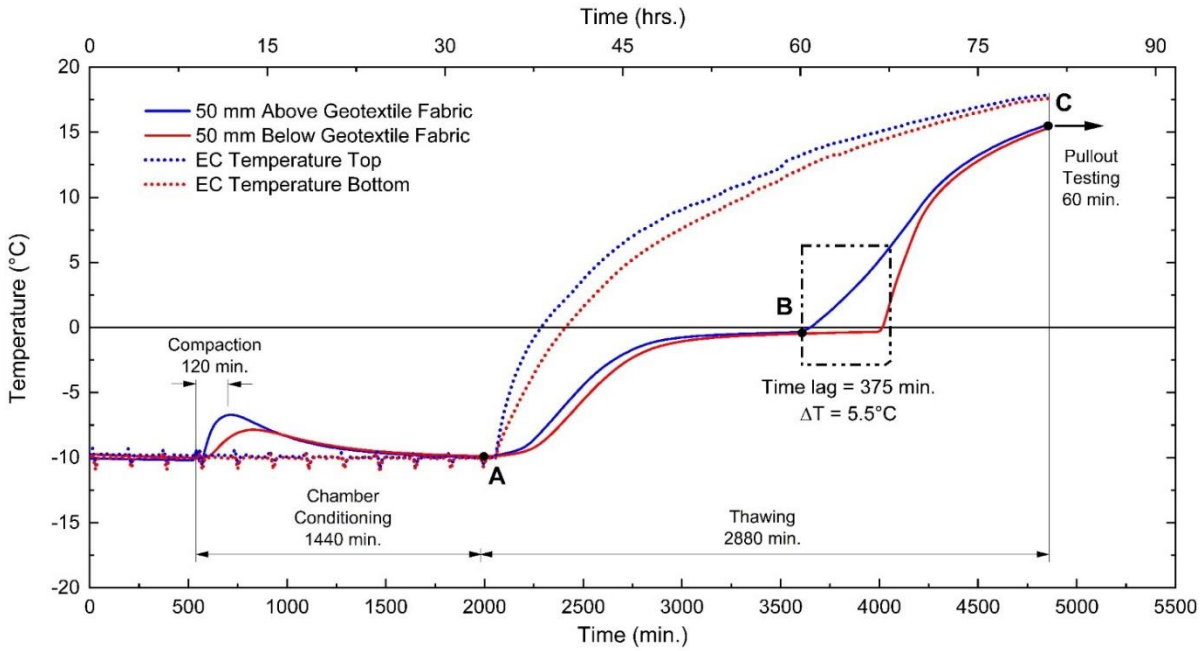

Fig. 4.6. Excavation of soil and cutting of geotextile after pullout test for calibration tests.

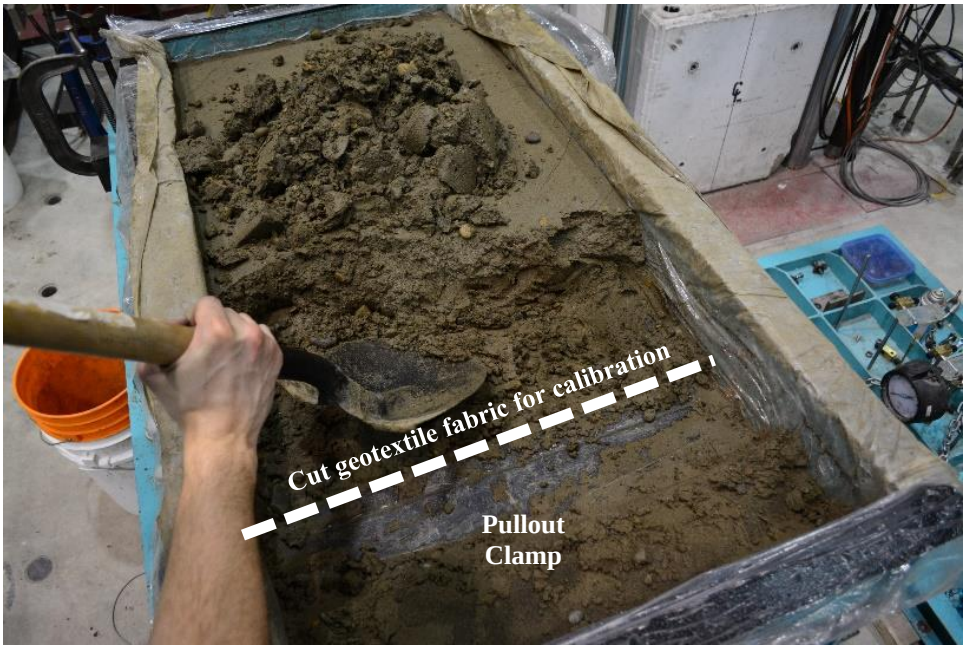

Fig. 4.7. Conceptual interpretation of pullout test results (redrawn from Alfaro et al. 1995b): (a) location of telltales, (b) horizontal displacement, (c) equivalent strain, and (d) average force along the length of the geotextile.

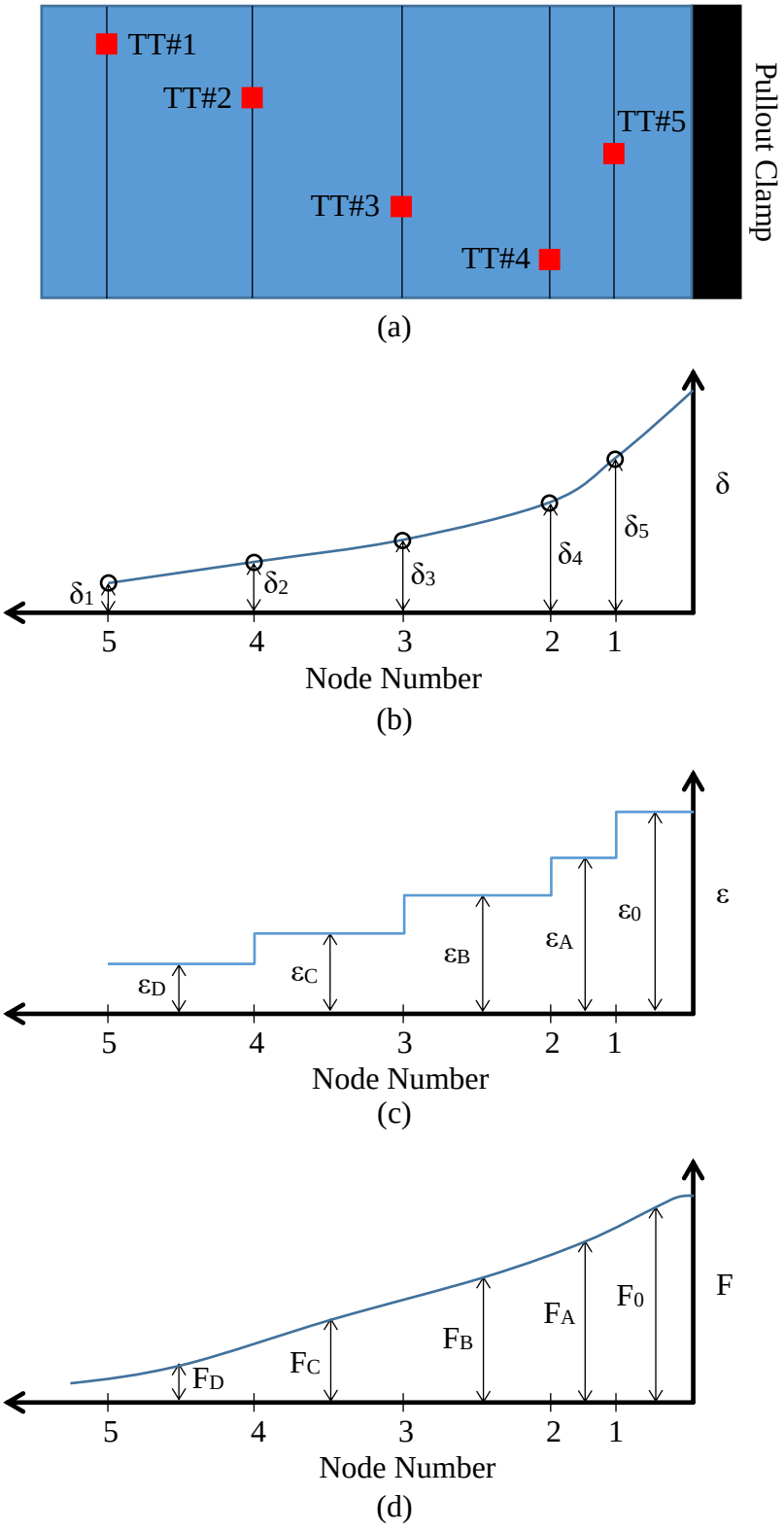

Fig. 4.8. Tensile test results for wicking and non-wicking geotextiles.

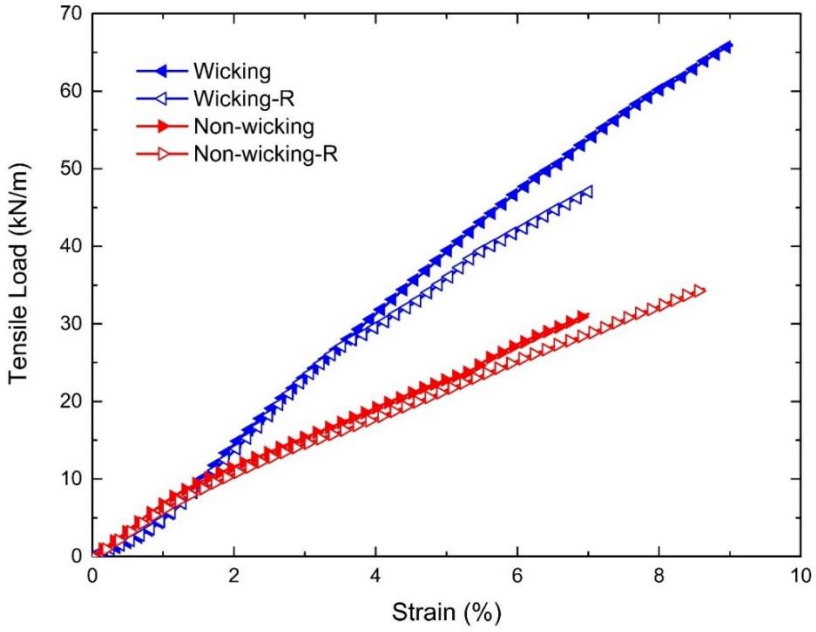

Fig. 4.9. Pullout test results from room HMC tests for wicking and non-wicking geotextiles: (a) gross pullout load, (b) calibration pullout load, and (c) net pullout load.

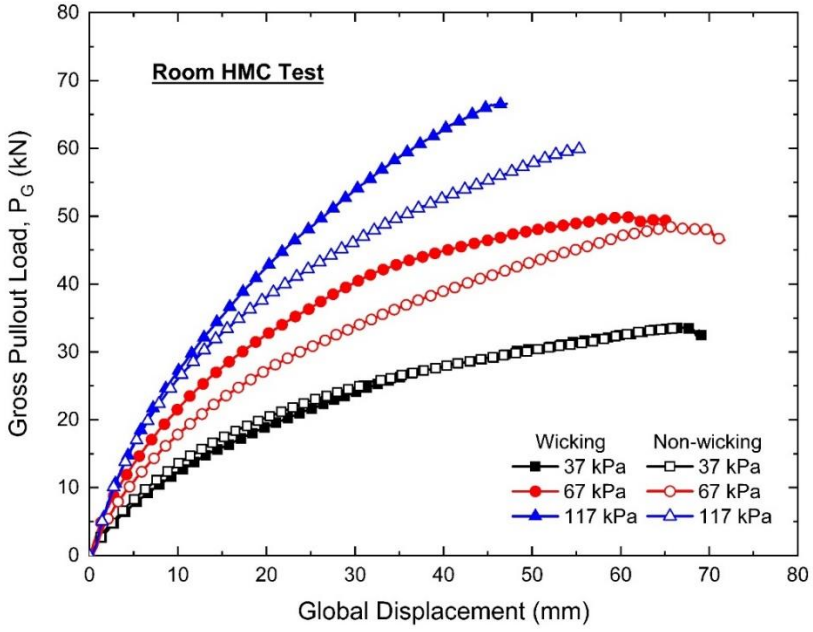

(a)

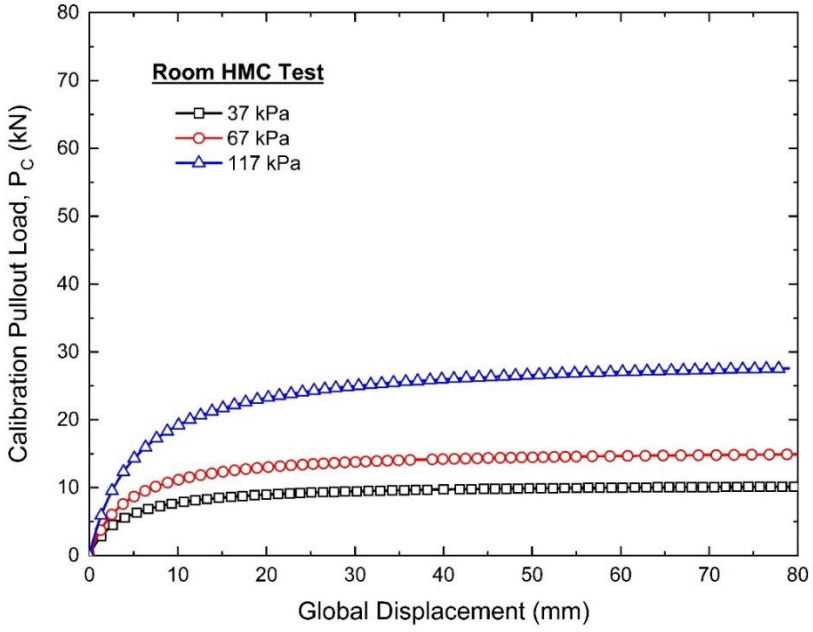

(b)

Fig. 4.9 (continued)

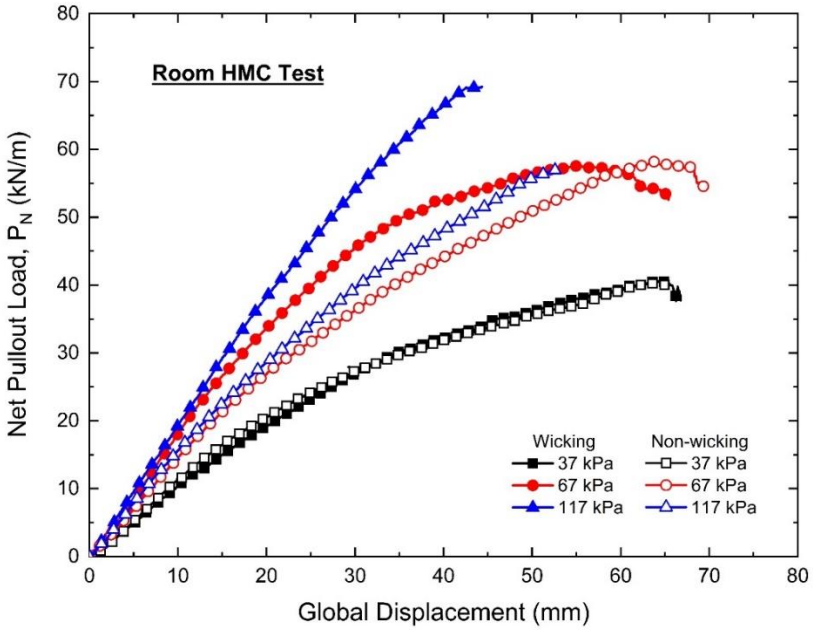

(c)

Fig. 4.10. Net pullout load from room OMC tests for wicking and non-wicking geotextiles.

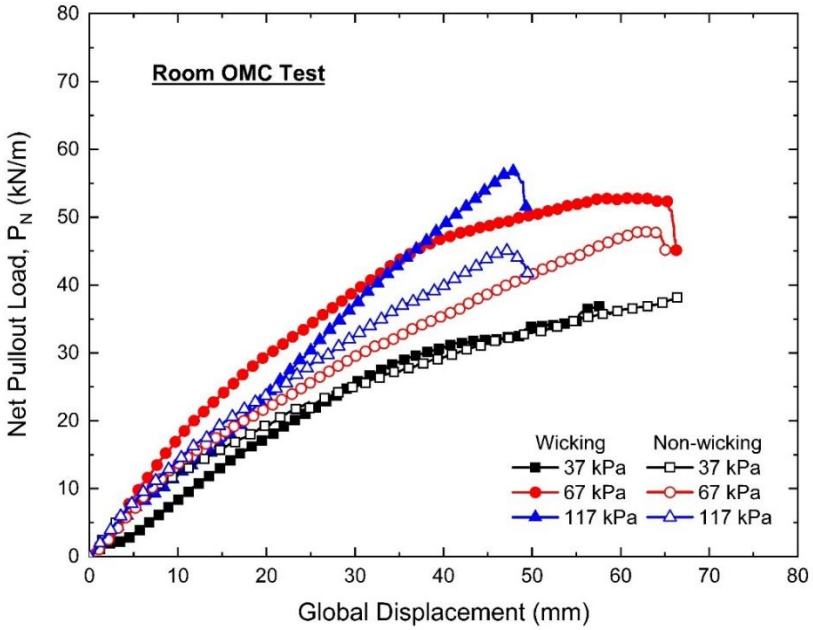

Fig. 4.11. Horizontal displacements along the geotextile from room HMC tests at 2% and EOT strains under different normal stresses: (a) wicking geotextile and (b) non-wicking geotextile.

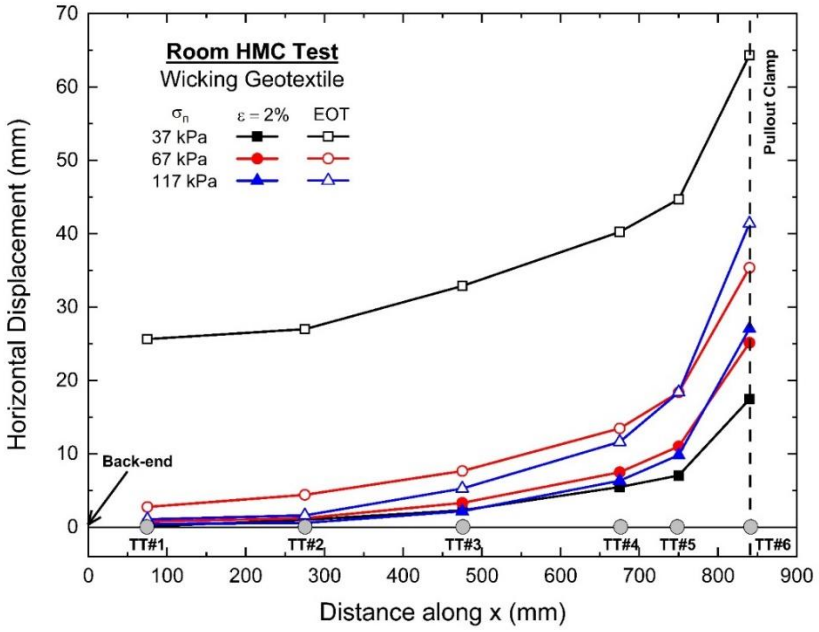

(a)

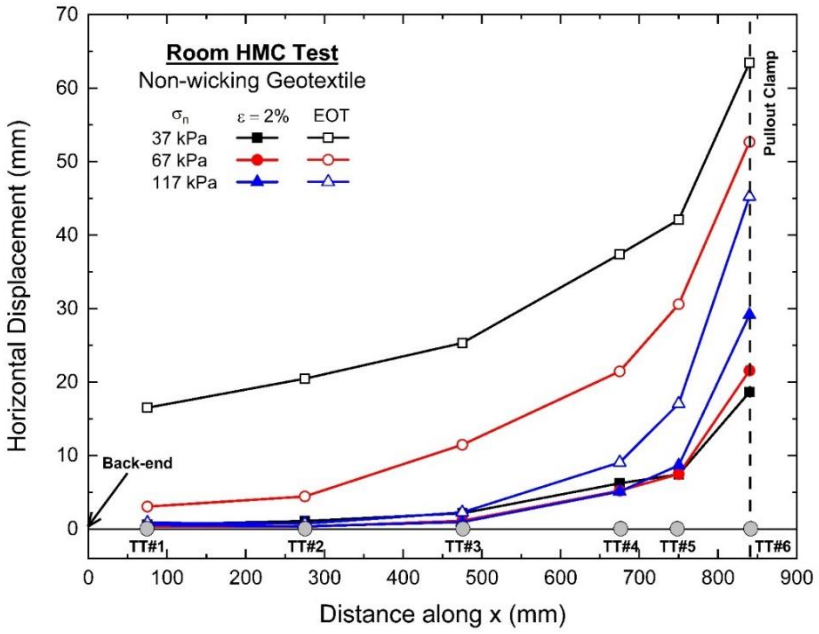

(b)

Fig. 4.12. Horizontal displacements along the geotextile from room OMC condition tests at 2% and EOT strains under different normal stresses: (a) wicking geotextile and (b) non-wicking geotextile.

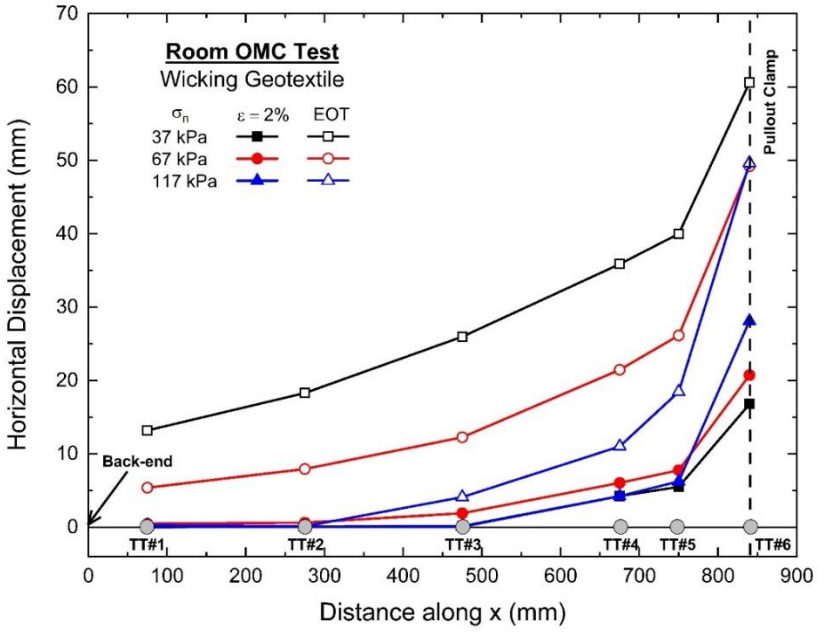

(a)

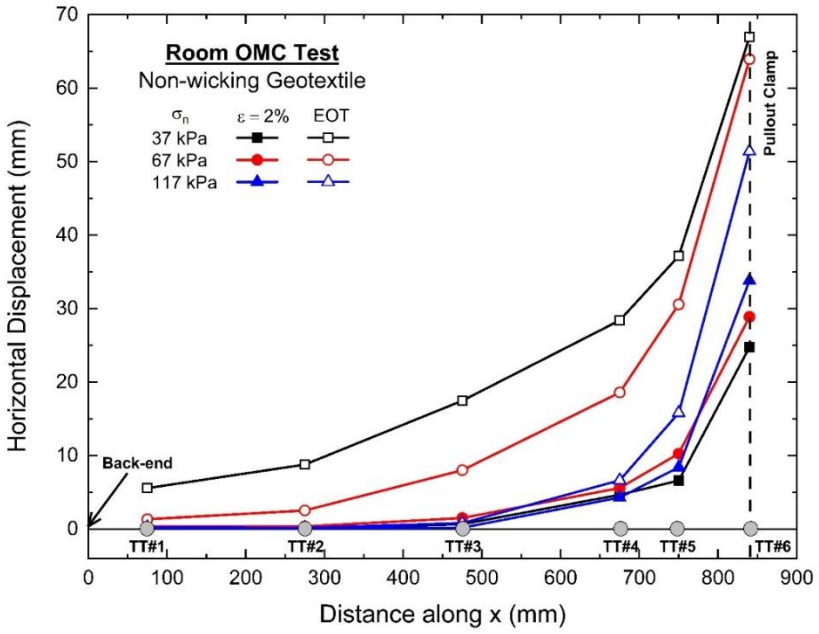

(b)

Fig. 4.13. Average pullout load along the geotextile from room HMC tests at 2% and EOT strains under different normal stresses: (a) wicking geotextile and (b) non-wicking geotextile.

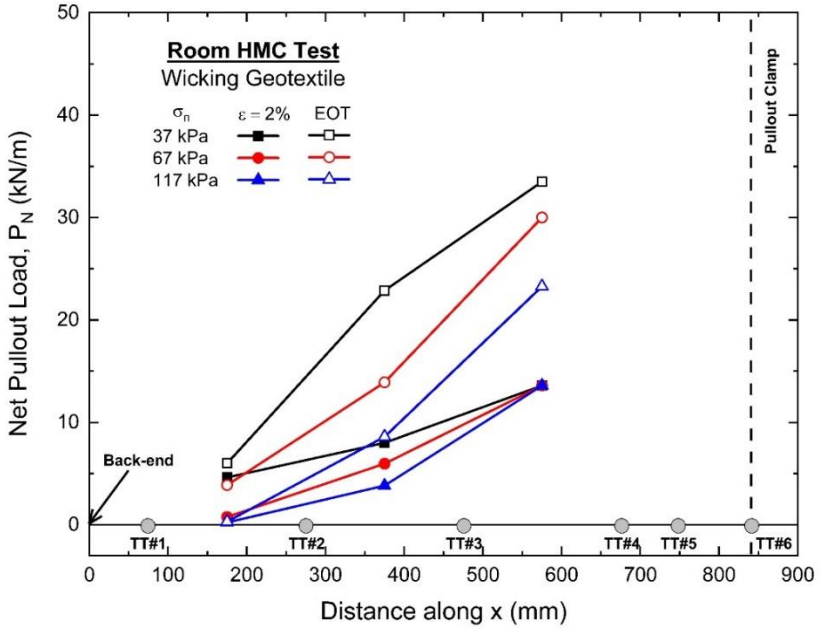

(a)

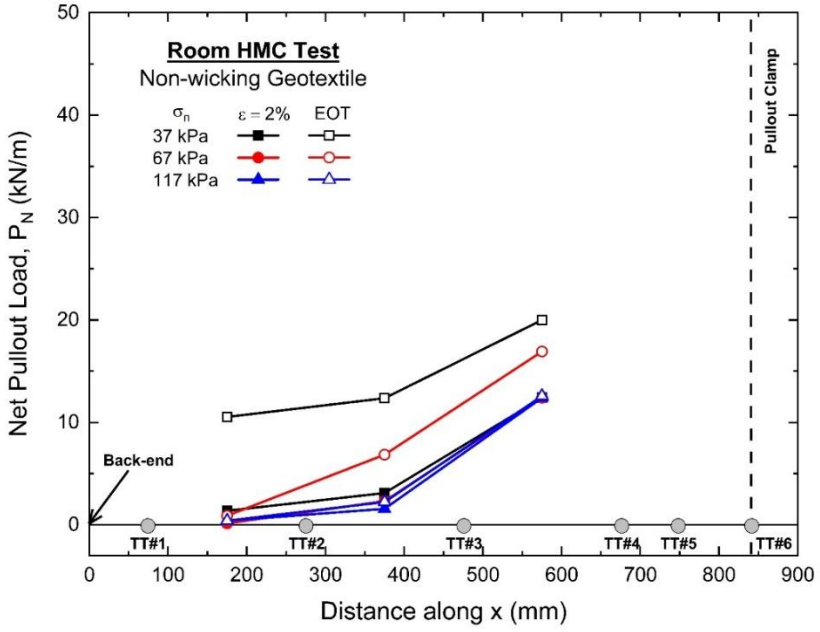

(b)

Fig. 4.14. Average pullout load along the geotextile from room OMC tests at 2% and EOT strains under different normal stresses: (a) wicking geotextile and (b) non-wicking geotextile.

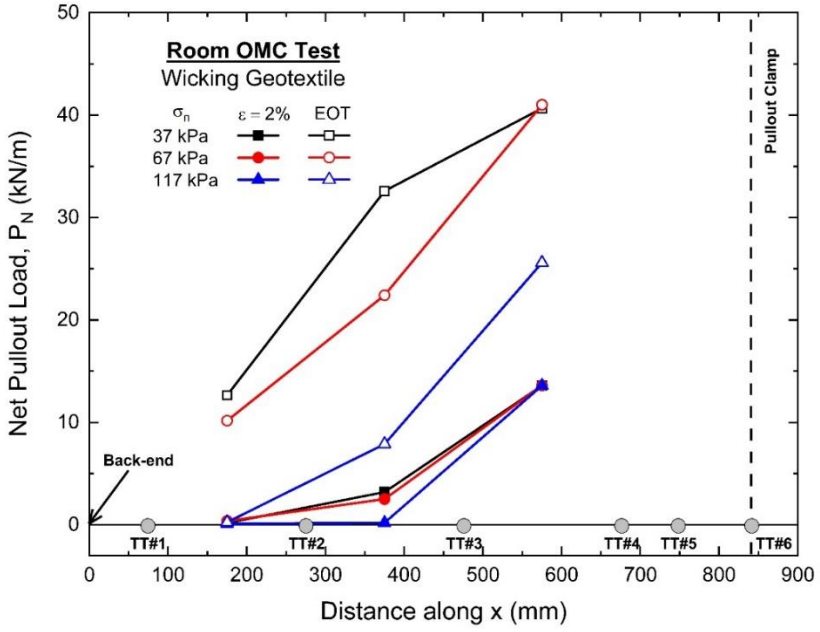

(a)

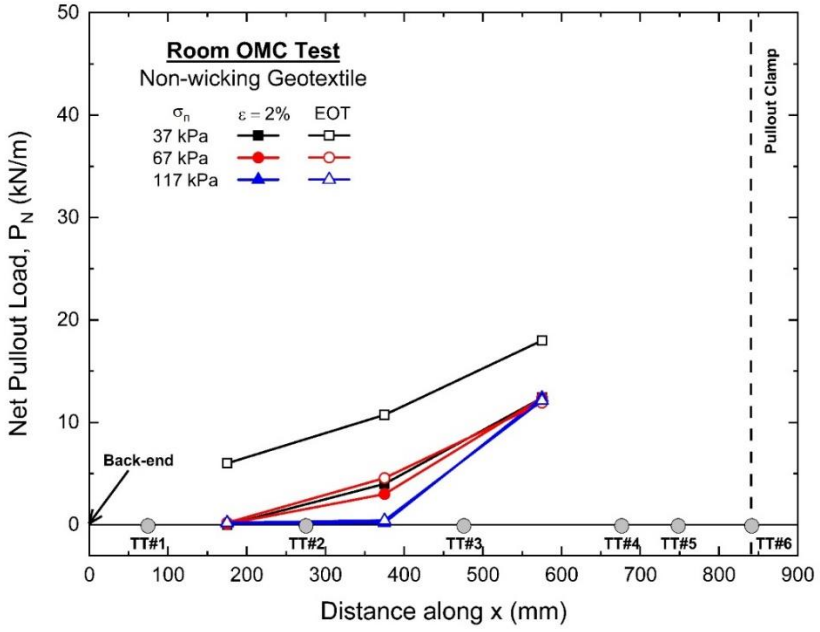

(b)

Fig. 4.15. Net pullout load from thawed HMC tests for wicking and non-wicking geotextiles.

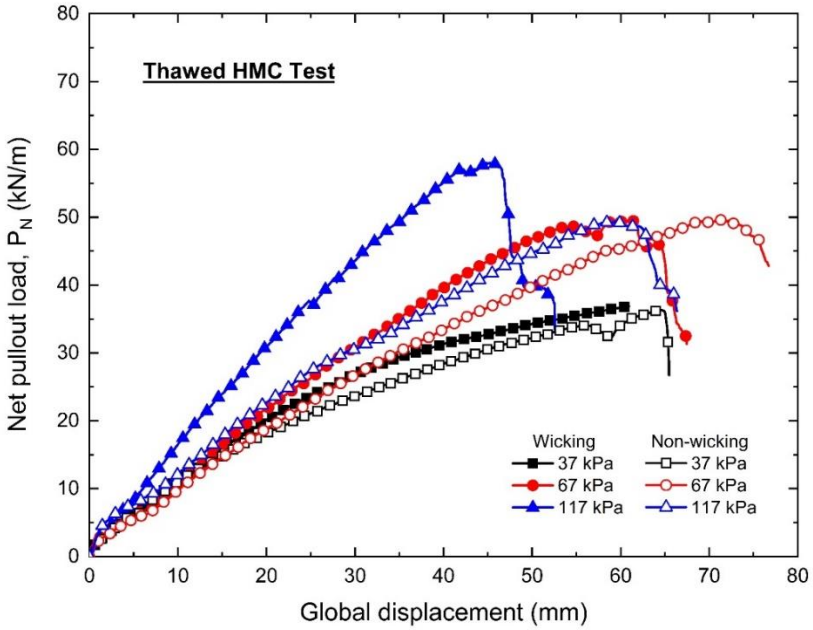

Fig. 4.16. Net pullout load from thawed OMC tests for wicking and non-wicking geotextiles.

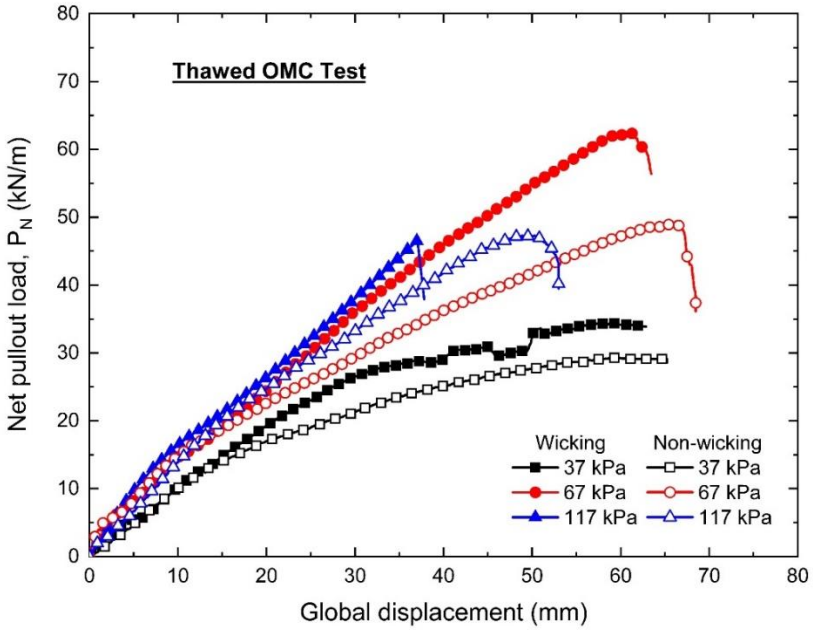

Fig. 4.17. Interface properties for wicking and non-wicking geotextile at (a) 2% strain and (b) EOT for room condition tests.

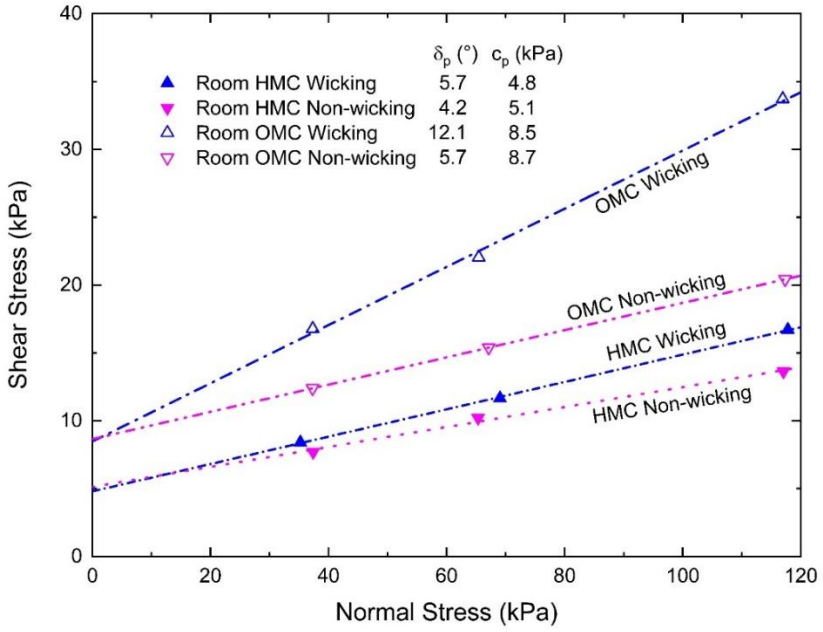

(a)

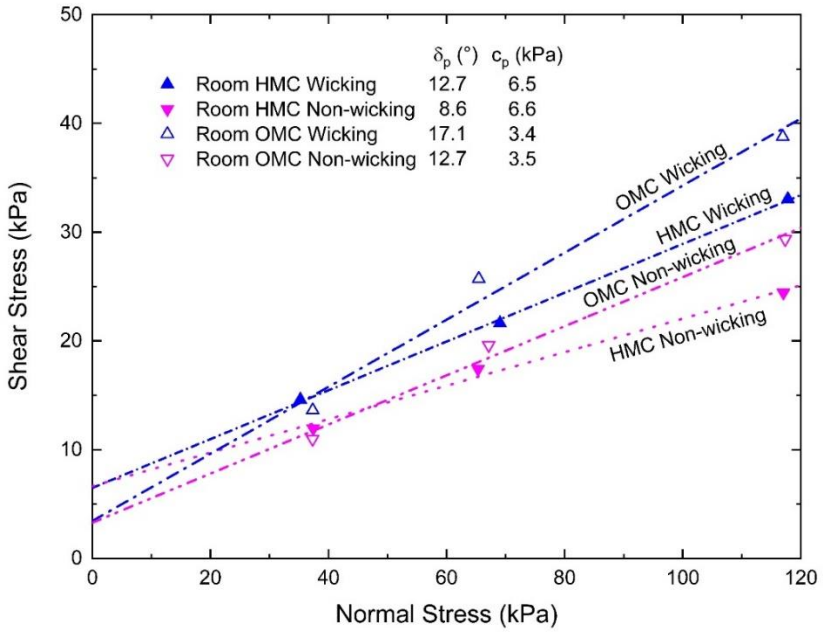

(b)

Fig. 4.18. Interface properties for wicking and non-wicking geotextile at (a) 2% strain and (b) EOT for thawed condition tests.

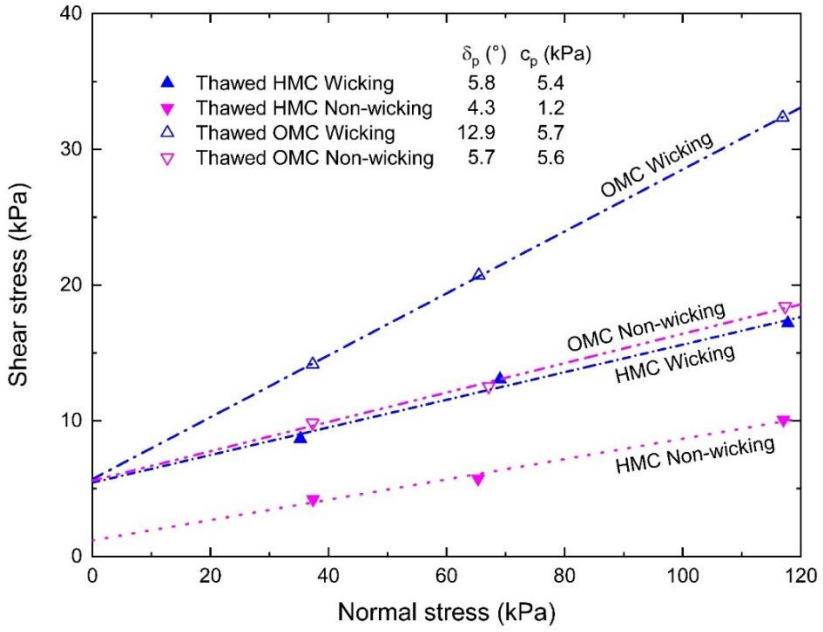

(a)

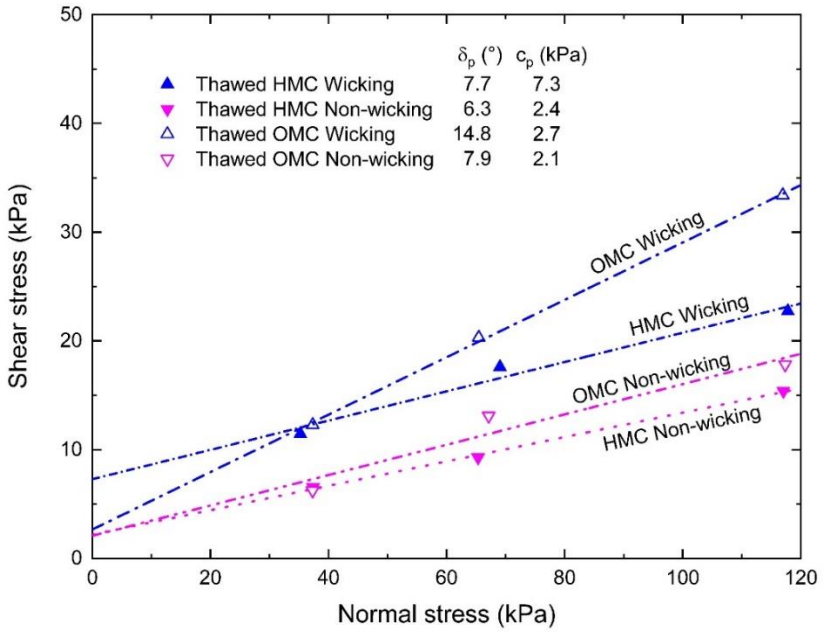

(b)

Fig. 4.19. Pullout test results from sand interface tests for wicking and non-wicking geotextiles for 50 kPa normal stress: (a) gross pullout load, (b) calibration pullout load, and (c) net pullout load.

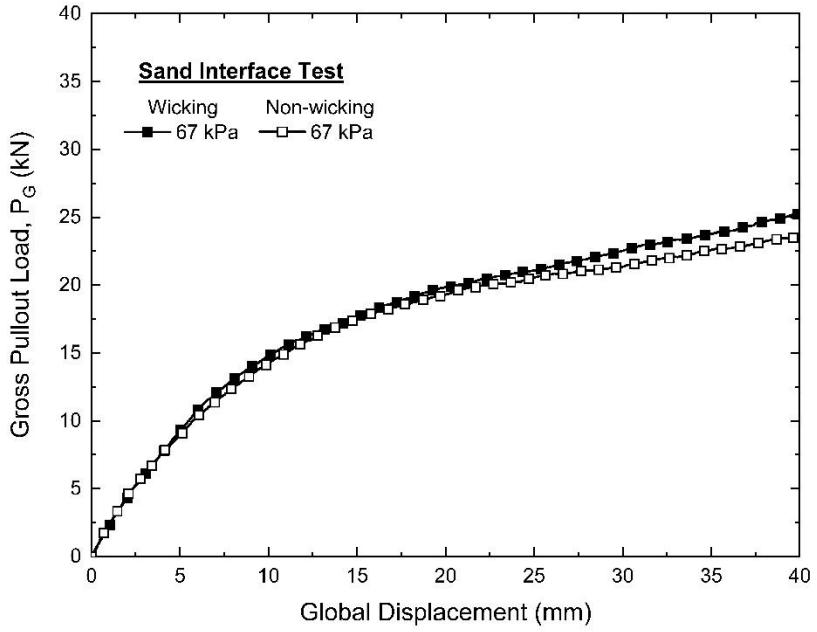

(a)

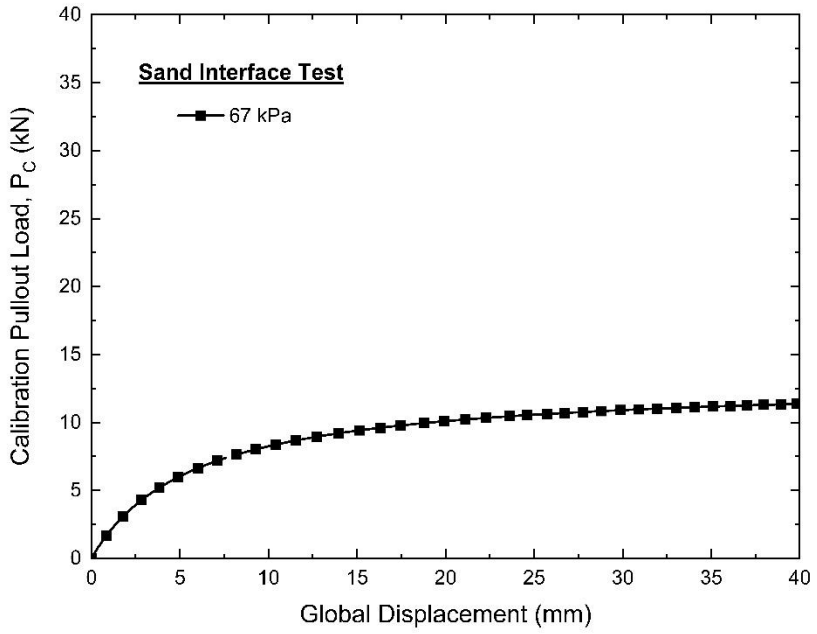

(b)

Fig. 4.19 (continued)

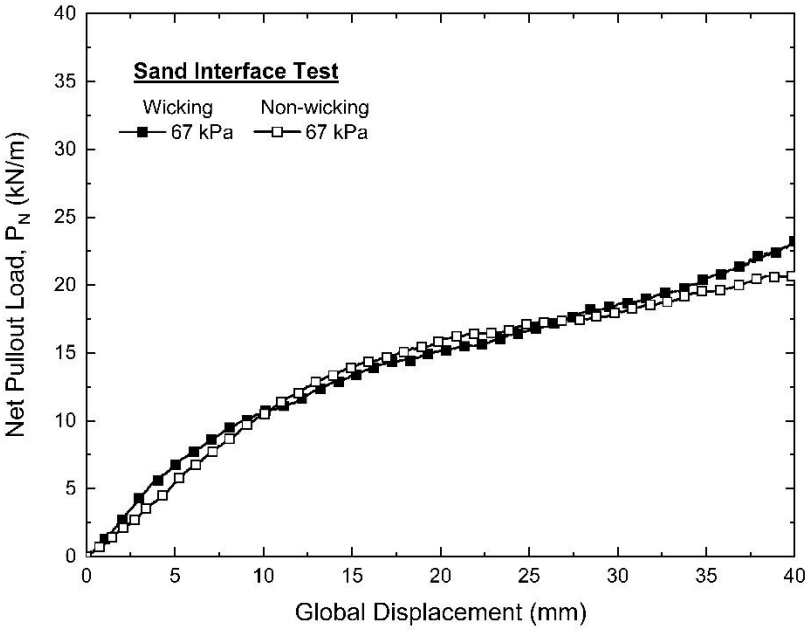

(c)

List of Notations and Acronyms in this Chapter

a	Hyperbolic intercept parameter
B	Width of the geotextile (mm)
b	Hyperbolic slope parameter
c_p	Apparent cohesion (kPa)
EC	Environmental chamber
EOT	End-of-test
F_{max}	Maximum pullout force (kN)
F_{min}	Minimum pullout force (kN)
H	Height (mm)
HMC	High moisture content
L	Length (mm)
L_e	Distance where displacements were recorded (mm)
LVDT	Linear Variable Differential Transformers
OMC	Optimum moisture content
P_C	Calibration pullout force (kN)
P_G	Gross pullout force (kN)
P_N	Net pullout force (kN)
T	Temperature (°C)
TT	Telltale
w	Moisture content (%)
W	Width (mm)
δ_{gross}	Global displacement (mm)
δ_p	Interface friction angle (°)
ε	Strain on the geotextile
σ_n	Normal stress (kPa)
τ_p	Total shear stress on the geotextile fabric (kPa)

CHAPTER 5

NUMERICAL MODELLING: THERMAL PERFORMANCE[1,2]

5.1. Introduction

As presented in Chapter 1, embankment thicknesses (fill height) vary along a project site due to terrain conditions where horizontal and vertical road alignment geometries have to be satisfied. They are typically designed to provide adequate insulation and minimize permafrost degradation under known climatic conditions. In addition to the thermal disturbance from the embankment, trends in air temperature due to climate change (IPCC 2014) have and will continue to pose challenges for the transportation system founded on permafrost (Biskaborn et al., 2019). Smith et al. (2015) reported that permafrost across North America has been generally been warming. This warming of permafrost combined with increasing mean annual air temperature may lead to the embankment instabilities (Jørgensen and Ingeman-Nielsen 2012) and manifest themselves in a variety of ways, ranging from longitudinal cracks at the embankment surface to lateral spreading of the side slopes (McGregor et al. 2010). In this chapter, thermal modelling was carried out for the test sections presented in Chapter 2, calibrated against monitored ground temperature data (Section 2.4.3), and applying near-term and long-term climate model scenarios to demonstrate

[1] This chapter has been submitted, accepted, and/or published in peer-reviewed journals and/or conference proceedings as follows:
De Guzman, E.M.B., Alfaro, M., Arenson, L.U., and Doré, G. 2020. Embankment Temperatures in Arctic Highways: Field Observations and Numerical Simulations. ASCE Journal of Geotechnical and Geoenvironmental Engineering (revision requested).

De Guzman, E.M.B., Kaluzny, S.W., Alfaro, M., Arenson, L.U., and Doré, G. 2019. Modelling embankment temperatures in Arctic highways using thermal modifiers and surface energy balance boundary conditions. 72nd Canadian Geotechnical Conference. St. John's, NL.

De Guzman, E.M.B., Alfaro. M., Arenson, L.U., Doré, G. 2019. Monitored Thermal Performance of Varying Embankment Thickness on Permafrost Foundations. 18th International Conference on Cold Regions Engineering. Quebec, QC.

[2] A list of notations and acronyms used in this chapter are found in page 219.

possible consequences of climate change on Artic infrastructure. Parametric models showing the influence of embankment heights, slope inclinations, and warming permafrost are also investigated.

5.2. Regional Temperatures from Weather Station

The air temperatures at the research site were presented in Section 2.4.1 (Fig. 2.7). The largest dispersion of data was observed between Inuvik and Tuktoyaktuk practically due to the longitudinal distance between the two stations. Inuvik is 3.2°C warmer than Tuktoyaktuk while the research site is 2.0°C colder and 1.2°C warmer than Inuvik and Tuktoyaktuk, respectively. There is no significant difference between the satellite measurement and the weather station at the research site. This gives confidence that satellite data can be used for different embankment sections along ITH to monitor air temperatures. The difference in mean daily air temperatures between Inuvik and Tuktoyaktuk indicates that the thermal boundary selected in a numerical model can impact the thermal regime of both the embankment fill and foundation soil depending on its location. Embankments constructed closer to Tuktoyaktuk (north of the research site) will have colder mean air temperatures and this translates to colder permafrost conditions.

5.3. Embankment Thermal Modelling

A complete account of the performance of the test sections was presented in Chapter 2. Finite element temperature modelling of the embankment was carried out using the commercially-available software TEMP/W[3] (Geo-slope International Ltd. 2018). The modelling procedure and calibration with field data from thermistor strings are presented in this section. Only the control and the thin embankment sections were modelled. The thermal effect of the woven geotextiles

[3] GeoStudio 2018 R2, release date 2018

were considered negligible as shown by the similar temperatures recorded by the thermistor strings in the reinforced section (see Appendix A).

Fig. 5.1 shows a photo of the west side of the embankment in March 2018 using a camera trap. Survey rods were erected at different locations in the embankment to approximately measure the snow depth. The survey rod in Fig. 5.1 was erected at the toe of the embankment and a snow thickness reading of 0.73 m was recorded. The locations of the thermistor nodes for the thick (control section) and thin embankments are shown in Fig. 5.2.

5.3.1. Material Properties

Thermal properties of the embankment fill and foundation soil used in TEMP/W are summarized in Table 5.1. The embankment fill material ranges from well-graded sand with silt and gravel to silty sand with gravel based on the Unified Soil Classification System (USCS) tests done by De Guzman et al. (2018)[4]. The foundation soil is predominantly organic based on the frozen drill cores obtained from the centreline and at an offset of 40 m from the embankment centreline during drilling in March 2017. The organic mat is approximately 7 m thick. This is underlain by highly plastic clay with some presence of cobbles based on visual inspection of the grab samples.

Equations proposed by Farouki (1981) were used to determine the unfrozen ($k_{unfrozen}$) and frozen (k_{frozen}) thermal conductivities of the embankment fill material as shown in Eq. 5.1 and Eq. 5.2, respectively.

$$k_{unfrozen} = 0.1442\ (0.7\log w + 0.4)\ (10)^{0.6243\rho_d} \quad \text{Eq. 5.1}$$

$$k_{frozen} = 0.01096\ (10)^{0.8116\rho_d} + 0.00461\ w\ \ (10)^{0.9115\rho_d} \quad \text{Eq. 5.2}$$

[4] Chapter 3 of this manuscript.

In the absence of test results, the frozen and unfrozen thermal conductivities were assumed to be similar to peats frequently found in northwestern Canada. De Guzman and Alfaro (2018) used a thermal probe for peat in Northern Manitoba. The unfrozen and frozen volumetric heat capacities for mineral soils in the embankment are calculated using Eq. 5.3 and Eq. 5.4, respectively, where c_{vw} = 4.187 MJ/m^3·°C and ρ_d and ρ_w are the unit mass of the dry soil and water, respectively. The specific heats 0.17, 1.0, and 0.5 correspond to mineral soil, water, and ice, respectively (Andersland and Ladanyi 2004). For organic soils such as peat, the 0.17 is replaced by 0.40.

$$c_{vu} = \left(\rho_d/\rho_w\right)\left(0.17+1.0\ (w/100)\right)\ c_{vw} \quad \text{Eq. 5.3}$$

$$c_{vf} = \left(\rho_d/\rho_w\right)\left[\left(0.17+1.0\ (w_u/100)\right)+0.5\ ((w-w_u)/100)\right]\ c_{vw} \quad \text{Eq. 5.4}$$

The volumetric water content (VWC) is the volume of liquid water per volume of soil and obtained by multiplying the gravimetric water content to the ratio of the density of the soil and density of water. It was assumed that the unfrozen water content (w_u) in Eq. 5.3 and Eq. 5.4 is 5% of the VWC as was similarly done in previous studies (De Guzman and Alfaro 2018, Flynn et al. 2016).

5.3.2. Embankment Geometry and Boundary Conditions

The cross-section of the embankment model in TEMP/W for the high embankment fill section is shown in Fig. 5.3. The surfaces of the embankment fill and foundation soil interacting with air temperatures are subdivided accordingly. The road surface is labelled as *Top*, while the slope is divided into three regions because of the different snow depths that can accumulate in these regions. The foundation soil immediately at the base of the embankment is labelled as *Toe*. Away from the toe, the ground surface is labelled as *Prairie*. The rightmost and leftmost boundaries are no flow boundaries, while a constant temperature of -4.3°C was applied at the base of the foundation soil based on temperature readings nearby the research site from 2015 to 2018. Only

half of the embankment was modelled because of assumed symmetry. A global mesh size of 0.3 m with triangular elements was used.

5.3.3. Modelling Approach

Because the thermistor strings and SAAs were installed during the construction phase and temperature monitoring was easily available during that period, a predefined temperature field was added in the numerical model where the initial temperature analysis was anchored. Temperature readings on April 19 and April 20, 2015 were used as spatial functions in a transient analysis. These spatial functions were only applied to the first model and subsequent models were created in a tree analysis using the previous model as its parent analysis but with the revised air temperatures applied and spatial functions removed. No intermediate steps were applied in between the monitoring period once the model was submitted for analysis. The analysis period ran from April 20, 2015 to August 31, 2018.

For embankment thermal modelling where there are no temperature sensors to provide initial conditions, a spin-up analysis is typically required in order to reach equilibrium for the embankment fill and foundation soil with an applied constant sinusoidal boundary condition representative of the temperatures expected where the embankment will be situated. Average temperature sinusoidal functions are applicable in this case because the same boundary conditions are being applied repeatedly until steady-state is reached where using actual temperatures will otherwise provide erratic changes. Spin-up analyses were done for the embankment sections and there were no significant differences between a 5-year and 10-year spin-ups in comparison with a predefined temperature field in the embankment discussed previously. Parametric studies for different embankment heights, slope inclinations, and air temperature conditions however will require such spin-up analyses to satisfy initial thermal equilibrium. Care should also be exercised

in selecting the thermal boundary conditions to be applied with respect to the existing conditions at the site.

The governing equation in TEMP/W is shown in Eq. 5.5 where the forced-convection heat transfer and the latent heat of vaporization are ignored. The default physical processes involved in TEMP/W include conduction heat transfer and changes in stored sensible energy and latent heat of fusion (Geo-slope International Ltd. 2018). In Eq. 5.5, C_p is the volumetric heat capacity, h_{sf} is the latent heat of fusion, k is the thermal conductivity, ρ_w is the density of water, and θ_{uwc} is the unfrozen volumetric water content. The parameter θ_{uwc} is a function of temperature that controls the rate of change in the latent energy of fusion per degree of temperature change. The volumetric heat capacity and the thermal conductivity are both defined for frozen and unfrozen states.

$$\left[C_p + \rho_w h_{sf}(\partial\theta_{uwc}/\partial T)\right](\partial T/\partial t) = \partial[k(\partial T/\partial y)]/\partial y \qquad \text{Eq. 5.5}$$

In the following two subsections, two approaches are discussed regarding the temperature applied at the ground surface. The air temperatures from satellite data obtained from NASA for the period of April 2015 to August 2018 were used in the model. Previous studies (e.g. Kong et al. 2019, De Guzman and Alfaro 2018, Flynn et al. 2016) have applied a fitting sine function to the temperature data. The sinusoidal function takes into account the day-to-day fluctuations and resolve them to an average; however, the smoothing curve ignores the extreme data sets during the peak summer and winter conditions which may either be helpful or detrimental to the results of the numerical analyses. This is extremely important in the context of climate change as an average sine function will ignore the warming trend which underestimates both the summer and winter months in a short-term analyses (typically less than 5 years) where peak temperature differences are in the range of 7°C to 10°C.

5.3.3.1. Thermal Modifier

The thermal modifier (TM) approach, commonly known as the n-factor approach, is where an empirically determined n-factor is used to translate the air temperature to the ground surface temperature typically to a depth of 100 mm from the soil surface which accounts for the net radiation, vegetation, snow cover, and ground thermal properties (Andersland and Ladanyi 2004). It is defined as the ratio of the of the ground surface freezing or thawing indices to the air freezing or thawing indices, respectively. An n-factor of 1 means that the ground temperature is the same as the air temperature. An n-factor less than 1 means that the ground temperature is cooler than the air temperature, while an n-factor greater than 1 means that the ground temperature is warmer than the air temperature. Table 5.2 summarizes the thermal modifiers used in the numerical model. The values in the specific locations where they were applied are typical of literature values and were adjusted accordingly to best match the results from the field. The varying $n_{freezing}$ for the slope accounts for the change in snow depth where the thickest snow is at *Slope Bottom*. The last entry on Table 5.2 is for the slope of the thin embankment section. The temperatures recorded from the thin embankment section can be to evaluate the entire thermal regime of the embankment section as will be presented in the following section.

Table 5.2 shows that the freezing and thawing n-factors for the toe and prairie are significantly less than that of the n-factors applied to the embankment fill. As discussed earlier, peat/vegetation is a great insulator and thus prevent significant thawing during the summer months. In the winter months and because of the presence of snow, the $n_{freezing}$ factors are reduced and with greater depth of snow at the toe the ground heat can not be extracted easily through the snow layer.

5.3.3.2. Surface Energy Balance

The surface energy balance (SEB) approach uses the energy transfer between the ground surface and the atmosphere. TEMP/W has a well documented approach for incorporating these energy transfers in a thermal model and as such only a general overview of the numerical solution is presented here. The surface energy balance equation for heat transfer analysis is given in Eq. 5.6.

$$(q_{ns} - q_{nl}) = q_{sens} + q_{lat} + q_g \qquad \text{Eq. 5.6}$$

In Eq. 5.6, q_{ns} and q_{nl} are the net solar (shortwave) and net terrestrial (longwave) radiations, q_{sens} is the sensible heat flux, q_{lat} is the latent heat flux, and q_g is the ground heat flux. The boundary condition applied at the ground surface is calculated by determining q_g (as a function of the ground temperature) in Eq. 5.6 and is taken as the remaining energy flux once all the other fluxes are satisfied.

The net solar radiation is the difference between the downwelling and upwelling shortwave radiations. Since the Earth's surface does not emit shortwave radiations, the upwelling shortwave radiation is entirely associated with the reflection of some of the downwelling radiation. The reflected portion of the downwelling shortwave radiation is known as albedo (α) which is highly dependent on the surface characteristics. Albedo in other words is the ratio of upwelling shortwave radiation to the downwelling shortwave radiation. In TEMP/W, the downwelling shortwave radiation (q_s) can be estimated based on the latitude of the project site (given earlier in Table 2.3 in Chapter 2), day of the year, and time of day. Combined with α, q_{ns} can be determined (Eq. 5.7). A highly reflective surface such as fresh snow will have an albedo close to unity while a black body that absorbs all radiation will have an albedo of zero.

$$q_{ns} = (1 - \alpha)\, q_s \qquad \text{Eq. 5.7}$$

The net terrestrial radiation is given in Eq. 5.8 where ε_s is the surface emissivity assumed to be 0.95 in TEMP/W, σ is the Stefan-Boltzmann constant (4.903 x 10-9 MJ/K^4/m^2/day), T_g is the absolute temperature of the ground surface, ε_a is the air emissivity, and T_a is air temperature.

$$q_{nl} = \varepsilon_s \sigma T_g^4 - \varepsilon_a \varepsilon_s \sigma T_a^4 \qquad \text{Eq. 5.8}$$

The first term is related to the longwave radiation emitted by the surface, while the second term is related to the reflected longwave radiation back to the Earth's surface due to the heating caused by the absorbed longwave radiation in the atmosphere. The parameter ε_a is a function of the air temperature and vapor pressure related to relative humidity.

Sensible heat is the energy required to change the temperature of a substance with no phase change while latent heat is the energy that is supplied or extracted to change the state of the substance without changing its temperature. Sensible heat flux represents the loss of energy by the surface by heat transfer to the atmosphere. It is positive when directed away from the surface into the atmosphere. Latent heat flux on the other hand represents a loss of energy from the surface due to evaporation. For practical purposes, TEMP/W requires the wind speed to estimate the heat transfer coefficient (h) at a reference height of 2 m to determine q_{sens} (Eq. 5.9). The wind speed at the test site was also obtained from satellite data of NASA. The latent heat flux is related to the actual evapotranspiration on site of which no data is available and thus was ignored in the model. It is further assumed that the latent heat flux is zero during the winter months.

$$q_{sens} = h \left(T_g - T_a\right) \qquad \text{Eq. 5.9}$$

The presence of snow in the winter months alters the SEB and modification to Eq. 5.6 is required. TEMP/W assumes that the q_{snow} is equal to the ground heat flux and that the snow has no capacity to store energy. The energy flux through the snow is given by Eq. 5.10 where k_{snow} is

the thermal conductivity of snow, T_{snow} is the temperature at the snow surface, T_g is the temperature at the ground surface, and h_{snow} is the depth of snow. The snow depths on site are estimated over a monthly period based on the snow depth readings observed from the images obtained from camera traps installed around the research site and also measured from previous site visits during the winter season.

$$q_{snow} = - k_{snow}\left[\left(T_g - T_{snow}\right)/h_{snow}\right] \quad \text{Eq. 5.10}$$

Combining Eq. 5.7, Eq. 5.8, Eq. 5.9, and Eq. 5.10 (when snow is present in the winter months) in Eq. 5.6, the ground temperature can be solved as the applied boundary condition at the ground surface. In summary, the parameters required for an SEB analysis in TEMP/W are the air temperature, wind speed, solar radiation (measured or estimated), albedo, relative humidity, and snow depth.

Table 5.3 and Table 5.4 summarize the albedo and snow depth at different locations in the embankment, respectively. The albedo values selected in the model were taken from NASA and adjusted accordingly to best match the results of the field data over a monthly period. The higher the albedo, the more reflective the surface is. As mentioned earlier, the snow depths in Table 5.4 were estimated based on the survey rod readings from images taken by camera traps at the research site. The thermal conductivity of snow at the *Toe* and *Prairie* surfaces is 15 kJ/days·m·°C, and taken as 55 kJ/days·m·°C for the *Slope Top, Slope Middle*, and *Slope Bottom*. The top surface is always cleared off from snow precipitation either mechanically (snow dozers) or naturally (drift). These values are within the range of snow thermal conductivities from Sturm et al. (1997) for different densities.

5.3.4. Results and Discussion

Fig. 5.4 presents the field data during the monitoring period at select thermistor nodes and the results of the thermal modelling using both TM and SEB approaches. The letter and number codings can be best understood when referring them from Fig. 5.2. Modelled results of select thermistor nodes at the top of the embankment (TS-C1) are shown in Fig. 5.4a to Fig. 5.4c. TS-C1 shows that there is uniform warming across the top of the embankment in response to the ambient air temperatures. Both approaches reasonably simulate the field data as well as the fluctuation in daily mean air temperatures. In general, the models reflected the same thickness of the frozen core estimated from the temperature readings of SAA-CV in Chapter 2 (SAA-RV in Appendix A).

The thermistor nodes along the base of the embankment (TS-C2) are shown in Fig. 5.4d to Fig. 5.4f. Node C2-B (Fig. 5.4d) is approximately 1.3 m directly below the slope face and model results show that the seasonal freezing and thawing temperatures can penetrate at this location. Node C2-D (Fig. 5.4e) is 3.3 m directly below the slope face above it and the temperature recorded and modelled are sitting close at -1.5°C. Node C2-G (Fig. 5.4f) has 4.7 m of embankment fill above it and results indicate that the core of the embankment is still frozen. The temperature recorded at C2-D and C2-G is colder by approximately 1.4°C in the second year of monitoring but 1.5°C warmer in the third year compared to the first year. In general, the SEB approach reasonably simulated the summer peaks for the three thermistor nodes presented, while the TM approach slightly underestimated it. The SEB approach slightly overestimated the winter temperatures for C2-B. Both TM and SEB approaches underestimated the winter temperatures at the core of the embankment by about 1.5°C.

The thermistor nodes at the foundation centreline (TS-C3) are shown in Fig. 5.4g to Fig. 5.4i. The thermistor nodes presented indicate the foundation soil where the warmest recorded

temperatures reach close to -4°C. Similar to the modelled results of TS-C2, the SEB approach shows good agreement in the summer to winter turnover but overestimates the winter to summer turnover. The trend in between periods are comparable to the field data. Although the TM approach slightly underestimates the warmest temperatures in the summer to winter turnover, the winter to summer turnover temperatures are simulated well. It is interesting to note that the recorded temperatures in the field have shown a warming trend since completion of construction and captured by both approaches. This warming trend is a result of both the observed warming air temperatures in the region as well as the possibility that the embankment is still undergoing changes to reach thermal equilibrium. Although the full height of the embankment is insulating the foundation centreline, climatic changes are still contributing to the warming temperatures in the foundation soil.

The thermistor nodes of the foundation toe (TS-C4) are shown in Fig. 5.4j to Fig. 5.4l. Node C4-B (Fig. 5.4j) is 1.5 m below the ground surface and it can be seen that the warmest recorded permafrost temperature is close to -1°C. The modelled results for both approaches generally follow the same trend as the field data. The TM approach overestimates the winter to summer turnover close to the ground surface, but showed agreeable results for the first two years of monitoring for C4-C (Fig. 5.4k) and C4-D (Fig. 5.4l). The field data however are 1.3°C warmer compared to the model results in the third year and 1.8°C warmer compared to the previous year field data. In between transition periods especially from summer to winter the SEB and TM approach respond differently but both reach the same turnover temperatures. The SEB approach model results are closer to field data in between transitions periods. The difference in results during the summer to winter turnover is possibly due to the volumetric water content of the foundation

soil. It is possible that there is more water present on site than anticipated during the thawing season for which the latent heat will take longer to be removed.

Fig. 5.5 shows the ambient air temperatures (Fig. 5.5a) at the site and the temperature contour plots through vertical sections at the crest (Fig. 5.5b) and toe (Fig. 5.5c) of the embankment using SEB approach during the three-year monitoring period. For clarity, only the range from -5°C to 5°C are plotted in Fig. 5.5b and Fig. 5.5c. In Fig. 5.5b, the time lag shows that the 0°C isotherm in the embankment fill trails from August to December of each year to a depth of 2.6 m from the road embankment surface; that is, the frozen core of the embankment is 2.7 m thick from the base of the embankment. In both Fig. 5.5b and Fig. 5.5c, the depth of heat extraction through the crest and toe are getting shallower while the warming air temperatures in the summer are getting deeper. The results presented provide an overview that the warming ambient air temperatures translate to warming of the embankment fill and foundation soil. Predictions made for thin and thick embankment fill sections may be stable for a short period of time but with warming conditions thawing might easily be exacerbated by slight increases in air temperature. Similar to the observations by other researchers (Romanovsky et al. 2010, James et al. 2013), colder permafrost exhibits a greater response to changing air temperatures compared to permafrost with temperatures closer to 0°C.

The measured temperature values over a period of time provide a means of calibrating a model in order to predict long-term performance with appropriate boundary conditions under climate change conditions. It is interesting to note that for both approaches the thermal models show that the slope of the frozen core in the embankment fill is parallel to the embankment slope. This can have implications in the movements of the embankment at or near the slope as will be presented in Chapter 6.

The frozen core of the embankment is by definition permafrost as the soil has remained continuously below 0°C for at least two years. It should be pointed out that the embankment is an engineered structure using naturally-occurring material, in this case frozen soil. The environment (winter conditions) when the embankment was constructed and the material (frozen soil) used to construct it means the thermal regime in the embankment was below 0°C. Furthermore, the embankment fill material provided insulation to the natural foundation soil, of which 0.5 to 0.7 m are within the seasonal thaw depth (active layer) and was frozen during embankment construction.

Although the TM approach provided comparable results with the field data, the factors selected were still empirical which required numerous simulations in order to match it. The values used in the model provide an initial estimate of behaviour which can be supplemented by instrumentation at site to further refine embankment thermal performance prediction. The SEB approach led to more accurate behaviour for the embankment fill and foundation soil especially during the turnover periods, but is more demanding on input parameters and requires more computational time to complete an analysis in comparison to the TM approach. Accurate parameter measurements for the SEB approach require specialized equipment and thus translate to cost in infrastructure projects. Most parameters (air temperature, wind speed, relative humidity, solar radiation, albedo) are otherwise available from satellite data in a regional scale.

Based on the observations presented earlier for both approaches, only the TM approach was used in modelling the thin embankment section. Fig. 5.6 shows the results of the thermal modelling for the thin embankment section in comparison with select thermistor nodes at its midslope. The cross-section in Fig. 5.3 was modified to reflect the thin embankment section (Fig. 5.2) and correct boundary conditions. Since the thermistor string was installed two years after construction, the model had to be calibrated using a spin-up analysis before comparisons can be made against the

thermistor readings. An initial thermal regime was determined and the thermal model was analyzed from 2015. As shown in Fig. 5.6, there is good agreement between the recorded field values and model values.

5.4. Climate Change Prediction Modelling and Analysis

5.4.1. Climate Parameters and Warming Scenarios

With climate change being an important consideration for embankment design, construction, and maintenance, climate modelling scenarios provided by the Canadian Centre for Climate Modelling and Analysis (CCCma) based on the Intergovernmental Panel on Climate Change (IPCC) Fifth Assessment Report (IPCC 2013) were used to determine thermal performance of the embankment for two time-scales: (a) near-term conditions – which were modelled in 10 and 30 years, and (b) long-term conditions – which were modelled to year 2100. A Climate Model (CM) is a numerical model consisting of the atmosphere, ocean, land, and sea ice components. An Earth System Model (ESM) is a climate model with added components of the carbon cycle in the land, atmosphere, and the ocean. The ESM explicitly models the movement of carbon throughout the Earth system. The near-term models use CM while the long-term models use ESM. The CCCma models were part of the Coupled Model Intercomparison Project Phase 5 (CMIP5) standard experimental protocol for studying the output of coupled atmosphere-ocean general circulation models (CGCM). The location of the research site for extracting boundary condition data from the climate models (e.g. near-surface air temperatures) lies between the latitude band of 66°58’21.66”N and 69°45’45.92”N, and between the longitude band of 130°46’52.5”W and 133°35’37.5”W. The resolution of the grid is in the order of 2°50”.

Table 5.5 summarizes the model scenarios used for the climate projection analyses. The Fourth Generation Coupled Global Climate Model (CanCM4) was used for near-term modelling using

decadal2005 and decadal2015. Decadal2005 runs for 30 years with a starting analysis time on January 1, 2005 and ending on December 31, 2035. Decadal2015 runs for 10 years with a starting analysis time on January 1, 2015 and ending on December 31, 2025. Decadal2005 has two initializations and are differentiated by decadal2005i1 and decadal2005i2. The decadal models have ten realizations each but only one was selected and analyzed to show the climate change effect on the embankment for near-term conditions. The Second Generation Earth System Model (CanESM2) was used for long-term modelling using RCP 2.6, RCP 4.5, and RCP 8.5. The values on these RCP models are representative concentration pathways which are the cumulative measurement of human emission of greenhouse gases from all sources expressed in W/m^2 (IPCC 2013). The RCP models run until 2100 with a starting analysis time on January 1, 2006 and ending on December 31, 2100. Similar to the near-term models, the RCP models have multiple realizations each but only one was selected for each analysis to demonstrate its influence on thermal performance. For both near-term and long-term conditions, the realization selected was the one that provided the warmest increase in air temperatures over the projected analysis period.

Both the TM and SEB approach were used for the climate projection analyses. The model parameters required in the SEB approach (Table 5.5) are readily available in both time-scales while the TM approach only requires the air temperatures. The snow precipitation estimates provided in the modelling scenarios do not include the fact that an embankment acts as a snow fence (wind-break) which alters the deposition of snow on the slopes. The snow depths and surface albedo used in the historical monitoring period were used for both time-scale models. In all of these climate models, the extra day from leap years in the month of February have been removed and thus the duration of each year is 365 days. For the TM approach, it was assumed that the n-factors do not change over the analyses periods.

Fig. 5.7 shows sample climate projections for air temperature, relative humidity, and wind speed for near-term (Fig. 5.7a, decadal2005i1) and long-term (Fig. 5.7b, RCP8.5) conditions. The primary factor contributing to the thermal regime change in the numerical model is the air temperature. Table 5.6 summarizes the increasing linear trend of temperature every year and the expected change in air temperature after the analyses periods. The most aggressive warming rate with this linear trend for the near-term condition is recorded for decadal2015. As expected, the warmest rate for the long-term condition is observed for RCP8.5 with an expected change of temperature of 9.33°C at the end of the century. The peak summer temperatures have been increasing but it is considerably warmer in the winter months from -40°C in 2010 to -25°C by 2100 affecting the freeze-up cycle. This observation further supports the choice of not using an average sinusoidal function and linear increase in temperature to represent the air temperature for long-term modelling as it grossly overestimates the response of the ground temperatures. Not superseding the discussion in the following section, a 1°C and 2°C warming rates from 2015 to 2100 were applied at the base of the model (bottom boundary) in addition to the original boundary condition (-4.3°C). There was no significant change observed in the model compared to the base models where a constant bottom boundary condition was used throughout the analyses period.

5.4.2. Results and Discussion

Fig. 5.8 shows a comparison of the near-term models for select thermistor nodes using both TM and SEB approaches. Only the maximum (Fig. 5.8a, Fig. 5.8c, Fig. 5.8e, Fig. 5.8g) and minimum (Fig. 5.8b, Fig. 5.8d, Fig. 5.8f, Fig. 5.8h) soil temperatures per year are shown. The SEB approach resulted to consistently warmer embankment fill temperatures (C2-D, C2-G) and at the foundation centreline (C3-B). The model temperatures at the toe however are warmer using the TM approach. The summary of warming rates for the maximum and minimum temperatures for the near-term

models using the SEB approach are summarized in Table 5.7. Decadal2005i2 has rates warmer than decadal2005i1 consistently for both temperature extremes per year. The warmest rate for the minimum yearly temperatures was recorded for decadal2015. The change in maximum soil temperatures is in the range of 1°C, but varies in the range of 3°C for the minimum soil temperatures. This indicates that there is a significant amount of heat being stored in the embankment fill and foundation soil during the winter months. Table 5.8 shows nodal temperatures at different locations using SEB approach at specific time steps (April 1 and October 31 of each analyses year) for the near-term climate models. The SEB approach was selected because the temperature models resulted to warmer soil temperatures for the embankment fill and foundation soil at the embankment centreline. The general trend of the nodal temperatures are all warming. The month of April is where the extent of winter temperatures typically are at their warmest. Node C2-G experiences considerable warming by 2035 using decadal2005i1. Results of the near-term climate models show that the core of the embankment will shrink from 2.7 m in 2018 to 2.1 m in 2035.

Fig. 5.9 shows a comparison of the long-term models for the same thermistor nodes as Fig. 5.8 using both TM and SEB approaches. Unlike the near-term climate models, the difference in soil temperatures is more evident in these plots. Similar observations are seen in the RCP models were the SEB approach resulted to warmer temperatures for C2-D, C2-G, and C3-B, but colder temperatures for C4-B. In Fig. 5.9c, C2-G shows that the temperatures of the base of the embankment are already above 0°C in 2080 with the SEB approach for RCP8.5 but is still frozen using the TM approach. The minimum temperatures for both approaches (Fig. 5.9d) using RCP8.5 after 2080 are trailing on the 0°C line. The minimum temperatures for these nodes are all fluctuating from 6°C to 8°C before 2080.

The warming rates using the maximum yearly temperatures for RCP 2.6 and RCP 4.5 for both approaches are relatively similar as summarized in Table 5.9. The minimum soil temperature at C3-B (Fig. 5.9f) remain below -2°C for RCP 2.6 and RCP 4.5 for both approaches but is sitting between -1.5°C and -1.75°C for RCP8.5. Ice-rich and warm permafrost has a high coefficient of compressibility and is quite sensitive to temperature change. In Fig. 5.9g, RCP8.5 using the TM approach shows that the seasonal thaw depth at the toe has gone deeper beyond 1.5 m from the original ground surface while the SEB approach for all RCP models at this location indicate that the ground remains frozen.

The depth of seasonal thawing from the temperature models for 2015 to 2018 is at 0.8 m from the natural ground surface (Fig. 5.5c). This is slightly overestimated compared to the field measurements presented in Chapter 2 (ranging from 0.5 to 0.6 m). Fig. 5.10 shows the temperature distribution with depth at different locations in the embankment for the long-term climate models using SEB approach. At the crest of the embankment, the frozen fill thawed by 0.2 m and 0.5 m from its original location in 2020 to 2100 for RCP 2.6 (Fig. 5.10a) and RCP 4.5 (Fig. 5.10b), respectively. RCP8.5 showed the largest temperature warming in Fig. 5.10c where the frozen fill was 2.7 m from the base of the embankment in 2020 but has thawed completely by 2100. At the embankment midslope (Fig. 5.10d), RCP 2.6 show that the depth of seasonal fluctuation is 2.7 m where the 0°C isotherm sits at the base of the embankment at this location. This increased by 0.4 m for RCP 4.5 (Fig. 5.10e) and 0.7 m for RCP8.5 (Fig. 5.10f) below the natural ground surface. The depth of thaw penetration at the toe increased to 1.3 m in RCP 2.6 (Fig. 5.10g) and to 1.5 m in RCP 8.5 (Fig. 5.10i). Table 5.10 summarizes the nodal temperatures at different locations for the long-term climate models. The temperature difference between 2020 and 2100 increases from RCP 2.6 to RCP 8.5. Node C2-G close to the base of the embankment will experience complete

thawing under RCP 8.5 conditions. There was a brief cooling period in 2050 (October 31) which may have retarded the warming of the soil for the subsequent years. The permafrost temperature underneath the embankment centreline (C3-B) approaching 2100 under RCP8.5 will experience about 2.3°C of warming which will make the permafrost likely unstable. It should be noted that the change in thermal properties due to changes in mechanical properties of the embankment fill and foundation soil are not considered in these climate models. The embankment fill and foundation soil densifies over time in addition to creep developing for soils between -2°C and 0°C. Ice-rich and warm permafrost has a high coefficient of compressibility and is quite sensitive to temperature change. The compressibility coefficient increases significantly when its temperature increases, especially close to 0°C (Qin et al. 2009, Arenson and Springman 2005). Creep of frozen soil may be considerable when the temperature of the permafrost layer is close to the thawing point (Yu et al. 2013, Ladanyi 1983). Results of the near-term and long-term climate models provide a preview of future temperature conditions where the thermal performance can be improved in anticipation of climate change effects. A warming rate of 1°C was applied at the base of the model over the period between 2020 and 2100. A marginal increase of 0.2°C was observed at the embankment midslope compared to the constant base model at the end of the analysis period. Some of the methods available in practice to improve the thermal performance of embankments are done by using thermosyphons to actively cool the embankment during the winter months, installation of ventilation ducts to promote passive cooling, or by adding foam insulation in the embankment near the natural foundation (Saboundjian 2008).

Fig. 5.11 and Fig. 5.12 show the temperature contours using both approaches for RCP8.5 from 2080 to 2090 and 2090 to 2100, respectively, at the crest of the embankment. The full height of the embankment is shown and 1 m into the foundation soil. Unlike the results in Fig. 5.5a where

the above 0°C air temperatures occur in shorter time spans, the air temperatures in Fig. 5.11a and Fig. 5.12a are 10°C warmer for both summer and winter months and the duration of below 0°C temperatures shorter. With the TM approach, the 0°C isotherm advanced as deep as 3.6 m from the crest of the embankment during the summer months (Fig. 5.11b). Using the SEB approach on the other hand (Fig. 5.11c) shows that two 0°C isotherms have developed. The first 0°C isotherm has penetrated as deep to the base of the embankment and past the natural ground surface by 2086. The 0°C isotherm close to the natural ground surface is the first isotherm that previously developed from seasonal air temperature changes. This was the 0°C isotherm that delineated the maximum depth that the summer temperatures can penetrate the embankment before it starts cooling again when it interacts with the winter air temperatures. Compared to the TM approach, with warmer air temperatures and other parameters used in the SEB approach this has pushed the original 0°C isotherm significantly to the base of the embankment.

As the second 0°C isotherm develops from summer to winter turnovers, a seasonal talik (bounded by the two 0°C isotherm) also developed although getting thinner over time to its minimum thickness around the month of June. The embankment fill has temperatures above 0°C from June to October for each observation year before the seasonal taliks form again on the next turnover period from summer to winter months. The first 0°C isotherm penetrates 0.3 to 0.4 m of the natural ground surface from 2087 until the end of the analyses period at 2100. The second 0°C isotherms shown in Fig. 5.11 and Fig. 5.12 are not the same as the 0°C isotherm observed in Fig. 5.5b. The former shows that the temperature enclosed in the isotherm are negative temperatures (winter months), while the latter shows that positive temperatures are enclosed. Because the second 0°C isotherm has not developed yet with the TM approach, the temperature enclosed by the isotherm are still positive temperatures (Fig. 5.11b). From 2090 to 2097 for the TM approach, the

second 0°C isotherm developed and thus the temperature enclosed are negative temperatures. The first 0°C isotherm is 1 m above the natural ground surface for the TM approach. In Fig. 5.12 the thickness of the seasonal talik has increased to 2 m during the winter months for the SEB approach. Fig. 5.13 shows the seasonal taliks observed in the temperature models using the SEB approach in 2070 and 2100 under RCP8.5. The seasonal talik in 2070 (Fig. 5.13a) has a thickness of 1.2 m, but grows to 4 m in 2100 (Fig. 5.13b). In both cases, the upper bound of the 0°C isotherm is parallel to the slope surface. The presence of a seasonal talik is concerning since excess pore pressures can develop due to traffic loading as the water from the thawed frozen fill gets trapped in the embankment leading to slope instabilities. The frozen core of the modelled embankment was completely thawed by 2100 as evidenced by the SEB approach for the RCP8.5 case. It can be inferred that thin embankment sections along the highway with thickness varying from 1.8 m to 2 m will have the embankment fill completely thawed in the summer following construction and accelerate the thawing of the permafrost foundation under near-term and long-term climate change conditions. Further discussion on the thermal performance of thin embankments are presented in Section 5.5.3

5.5. Parametric Studies Under Climate Change Conditions

Parametric studies were conducted to investigate how varying embankment thickness and slope inclinations influence the overall thermal regime of the embankment fill and foundation soil.

5.5.1. Modelling Approach

The TM approach presented in Section 5.3.3.1 was used for the boundary conditions of the parametric studies. This was selected because of the reduced computational effort required to complete the analyses and eliminating the need to solve the individual heat fluxes in Eq. 5.6 that

are provided by CCCma in a regional scale. The commercially-available software ABAQUS[5] (Smith, 2014) was used to build the parametric cross-sections in anticipation of using fully-coupled and sequentially-coupled thermal-mechanical models in Chapter 6 as GeoStudio 2018 (TEMP/W and SIGMA/W) does not have this capability in any of the programs available in their software suite. The Geostudio suite is more user-friendly compared to ABAQUS for thermal or deformation modelling done in isolation. The same material properties (Table 5.1) for the embankment fill and foundation soil were used in ABAQUS. Before modelling the parametric sections, the thick embankment was modelled beforehand under similar conditions as TEMP/W to ensure that ABAQUS will yield similar results.

Unlike the control and reinforced sections, no thermistor strings are available for the other cross-sections in the parametric models and thus a spin-up analysis is needed to establish the equilibrium thermal condition for the embankment fill and the foundation soil for each case. Average sinusoidal boundary conditions considering the freezing and thawing n-factors were applied at each section of the embankment and foundation for a period of five years. All spin-up analyses end on April 20 of each year simulating the time when the embankment construction was completed. Additionally, the sinusoidal function was extended through the monitoring period to investigate the difference between actual and average thermal boundary conditions.

5.5.2. Embankment Geometry and Temperature Conditions

Fig. 5.14 shows the conceptual model in ABAQUS and the observation points for analysis. Table 5.11 summarizes the embankment heights and slope inclinations investigated. All cases in Table 5.11 were subjected to the actual temperature conditions discussed in Section 5.3.2 as well

[5] Version 6.14, release date 2014.

as the near-term and long-term climate change conditions in Section 5.4.1. The slopes were divided in three equal lengths (*Slope Top*, *Slope Middle*, *Slope Bottom*) where the thermal boundaries for the TM approach were applied.

5.5.3. Results and Discussion

Fig. 5.15 shows a comparison of the monitored temperatures at different thermistor string locations in the embankment fill and foundation soil. There are slight differences in numerical values between the two software under pure heat transfer analysis, but the results are otherwise consistent in the expected thermal behaviour with respect to the measured field data. Fig. 5.16 shows the difference in results between the two boundary conditions at difference thermistor locations in the embankment fill and foundation soil. It is clear from these numerical results that the selection of temperature boundary conditions greatly influences the results of the model. Actual air temperatures should be used whenever possible when conducting a thermal analysis.

Fig. 5.17 shows the comparison of model temperatures for the embankment heights and slope inclinations at different nodal locations. These graphs show that the greatest influence on the thermal regime of the embankment fill and foundation soil is the thickness of the embankment. The slope inclination does not significantly influence Node A (Fig. 5.17a), Node C (Fig. 5.17c), and Node D (Fig. 5.17d) but some slight changes were observed for Node B (Fig. 5.17b) and Node E (Fig. 5.17e). The interaction at the embankment and foundation interface close to Node D is neither influenced by height nor slope inclination. Node B is directly below the crest of the model embankments at their midheight, while Node E is 0.5 m below the natural ground surface at the embankment midslope. These slight changes in temperature are attributed to the change in slope inclination, where the gentler slope 4H:1V provided additional insulation.

Fig. 5.18 and Fig. 5.19 shows the near-term and long-term temperature conditions, respectively, for different embankment thicknesses at a constant slope inclination of 3H:1V. Similar to the observations earlier (Section 5.4.2), model results for near-term conditions indicate that the embankments will remain stable. The 4 m and 6 m thicknesses are providing adequate insulation at the core of the embankment fill, but the 2 m thickness shows the embankment completely thawed. It is noted however that all embankment thicknesses are providing insulation to the permafrost foundation. Under long-term conditions (Fig. 5.19), the 4 m and 6 m thick embankments indicate that Node A is still continuously frozen for RCP 2.6 and RCP 4.5, but the 4 m embankment shows continuous thawing as early as 2080 in RCP 8.5. The warmest temperature of Node A for the 6 m embankment is -2°C in 2020 and gradually increased to -0.8°C by 2100. For RCP 2.6 and RCP 4.5, the cold temperatures in the winter months for the 4 m and 6 m embankments range between -5°C and -10°C, but this range decreases to -0.8°C to -2°C for RCP 8.5. Remediation for RCP 2.6 and RCP 4.5 scenarios based on these results do not seem to constitute aggressive measures to maintain thermal stability, but embankment cooling must be employed before 2080 under RCP8.5 scenario. Thermal equilibration and optimizing the heat extraction should be the primary method for improving thermal performance. For example, snow removal from the slopes over the course of several years can be done before 2080 to cool the embankment naturally and insulation can be added on the slopes at its coldest temperatures to reduce the expected thermal degradation under this climate scenario.

Fig. 5.20, Fig. 5.21, and Fig. 5.22 shows the 0°C isotherm for two time steps (January 2070 and January 2100) for all model embankment thicknesses and slope inclinations under RCP8.5 scenario. In all cases, the talik that has formed (grey region) grew larger by 2100. The black regions indicate temperature below 0°C. The talik is primarily contained in the foundation for the 2 m

embankment, but this extended to the embankment fill for 4 m and 6 m embankments. In Fig. 5.21, the extent of the talik is primarily underneath the crest toward the toe of the embankment. Thaw weakening of the previously frozen foundation will lead to slope instabilities which can be in the form of cracks developing at the crest of the embankment due to significant lateral displacements. In Fig. 5.22, the thickness of the talik at the toe is thicker compared to that in Fig. 5.20 and Fig. 5.21, and its extent is now visible to the embankment centreline in 2100. The talik in Fig. 5.22b, Fig. 5.22d, and Fig. 5.22f are parallel to the slope surface. It is hypothesized that movements will occur in these formed taliks. The mechanical performance of these embankments are explored further in Chapter 6.

5.6. Summary and Conclusions

Thermal numerical models using thermal modifier and surface energy balance approaches have been developed for thick and thin embankment sections along ITH calibrated with field data since 2015. Air temperatures in the region have been warming as recorded by the weather stations and satellite data which resulted to warmer soil temperatures both in the summer and winter months. With confidence in the calibrated model, near-term and long-term climate models were implemented. The following conclusions are drawn:

1. The recorded air temperatures from the weather stations indicate that the location of the embankment along the highway greatly impacts its thermal performance. The models presented in this paper are in a region 1.2°C warmer than the air temperatures in Tuktoyaktuk. Warmer air temperatures and warmer permafrost conditions will contribute in accelerating thawing of the embankment fill and foundation soil.

2. Embankment thermal design should account for reasonable assumptions on material properties and expected temperature boundary conditions to best simulate thermal performance. Supplementing the model with measured field data greatly improved its reliability.

3. The results of thermal modelling are highly dependent on the modelling approach selected. The thermal modifier approach uses empirical values that lump all factors together to transform the air temperature to ground surface temperatures, while the surface energy balance approach requires complex input parameters that require sophisticated and expensive instrumentations to obtain accurate values. The difference in soil temperatures between the two approaches is an inherent variable a designer should assess. The snow depth and albedo was assumed to be constant throughout the analyses for the surface energy balance approach which may not be accurate for future conditions. The snow depth and albedo available from satellite data are on a regional scale which do not account for existing infrastructure in the region.

4. The results of near-term and long-term climate models provided an insight when remediation can be employed to impede permafrost degradation and maintain embankment thermal stability. Because climate models are done on a regional scale, historical and present-day meteorological data from local weather stations are still indispensable source of data in engineering design of new linear infrastructure.

5. The parametric models investigated showed that the thickness of the embankment, in addition to the ambient air temperatures, are the key factors in preserving the permafrost in the foundation soil and maintaining a frozen core in the embankment fill. The slope inclination does significantly influence the temperatures at the core of the embankment, but provide additional insulation to the foundation as the inclination of the slope is decreased.

The thermal models presented do not take into account the deformation of the embankment but they provide reasonable estimates of the embankment thermal regime over time. Thawing of the previously compacted frozen soil during the monitoring period and the effects of climate warming on overall embankment performance are investigated in Chapter 6 using coupled thermal-mechanical models.

Table 5.1. Summary of TEMP/W model parameters.

Property	Units	Foundation	Fill
Unfrozen thermal conductivity	kJ/days·m·°C	45	122.5
Frozen thermal conductivity	kJ/days·m·°C	120	163.9
Unfrozen volumetric heat capacity	$kJ/m^3 \cdot °C$	5282.2	2171.4
Frozen volumetric heat capacity	$kJ/m^3 \cdot °C$	2869.7	1613.9
Volumetric water content	m^3/m^3	5	0.3

Table 5.2. Thermal modifiers (n-factors) used in TEMP/W model.

Location	$n_{freezing}$	$n_{thawing}$
Top	0.95	1.00
Slope Top	0.92	1.00
Slope Middle	0.83	1.00
Slope Bottom	0.55	1.00
Toe	0.20	0.55
Prairie	0.20	0.45
Slope (Thin embankment)	0.65	1.00

Table 5.3. Albedo applied to the model at different locations.

Month	Top	Slope Top	Slope Middle	Slope Bottom	Toe	Prairie
January	0.12	0.15	0.35	0.70	0.70	0.70
February	0.12	0.15	0.35	0.70	0.70	0.70
March	0.12	0.15	0.33	0.65	0.65	0.65
April	0.15	0.20	0.20	0.65	0.65	0.65
May	0.10	0.10	0.10	0.10	0.25	0.25
June	0.10	0.10	0.10	0.10	0.25	0.25
July	0.10	0.10	0.10	0.10	0.25	0.25
August	0.10	0.10	0.10	0.10	0.25	0.25
September	0.10	0.10	0.10	0.10	0.25	0.25
October	0.12	0.12	0.12	0.18	0.25	0.25
November	0.12	0.15	0.22	0.80	0.80	0.80
December	0.12	0.15	0.25	0.75	0.75	0.75

Table 5.4. Snow depth at different locations of the embankment (units in metres).

Month	Top	Slope Top	Slope Middle	Slope Bottom	Toe	Prairie
January	0	0.16	0.30	0.55	0.60	0.55
February	0	0.20	0.40	0.60	0.65	0.60
March	0	0.20	0.47	0.70	0.73	0.70
April	0	0.10	0.20	0.65	0.65	0.60
May	0	0	0	0	0	0
June	0	0	0	0	0	0
July	0	0	0	0	0	0
August	0	0	0	0	0	0
September	0	0	0	0	0	0
October	0	0.03	0.05	0.07	0.07	0.07
November	0	0.04	0.07	0.20	0.20	0.20
December	0	0.06	0.17	0.50	0.50	0.48

Table 5.5. Summary of models used in temperature analyses.

CMIP5	CanCM4 – Climate Model	CanESM2 – Earth System Model
Model	decadal2005 (30yr run) decadal2015 (10yr run)	RCP 2.6, 4.5, and 8.5
Analyses Procedure	Thermal Modifiers (TM) Surface Energy Balance (SEB)	
Parameters	Temperature, Solar Radiation, Wind Speed, Relative Humidity, Albedo, Snow Depth,	

Table 5.6. Air temperature warming rate using a linear projection for each climate scenario.

Projection	Model Analyses	Average warming rate (°C/yr)	ΔT at end of model (°C)
Near-term Conditions	decadal2005i1	0.100	3.01
	decadal2005i2	0.092	2.77
	decadal2015	0.216	2.16
Long-term Conditions	RCP 2.6	0.024	2.24
	RCP 4.5	0.037	3.50
	RCP 8.5	0.098	9.33

Table 5.7. Warming rates at different node locations using TM and SEB approaches for near-term conditions.

Condition	Model Analyses	Temperature (°C/yr)							
		TM				SEB			
		C2-D	C2-G	C3-B	C4-B	C2-D	C2-G	C3-B	C4-B
Maximum Yearly Temperatures	decadal2005i1	0.008	0.014	0.011	0.005	0.008	0.015	0.022	0.003
	decadal2005i2	0.012	0.019	0.026	0.012	0.014	0.024	0.034	0.003
	decadal2015	0.002	0.018	0.019	-0.001	0.009	0.050	0.060	0.017
Minimum Yearly Temperatures	decadal2005i1	-0.009	0.009	0.044	0.066	0.036	0.038	0.065	-0.002
	decadal2005i2	0.034	0.019	0.053	0.074	0.063	0.058	0.081	0.035
	decadal2015	0.035	0.080	0.053	-0.024	0.196	0.224	0.150	0.000

Table 5.8. Nodal temperatures at different locations in the embankment at different time steps for CanCM4 (near-term) using SEB approach.

Model Analyses	Node	Temperature (°C)							
		April 1				October 31			
		2020	2025	2030	2035	2020	2025	2030	2035
decadal2005i1	C2-D	-11.92	-10.73	-10.76	-8.51	-0.73	-0.56	-0.61	-0.44
	C2-G	-10.23	-8.75	-9.30	-7.40	-2.13	-1.91	-1.94	-1.74
	C3-B	-5.83	-4.82	-4.92	-4.54	-4.08	-3.73	-3.75	-3.50
	C4-B	-10.78	-6.93	-8.88	-8.58	-1.15	-0.87	-0.91	-0.91
decadal2005i2	C2-D	-11.80	-11.75	-9.43	-11.03	-0.51	-0.65	-0.38	-0.67
	C2-G	-9.94	-9.61	-7.77	-9.38	-1.99	-2.09	-1.66	-2.07
	C3-B	-5.50	-5.07	-4.35	-5.15	-3.91	-3.99	-3.39	-3.88
	C4-B	-9.31	-9.70	-8.87	-9.73	-0.84	-1.03	-1.01	-0.98
decadal2015	C2-D	-10.95	-11.03	---	---	-0.71	-0.81	---	---
	C2-G	-9.60	-9.13	---	---	-2.17	-2.11	---	---
	C3-B	-5.99	-4.90	---	---	-4.08	-3.86	---	---
	C4-B	-8.23	-9.33	---	---	-1.05	-1.00	---	---

Table 5.9. Warming rates at different node locations using TM and SEB approaches for long-term conditions.

Condition	Model Analyses	Temperature (°C/yr)							
		TM				SEB			
		C2-D	C2-G	C3-B	C4-B	C2-D	C2-G	C3-B	C4-B
Maximum Yearly Temperatures	RCP 2.6	0.003	0.005	0.005	0.002	0.003	0.003	0.005	0.004
	RCP 4.5	0.005	0.007	0.009	0.005	0.006	0.005	0.008	0.003
	RCP 8.6	0.021	0.021	0.026	0.019	0.055	0.027	0.021	0.006
Minimum Yearly Temperatures	RCP 2.6	0.018	0.017	0.013	0.010	0.025	0.016	0.013	0.049
	RCP 4.5	0.029	0.027	0.020	0.014	0.047	0.032	0.022	0.047
	RCP 8.6	0.136	0.111	0.066	0.036	0.122	0.103	0.058	0.070

Table 5.10. Nodal temperatures at different locations in the embankment at different time steps for CanESM2 (long-term) using SEB approach.

Model Analyses	Node	Temperature (°C)									
		April 1					October 31				
		2020	2030	2050	2070	2100	2020	2030	2050	2070	2100
RCP 2.6	C2-D	-7.38	-9.14	-5.89	-4.35	-3.63	-0.18	-0.35	0.11	0.27	0.08
	C2-G	-6.26	-7.46	-5.62	-4.46	-3.88	-1.34	-1.62	-5.28	-1.01	-1.15
	C3-B	-3.58	-3.74	-2.84	-2.78	-2.35	-2.92	-3.32	-2.63	-2.45	-2.56
	C4-B	-6.71	-0.73	-3.65	-4.28	-0.44	-0.75	-0.58	-0.50	-0.47	-0.51
RCP 4.5	C2-D	-10.26	-6.74	-4.64	-3.24	-2.22	-0.51	-0.17	0.07	0.43	0.16
	C2-G	-8.57	-5.97	-3.97	-3.96	-3.30	-1.83	-1.28	-4.44	-0.91	-0.98
	C3-B	-4.67	-3.43	-2.33	-2.07	-2.01	-3.60	-2.81	-2.43	-2.20	-2.24
	C4-B	-7.03	-2.90	-2.27	-1.81	-1.11	-0.84	-0.58	-0.50	-0.41	-0.43
RCP 8.5	C2-D	-8.13	-6.76	-3.78	0.01	0.10	-0.38	-0.26	0.24	0.99	2.18
	C2-G	-6.64	-5.74	-3.73	-0.48	0.03	-1.61	-1.35	-3.98	-0.60	1.03
	C3-B	-3.41	-3.52	-2.44	-1.52	-0.96	-3.26	-2.87	-2.31	-1.62	-0.98
	C4-B	-6.25	-0.97	-1.97	-3.39	-0.45	-0.89	-0.55	-0.31	-0.57	-0.31

Table 5.11. Embankment heights and slope inclinations investigated in ABAQUS.

Embankment Height	Slope Inclination		
	2H:1V	3H:1V	4H:1V
2 m	H2S2	H2S3	H2S4
4 m	H4S2	H4S3	H4S4
6 m	H6S2	H6S3	H6S4

Fig. 5.1. Survey rod on the west side of the embankment for snow depth monitoring.

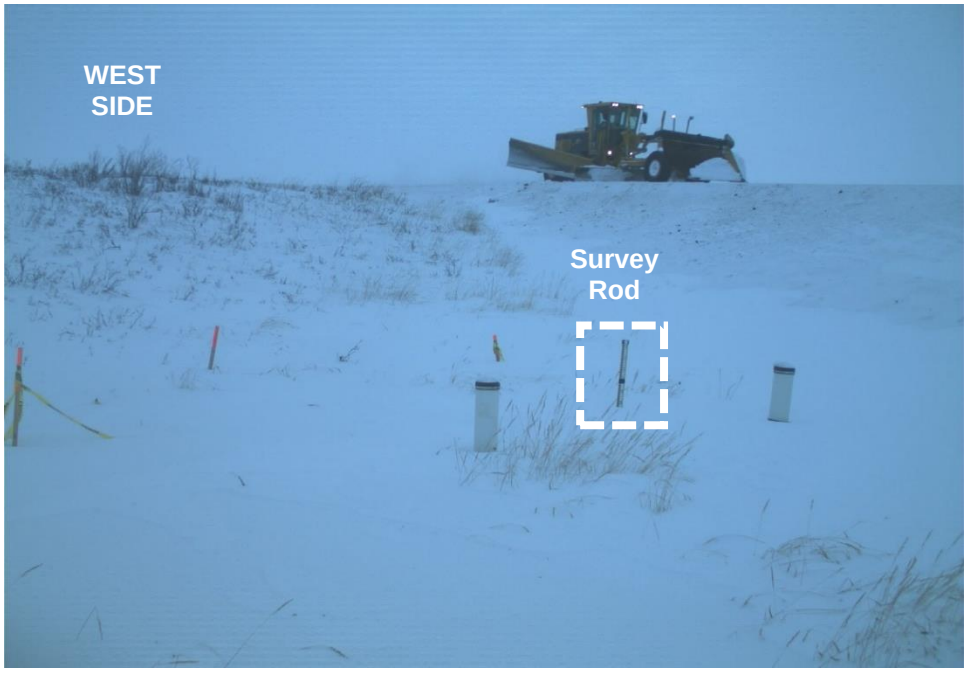

Fig. 5.2. Cross-sections and locations of temperature sensors in the (a) thick and (b) thin embankment test sections.

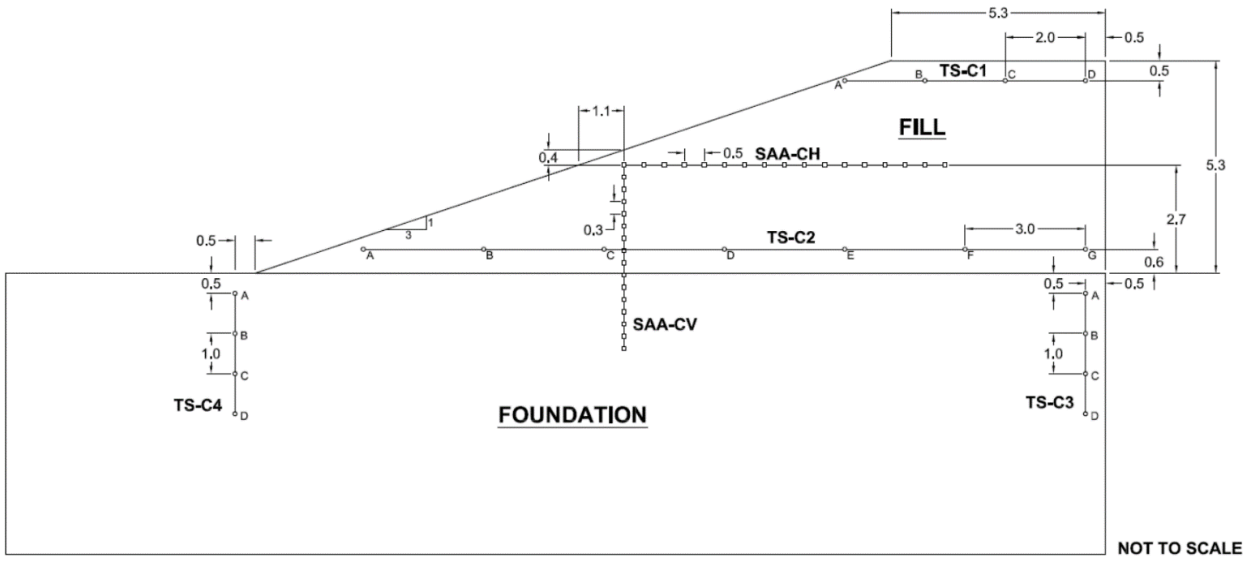

(a)

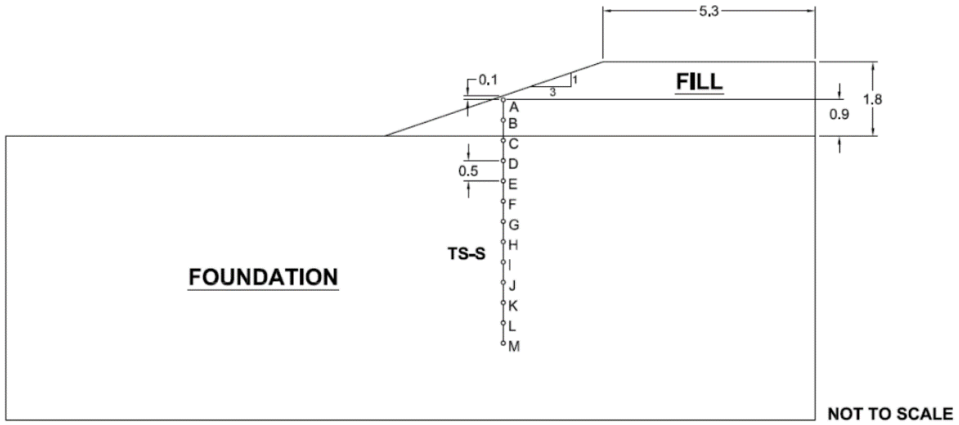

(b)

Fig. 5.3. Cross-section of an embankment model in TEMP/W and location of boundary conditions (in reference to Table 5.2, Table 5.3, and Table 5.4).

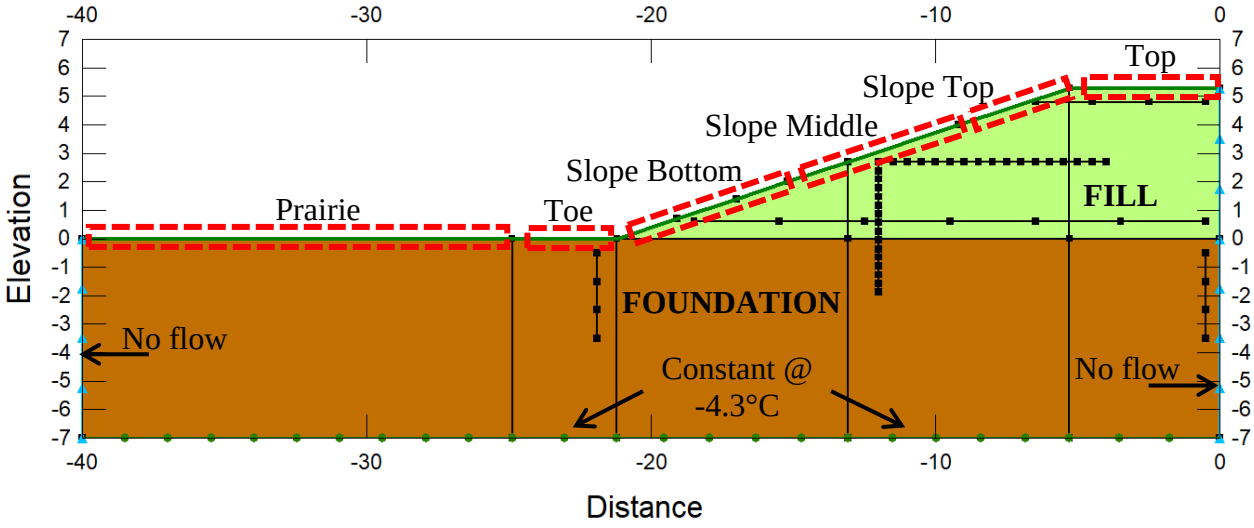

Fig. 5.4. Comparison of measured (thermistor nodes) and modelled (TEMP/W) temperature values at different locations in the embankment fill and foundation soil using TM and SEB approaches: (a) C1-B, (b) C1-C, (c) C1-D, (d) C2-B, (e) C2-D, (f) C2-G, (g) C3-B, (h) C3-C, (i) C3-D, (j) C4-B, (k) C4-C, and (l) C4-D.

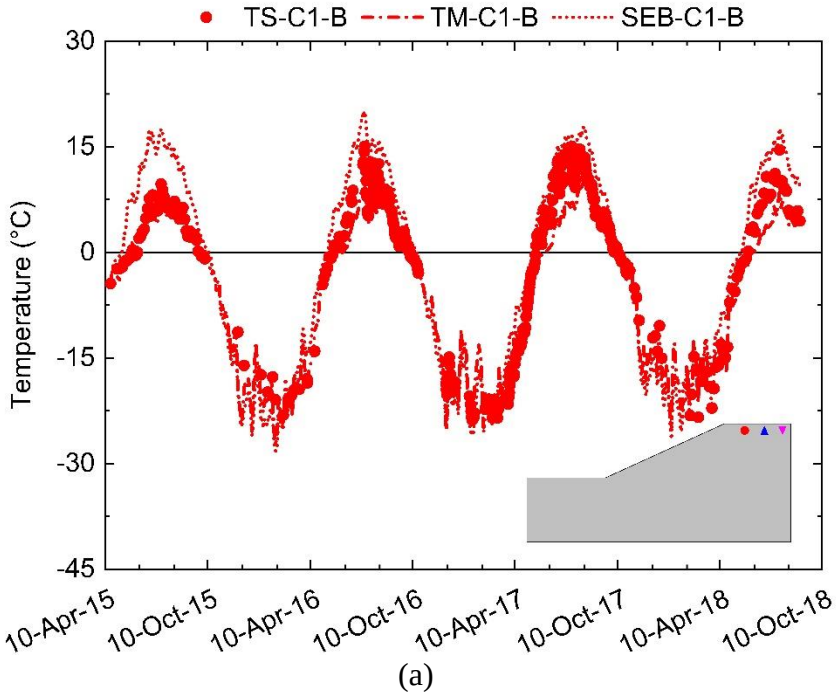

(a)

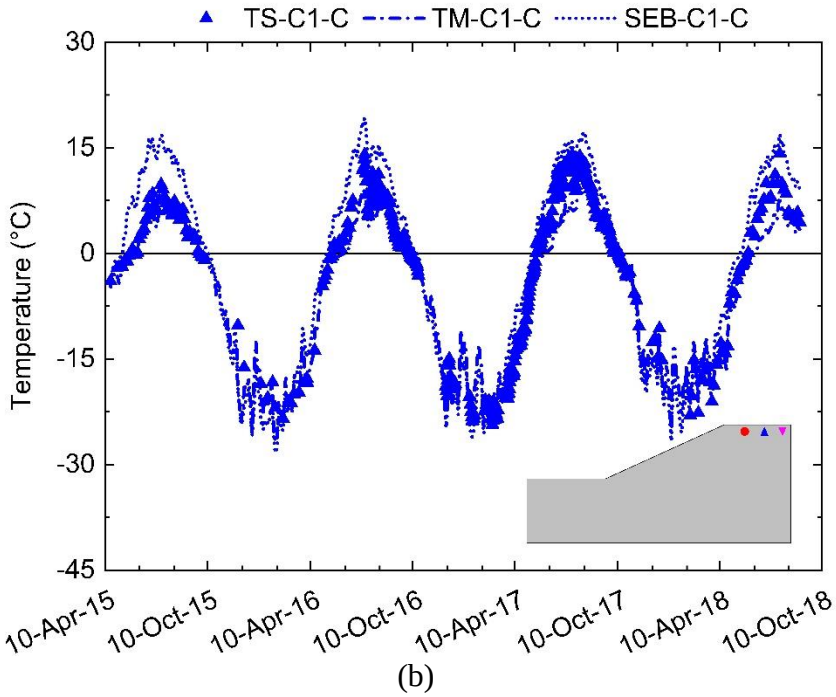

(b)

Fig. 5.4 (continued)

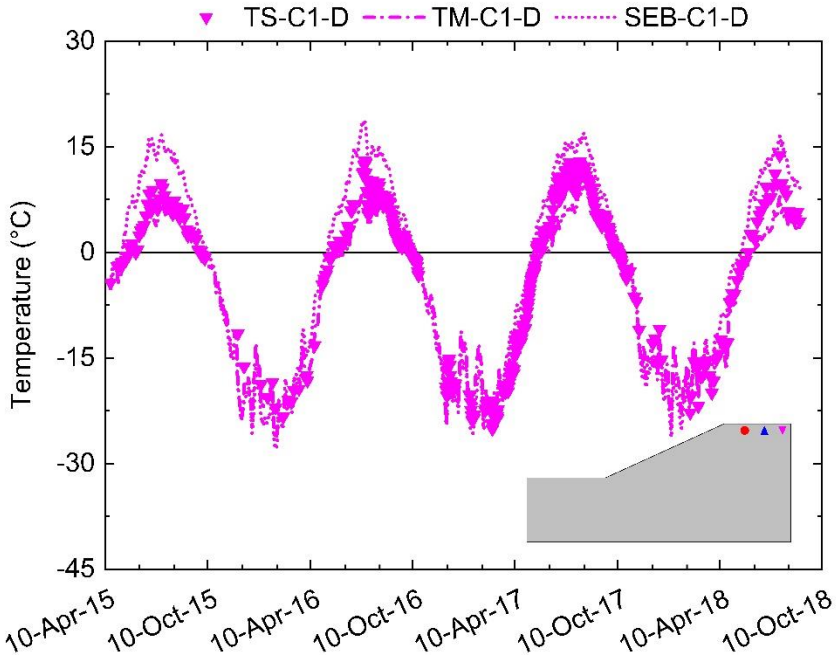

(c)

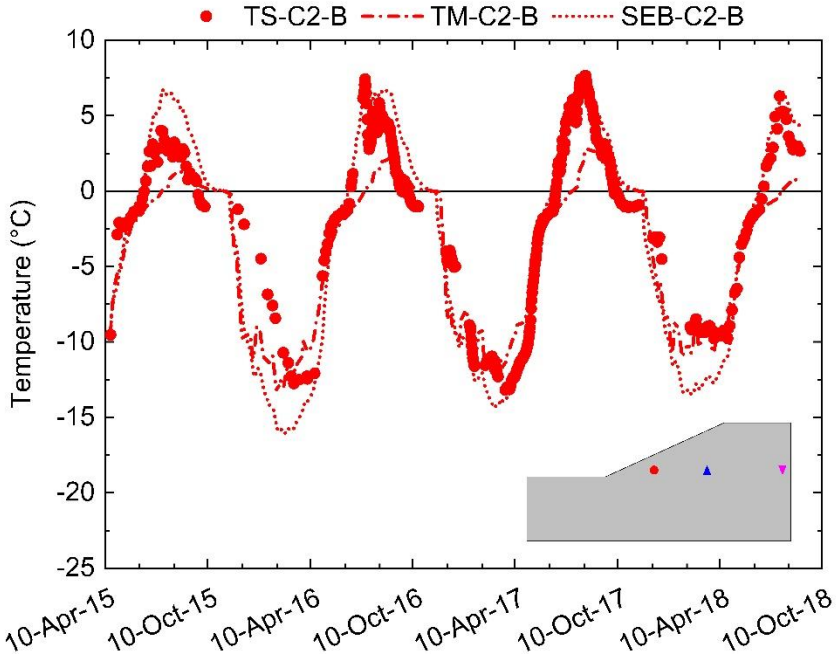

(d)

Fig. 5.4 (continued)

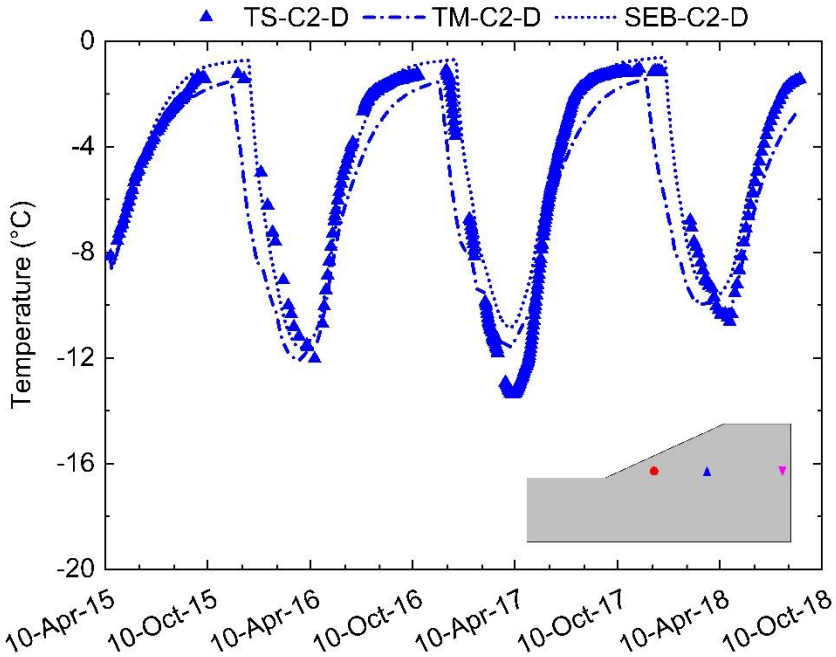

(e)

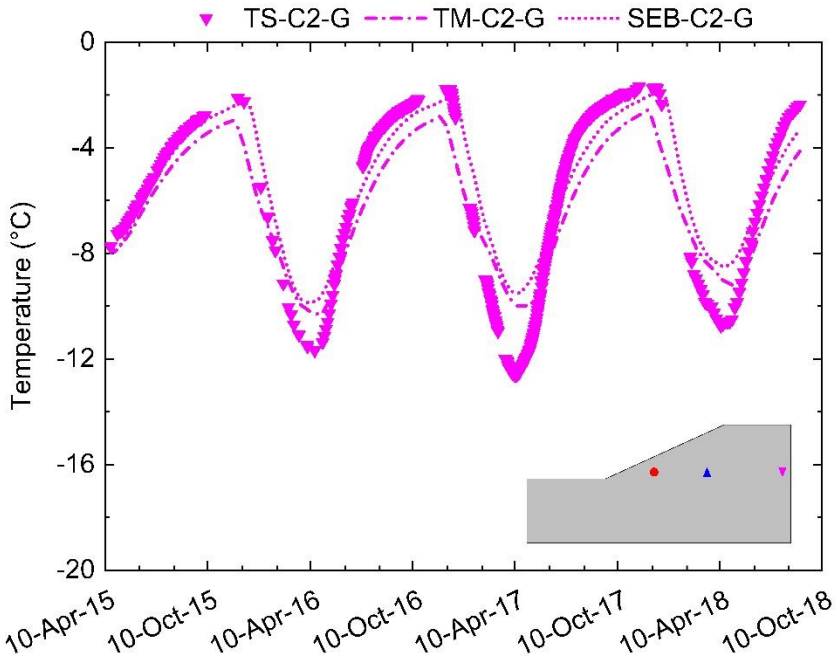

(f)

Fig. 5.4 (continued)

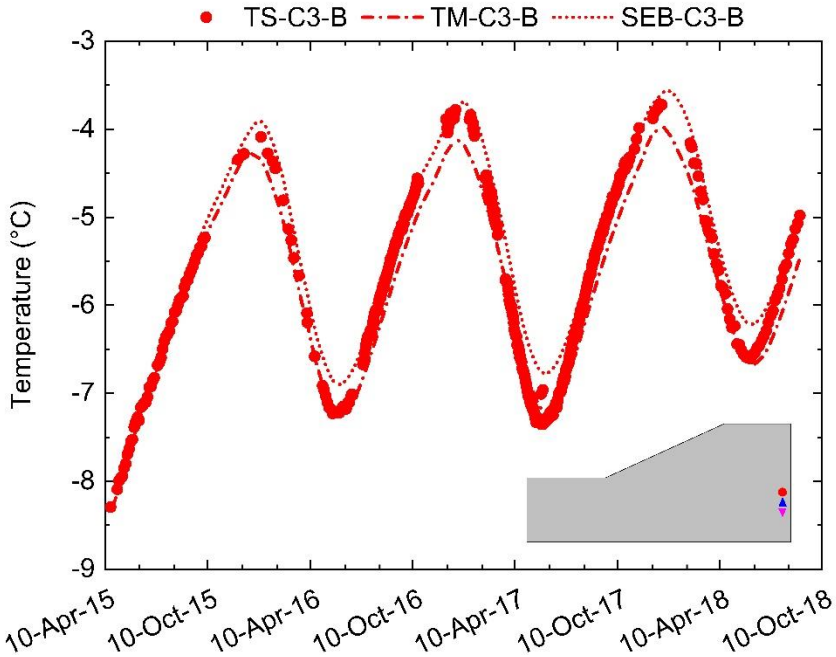

(g)

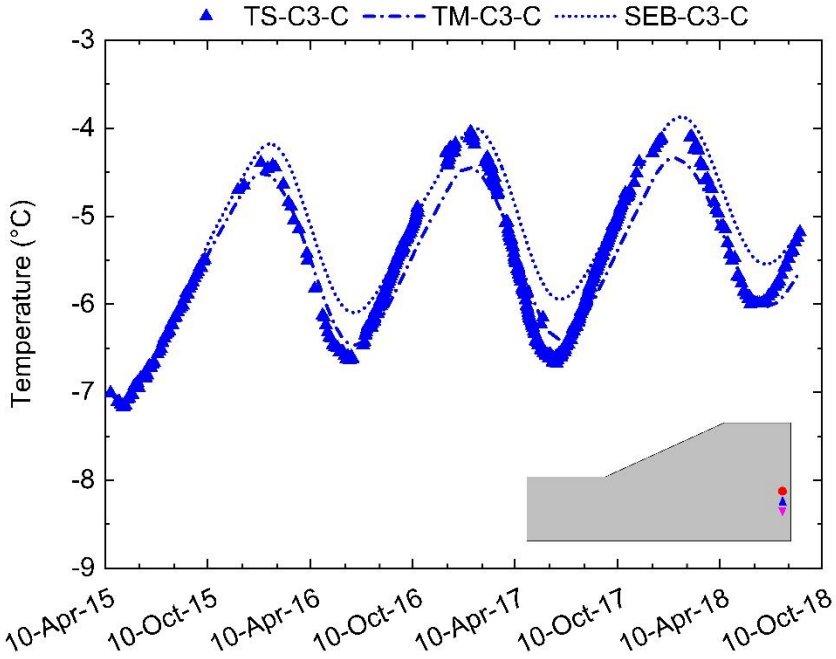

(h)

Fig. 5.4 (continued)

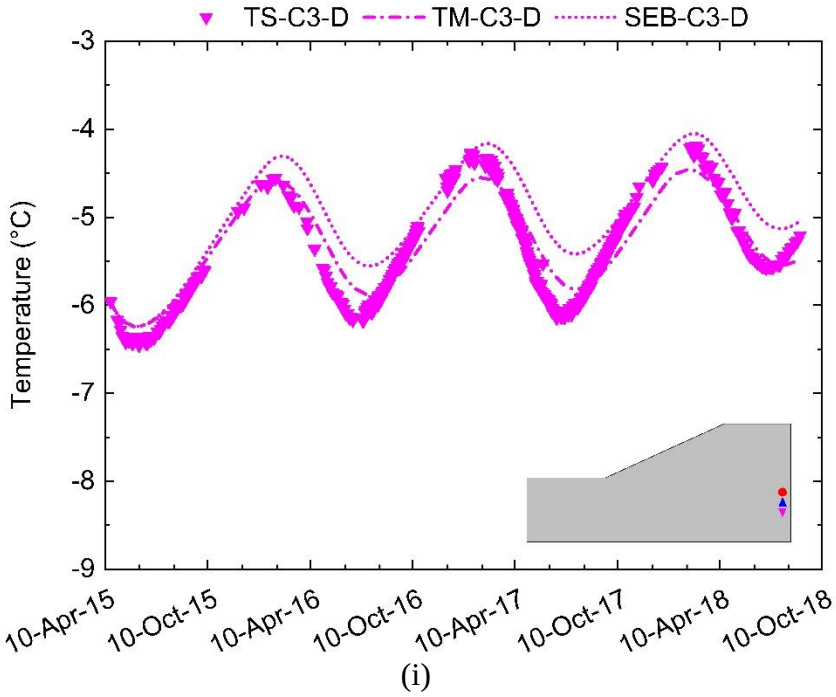

(i)

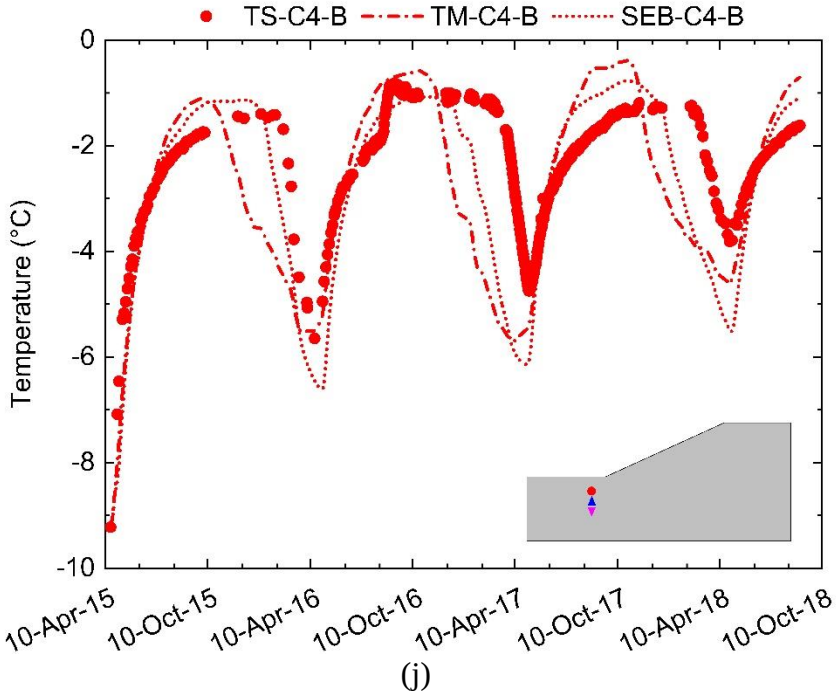

(j)

Fig. 5.4 (continued)

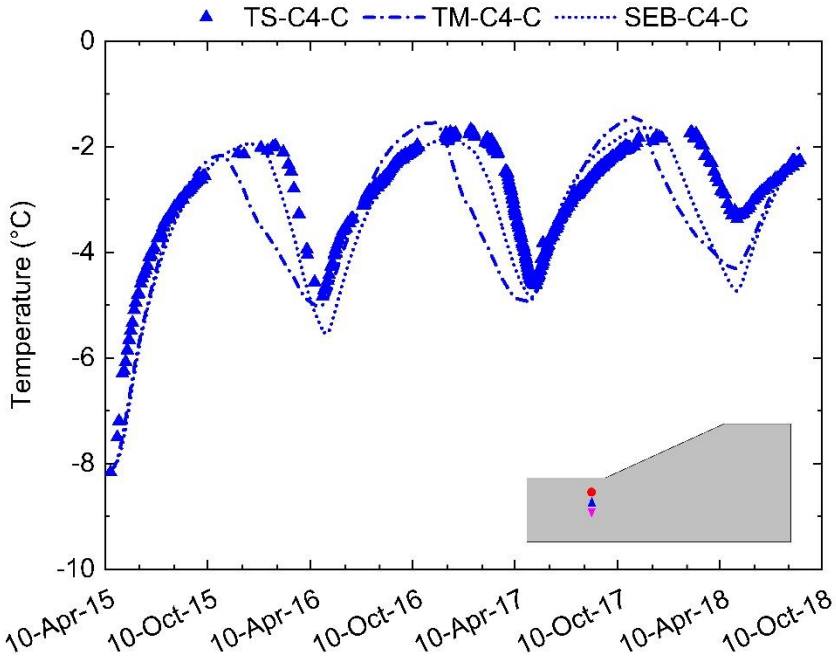

(k)

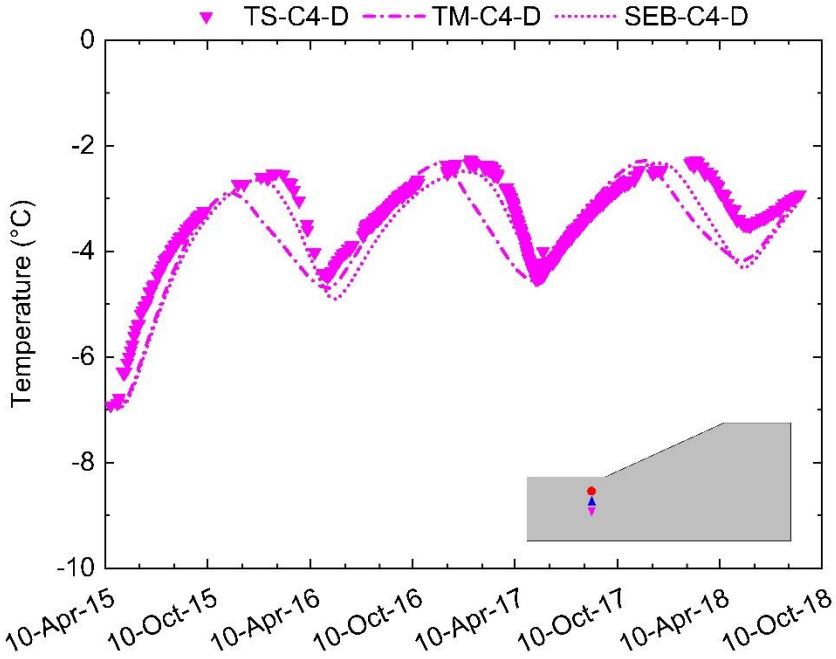

(l)

Fig. 5.5. Temperature contour plots at different locations in the embankment for the three-year monitoring period using SEB approach: (a) air temperature, (b) crest, and (c) toe.

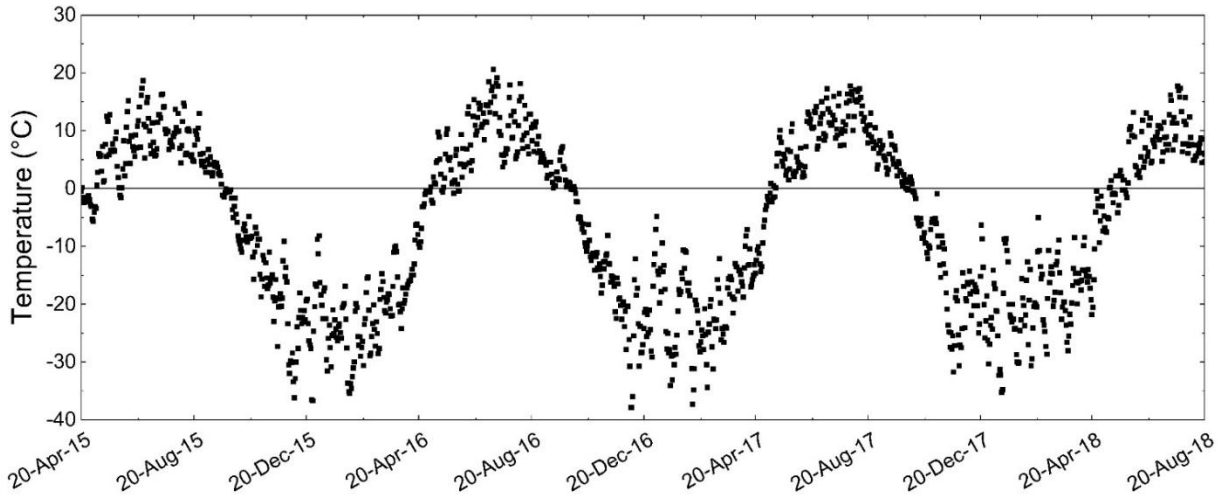

(a)

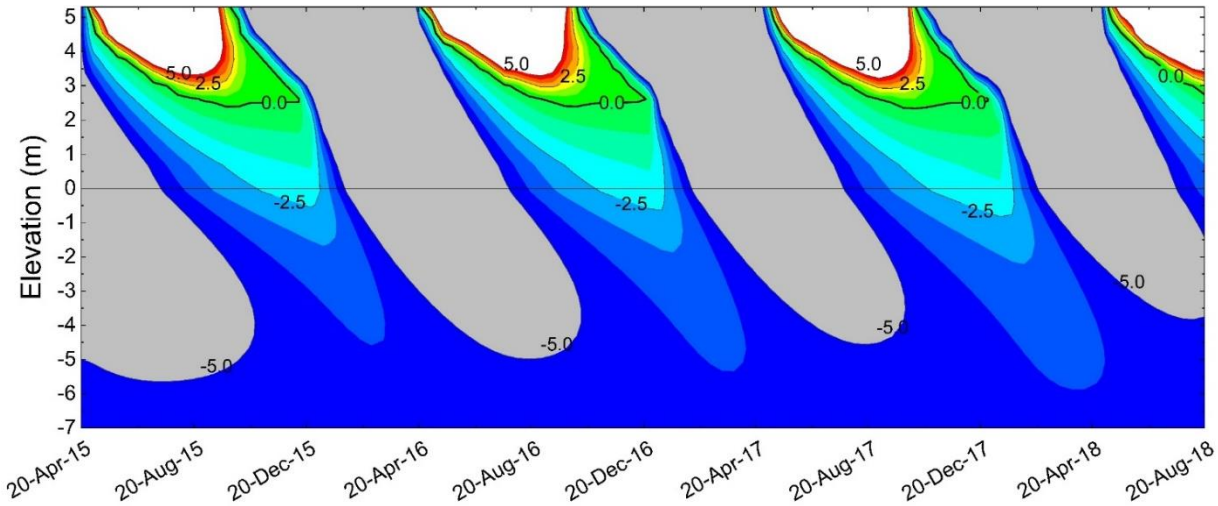

(b)

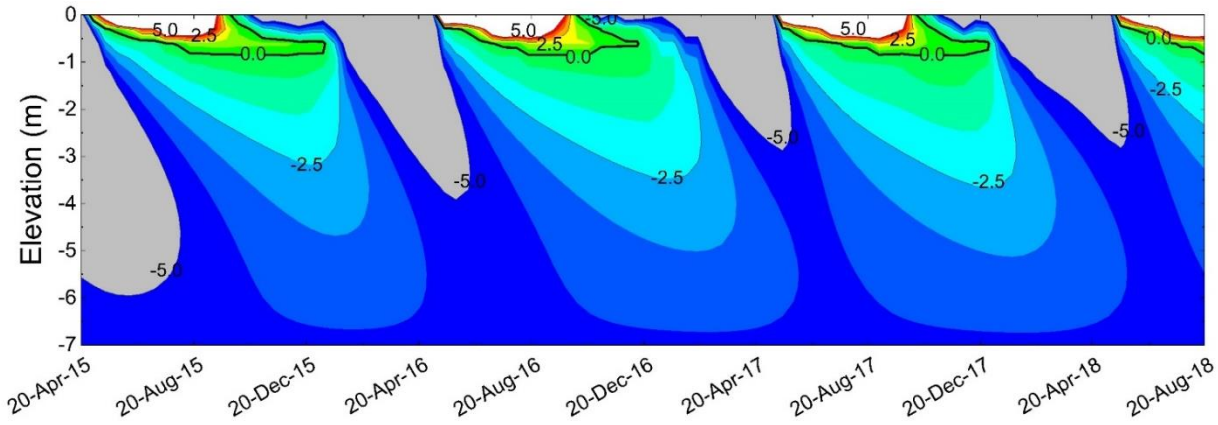

(c)

Fig. 5.6. Comparison of field and numerical model results at select thermistor locations for the thin embankment section.

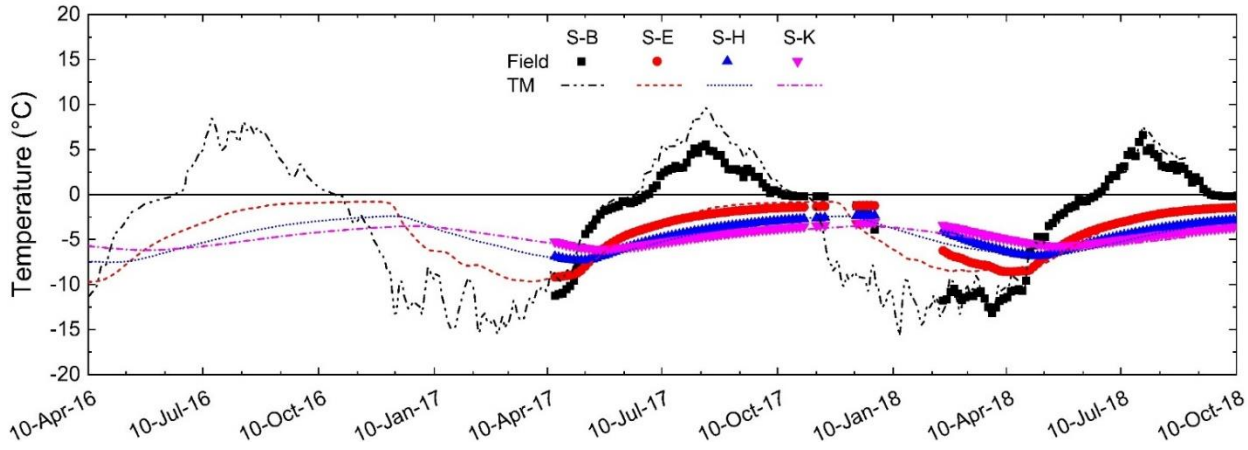

Fig. 5.7. Climate projection for temperature, relative humidity, and wind speed for (a) decadal2005i1 (near-term) and (b) RCP 8.5 (long-term).

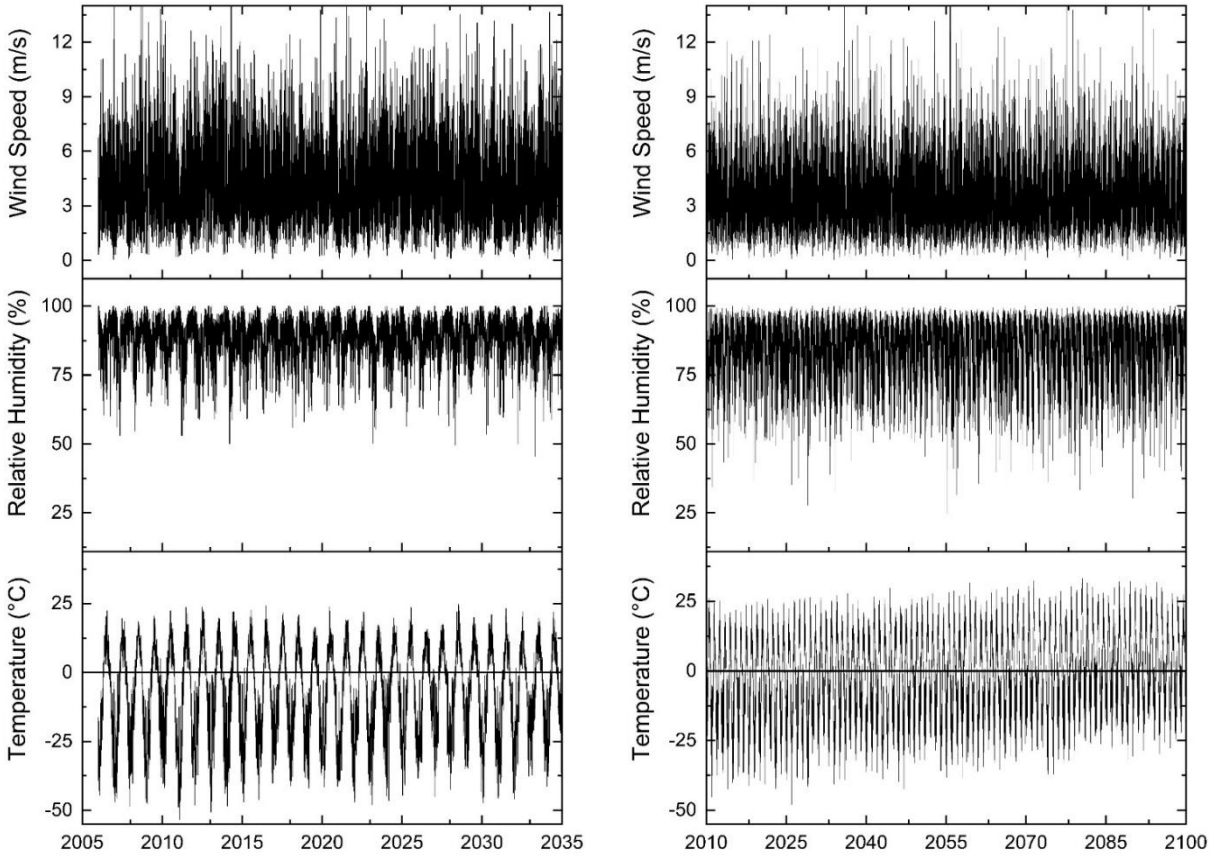

(a) (b)

Fig. 5.8. Comparison of (a, c, e, g) maximum and (b, d, f, h) minimum yearly temperatures for decadal (near-term) models using TM and SEB approaches for select thermistor locations: (a, b) C2-D, (c, d) C2-G, (e, f) C3-B, and (g, h) C4-B.

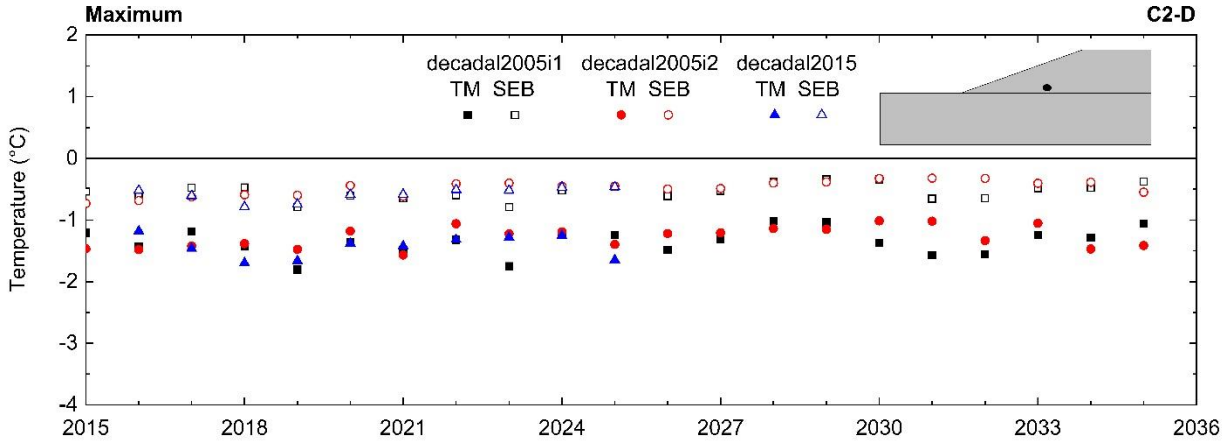

(a)

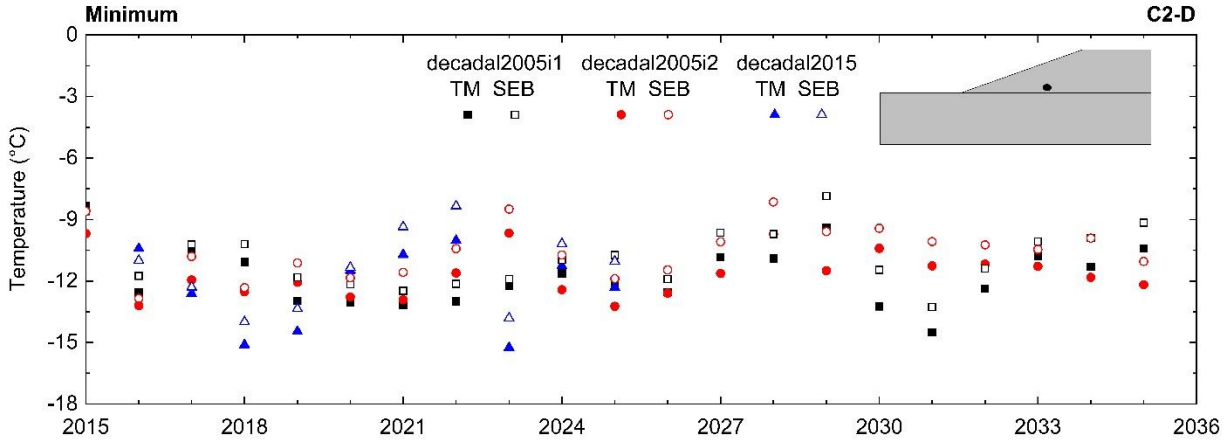

(b)

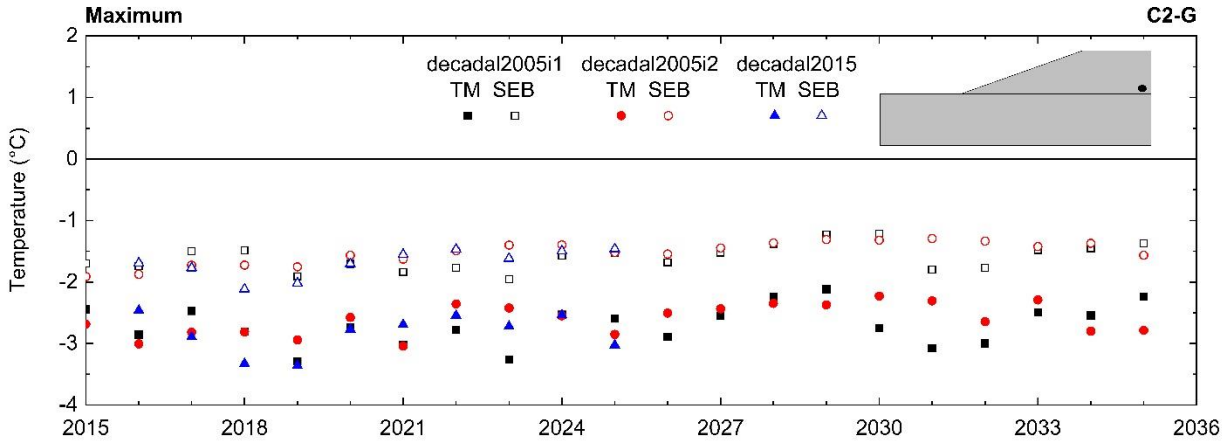

(c)

Fig. 5.8 (continued)

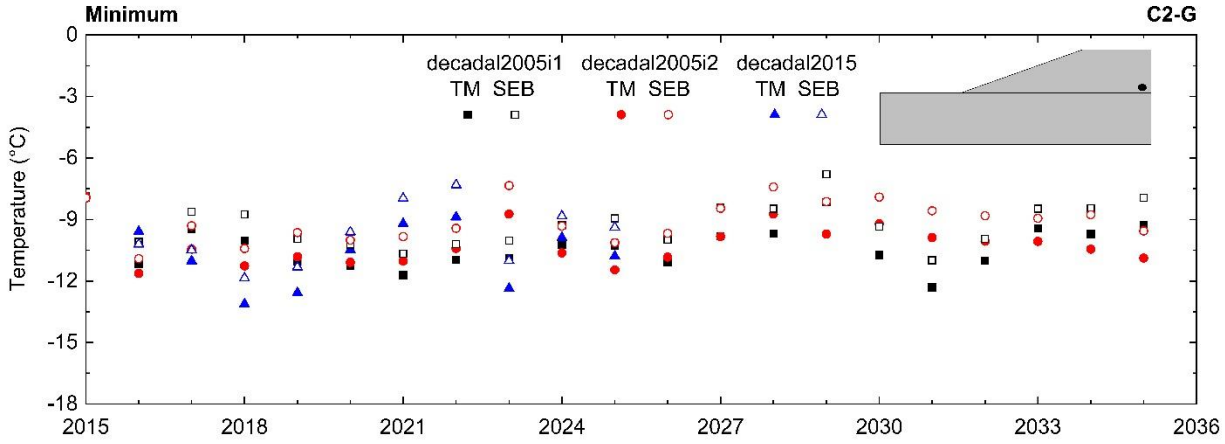

(d)

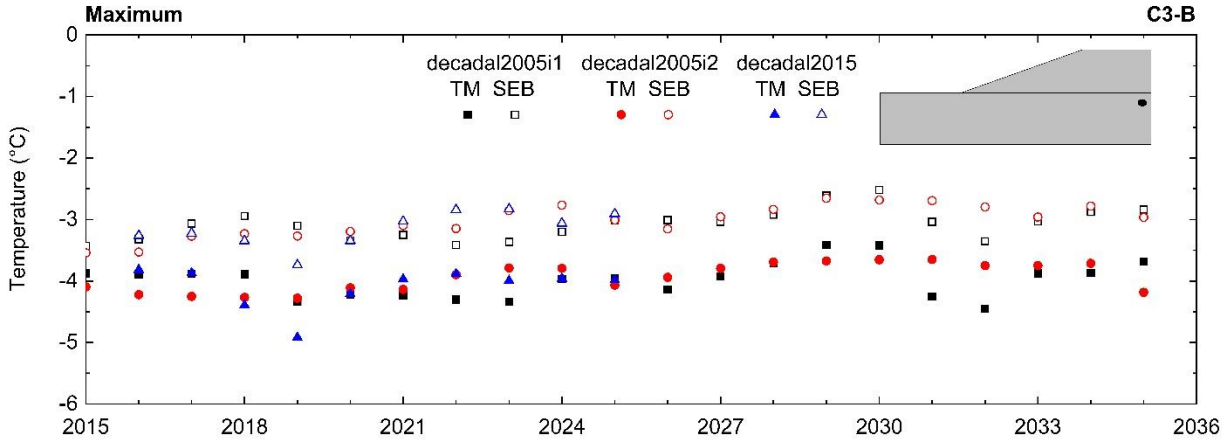

(e)

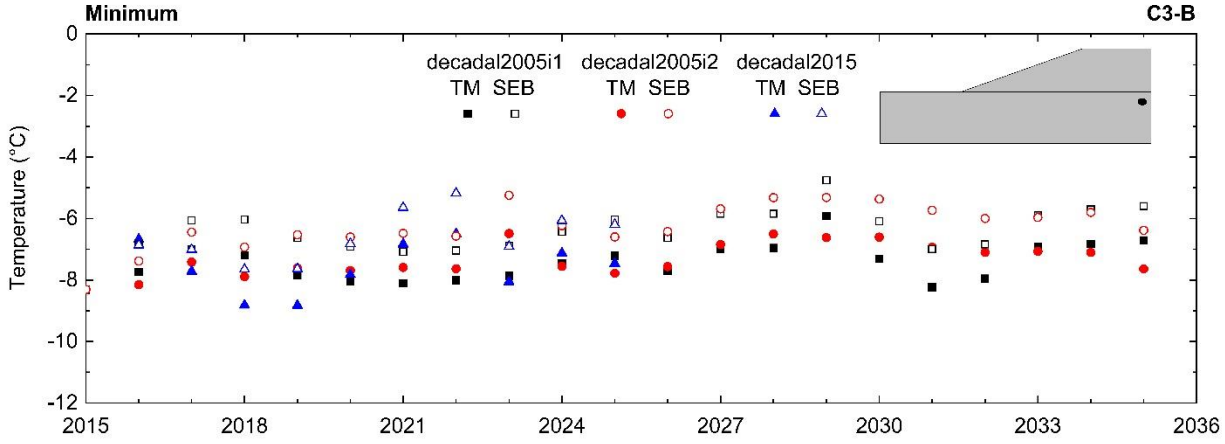

(f)

Fig. 5.8 (continued)

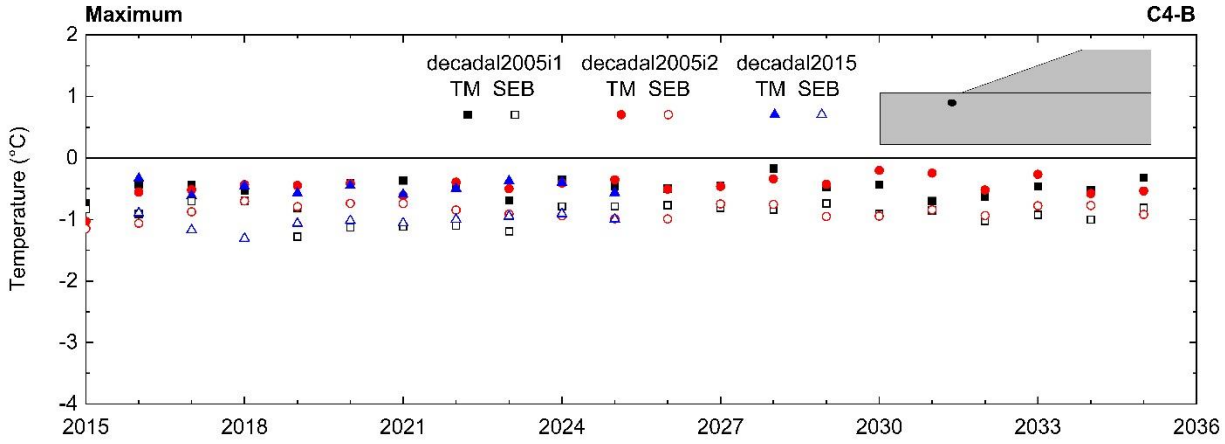

(g)

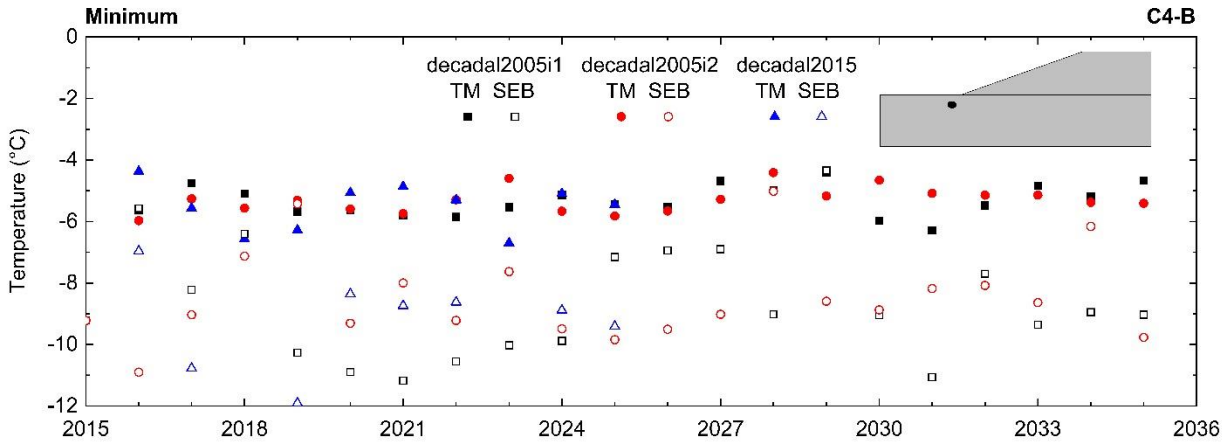

(h)

Fig. 5.9. Comparison of (a, c, e, g) maximum and (b, d, f, h) minimum yearly temperatures for RCP (long-term) models using TM and SEB approaches for select thermistor locations: (a, b) C2-D, (c, d) C2-G, (e, f) C3-B, and (g, h) C4-B.

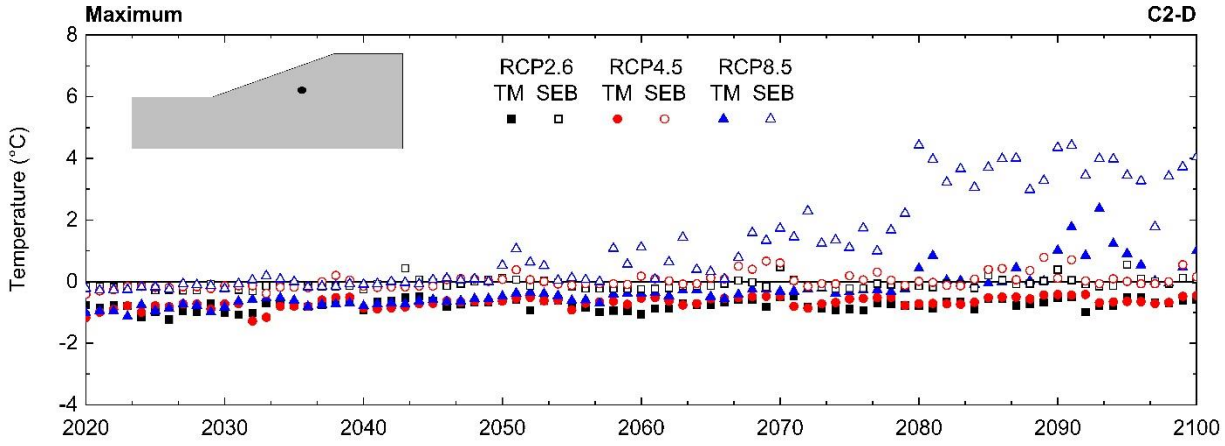

(a)

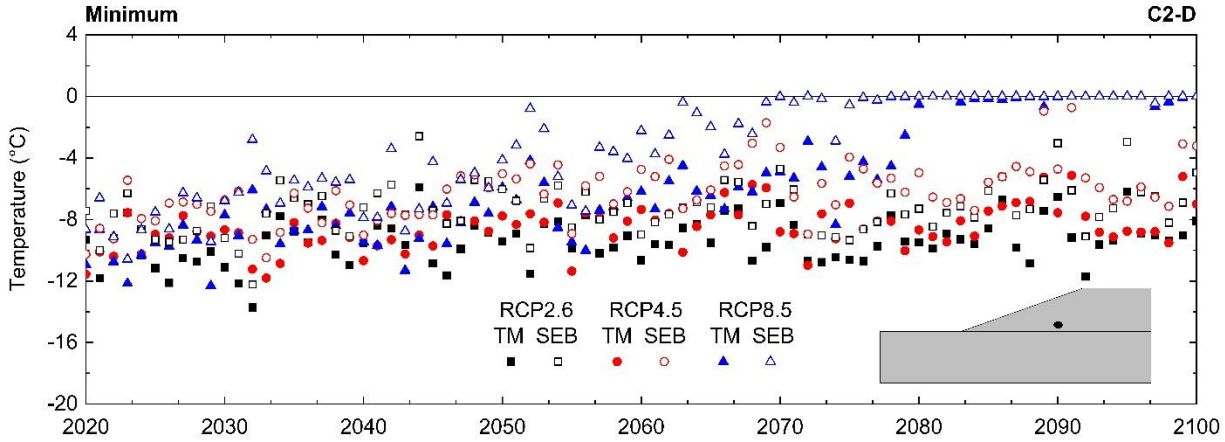

(b)

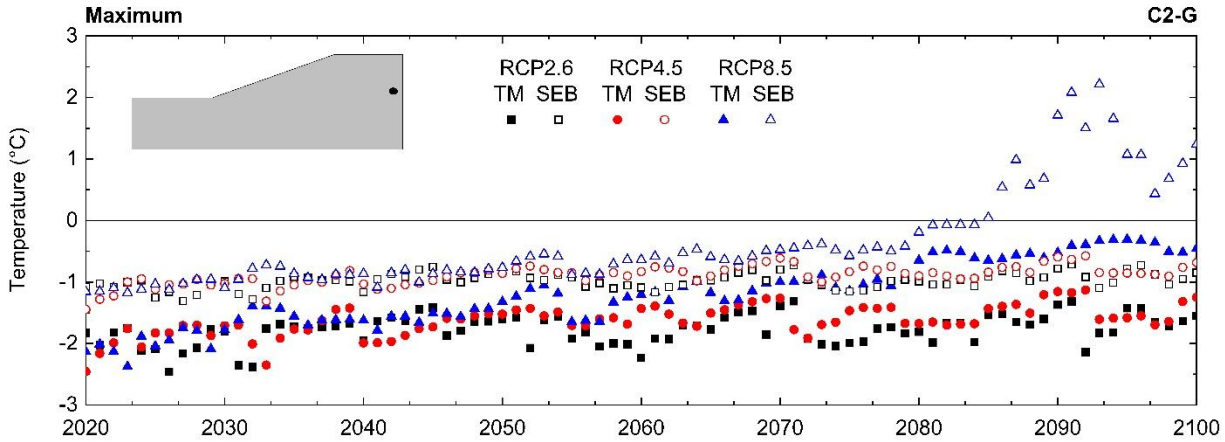

(c)

Fig. 5.9 (continued)

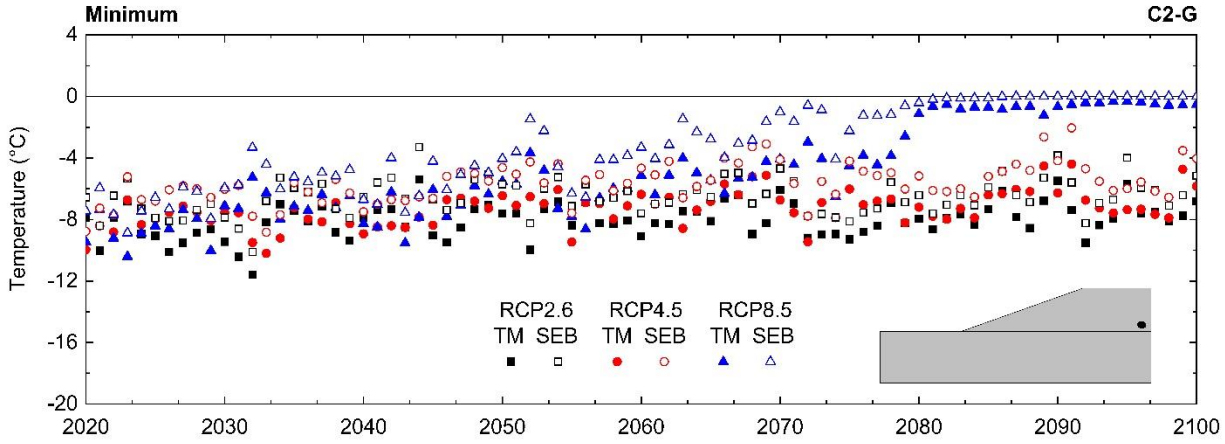

(d)

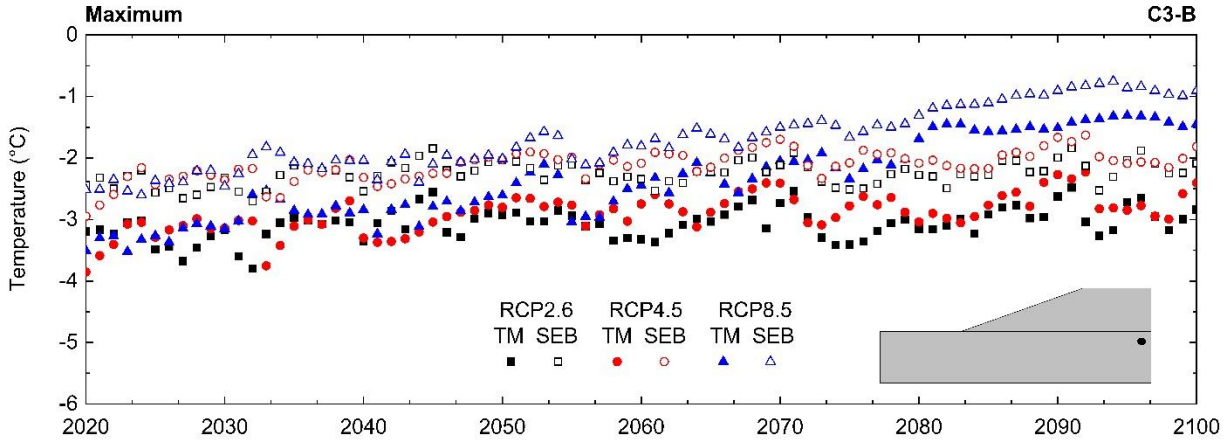

(e)

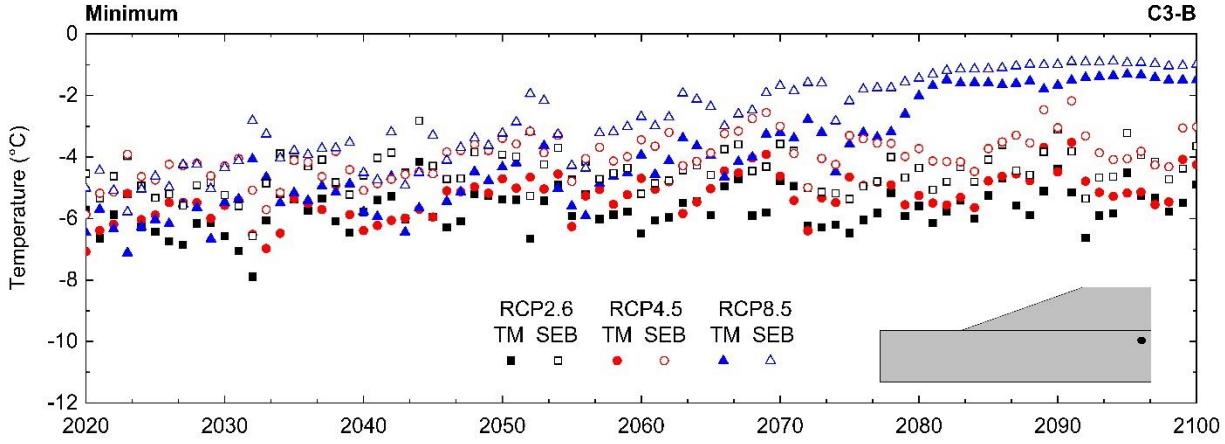

(f)

Fig. 5.9 (continued)

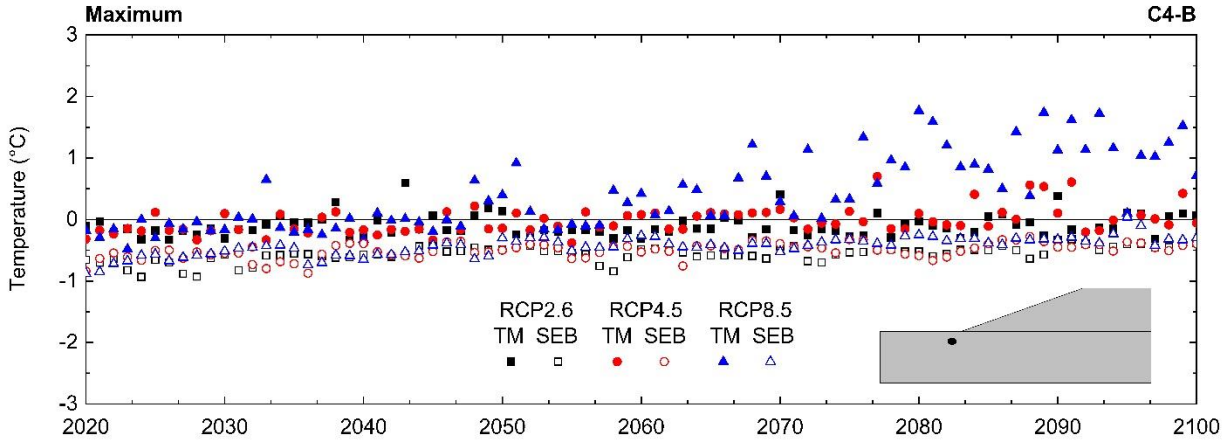

(g)

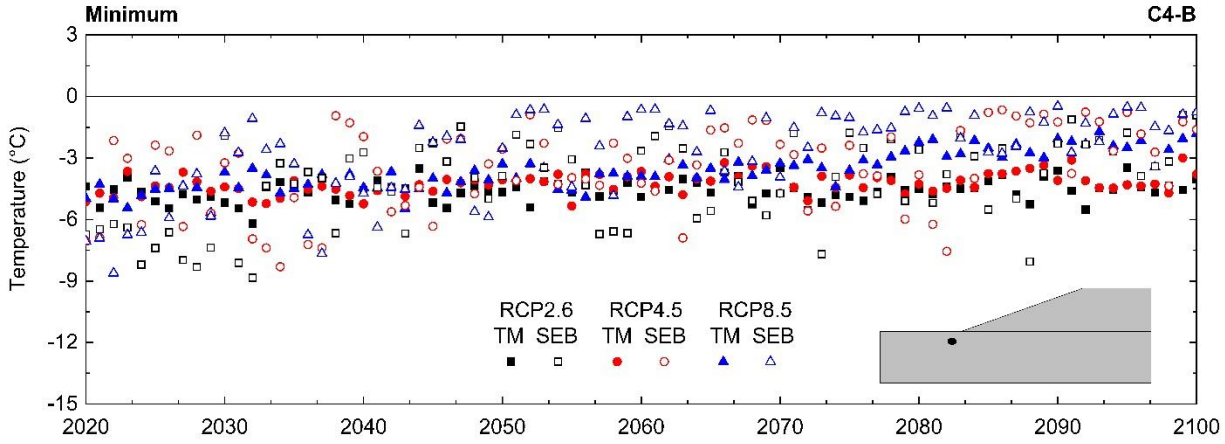

(h)

Fig. 5.10. Temperature distribution along the crest (a, b, c), midslope (d, e, f), and toe (g, h, i) for RCP 2.6 (a, d, g), RCP 4.5 (b, e, h), and RCP 8.5 (c, f, i) using SEB approach.

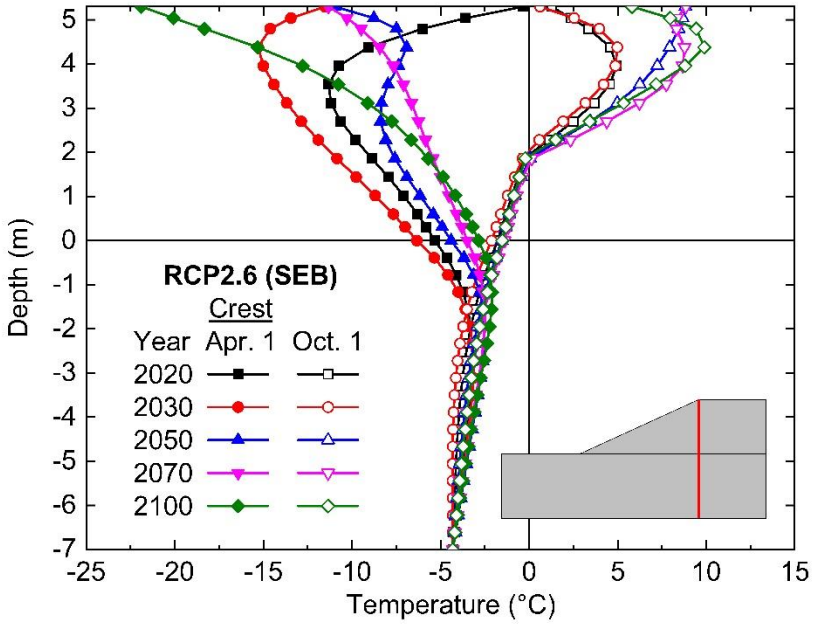

(a)

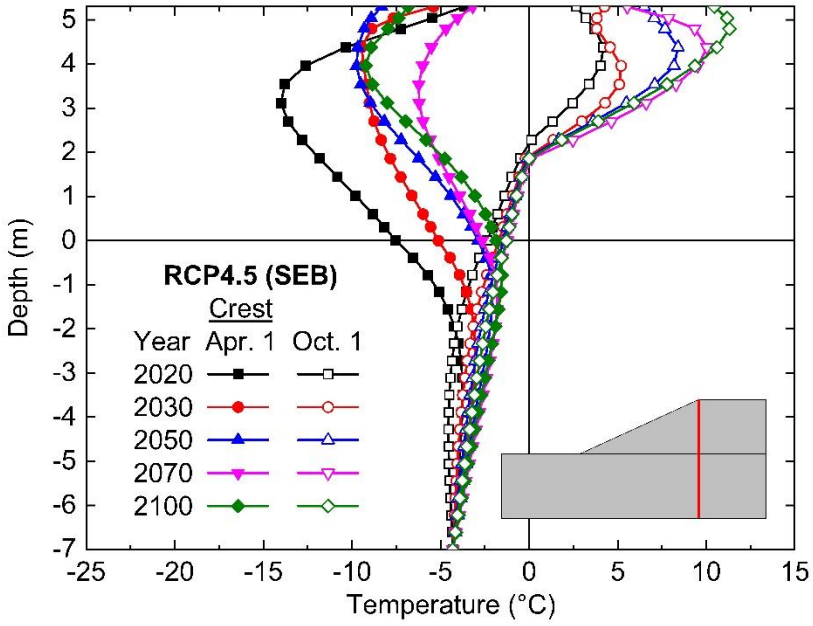

(b)

Fig. 5.10 (continued)

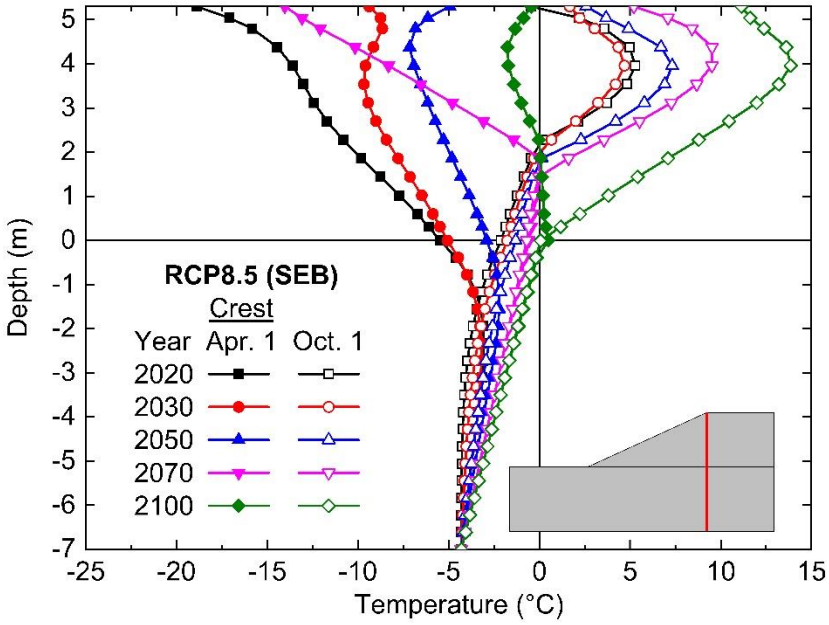

(c)

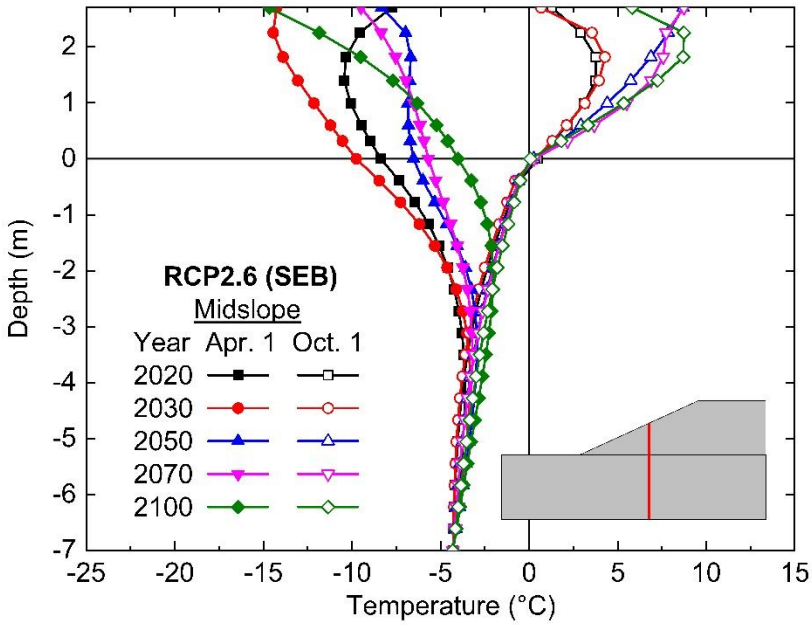

(d)

Fig. 5.10 (continued)

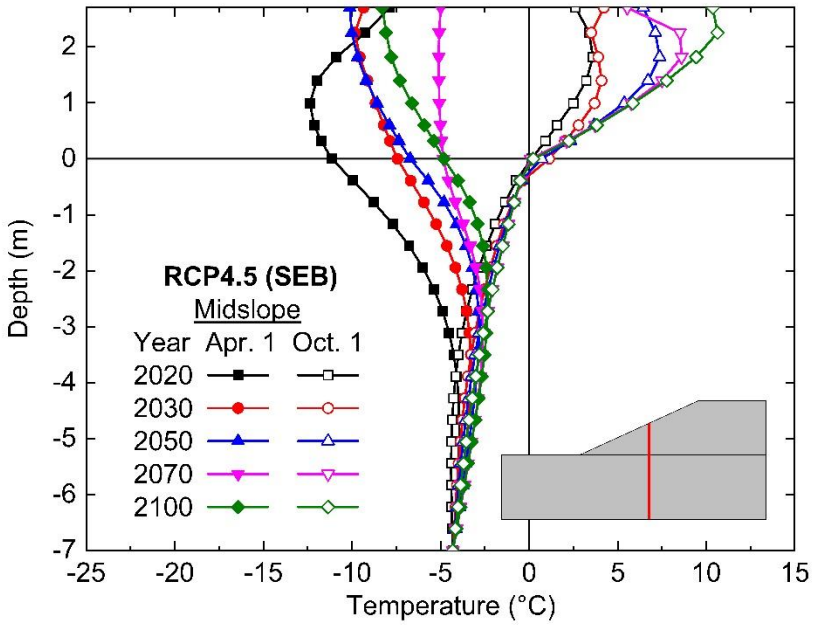

(e)

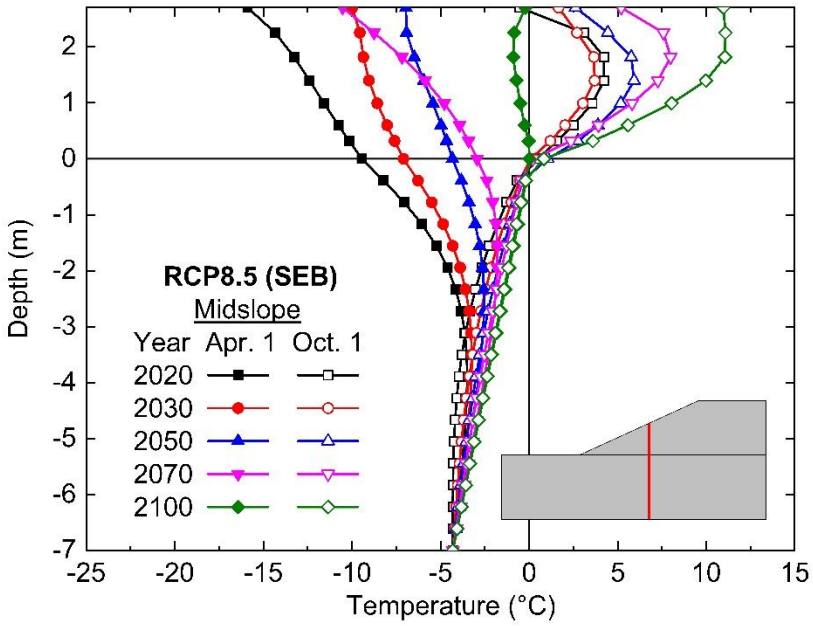

(f)

Fig. 5.10 (continued)

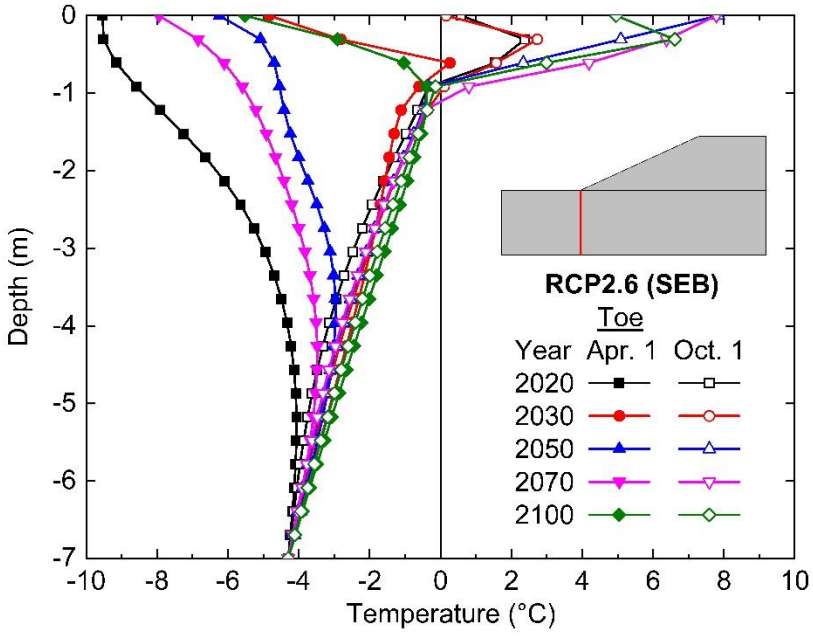

(g)

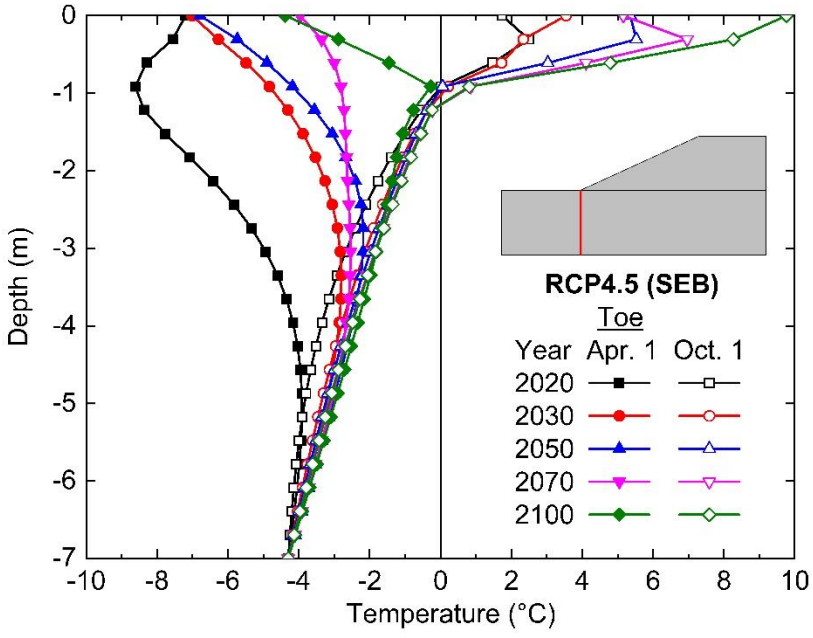

(h)

Fig. 5.10 (continued)

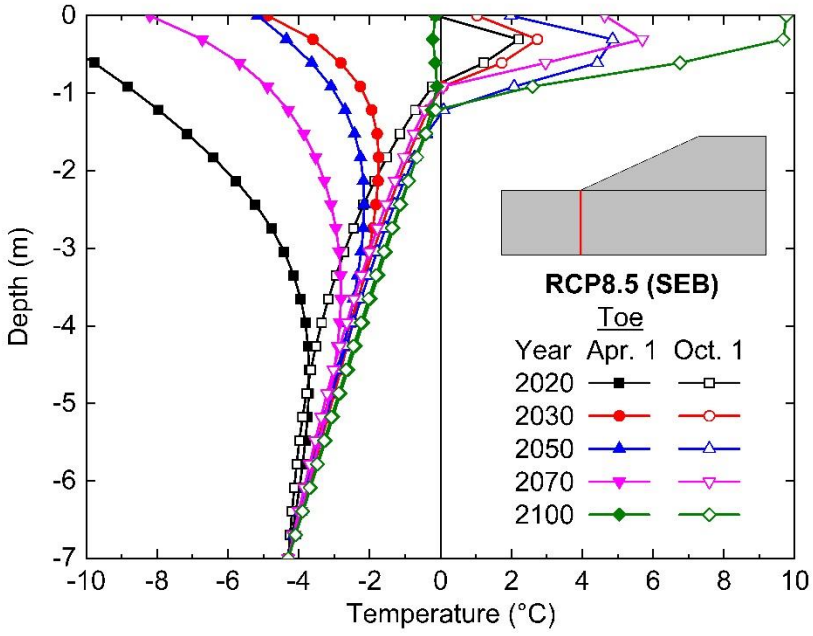

(i)

Fig. 5.11. Temperature contours at the crest for RCP 8.5 from 2080 to 2090: (a) air temperature, (b) TM approach, and (c) SEB approach. Each year on the x-axis starts on January 1.

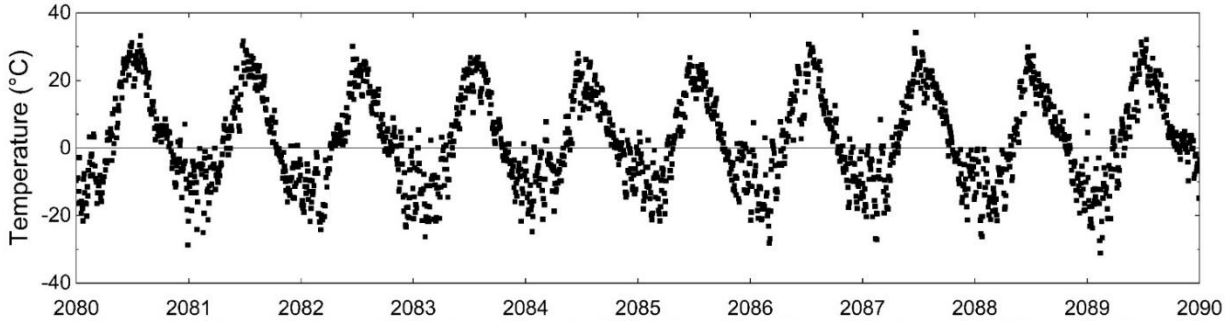

(a)

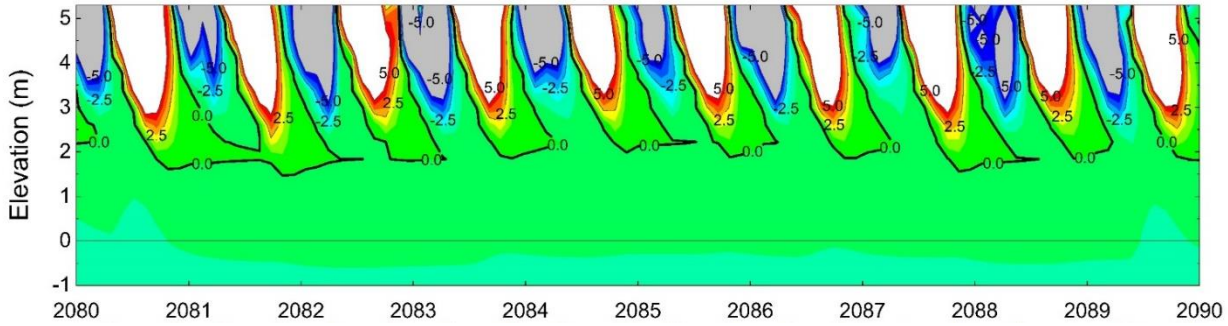

(b)

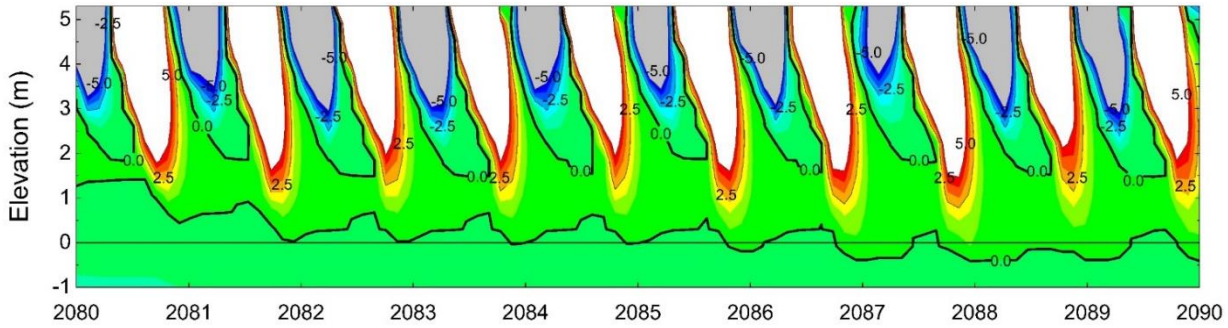

(c)

Fig. 5.12. Temperature contours at the crest for RCP 8.5 from 2090 to 2100: (a) air temperature, (b) TM approach, and (c) SEB approach. Each year on the x-axis starts on January 1.

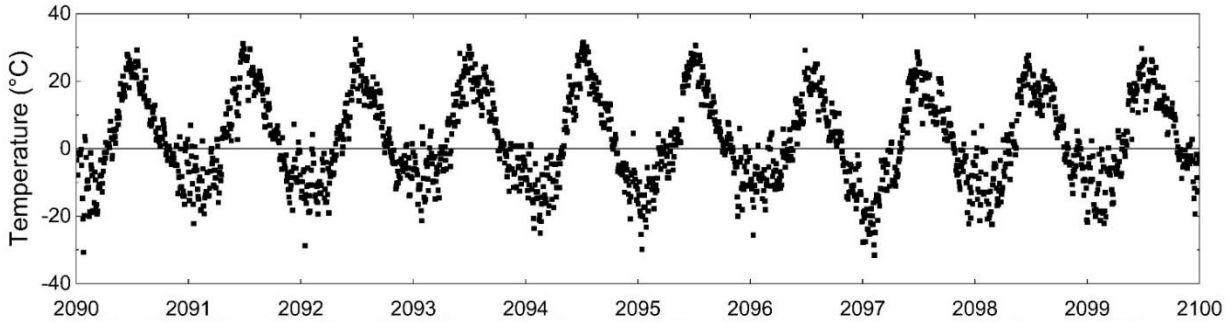

(a)

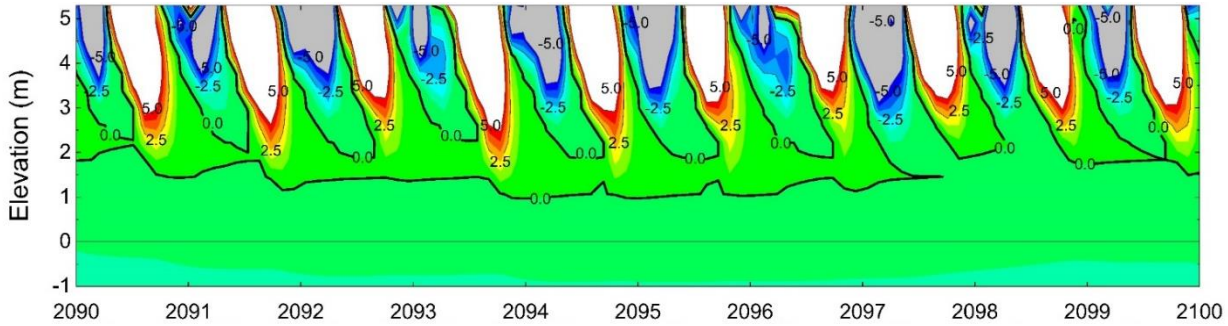

(b)

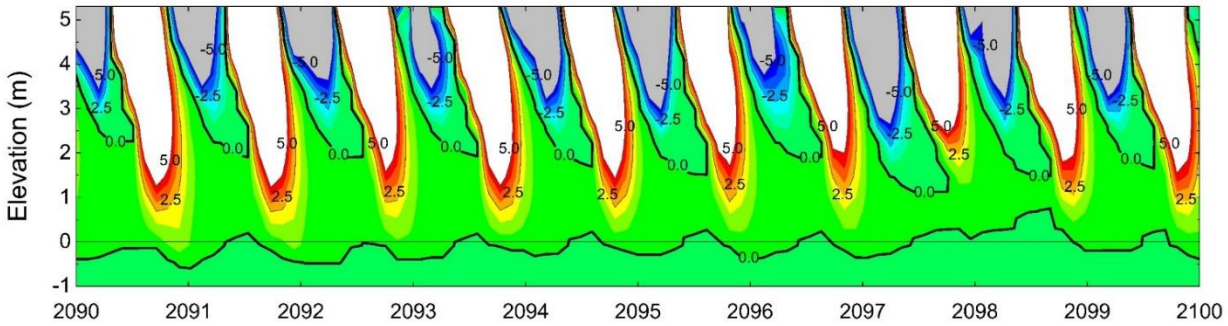

(c)

Fig. 5.13. Taliks observed in the model during the winter season (January) in (a) 2070 and (b) 2100 using SEB approach under RCP 8.5.

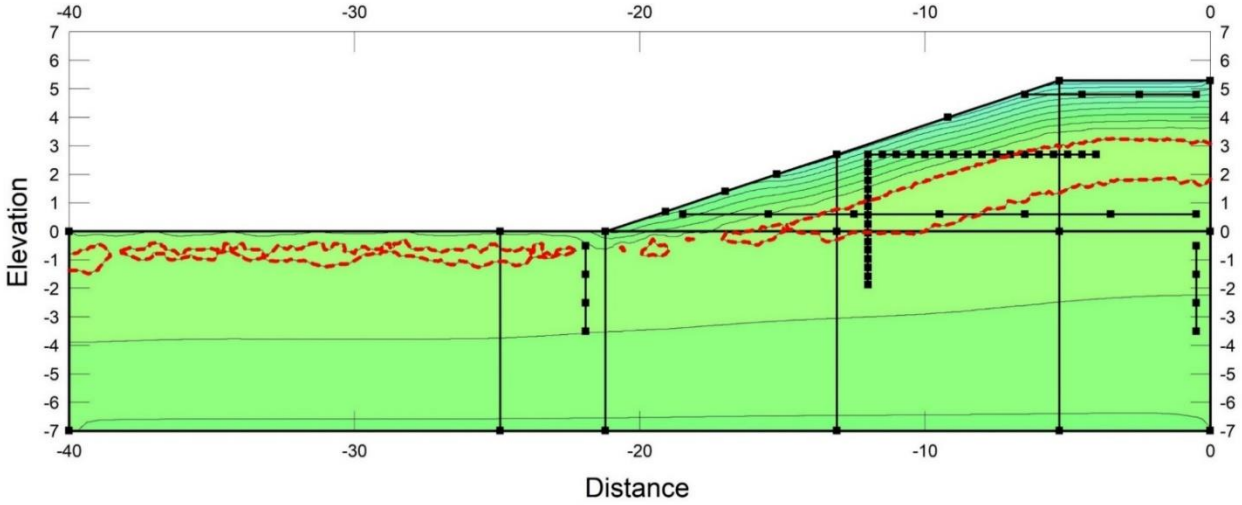

(a)

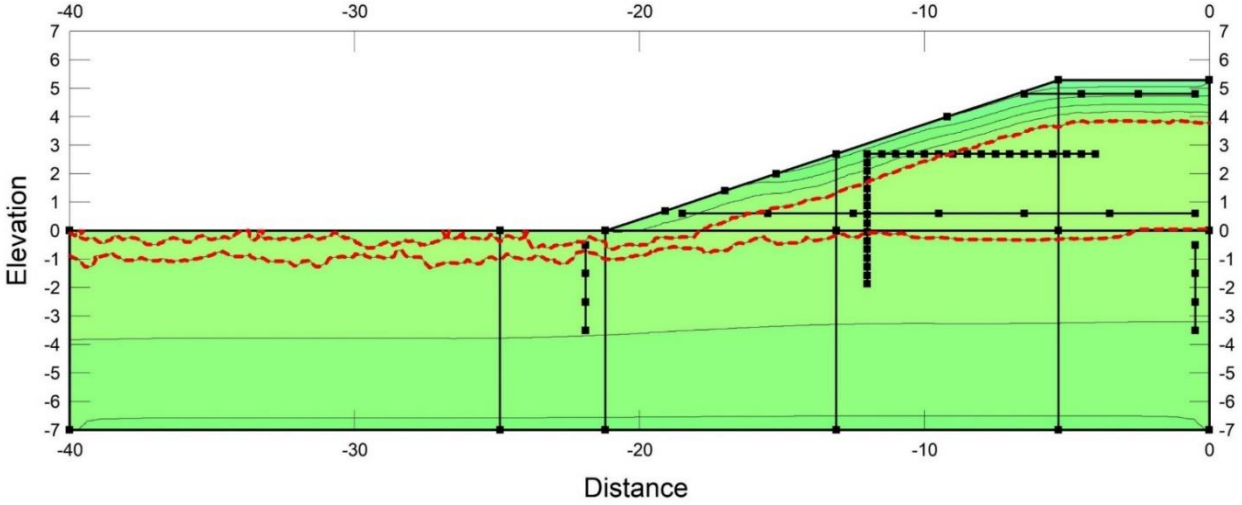

(b)

Fig. 5.14. Observation nodes for different embankment configurations. H is the height of the embankment varied at 2 m, 4 m, and 6 m. S is the horizontal run for a 1 m rise on the vertical varied at 2 m, 3 m, and 4 m.

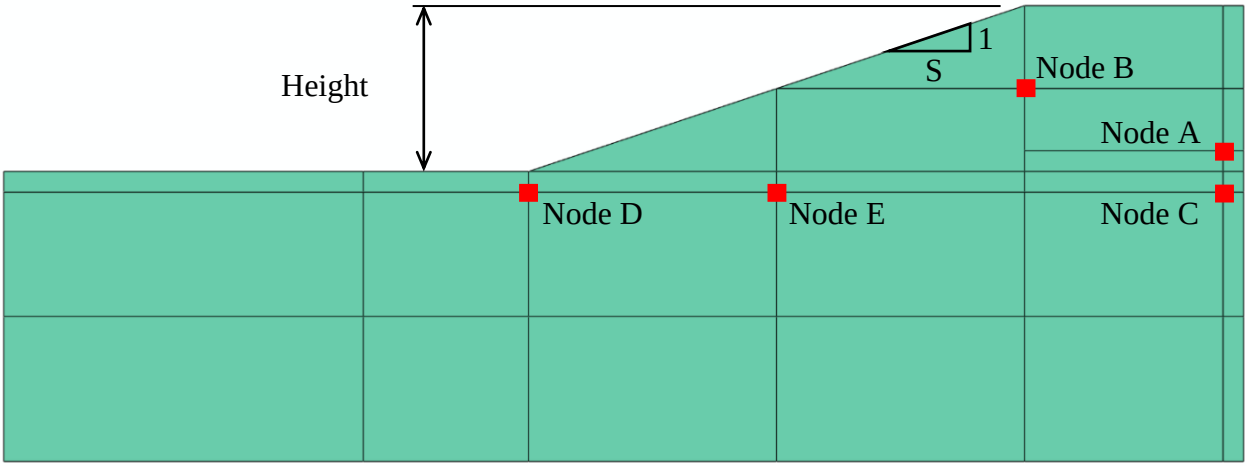

Fig. 5.15. Comparison of nodal temperatures at the (a) top, (b) base, (c) centerline, and (d) toe between field monitored values, TEMP/W, and ABAQUS.

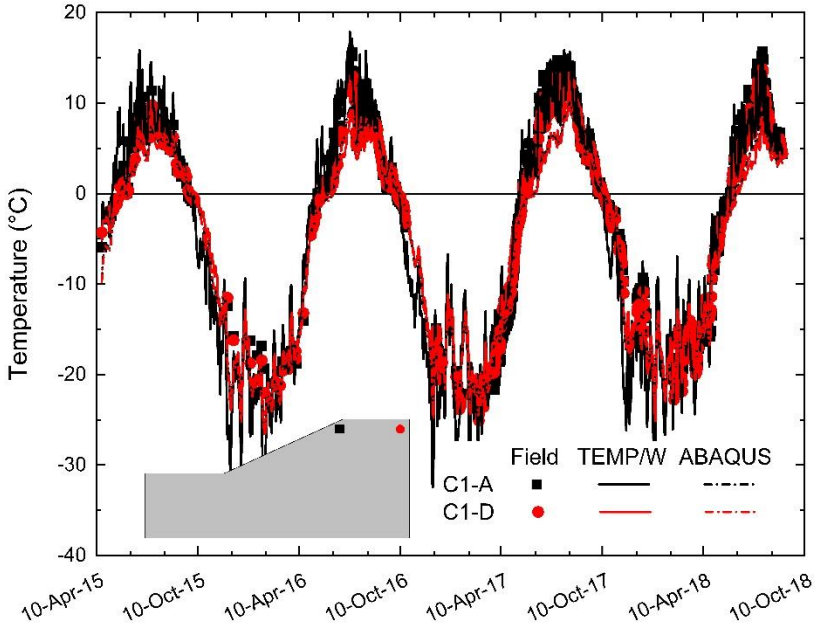

(a)

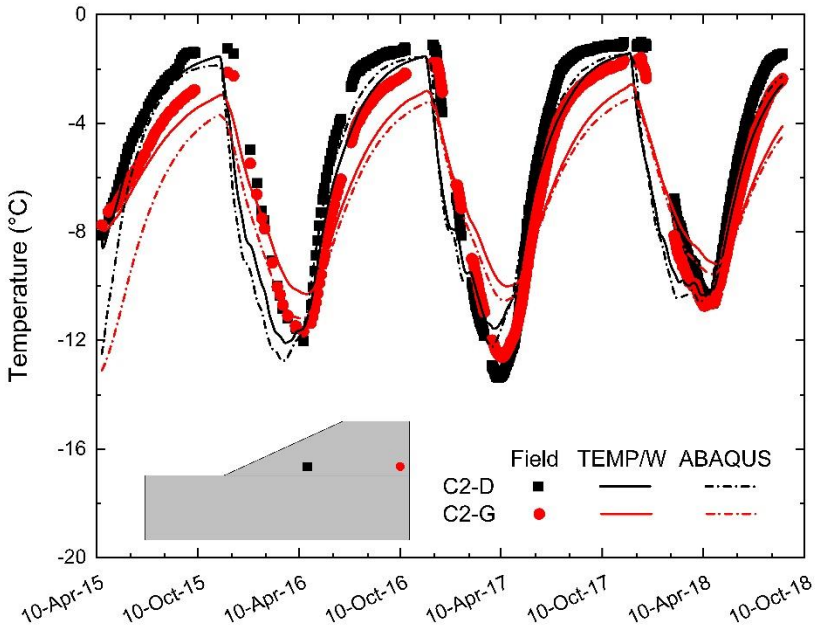

(b)

Fig. 5.15 (continued)

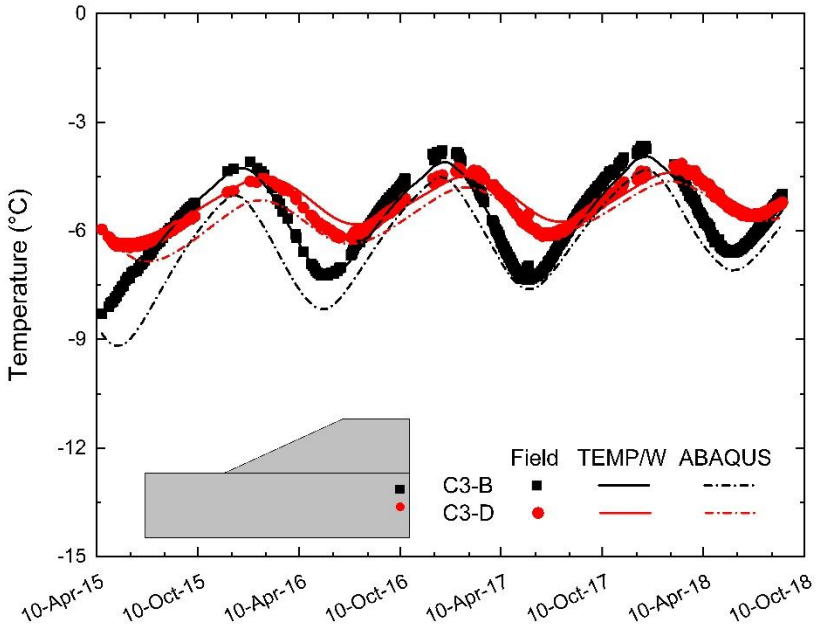

(c)

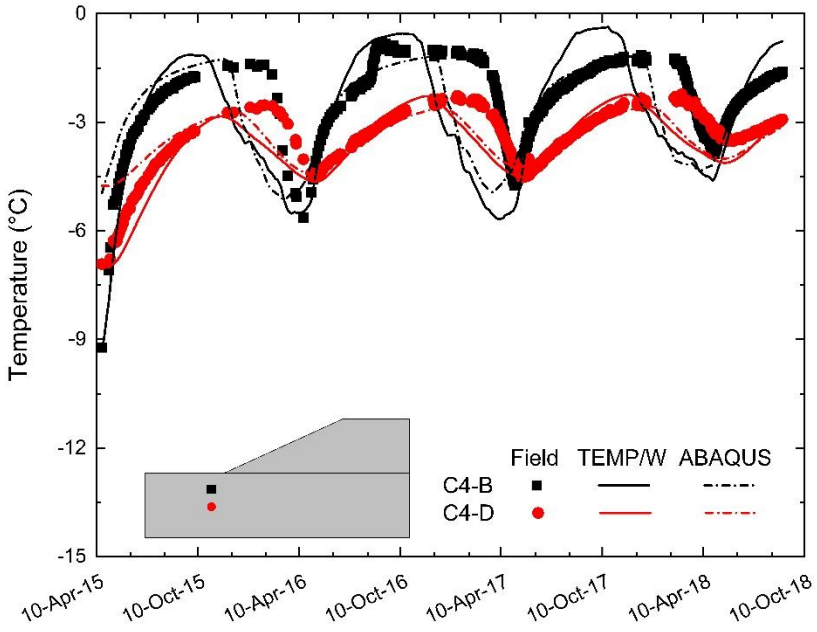

(d)

Fig. 5.16. Comparison of nodal temperatures at the (a) top and (b) base using -3yrAct and -3yrAve.

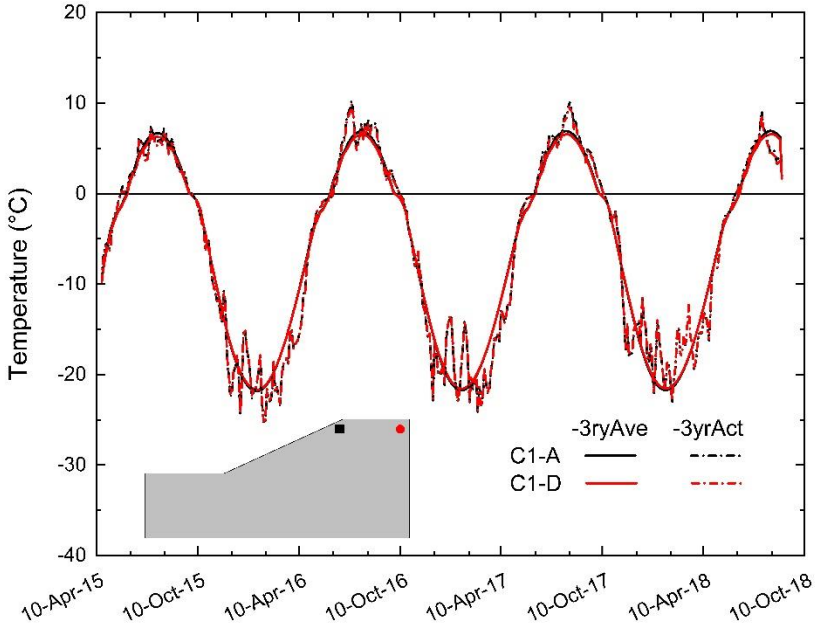

(a)

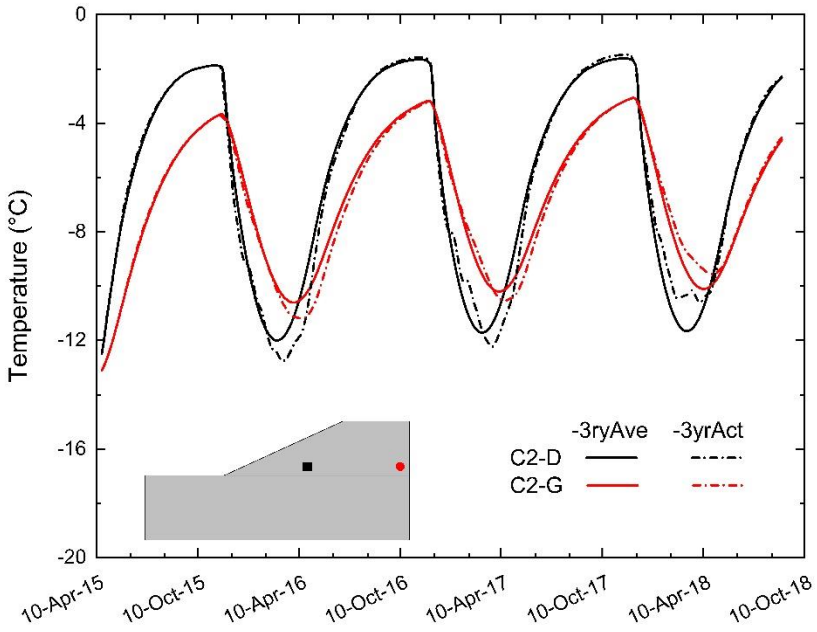

(b)

Fig. 5.17. Comparison of temperatures for different embankment configurations at observation nodes under three-year temperature conditions: (a) Node A, (b) Node B, (c) Node C, (d) Node D, and (e) Node E.

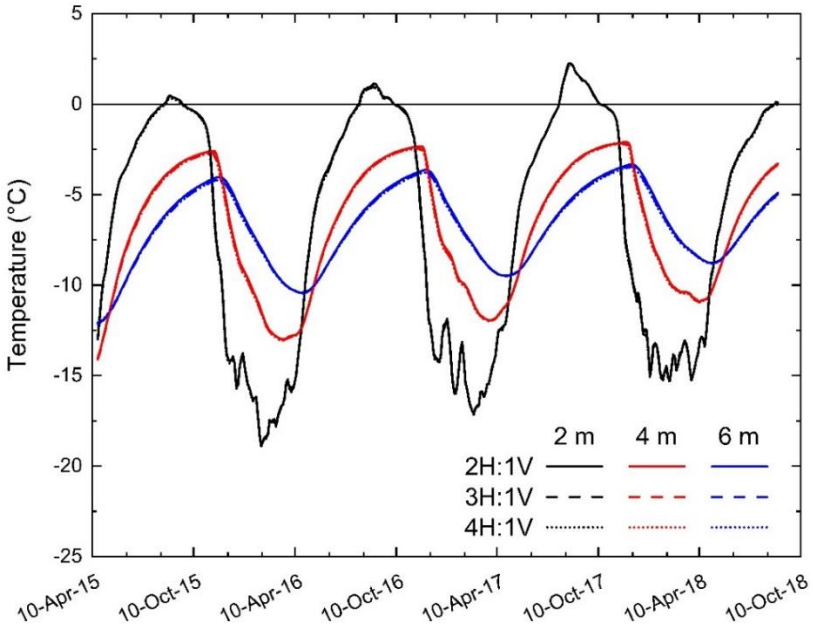

(a)

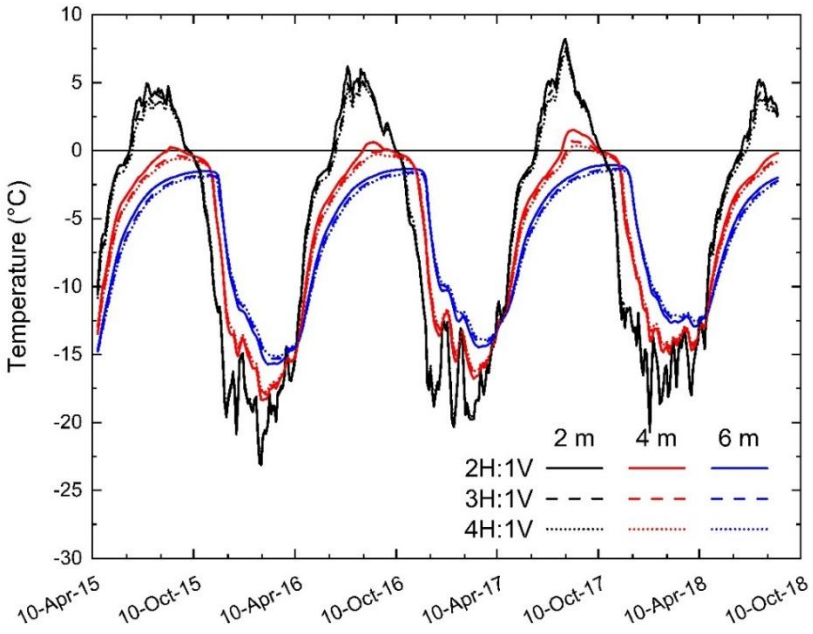

(b)

Fig. 5.17 (continued)

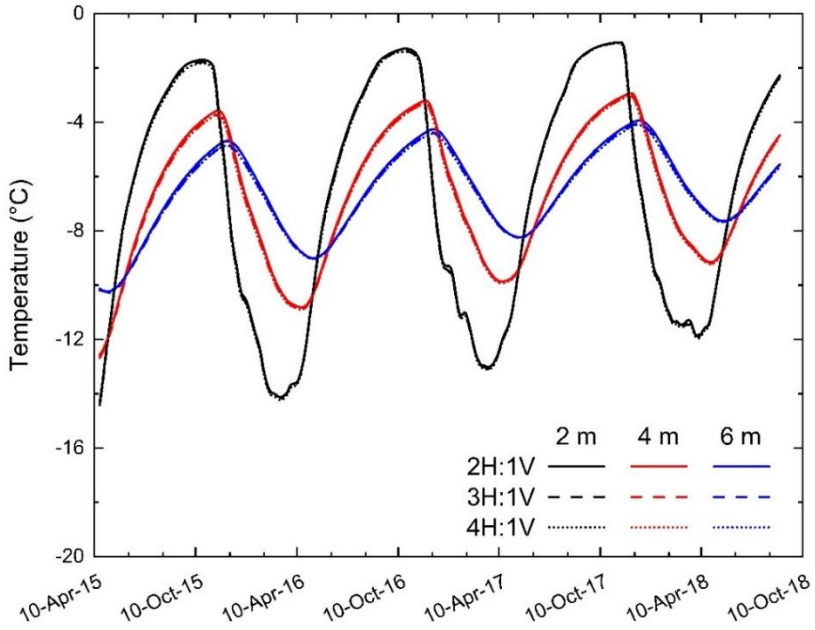

(c)

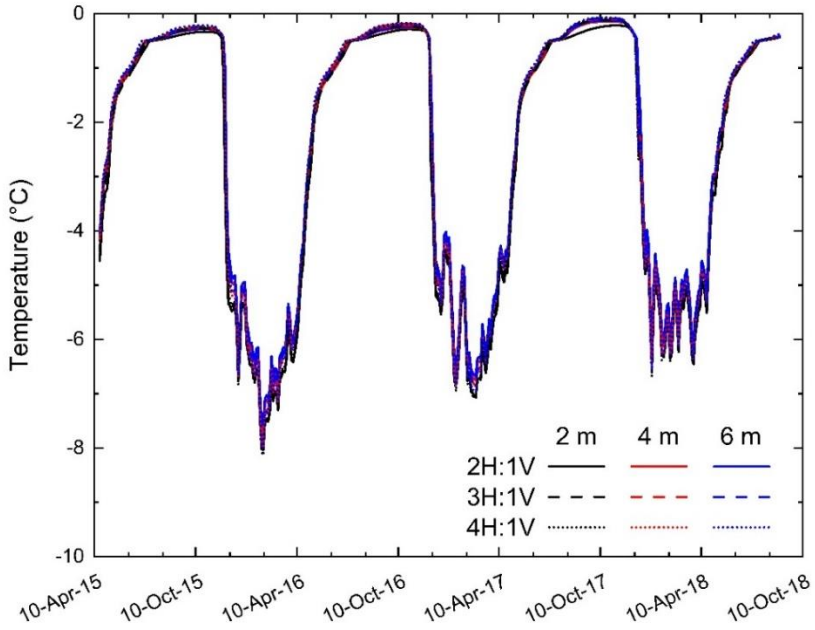

(d)

Fig. 5.17 (continued)

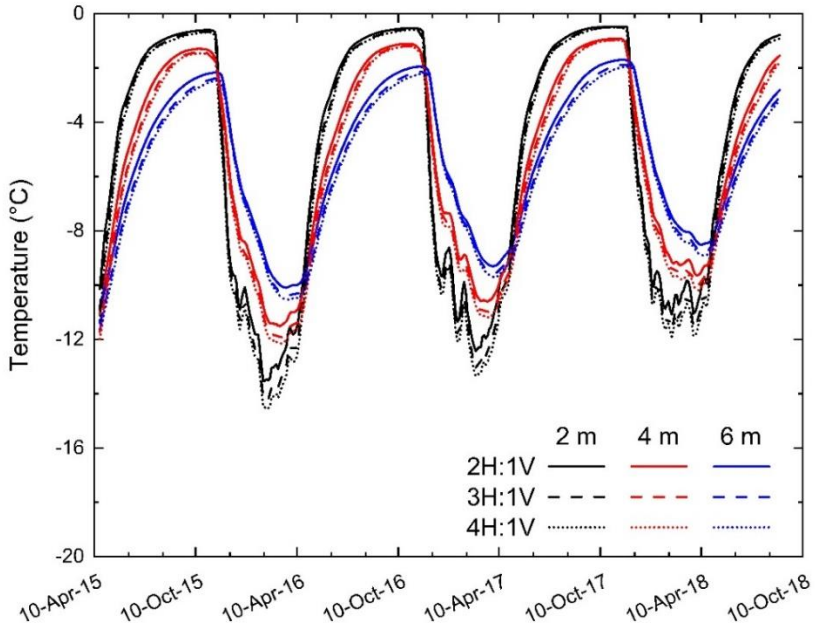

(e)

Fig. 5.18. Near-term temperature conditions for three different embankment heights at Node A: (a) d2005i1, (b) d2005i2, and (c) d2015.

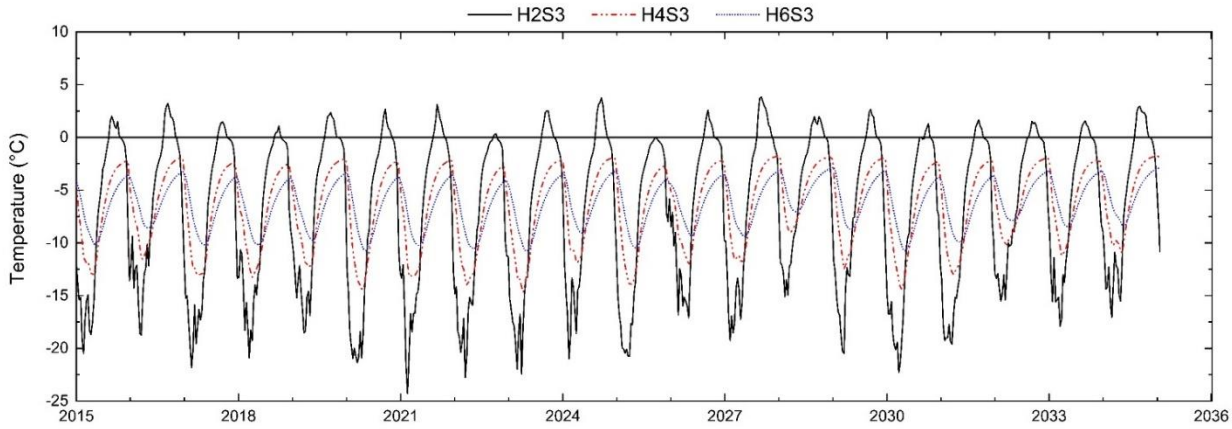

(a)

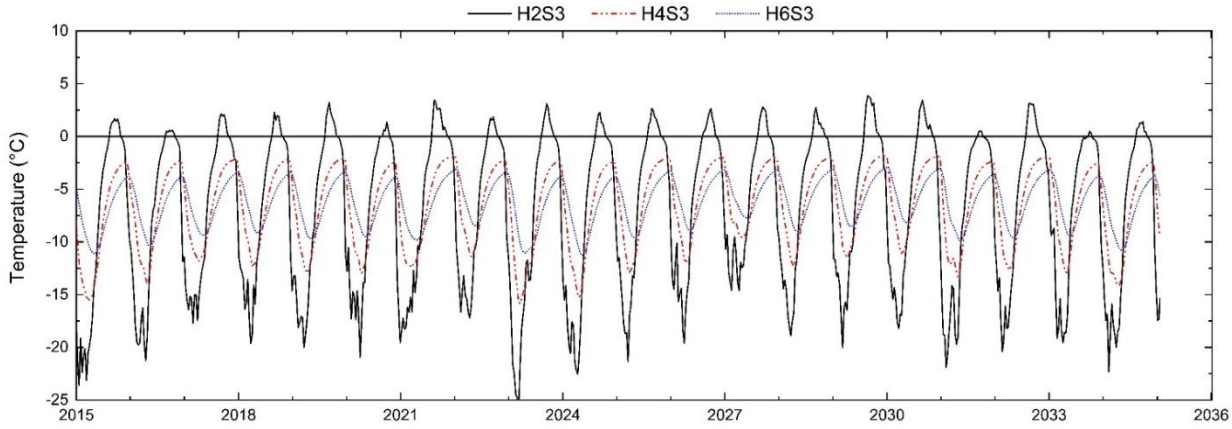

(b)

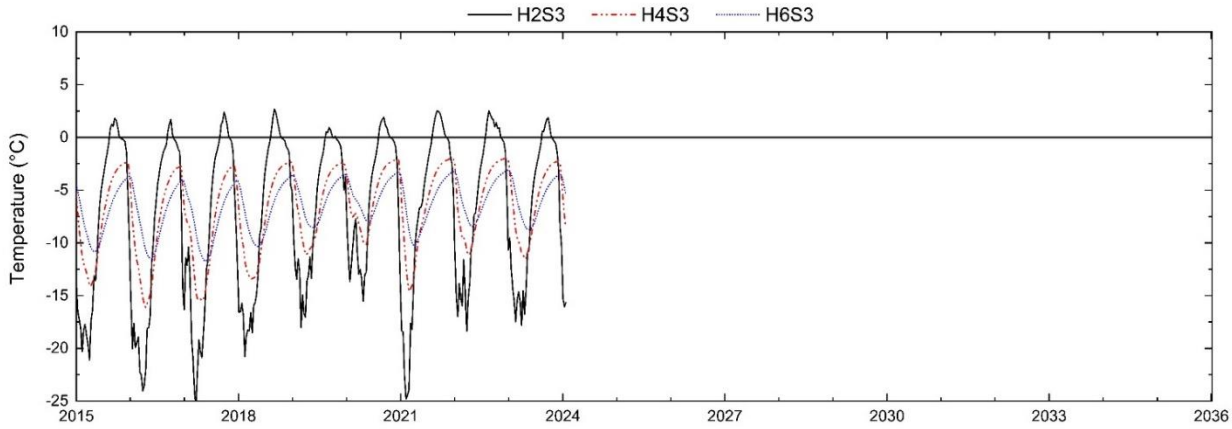

(c)

Fig. 5.19. Long-term temperature conditions for three different embankment heights at Node A: (a) RCP 2.6, (b) RCP 4.5, and (c) RCP 8.5.

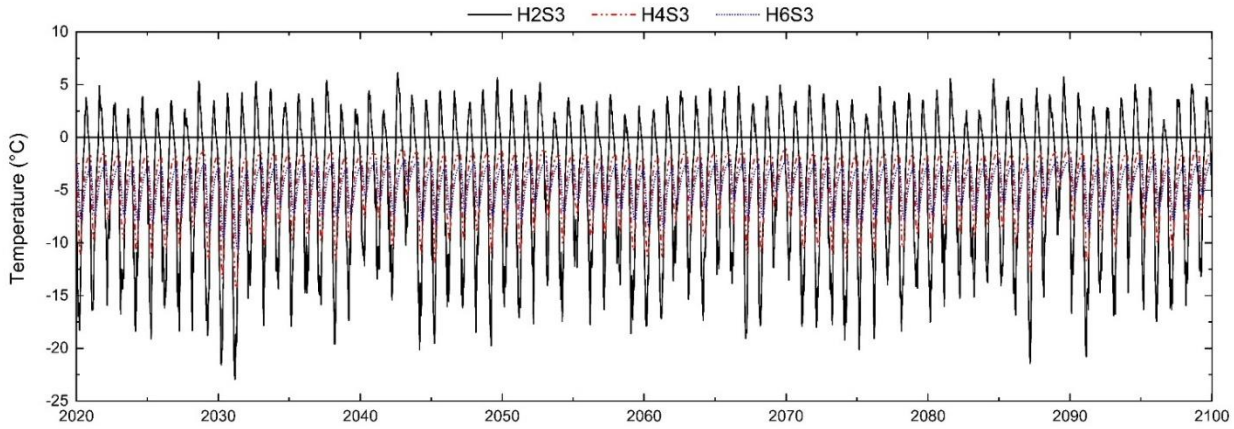

(a)

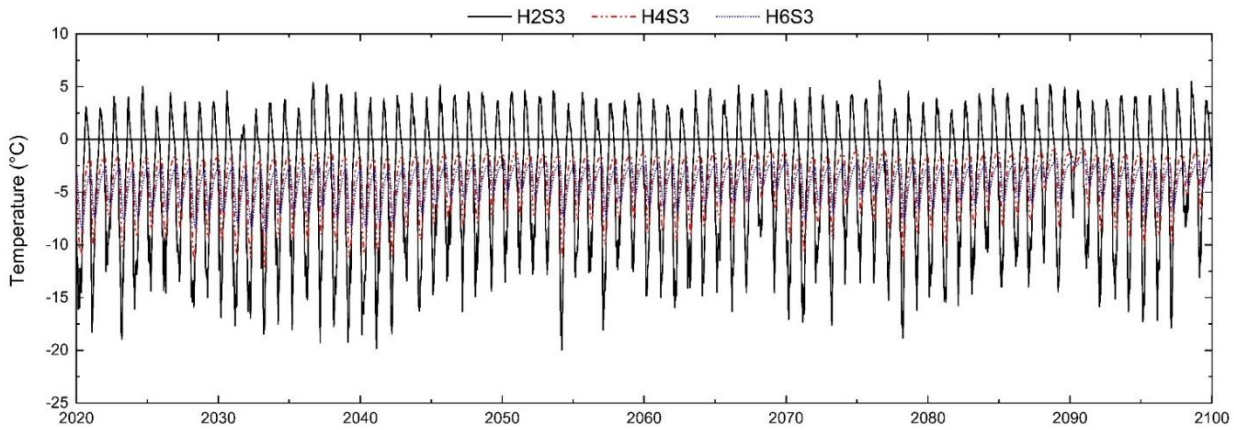

(b)

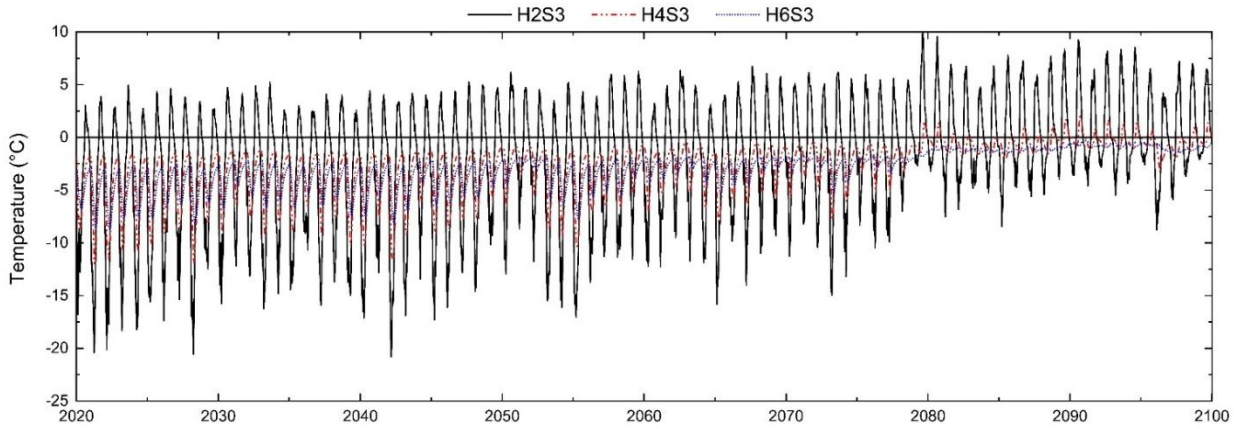

(c)

Fig. 5.20. Zero-degree isotherm during winter (January) of 2070 (a, c, e) and 2100 (b, d, f) for 2 m embankment with different slope configurations under RCP 8.5 conditions.

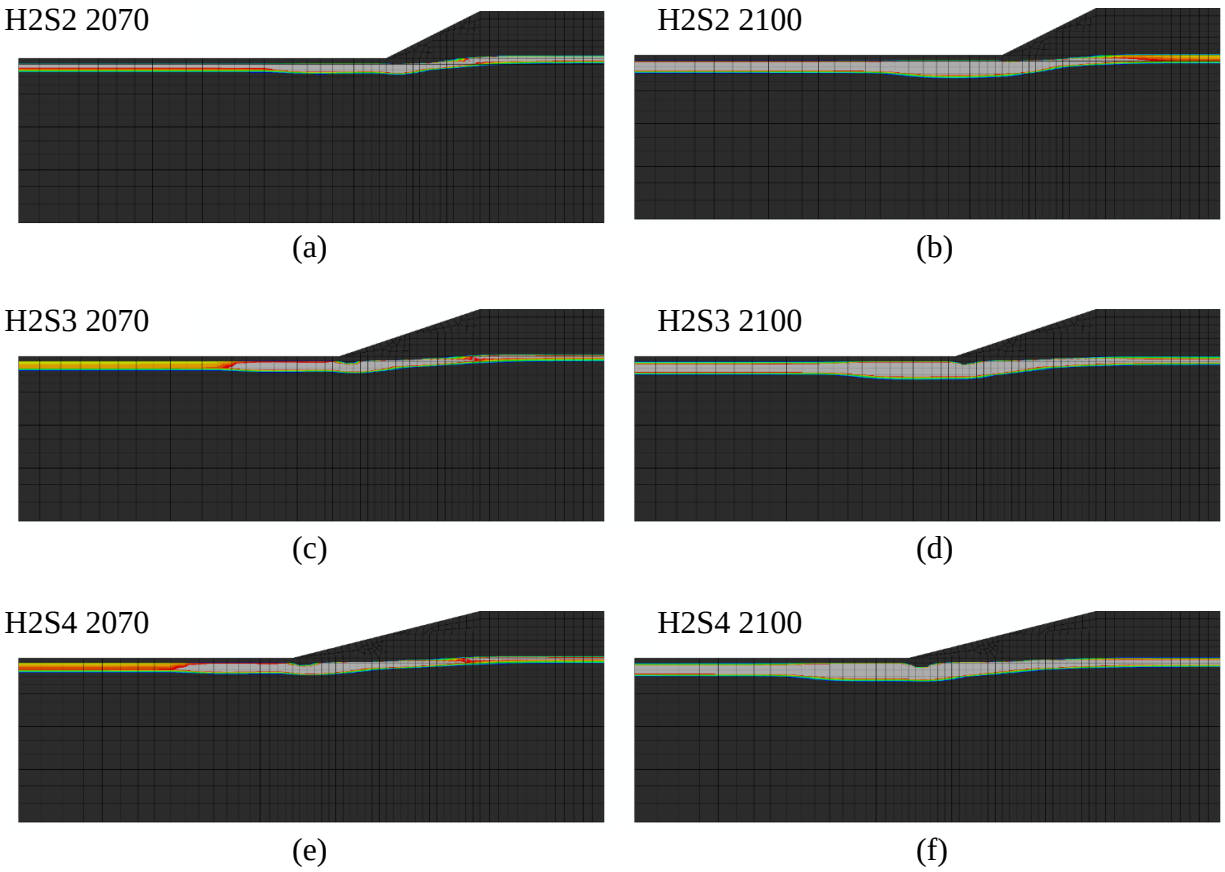

Fig. 5.21. Zero-degree isotherm during winter (January) of 2070 (a, c, e) and 2100 (b, d, f) for 4 m embankment with different slope configurations under RCP 8.5 conditions.

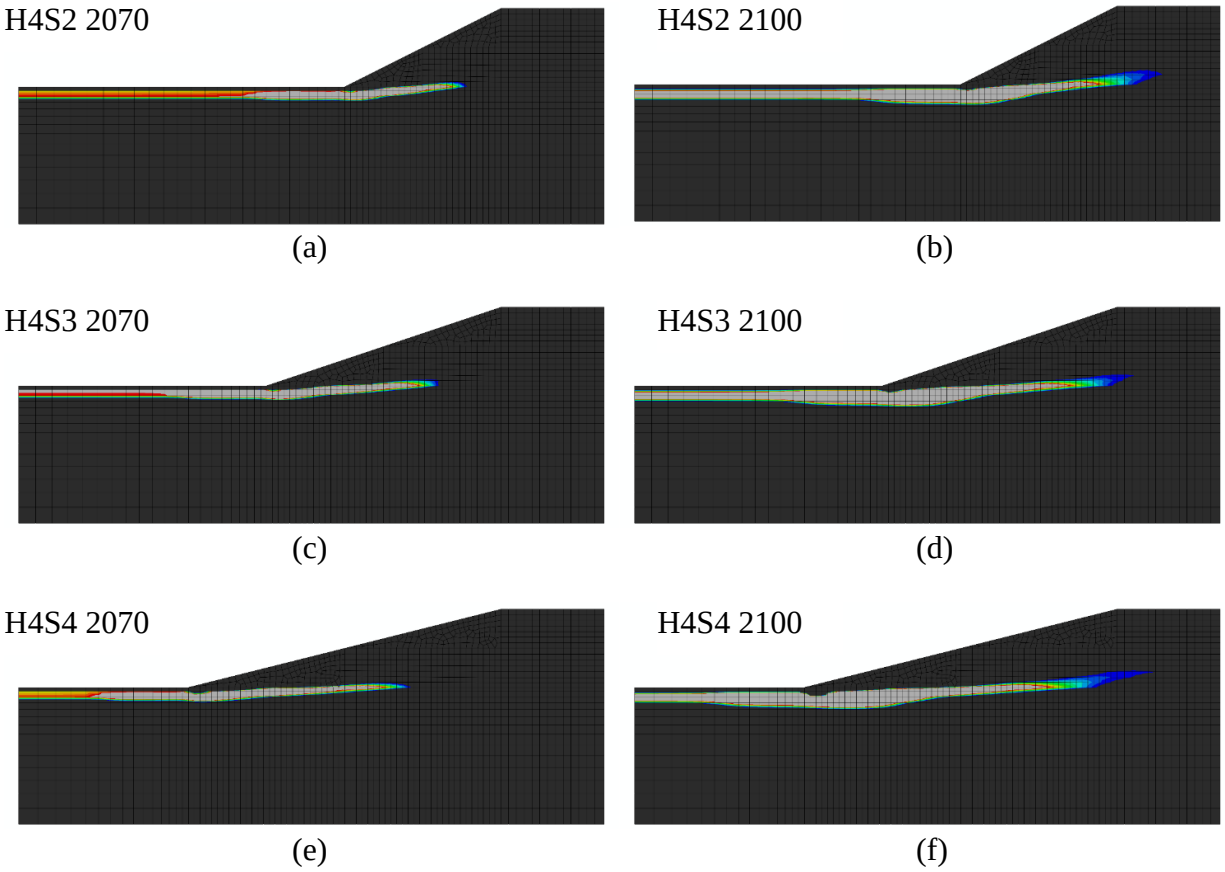

Fig. 5.22. Zero-degree isotherm during winter (January) of 2070 (a, c, e) and 2100 (b, d, f) for 6 m embankment with different slope configurations under RCP 8.5 conditions.

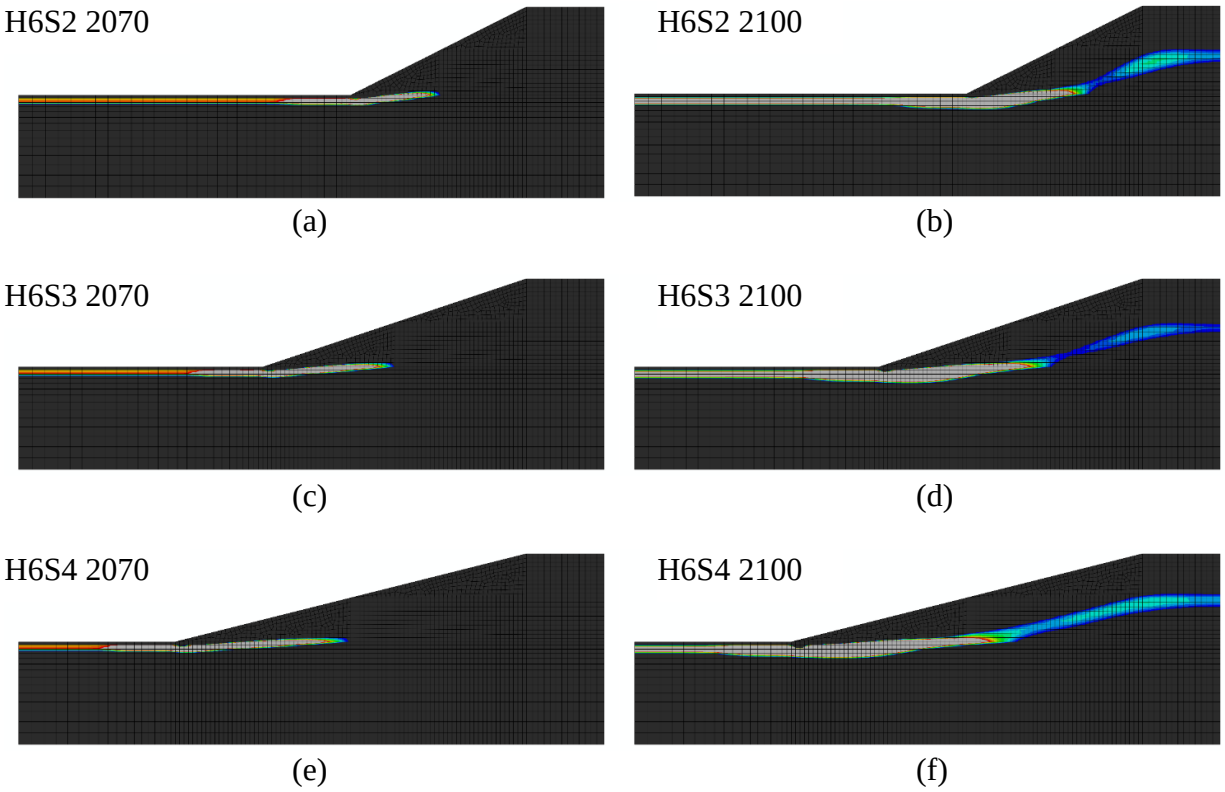

List of Notations and Acronyms in this Chapter

-3yrAct	Three-year actual air temperatures
-3yrAve	Three-year average sinusoidal air temperatures
CanCM4	Fourth Generation Coupled Global Climate Model
CanESM2	Second Generation Earth System Model
CCCma	Canadian Centre for Climate Modelling and Analysis
CGCM	Coupled General Circulation Model
CM	Climate Model
CMIP5	Coupled Model Intercomparison Project Phase 5
c_{vf}	Frozen volumetric heat capacity (kJ/m^3·°C)
c_{vu}	Unfrozen volumetric heat capacity (kJ/m^3·°C)
c_{vw}	Volumetric heat capacity of water (MJ/m^3·°C)
ESM	Earth System Model
h	heat transfer coefficient at 2 m
IPCC	Intergovernmental Panel on Climate Change
k_{frozen}	Frozen thermal conductivity (kJ/days·m·°C)
k_{snow}	Snow thermal conductivity
$k_{unfrozen}$	Unfrozen thermal conductivity (kJ/days·m·°C)
$n_{freezing}$	Freezing n-factor
$n_{thawing}$	Thawing n-factor
q_g	Ground heat flux
q_{lat}	Latent heat flux
q_{nl}	Net terrestrial (longwave) radiation
q_{ns}	Net solar (shortwave) radiation
q_s	Downwelling shortwave radiation
q_{sens}	Sensible heat flux
q_{snow}	Snow heat flux
RCP	Representation Concentration Path
SEB	Surface energy balance approach
T_a	Air temperature
T_g	Absolute temperature of the ground surface
TM	Thermal modifier approach
T_{snow}	Temperature of snow at the ground surface
VWC	Volumetric water content (m^3/m^3)
w	Water content (%)
w_u	Unfrozen water content (%)
α	Albedo

ε_a	Air emissivity
ε_s	Surface emissivity
ρ_d	Dry density (kg/m^3)
ρ_w	Water density (kg/m^3)
σ	Stefan-Boltzmann constant

CHAPTER 6

NUMERICAL MODELLING: MECHANICAL PERFORMANCE[1,2]

6.1. Introduction

Chapter 2 presented the monitored thermal and mechanical performance of the embankment test sections interpreted from the recorded instrumentation data. In Chapter 3, shear strength and stiffness properties of the fill material were obtained from a series of large-scale direct shear tests subjected to different environmental conditions (frozen, thawed, and cyclic freeze-thaw). Similarly, the interface strength properties between soil and the woven geotextiles (wicking/non-wicking) were determined from pullout tests under different moisture and compaction conditions in Chapter 4. Chapter 5 showed the thermal numerical modelling conducted on the control (unreinforced) section from April 2015 to August 2018, as well as numerical simulations under near-term and long-term climate change conditions. The thermal numerical models, which were conducted under pure heat transfer conditions, do not take into account the deformation occurring in the embankments as the soil undergoes freezing and thawing in response to the seasonal temperature cycles. In this chapter, coupled-thermal numerical models were developed in ABAQUS using the material property inputs from Chapter 3 and Chapter 4 and were calibrated against the recorded data from Chapter 2. Once calibrated, parametric models considering the

[1] This chapter is being prepared for the following submissions in peer-reviewed journals:
De Guzman, E.M.B., Alfaro, M.C., Doré, G., and Arenson, L.U. 2020. Performance Monitoring and Numerical Simulation of Embankments in Cold Regions Environment. Géotechnique.

De Guzman, E.M.B., Alfaro, M.C., Arenson, L.U., and Doré, G. 2020. Reinforced Embankments in the Arctic: Field Observations and Numerical Simulations. Geosynthetics International.

De Guzman, E.M.B., Alfaro, M.C., Arenson, L.U., and Doré, G. 2020. Parametric Study on Embankment Slopes In Cold Regions Environment With and Without Reinforcement. ASCE International Journal of Geomechanics.

[2] A list of notations and acronyms used in this chapter are found in page 318.

influence of embankment height and slope inclination for unreinforced embankments, and in addition the effect of reinforcement length and vertical spacing for reinforced embankments, were investigated. Climate change and forced warming boundary conditions were also used to investigate their influences on the displacements occurring in these embankments.

6.2. Coupled Thermal-Mechanical Modelling

6.2.1. Material Properties

6.2.1.1. Soil Properties

The thermal properties for the embankment fill and foundation soil from Table 5.1 are summarized again in Table 6.1 consistent with the terminologies and units used in ABAQUS. Determination of these properties were presented in Section 5.3.1. Equations proposed by Farouki (1981) were used to determine the unfrozen and frozen thermal conductivities of the embankment fill material. The frozen and unfrozen thermal conductivities for the peat were obtained by De Guzman and Alfaro (2018) using a thermal probe for peat in Northern Manitoba which was assumed to have similar properties with those in test sections along ITH. Mechanical and hydraulic properties for the embankment fill and foundation soil are summarized in Table 6.2. The shear strength of the fill material was obtained from De Guzman et al. (2018)[3] from large-scale direct shear tests subjected to different environmental conditions (frozen, thawed, cyclic freeze-thaw). The shear strength properties obtained by De Guzman and Alfaro (2018) for amorphous peat above 0°C were used for the foundation soil. The Modified Drucker-Prager/Cap plasticity model was selected to define the inelastic behaviour of the fill material and foundation soil as it has been widely used in geotechnical engineering and considers the effect of stress history, dilatancy, and the effect of

[3] Chapter 3 of this manuscript.

intermediate principal stresses (Helwany 2007). The following equations were used to convert the material properties applicable to plane strain problems for this plasticity model in ABAQUS:

$$\tan\beta = \sqrt{3}\sin\theta \Big/ \sqrt{1+(\sin^2\theta/3)} \qquad \text{Eq. 6.1}$$

$$d = \sqrt{3}c\cos\theta \Big/ \sqrt{1+(\sin^2\theta/3)} \qquad \text{Eq. 6.2}$$

where θ is friction angle of the soil in degrees, c is the cohesion in kPa, and β and d are the angle of friction and material cohesion, respectively, for this plasticity model.

The frozen deformation properties (λ and κ, which are the compression and recompression indices, respectively) were obtained from triaxial consolidation tests conducted at Université Laval on reconstituted frozen soil samples. There are negligible deformations occurring when the soil is at its frozen state. The thawed deformation properties of the fill material were determined from several modelling iterations to obtain a best fit with the field results. The thawed deformation properties of the foundation soil were obtained from De Guzman and Alfaro (2018). However, frozen deformation properties were unavailable in their research. It was therefore assumed that the frozen properties have the same values as the frozen fill material where no significant displacements are expected when the soil is frozen. These deformations properties are needed to define the plastic volumetric strain hardening curve of both materials determined from the following equation:

$$\varepsilon_{vol}^{pl} = [(\lambda - \kappa)/(1 + e_o)] \times \ln p'/p_b' \qquad \text{Eq. 6.3}$$

where ε_{vol}^{pl} is the plastic volumetric strain, e_o is the initial void ratio, p_b' is the hydrostatic compression yield stress, and p' is the mean effective stress. The parameter p_b' is the defining

position of the cap in the plasticity model where the initial ε_{vol}^{pl} is zero, while p' is any mean effective stress to define the hardening curve. The parameter $p_b^{'}$ was assumed to be 75000 Pa with an incremental increase in p' of 10000 Pa until 305000 Pa. It was assumed that the hydraulic conductivities of the fill material and foundation soil are very low under frozen conditions. The hydraulic conductivities in unfrozen condition were estimated from typical values available in the literature supported by several modelling iterations to obtain a best fit with the field results and were made dependent on void ratios once the temperatures reach 0°C.

6.2.1.2. Geotextile Properties

The interface strength properties between the wicking geotextile and the soil used in the reinforced embankment models are summarized in Table 6.3 based on the results obtained from Chapter 4. The interface friction angle between the soil and the geotextile were translated as contact properties in ABAQUS. A high interface friction angle was assumed when the temperature field in the embankment was below 0°C to simulate the behaviour that no sliding is occurring during the winter months as very small horizontal displacements were observed from the vertical SAA (SAA-RV). The wicking geotextile was idealized as a structural membrane element with a thickness of 3 mm. The small apparent cohesion recorded from the pullout tests were ignored since the basic friction model available in ABAQUS simulating the contact properties does not have the capability to incorporate this in the simulation. Ignoring the apparent cohesion results in a conservative estimate of the displacements. As presented in Chapter 4, a non-wicking geotextile with relatively the same tensile strength at 2% and the same surface properties under dry conditions were tested under similar moisture and compaction conditions and its properties are also summarized in Table 6.3. These non-wicking geotextiles were implemented in the same reinforced embankment model to understand the benefit of the wicking function on woven geotextiles when

used as slope reinforcement. In addition to the interface friction, a thermal conductance property was added at the top and bottom of the geotextile layers to ensure thermal flow between the soil layers above and below these geotextiles. The geotextiles were assumed to have the same thermal conductivity as the embankment fill. The similarity in recorded temperature values between the control section and reinforced section (Appendix A) presented in Chapter 2 supports this assumption.

6.2.2. Embankment Geometry and Boundary Conditions

The cross-sections of solid and staged models in ABAQUS are shown in Fig. 6.1 and Fig. 6.2, respectively. The solid section was made of one solid part and was subdivided to two sections: (a) embankment fill and (b) foundation soil. The staged section was made of several independent parts and were assembled to represent the reinforced section. For the staged section, the embankment fill has five parts of the same material properties to simulate each fill layer, with four layers of geotextiles sandwiched in between these parts near the slope, and the foundation soil as one whole part. The geotextile reinforcements are shown in red in Fig. 6.2. Both solid and staged cross-sections were also cut at multiple locations where nodal results will be saved for comparison with field data. Tie constraints were used on soil to soil surfaces in the staged section, while contact properties were used at the top and base of the geotextile surfaces to simulate the reinforcement sliding. Tie constraints ‘tie’ two surfaces together as if they were part of a whole even with different meshing configurations and thus adds complexity in solution convergence, while contact properties allow the user to input the tangential, normal, and thermal behavior (e.g. thermal conductance) between the interface of two separate and different materials. The main advantage of modelling using solid sections is that it eliminates the need of using tie constraints; however, the presence of the geotextile layers in the model required approaching the simulation using tie

constraints and contact properties. Both solid and staged models have a thickness of 3 m in the y-direction. The global datum (0, 0, 0) is established at the interface of the embankment fill and foundation soil. Only half of the embankment was modelled due to assumed symmetry.

For the stress-deformation part of analysis, the left-vertical and right-vertical sections of the model were restrained in the x- and y- directions. The base of the model was restrained in all directions, while the x-z plane was restrained in the y-direction. A zero pore pressure boundary condition was also assigned at the natural ground surface, slope faces, and top of the embankment to allow seepage across these surfaces. The geotextile layers in Fig. 6.2 were also restrained in the y-direction. For the heat transfer part of the analysis in both cross-sections, the surfaces of the embankment fill and foundation soil interacting with the ambient air temperature were subdivided accordingly. The road surface is labelled as *Top*, while the slope is divided into three regions because of the different snow depths that can accumulate in these regions. The surface on the foundation soil immediately at the base of the embankment is labelled as *Toe*, and outside this the foundation surface is labelled as *Prairie*. The rightmost and leftmost boundaries are no flow boundaries, while a constant temperature of -4.3°C was applied at the base of the foundation soil based on temperature readings nearby the research site. The corresponding freezing ($n_{freezing}$) and thawing ($n_{thawing}$) n-factors were applied to these boundary conditions at the ground surface.

As discussed in Chapter 5, the thermal modifier (TM) approach, commonly known as the n-factor approach, is where an empirically determined n-factor is used to translate the air temperature to the ground surface temperature typically to a depth of 100 mm from the soil surface which accounts for the net radiation, vegetation, snow cover, and ground thermal properties (Andersland and Ladanyi 2004). It is defined as the ratio of the of the ground surface freezing or thawing indices to the air freezing or thawing indices, respectively. Table 6.4 summarizes the thermal modifiers

used in the numerical model. The values in the specific locations where they were applied are typical of literature values and were adjusted accordingly to best match the results from the field. Fig. 6.3 shows a comparison of the actual and average sinusoidal ambient air temperatures used in the models. In Chapter 2, the increase in ambient air temperatures at the research site led to increased thaw depths at midslope of both control and reinforced embankments and translated to additional deformations. Chapter 5, which used TEMP/W and ABAQUS to simulate the temperatures at the test sections, also demonstrated this behaviour.

For both cross-sections, the meshing applied to the foundation soil is finer at the interface closer to the embankment fill and increases to a coarser size towards the base and outside the embankment footprint. The embankment slopes have a mesh size of 0.3 m, while the width of the road at the top of the embankment towards the foundation has a mesh size of 0.4 m. A smaller global mesh size of 0.2 m and 0.3 m was attempted for the soil elements, which provided comparable results with the final mesh sizes used. All geotextile layers in the reinforced embankment have a mesh size of 0.2 m.

6.2.3. Modelling Approach

The control (unreinforced) section was modelled using a fully-coupled (CP) approach where the heat transfer (thermal) and stress and deformation (mechanical) occurring on the soil elements are solved simultaneously in a single analysis. In this type of analysis, the soil is modelled using coupled elements with displacement, pore pressure, and temperature degrees of freedom at its nodes. The CP approach uses two predefined fields at the beginning of the analysis: (a) an initial temperature field and (b) an initial stress field. The initial temperature field was established by conducting a heat transfer spin-up analysis. The heat transfer spin-up analysis is similar to the approach presented in Section 5.3.3 where a constant sinusoidal temperature function is applied at

the surfaces exposed to the ambient air temperature including the effect of n-factors and a constant temperature boundary of -4.3°C at the base of the model. Only DC3D8 (8-noded linear heat transfer brick) type of elements were used in the spin-up analysis. The embankment was assumed to have an initial temperature of -12°C and -8°C for the foundation. It was observed during preliminary numerical simulations that without these two initial temperatures the duration of the spin-up analysis was greatly prolonged. The initial thermal equilibrium state was achieved once the nodal temperatures were showing the same year-to-year temperature values for the duration of the simulation. In general, the initial thermal equilibrium state was achieved within a spin-up duration of five years. For the initial stress field, a geostatic analysis was done by determining the stresses in the embankment fill and foundation soil due to their body forces. The C3D8P (8-noded brick, trilinear displacement, trilinear pore pressure) type of elements were used in the model. The geostatic stresses in the foundation soil were adjusted accordingly upon application of the body forces from the embankment fill layers until a new stress equilibrium is achieved. Once these two predefined fields are imported to a global model (labelled as CP model), both thermal and mechanical boundary conditions were activated simultaneously with C3D8PT (C3D8P elements with temperature degree of freedom) type of elements. The thermal boundaries applied at the ground surface were modified to reflect the actual three-year temperature data from the research site (Fig. 6.3) from April 20, 2015 to August 31, 2018. A similar model with an average sinusoidal temperature based on the actual three-year data was also implemented. Using an average sinusoidal temperature boundary reduces convergence issues during the analysis. However, it does not capture the warming behavior in the three-year monitoring period (see Fig. 5.16). The sinusoidal function is shown in Eq. 6.4, with the following parameters: y_o = -7.21671, x_c = -5.87595,

ω = 184.69096, and A = 18.51309, where y_o, x_c, ω, and A are the offset, phase shift, period, and amplitude parameters, respectively.

$$y = y_o + A \sin(\pi (x - x_c)/\omega) \quad \text{Eq. 6.4}$$

The presence of the geotextile layers on the embankment limits the use of the CP approach. The geotextiles were modelled as structural elements, but the pore pressure degree of freedom is not available in this type of element in ABAQUS. In addition, geotextiles do not have any bending stiffness and their behaviour can be idealized either as membrane or shell elements. Membrane elements only have the displacement degrees of freedom (u_x, u_y, u_z), while shell elements have the rotational and temperature degrees of freedom in addition to the displacement ones. Because there is no direct coupling between shell and solid surfaces in ABAQUS that would satisfy the degrees of freedom for both types of elements (e.g. pore pressure), a sequentially-coupled approach (SQ) was employed. In this approach, a heat transfer analysis is first conducted for the same analysis duration as the expected duration of the deformation analysis. The temperature field for each time step in the heat transfer analysis is referenced in the deformation analysis to invoke the corresponding material properties dependent on that temperature. Membrane elements are more computationally efficient in the deformation analysis because it eliminates the other degrees of freedom not needed for this type of simulation, but it does not have the temperature degree of freedom available at its nodes. Shell elements can be idealized as a membrane in ABAQUS to overcome this shortcoming. Without this idealization, at least five degrees of freedom will be present along the thickness of the shell and the added complexity of the rotational degrees of freedom. For both temperature spin-up and actual heat transfer analysis, DS4 (4-noded heat transfer quadrilateral shell) elements were used for the geotextiles, and DC3D8 elements were used for the embankment fill and foundation soil.

For both geostatic stress equilibration and deformation analysis in the reinforced models, C3D8P were used for the embankment fill and foundation soil, while M3D4 (4-noded quadrilateral membrane) elements were used for the geotextile. As mentioned in the previous section, tie constraints and contact properties were used in between layers where the geotextiles were installed. No slippage was allowed during the geostatic stress step. This was modified in the subsequent step to reflect the change in properties as the embankment slope thaws. The thermal conductance between the soil and the geotextile were set to a high value to ensure that the geotextile does not inhibit thermal flow. Both membrane and shell elements do not have the pore pressure degree of freedom. The contact properties however take into account the effect of permeability and suction through its interface resistance based on the pullout tests presented in Chapter 4. The wicking geotextile has a larger interface resistance compared to the non-wicking geotextile.

Table 6.5 summarizes the solid and staged models for the two approaches to simulate the control and reinforced sections. Because of the difference between the two approaches primarily due to the presence of the geotextile reinforcement, the SQ approach of the reinforced section (RSQ) cannot be directly compared to the results of the control section using CP approach. The SQ approach was also used on a staged control section (unreinforced, USQ) to establish comparable results. Comparisons between the solid and staged models using the CP approach, the CP and SQ approach for the solid control section, and the SQ approach between the solid and staged control sections were also investigated. Table 6.6 summarizes the model attributes for the control and reinforced sections for the three-year period and climate change conditions.

Fig. 6.4 shows the cross-section of the solid section and the nodal locations where model temperatures and displacements (SAA-CV, SAA-CH) were made. This is the cross-section where results were determined for the CHT, CCP, and CSQ models. Similarly, Fig. 6.5 shows the cross-

section of the staged section and the nodal locations where model displacements (SAA-RV, SAA-RH) were obtained. This is the cross-section where results were determined for the RHT, UHT, RSQ, USQ, and UCP models.

6.2.4. Results and Discussion

6.2.4.1. Control Section

Fig. 5.16 in Chapter 5 showed the comparison between using an average sinusoidal function (-3yrAve) and actual air temperature (-3yrAct) as boundary conditions in a pure heat transfer analysis. These results demonstrated that using the actual air temperatures provided better numerical results closer to recorded field data. This comparison was also done in the CCP model and the results are shown in Fig. 6.6. Along the base thermistor in Fig. 6.6b and the centreline foundation in Fig. 6.6c, the maximum turnover peaks match well with recorded field data but overestimates the coldest temperatures. As expected, using the actual air temperature captured the warming soil temperatures in the embankment fill and foundation soil. Using an average sinusoidal temperature function is more computationally efficient in reducing convergence issues from day-to-day temperature fluctuations, but it does not reflect the warming temperature and may impact the overall thermal results especially in longer simulations (e.g. near-term and long-term climate change conditions). All subsequent models investigated are using the actual air temperatures at the research site for the three-year monitoring period, as well as the predicted air temperatures under climate change conditions from CCCma (see Section 5.4).

Comparison of temperatures between CHT and CCP models are shown in Fig. 6.7. Fig. 6.7a and Fig. 6.7d show that the results are similar between the two approaches against the recorded field data. This can be attributed to the nodal locations observed since they are close to the applied temperature boundary conditions and not significantly influenced by other elements. In Fig. 6.7b

and Fig. 6.7c, the maximum turnover temperatures for the CCP model reasonably follow the recorded field data, but the minimum soil temperatures are overestimated. The CHT models on the other hand show that the maximum turnover temperatures are underestimated, but the coldest temperatures are closer to the recorded ones. The warmest soil temperatures are of more interest in a practical sense since these temperatures contribute to the deformation occurring in the embankment. Although there is a difference between the two approaches, it is noteworthy to mention that the model results show the same warming trend observed from the recorded field data. Fig. 6.7d shows the model temperatures in comparison to the field data were achieved in both analyses at their warmest and coldest temperatures. The model results however show earlier cooling during the winter months. As mentioned in Section 5.3.4, this difference in results may be due to the volumetric water content of the soil. In CCP, the displacement, pore pressure, and temperature degrees of freedom are solved simultaneously whereas CHT only solves for the temperature. The difference in model temperatures indicates that the model deformations from the CP approach (CCP) can differ from the SQ approach (CSQ) that uses the temperatures assigned to its nodes from a heat transfer analysis (CHT) to drive the mechanical part of the analysis.

To further reinforce the results of Fig. 6.7, Fig. 6.8 shows the results at the maximum extent of the 0°C isotherm before below 0°C temperatures set in at the ground surface boundaries from CHT (Fig. 6.8a) and CCP (Fig. 6.8b) approaches. The 0°C isotherm in Fig. 6.8a is parallel to the slope surface similar to what was observed in the TEMP/W models in Chapter 5. In Fig. 6.8b, there was additional thawing that occurred in the CCP model near the toe of the embankment to the left of SAA-CV which will lead to larger displacements at the midslope of the embankment. From this temperature difference, it is expected that warmer air temperatures will result to larger displacements at the slopes.

Fig. 6.9a shows a comparison of the measured horizontal displacements from the vertical SAA (SAA-CV) with the model results at midslope of the embankment using the CP approach. Over the three-year period, the model results show reasonable agreement with the displacement trend where the increasing thaw depths led to additional displacements. The displacements at the top node of the SAA are slightly underestimated for August 2015, 2016, and 2017, but this difference reduced with time. The model results of the underlying nodes follow the same trend of the field data. The model displacements 1 m above the natural ground surface are slightly larger compared to the monitored values. SAA-CV indicates that there is no movement 0.6 m above the natural ground surface where the ground might still be frozen, whereas the model results show that the frozen soil is only 0.4 m above the natural ground surface. Fig. 6.9b shows a comparison of the measured vertical displacements from the horizontal SAA (SAA-CH) with the model results at midheight of the embankment. The model results underestimated the observed values but show the same trend of increasing displacements over time. The horizontal distance of the frozen core has decreased from 9 m in August 2015 to 7.5 m in August 2018 from the embankment centreline. The vertical displacements increased as the size of the frozen core decreased; that is, displacements were mobilized as the temperature in the embankment increased. Fig. 6.10 shows the horizontal displacement at the top node of SAA-CV (P1 in Fig. 2.15a) compared with the CCP model with respect to time. The recorded field data is shown in the negative direction to indicate the global direction of movement (see Fig. 6.1 for axis directions) in contrast with Fig. 2.17 where the horizontal displacements are in the positive direction. It can be observed that there is some rebound occurring during the turnover months where the ground surface boundary condition changes from positive to negative temperatures. This rebound is a consequence of how the model treats the temperature dependency of the material properties provided earlier. While there is some difference

in displacements between these turnover months, the general trend of accumulating displacements is consistent with the recorded field data. As expected, there were little to no movements occurring during the winter months while displacements occur when the slope experiences positive temperatures. The overall magnitude and trend of the model results reasonably achieved the same results with the recorded field data especially during the first summer thawing were significant displacements occurred. This provides confidence that the modelling approach is satisfactory to assess the thermal and mechanical performance of different embankment configurations as will be presented in Section 6.3. Fig. 6.11 shows the global displacement vectors of the model control section for August 2015 (Fig. 6.11a) and August 2018 (Fig. 6.11b).

Fig. 6.12 shows the comparison of the horizontal (Fig. 6.12a) and vertical (Fig. 6.12b) displacements using the average sinusoidal and actual temperature boundary conditions using the CP approach. In both horizontal and vertical directions, the displacements are the same in August 2015. Results show that the model with the -3yrAct led to larger displacements over time, with the greatest difference observed in August 2018. The thickness and extent of the frozen core are smaller when the -3yrAct is used. Although the model results are an idealization of the actual behaviour of the control section in the field, the results from Fig. 6.12 indicate that using the actual temperature conditions on site led to closer results to the recorded field values (see Fig. 6.9).

As presented in Table 6.5, the control section can be modelled in two different approaches using two different cross-sections. It is important to demonstrate how different modelling approaches influence the numerical results. Fig. 6.13 shows a comparison between the CCP, CSQ, UCP, and USQ models. Comparing CCP and CSQ models for SAA-CV, the thaw depth has increased over time based on the modelled horizontal displacements for both approaches but the CCP model is 0.4 m deeper than the CSQ model. The horizontal displacements relatively follow

the same movement for the first 2 years (Fig. 6.13a), but the following 2 years (Fig. 6.13b) showed that CSQ overestimated the displacements 1.5 m above the natural ground surface. The vertical displacements in Fig. 6.14 show that the CCP model displaced more than the CSQ model by approximately 30% at the tip of SAA-CH. Both approaches show the same location of the frozen core consistent with the results presented in Fig. 6.8.

Comparing CCP and UCP models for SAA-CV, the thaw depth is relatively the same for the first 2 years (Fig. 6.13a). The CCP model however has a thaw depth about 0.1 m deeper than the UCP model on August 2018. The CCP model showed increasing horizontal displacements over time in the range of 5-10 mm in 2016 to about 25-30 mm in 2018 with respect to its vertical depth. The vertical displacements of the CCP model in Fig. 6.14 are larger than the UCP models by about 30% in August 2017 and August 2018. The mesh size was kept the same for the location of SAA-CV and SAA-CH in both models, but the different geometries of each soil layer and how the software processes nodal results in between soil layers using tie constraints influenced the overall displacements. The vertical displacements between the CSQ and USQ show similar trends and magnitudes from August 2015 to August 2018, but the horizontal displacements at the top of SAA-CV in the CSQ model is 13% greater than the USQ model and reduces to the same values at the thaw depth of 0.7 m above the natural ground surface. In all model approaches, performing the numerical analysis for a short time (1 year) resulted to similar results, but over time the displacements started to vary because of the change in thermal regime in the embankment fill related to the boundary conditions applied. Although the model approaches resulted to different horizontal and vertical displacements, they are within the range of 25 to 50 mm from the recorded field data. The CP approach is desirable in modelling embankments in the Arctic, but using the sequential approach will provide adequate estimates of displacements as long as the thermal profile

of the embankment fill and foundation soil simulate what is expected in the field as demonstrated in Chapter 5. With confidence from these results, the CP approach was used to investigate the effects of different embankment configurations as presented in Section 6.3. The control test section is also investigated under climate change conditions in Section 6.4.

6.2.4.2. Reinforced Section

With the limitations of the modelling approach presented in Section 6.2.3, the results of the CCP model cannot be directly compared using the sequential approach for the reinforced section (RSQ). The RSQ model was therefore compared with the results of the USQ model of the control section. Fig. 6.15 shows the horizontal (Fig. 6.15a) and vertical (Fig. 6.15b) displacements from the RSQ model compared to recorded field data of SAA-RV and SAA-RH, respectively. There is a noticeable difference between the recorded and simulated results. The horizontal displacement of the soil between Layer 1 (L1, 1.8 m) and Layer 2 (L2, 2.7 m) from SAA-RV shows a linear variation of displacement with depth accumulating over time. The RSQ model displacements on the other hand show this to be curved, with the top node of the layer observed to be less than the recorded one. With respect to depth, the horizontal displacements just above L1 from August 2015 to August 2017 show that it is slightly overestimated by 5 to 10 mm, but this difference increased to 50 mm in August 2018. These displacements are related to temperatures modelled in a pure heat transfer analysis and are similar to the results in USQ. A basic friction model was used to simulate the interface sliding between the geotextile reinforcement and the soil. The difference in recorded and model horizontal displacements ranged from 40 to 65 mm. The underestimated displacements below L2 is offset by the overestimation in displacements above L1. Although the accumulated vertical displacements in the model (Fig. 6.15b) increased over time, the model results underestimated the recorded field data of SAA-RH. The model results show how the core of the

embankment has decreased in the monitoring period similar to what was observed in the USQ model. Further studies are recommended to apply more sophisticated interface models (e.g. Duncan and Chang model) between the geotextile and the soil which may improve the numerical results presented.

A comparison of the horizontal (Fig. 6.17a) and vertical (Fig. 6.17b) displacements from the RSQ model with the results of the USQ model is shown in Fig. 6.17. Both models are using the thermal regime in the embankment fill and foundation soil from a pure heat transfer analysis and as expected the depth of seasonal freezing and thawing and its corresponding thickening over time are the same. The displacements in both directions are reduced with the use of these geotextile reinforcements. The results provide confidence that the interface shear strength (derived from pullout tests) and tensile strength from tensile tests are contributing in reducing displacements. The influence of reinforcement length, vertical spacing, and slope configuration are presented in Section 6.3. Fig. 6.16 shows the global displacement vectors of the model reinforced section for August 2015 (Fig. 6.16a) and August 2018 (Fig. 6.16b).

Fig. 6.18 shows the horizontal displacements along the geotextile layers in the RSQ model. A fictitious geotextile was superimposed at the zero line to indicate where the displacements were obtained in the model. Note that the mesh size of the geotextile layers in the model is 0.2 m, but the nodal locations presented are spaced every 0.8 m. These horizontal displacements are in the negative direction with respect to the global coordinates of the model in Fig. 6.2. Layers L1 and L2 show that approximately 1 m of the geotextile is still embedded in frozen core of the embankment. Layer 3 (L3, Fig. 6.18c) had 1 m of its length embedded in the frozen core in August 2017, but this has completely thawed in August 2018. Layer 4 (L4, Fig. 6.18d), which is closest to the road surface, has completely thawed in the first summer following construction. The largest

displacements occurred at the nodes closest to the embankment slope, with the greatest magnitude occurring during the summer following construction. Fig. 6.19 shows the corresponding strains along these geotextile layers from Fig. 6.18. The maximum axial strains in Fig. 6.19a to Fig. 6.19c are located close to the seasonal extent of the thaw depth. This corresponds to the maximum change in horizontal displacements in Fig. 6.18 over a known distance along the geotextile. Fig. 6.19d (L4) shows that the maximum strains occur close to the embankment shoulder. These strains are significantly larger than the ones presented in Fig. 2.20. The measured strain gauge readings were from a 1 inch (25.4 mm) gauge, while the strains in the model were taken from a 200 mm element mesh calculated from the displacements of two adjacent nodes to that element. Although these strain values are significantly larger than what was recorded from the field, the overall displacement of the RSQ model are what was observed from SAA-RV. The model strains are also increasing over time and shifting to the left in Fig. 6.19, indicating that the thaw depth is increasing and larger displacements are occurring at the slopes. There was no attempt made to simulate the geotextile layers using a mesh of 25 mm. With the limitations presented earlier (e.g. friction model, contact properties, tie constraints), a decrease in mesh size will greatly increase the computational effort to reach a converged solution.

Fig. 6.20 shows a comparison of the horizontal displacements between the wicking geotextile (labelled as W) used along ITH and a comparable geotextile without the wicking function (labelled as NW, non-wicking). The tensile capacity and interface shear resistance of this non-wicking geotextile were determined in Chapter 4. In the first summer thawing following construction (August 2015), NW model displaced by 11 mm more than the W model. This difference increased to 28 mm by August 2018. Using wicking geotextiles reduced the horizontal displacements; however, this reduction in comparison with a non-wicking geotextile is not significant. The benefit

of using woven geotextiles as slope reinforcement in general reduces displacements, but the type of woven geotextile (wicking, non-wicking) to mobilize this function should be evaluated based on project requirements and costs. In the case of thawing soils at embankment slopes and the influence of a variable climate as its boundary condition, any effort to reduce the horizontal displacements will improve its performance. It should be noted that the effect of wicking geotextiles on the potential reduction in moisture content of the soil was neither determined in the field nor in the laboratory and therefore was not considered in the modelling. Only the difference in interface shear strength based on laboratory test results were considered.

The results presented in the control section showed how the modelling approach influenced the results. Without the added complexity of using shell elements to model the geotextile reinforcement and the contact properties for the interface resistance, the model is resolved as a USQ model. Nevertheless, the RSQ model results reasonably support the recorded field data and using woven geotextiles can reduce the displacements developing due to the seasonal freezing and thawing at the embankment slopes.

6.3. Parametric Studies for Unreinforced and Reinforced Embankments

6.3.1. Embankment Geometry

The parametric unreinforced and reinforced embankment models were subjected to the temperature boundary conditions at the research site from April 2015 to August 2018. Similar to the boundary conditions presented in Section 5.3.2, the embankment slopes were divided into three regions (*Slope Top*, *Slope Middle*, *Slope Bottom*) for the application of different n-factors at these locations. For the unreinforced embankments, three heights were investigated: (a) H = 2 m, (b) H = 4 m, and (c) H = 6 m, and three slope inclinations: (a) 2H:1V, (b) 3H:1V, and (c) 4H:1V. Note that the height of the embankment at the test sections is about 5.3 m with a slope inclination

of 3H:1V. All unreinforced embankments were modelled using the CP approach on solid cross-sections. The foundation depth is 7 m, with a width of 40 m from the embankment centreline. Only half of the embankment was modelled due to symmetry. As demonstrated in Section 5.5, spin-up analyses were conducted for each model embankment to reach thermal equilibrium for the initial temperature field. Table 6.7 summarizes the models analyzed for the unreinforced sections.

Fig. 6.21 shows the staged layers for the reinforced embankments. Fig. 6.21a and Fig. 6.21c show the reinforcement spacing of 0.6 m with embankment slopes of 2H:1V and 3H:1V, respectively. Similarly, Fig. 6.21b and Fig. 6.21d show the reinforcement spacing of 0.9 m with embankment slopes of 2H:1V and 3H:1V, respectively. All reinforced embankments were modelled using the SQ approach on staged cross-sections. For these models, the reinforcement length was varied between 6 m and 8 m. All reinforced embankments have a constant height of 6 m. The foundation depth is 7 m, with a width of 40 m from the embankment centreline. Only half of the embankment was modelled due to assumed symmetry. A spin-up analyses were conducted for each model embankment to reach initial thermal equilibrium. A pure heat transfer analysis was conducted afterwards to obtain the thermal regime in the embankment fill and foundation soil for the duration of the analysis. Table 6.8 summarizes the models analyzed for the reinforced sections using wicking geotextiles. The corresponding unreinforced embankments using staged cross-section are summarized in Table 6.9.

6.3.2. Results and Discussion

6.3.2.1. Unreinforced Embankments

6.3.2.1.1. Effect of Embankment Height

For the 2 m embankments in Fig. 6.22, the model results in August 2015 indicate that the embankment fill has completely thawed but the 0°C temperature was preserved to the natural

ground surface. Preserving the 0°C temperature and allowing the permafrost table (originally at 0.5 m below the natural ground surface) to aggrade to the natural ground surface was the original design for this embankment height. The maximum thaw depth at the crest (Fig. 6.22a) is at the original location of the permafrost table by August 2018. In Fig. 6.22b, the thickness of the embankment fill at the midlsope provided some insulation in August 2015 bringing the 0°C temperature 0.3 m above its original location, but by August 2018 the 0°C temperature was found at its original depth at 0.5 m below the natural ground surface. The warmer air temperatures recorded for the subsequent years resulted to deeper seasonal freezing and thawing depths. The vertical displacements along the midheight of the 2 m embankments (Fig. 6.22c) in August 2015 was on average 50 mm, but with the thawing of the previously frozen foundation soil, this resulted to an additional displacement of 200 mm.

Fig. 6.23 and Fig. 6.24 show the displacements for the 4 m and 6 m thick embankments, respectively. Unlike the 2 m thick embankments, parts of the embankment fill at the crest has remained frozen. At the crest of the 4 m embankments (Fig. 6.23a), the thickness varied from 1.4 m to 2 m above the natural ground surface for H4S2 and H4S4, respectively, by August 2018. At the crest of the 6 m embankments (Fig. 6.24a), the thickness varied from 3.6 m to 4.2 m above the natural ground surface for H6S2 and H6S4, respectively, in the same period. As the fill thickness increased, the thickness of the frozen core at the crest consequently increased. In Fig. 6.23b at the midslope of the 4 m embankments, the 0°C temperature is at the natural ground surface in August 2015, but this has decreased to a depth of 0.5 m below the natural ground surface by August 2018. In Fig. 6.24b at the midslope of the 6 m embankments, the 0°C temperature is 1.2 m above the natural ground surface in August 2015 and reduced to the natural ground surface by August 2018. The horizontal displacements at the midslope increased as the embankment height increased. This

should be expected because more thawed fill material above the midslope is mobilized with thicker embankments. In Fig. 6.23c, the midheight location at 2 m have remained frozen for H4S4 within the embankment crest towards the embankment centreline until August 2018. Results from H4S2 and H4S3 show some vertical displacements at the crest which indicates shrinking of the frozen core as a consequence of warmer air temperatures. In Fig. 6.24c, the core has remained frozen within the embankment crest towards the embankment centreline.

Table 6.10 summarizes the change in thaw distances at different locations in the embankment fill between August 2015 and August 2018. As indicated in Chapter 2, the frozen core of the embankment is by definition permafrost because the soil has remained continuously below 0°C for at least 2 years. It should be pointed out that the embankment is an engineered structure using frozen soil. The thermal regime in the embankment fill and the foundation soil from all spin-up analyses was frozen similar to winter construction conditions. Under these conditions, the permafrost table aggraded into the embankment fill for the 4 m and 6 m thick embankments. The frozen core of these embankments, however, have been shrinking since the beginning of the analyses due to the warmer air temperatures recorded at the region used as boundary conditions in the model.

6.3.2.1.2. Effect of Slope Inclination

The influence of slope inclination is also shown in Fig. 6.22 to Fig. 6.24 for the 2 m, 4 m, and 6 m embankments, respectively. In Section 5.5, it was discussed how the slope inclination at select nodes do not significantly influence the thermal stability of the embankment. It can be seen however that S2 resulted to the largest initial displacements for all embankment heights. As summarized in Table 6.11 and Table 6.12, S2 had the largest increase in horizontal displacements between August 2015 and August 2018 for both crest and midslope locations, respectively. The

percent reductions as the slope inclination was decreased are also summarized in Table 6.11 and Table 6.12. These percent reductions are in reference to the maximum displacements (Δ_{max}) from S2. The 4 m and 6 m thick embankments benefitted most from reducing the slope inclination from S2 to either S3 or S4 at the crest of the embankment, while larger percent reductions were observed for the 2 m embankments at its midslope. This difference in improvement between the 2 m (thin) and 4 m and 6 m (thick) embankments is related to how the displacements are developing with respect to the presence of the frozen core. In Table 6.11 and Table 6.12, reducing the slope inclination from S3 to S4 significantly reduced the displacements for H4 and H6 embankments at the crest and midslope locations, respectively. Although this approach of reducing slope inclinations might be promising in mitigating displacements and maintaining thermal stability, a larger embankment volume would be required which will translate to increase in project costs.

In terms of vertical displacements along the midheight of the embankment (Table 6.13), there is no significant improvement when the slope inclination is decreased for the 2 m embankment at its outermost node and underneath the crest. The general trend for the model results in August 2015 indicate that these vertical displacements are getting smaller. A large increase in vertical displacements were observed by August 2018, especially for H4S2 and H6S2. Similar to the horizontal displacements, decreasing the slope inclination for H4 and H6 embankments led to a reduction in vertical displacements. For all slope inclinations, H4 and H6 embankments indicated that the soil within the region of the embankment midheights and from the embankment crest to the centreline is still frozen. Only H2 embankments showed complete thawed embankment fill during the summer following construction (Fig. 6.22c). Once the original seasonal thaw depth before embankment construction thawed as is the case for the H2 embankments due to warmer air temperatures in 2018, vertical displacements underneath the crest increased on average by

200 mm. This significant increase in settlements is attributed to the high compressibility of the peat foundation once it reaches an unfrozen state (De Guzman and Alfaro 2016). Although the core of the H4 and H6 embankments have remained frozen, the size of this frozen core has decreased as summarized earlier in Table 6.10.

6.3.2.2. Reinforced Embankments

Based on the results of the parametric study on unreinforced embankments, only H6S2 and H6S3 embankments were investigated for the parametric study on reinforced embankments. This is primarily due to the largest displacements recorded by August 2018. The addition of reinforcement layers on H6S2 and H6S3 is an alternative to decreasing the slope inclination to 3H:1V and 4H:1V, respectively. As demonstrated in the RSQ model in Section 6.2.4.2, SQ model results cannot be directly compared to CP model results because of the modelling approach. Equivalent USQ models were developed for staged cross-sections with the two different slopes and soil layer thickness as base cases to study the influences of reinforcement vertical spacing and reinforcement length. These models were summarized in Table 6.9 and the horizontal displacements between August 2015 and August 2018 are shown in Fig. 6.25. Although there are no reinforcements included in these models, the soil thicknesses in these cases are analogous to the vertical spacings (Sp6 and Sp9) between the reinforcement layers. There are slight differences between the results of the models using two different soil thicknesses, which is attributed to the element meshing at the midslope of these embankments. In general, the overall trend of displacements are the same for both soil thicknesses, with a difference between 5 and 12 mm. Similar to the behaviour observed in the unreinforced embankments using the CP approach, embankments with S2 developed larger displacements compared to S3. By August 2018, the S2 embankments displaced an additional

475 mm from August 2015, while the S3 embankments displaced by 240 mm. Simply reducing the slope inclination resulted to a 44% reduction in horizontal displacements at the midslope.

6.3.2.2.1. Effect of Reinforcement Length

Fig. 6.26 shows the extent of the thawed core for S2 (Fig. 6.26a) and S3 (Fig. 6.26b). A fictitious line is superimposed in this figure to show the conceptual embedment of the geotextile in the model. The vertical spacing shown is 0.9 m (Sp9), but these were also done for the 0.6 m (Sp6) case.

Fig. 6.27 shows the horizontal displacements for the S2 models using two reinforcement lengths considering Sp6 (Fig. 6.27a) and Sp9 (Fig. 6.27b). Considering the vertical spacing as constant, the horizontal displacements along the observation line (Fig. 6.21) are relatively the same using either 6 m or 8 m geotextiles. For S2L6Sp6, the first five layers of reinforcement from the bottom of the embankment are on average embedded by 1.7 m to the frozen core at the maximum extent of the seasonal thaw depth. The sixth layer from the bottom is embedded by 1.2 m to the frozen core, while the seventh to ninth layers are embedded in seasonal thaw depth. Similarly for S2L8Sp6, the first five layers of reinforcement from the bottom are on average embedded by 3.7 m, the sixth layer at 3.2 m, and the seventh to ninth layer within the seasonal thaw depth. Similar embedment depths were observed for S2Sp9 (Fig. 6.27b), with less reinforcement installed for larger vertical spacing. The first three layers of reinforcement are 1.7 m and 3.7 m embedded in the core for L6 and L8, respectively. The fifth and sixth layers for Sp9 are within the seasonal thaw depth. Based on these results, a 1.7 m embedment length in the frozen core provides restraint from horizontal movements for S2 under the environmental conditions the model was subjected to. Anything beyond this length does not significantly improve the performance of the embankment. It should be noted however that under long-term climate conditions, the frozen core will shrink

over time and this added benefit might not be a available in future circumstances. On average, the geotextile reinforcement provided a 70% reduction in horizontal displacements for S2Sp6 and a 60% reduction for S2Sp9 with respect to the unreinforced embankment along the observation line in Fig. 6.25.

Fig. 6.28 shows the horizontal displacements for the S3 models using two reinforcement lengths considering Sp6 (Fig. 6.28a) and Sp9 (Fig. 6.28b). This change in slope configuration will change the thermal regime of the model embankments and therefore the length of the geotextile embedded in the frozen core. S3Sp6 and S3Sp9 using 6 m have all layers of reinforcement within the seasonal thaw depth. These geotextile layers, although only embedded outside the frozen core, provided 33% and 20% reduction in horizontal displacements for Sp6 and Sp9, respectively, compared to the unreinforced embankment in Fig. 6.25. For S3Sp6 and S3Sp9, lengthening the reinforcement to 8 m intercepted the frozen core with an embedment length of 2 m. Similar to S2, the seventh to ninth layers for S3Sp6, and the fifth and sixth layers for S3Sp9 are within the seasonal thaw depth. With an additional geotextile length of 2 embedded in the frozen core, the Sp6 model showed a reduction in horizontal displacements by 53%, and the Sp9 model showed 38%.

6.3.2.2.2. Effect of Reinforcement Spacing

Fig. 6.29 and Fig. 6.30 show the horizontal displacements at the midslope for S2 and S3, respectively, with the reinforcement length held constant. For all cases, a larger vertical spacing (Sp9) resulted in larger horizontal displacements along the observation line in reference to Fig. 6.21. As discussed in the previous section, the length of the reinforcement for S2 did not influence the horizontal displacements. With a tighter vertical spacing, the displacements were reduced by 27% for the soil between elevations 2.8 m and 3.7 m, and by 69% for the soil between 1.9 m and

2.8 m. For S3 with the reinforcement embedded in the frozen core (Fig. 6.30b), the displacements were reduced by 23% for the soil between elevations 2.8 m and 3.7 m, and by 53% for the soil between 1.9 m and 2.8 m. These results indicate that a tighter vertical spacing is beneficial when used for steeper slopes.

The S2 and S3 models demonstrated that addition of geotextiles in thawing slopes can reduce the horizontal displacements for a similar unreinforced embankment. A combination of tighter vertical spacing and longer reinforcement embedded in the frozen core provided the most benefit in limiting displacements as the slopes undergo seasonal freezing and thawing cycles. It should be noted that a tighter vertical spacing will require quality control as each soil lift is compacted under frozen conditions and may delay project delivery time, while reinforcement layers (woven geotextiles) have to be long enough to intercept the potential location of a frozen core.

6.4. Embankment Performance of Test Sections Under Climate Change Conditions

The control and reinforced embankment models in Section 6.2.4 were subjected to climate change temperature boundary conditions. The control section model was subjected to both near-term and long-term models, while the reinforced section model was only subjected to near-term conditions only, specifically d2015 providing results until the end of 2024. An unreinforced model (USQ-d15) was developed to establish comparable results with the reinforced model (RSQ-d15) using the SQ approach.

6.4.1. Control Section

The model horizontal displacements at the midslope of the control selection using d2015 is shown in Fig. 6.31a, while Fig. 6.31b shows the results using RCP 8.5. RCP 8.5 was selected because it is the most aggressive of the long-term climate change models. The recorded field data from

SAA-CV in 2015 and 2018 are also superimposed in these figures. In both climate change models, the results overestimated the recorded field data with larger discrepancies using RCP 8.5. The aggressive temperatures of RCP 8.5 shows that by 2018 the frozen soil at the midslope would have completely thawed, and by 2034 the thaw depth would have gone as deep as the location of the original permafrost table before embankment construction. While the results in Fig. 6.31 may be considered conservative compared to recorded field data, local climate conditions (Fig. 6.9) still provided the most accurate results. As mentioned in Chapter 5, these climate change models are in a regional scale and may not provide accurate results when used to evaluate overall embankment performance as they do not consider local ground conditions.

Fig. 6.32 shows a comparison of the horizontal displacements in 2020 (Fig. 6.32a) and 2024 (Fig. 6.32b) using the near-term and long-term climate change models. Although d2005i1 and d2005i2 near-term models and RCP 2.6, RCP 4.5, and RCP 8.5 long-term models provide boundary conditions until 2035 and 2100, respectively, model results are only assessed until the end of 2024. In addition, excessive displacements at the thawed region between the interface of the embankment fill and foundation soil at the midslope of the embankment were encountered using the available climate change models and thus limited the simulation for long-term conditions for both control and reinforced test sections regardless of the approach used. The model results in Fig. 6.30 show some discrepancies as to which boundary condition with respect to time scale provided the most conservative results. Fig. 6.30b shows that RCP 2.6 provided the largest horizontal displacements using the long-term models; however, it was demonstrated in Chapter 5 that RCP 8.5 provides the warmest condition for these scenarios. This discrepancy is attributed to the actual model temperatures used where some years are colder or warmer compared to other years. The model results are only until 2024 and the warmer temperatures for the warmer climate

models were encountered at around 2050. It is clear that using the long-term models in a coupled thermal-mechanical model overestimates the displacements compared to the recorded displacements in the same time-scale (e.g. August 2015, August 2018). The displacement in the embankment fill using the long-term models is on average 28% greater than the near-term models in 2020, and the discrepancy grew to 44% in 2024. The thaw depths for these models have relatively remained at the same location with respect to time, where near-term models showed no movement at the natural ground surface, and long-term models showed no movement 0.25 m below this. The difference in accumulated displacements for these models is due to the changes in the maximum and minimum temperatures from year to year turnovers. Based on these model results of the control section, only the d2015 near-term model was used for the reinforced embankment model in the following section.

6.4.2. Reinforced Section

Fig. 6.33 shows the horizontal displacements at the midslope of the RSQ model using d2015 temperature boundary conditions. The recorded field data for SAA-RV are also superimposed in this figure. It can be seen that the d2015 model results are relatively comparable to the recorded field data. The top nodes of the model were still underestimated, but the nodes below 2 m follow the displacement trend recorded in August 2018. As discussed in the previous section, the near-term model overestimates the displacements of the control section and this observation is also confirmed with the USQ model. Although these displacements are larger compared to calibration results (Fig. 6.13a), the geotextiles installed will provide reinforcement as the frozen core of the embankment and embedment depth length of the geotextile in this frozen region decreases. The horizontal displacements are still accumulating as the thaw depth increases but as shown in Fig.

6.31b, the addition of woven geotextiles provided a 69% reduction in displacements in a comparable model without it for both 2020 and 2024.

6.5. Forced Warming Conditions on Reinforced Embankments

The complexity and uncertainty with the climate boundary conditions provided by CCCma and the computational effort required to accomplish these models presented some difficulties in assessing the performance of the parametric reinforced embankments. In order to investigate embankment displacements due to the effect of the frozen core thawing over time driven by climate change, the original boundary condition used was modified such that the air temperature is held constant once it reaches a temperature of 20°C until a significant part of the frozen core is reduced. This modelling approach, labelled as forced warming conditions (FWC) in this manuscript, is analogous to construction conditions where frozen soil is used during winter construction but the air temperatures in the area following summer construction are not cold enough to maintain a frozen core and develop a new permafrost table within the embankment over time. The use of the FWC approach is also advantageous in evaluating the performance of reinforced embankments once the buried length in the frozen core experiences above 0°C temperature. The FWC approach was first applied to the control (unreinforced) and reinforced test sections followed by the parametric reinforced embankments. Similar to Section 6.3, the reinforced test section and parametric reinforced embankments are using the SQ approach with staged models. Equivalent unreinforced embankments using staged models are also presented to establish comparable results.

6.5.1. Control and Reinforced Test Sections

Fig. 6.34 shows the model horizontal displacements of using FWC on the control (USQ) and reinforced (RSQ) test sections. In Fig. 6.34, THES indicates the thawed horizontal extent from slope, which in this case is equivalent to 8.4 m. The results of the USQ model are denoted by NR,

while the results of the RSQ models using the original geotextile properties (denoted by O), higher interface properties (denoted by HI), and higher elastic modulus (denoted by HE). The result of the O model is almost the same as the USQ model at THES = 8.4 m, but once the frozen core reduces in size it shows displacements larger than the USQ model. This indicates that tensile capacity and the interface resistance between the soil and the geotextile have been exceeded where localized displacements were occurring at GL1 (geotextile layer no. 1). In order to improve the contribution of the geotextiles, two approaches were investigated: (1) increase the interface strength between the soil and the geotextile, and (2) increase the elastic modulus of the geotextile.

The soil-geosynthetic efficiency factor (E_f) is defined as the ratio of $\tan\delta$ at the soil-geotextile interface divided by $\tan\phi'$ of the soil. With the original properties of the wicking geotextile, E_f is approximately equal to 0.4. According to Jewell (1996) this ratio can range from a value between 0 and 1 for geotextiles, where ratios approaching unity more desirable. Using an E_f set to unity, the $\tan\delta$ used for the HI model was approximately equal to 0.6. Based on the model results in Fig. 6.34, there was no significant improvement in the HI model for both THES state and at a reduced frozen core. It should be noted that the increased interface strength is fictitious in this case since this property is highly dependent on the soil material interacting with the geotextile.

The elastic modulus of the geotextile was doubled for the HE model. Using this approach, both THES and reduced frozen core states showed the horizontal displacements to be smaller than the USQ model. Beyond the thawed length, the displacements observed with the HE model are slowly approaching the displacements in the USQ model indicating that there are still localized movements occurring in between the geotextile layers but the increased elastic modulus contributed in reducing these displacements. Unlike the HI model, a designer would have more control with the selection of the elastic modulus of the geotextile given these observations under

FWC. Unfortunately, the wicking geotextile used in the reinforced test section only comes in one tensile strength. The comparable non-wicking geotextile, although displacing more than the wicking geotextile (Fig. 6.20), has the least tensile strength among two other geotextiles in the same commercial reinforcement catalogue. The interface properties of the non-wicking geotextile were determined from pullout tests but this was not used in any of the test sections along ITH. Based on these results, it is clear that embedding the geotextile in the frozen core, if it exists in the right environmental conditions, is beneficial in reducing the displacements in reinforced slopes. Furthermore, larger displacements for reinforced slopes should be accounted for once the frozen core is reduced or completely gone, which can be reduced if geotextiles with higher tensile strength are used. There was no attempt made to revise the vertical reinforcement spacing of the reinforced test section, but insights from Section 6.3.2.2 indicate that vertical spacing of 0.6 m will further reduce these displacements in combination with the increase in elastic modulus of the geotextile.

6.5.2. Parametric Reinforced Embankments

From the results presented in Section 6.3.2.2, a tighter vertical spacing of 0.6 m provided the least horizontal displacements for the two slope configurations and two reinforcement lengths investigated. The FWC was applied only to models S2Sp6 and S3Sp6 in Table 6.9 (unreinforced), and S2L6Sp6, S2L8Sp6, S3L6Sp6, and S3L8Sp6 in Table 6.8 (reinforced). The model cross-sections were previously shown in Fig. 6.21a and Fig. 6.21c for 2H:1V and 3H:1V, respectively. The models were compared at three distinct time steps: (1) when THES = 6 m, (2) when THES = 8 m, and (c) at a reduced frozen core size. It should be noted that when THES = 6 m, the 6 m geotextiles were completely above 0°C for the S2L6 and S3L6 models, while some length of the geotextiles were still embedded in the frozen core for the S2L8 and S3L8 models. All of the geotextiles have temperatures above 0°C at the reduced core size. Only HE was added to these

parametric reinforced embankment sections and were compared to models using the original reinforcement properties.

Fig. 6.35 shows the model horizontal displacements for 2H:1V slope configuration using 6 m (Fig. 6.35a) and 8 m (Fig. 6.35b) reinforcement lengths. The GL#s indicate the geotextile layer number, with the lowest number closes to the base of the embankment. The time steps where the frozen core are also indicated in the figures under the column Day for easier reference. When THES = 6 m on Day 166 for the 6 m geotextile, the horizontal displacements were reduced by 34.2% compared to NR. However, as the frozen core decreases, larger displacements also developed. The 8 m geotextile (Fig. 6.35b) shows that using the original geotextile properties for this slope configuration still has less displacements compared to its unreinforced state, but this is only observable when the frozen core is just at the edge of the geotextile at THES = 8 m on Day 262. By Day 304, the horizontal displacements are almost the same as if it were unreinforced. By increasing the elastic modulus twice its original value (HE models), the displacement was improved by 11.3% for the 6 m geotextile and 39.1% for the 8 m geotextile compared to their unreinforced models in a reduced core state. Again, these results support the observations presented earlier that a longer geotextile combined with a higher tensile strength improves embankment performance by reducing displacements.

The model displacements in Fig. 6.35 only show results at the embankment midslopes. In order to have a better understanding of the overall movement occurring at these thawing slopes, Fig. 6.36 and Fig. 6.37 show the global displacement vectors for 2H:1V slope configuration at THES = 8 m (Day 262, Fig. 6.36a to Fig. 6.36c) and at a reduced core (Day 304, Fig. 6.37a to Fig. 6.37c) using HE models, respectively. The location of the frozen core are also superimposed in these figures. The displacements presented in Fig. 6.35 were taken from the midslope (solid black vertical line

in Fig. 6.36 and Fig. 6.37). The vectors show the transition of the unreinforced slope and when the geotextiles were added. It should be noted that Fig. 6.36b and Fig. 6.37b have reinforcement lengths of 6 m, whereas the THES is at 8 m. The displacements vectors transitioned to larger values as the frozen core thawed. Interestingly, the global displacements developing are moving along with the movement of the frozen core similar to the observations recorded for the test sections.

Fig. 6.38 shows the horizontal displacements for 3H:1V slope inclination using 6 m (Fig. 6.38a) and 8 m (Fig. 6.38b) reinforcement lengths. Similar to Fig. 6.34 and Fig. 6.35, the GL#s indicate the geotextile layer number, with the lowest number closes to the base of the embankment. The horizontal scale in Fig. 6.38 is half of the scale presented in Fig. 6.35, indicating how displacements can be significantly reduced by modifying the slope inclination. There is only about 34% difference for THES at 6 m, but this discrepancy grows as the frozen core shrinks. The displacements for S3L6Sp6 for THES at 8m using the original geotextile properties show that they are almost the same as the unreinforced embankment, while there is about 28% reduction in horizontal displacements when a longer reinforcement is used as shown in S3L8Sp6 (Fig. 6.38b). At a reduced frozen core, the reinforced models displaced greater than the unreinforced embankments. The continuous thawing of the frozen core resulted in the reinforced zone to be part of the entire active zone beyond the frozen core. This is analogous to installing geotextile reinforcements that do not have adequate length embedded in the restrained zone. The coefficient of interaction between the soil and the geotextile is less than unity and thus create a weak link in the active zone. Using a higher elastic modulus (HE models), the displacement at this reduced frozen core resulted to almost the same displacements for the 6 m geotextile, but an improvement of 15.4% with the 8 m geotextile. Fig. 6.39 and Fig. 6.40 show the global displacement vectors for 3H:1V slope configuration at THES = 8 m (Day 151, Fig. 6.39a to Fig. 6.39c) and at a reduced

core (Day 238, Fig. 6.40a to Fig. 6.40c) using HE models, respectively. Similarly, the displacements presented in Fig. 6.38 were taken from the midslope (solid black vertical line in Fig. 6.39 and Fig. 6.40). It is clear that the longer geotextiles provided the least displacements with higher elastic modulus.

6.6. Summary and Conclusions

The properties obtained from the large-scale direct shear test for the embankment fill and the pullout tests on the wicking and non-wicking geotextiles were used to develop numerical models to investigate the instrumented control and reinforced test sections presented in Chapter 2. The recorded field data from the thermistor strings and SAAs were used to calibrate the numerical models using a fully-coupled approach and a sequentially-coupled approach for the control and reinforced sections, respectively. Once calibrated, parametric studies were done to investigate the influence of embankment height, slope inclination, reinforcement length, and reinforcement spacing on embankment performance. The following conclusions are made:

1. The fully-coupled approach used in the control section resulted to reasonably accurate results when calibrated against the recorded field data on temperatures and displacements using the actual air temperatures during the monitoring period. Using an average sinusoidal air temperature as an alternative boundary condition underestimated both the temperatures and displacements. Similar to the recorded field data, the largest incremental displacements occurred during the summer following winter construction.
2. The sequentially-coupled approach used to model the reinforced section slightly underestimated the horizontal displacements at the midslope. A comparable control section using the same approach showed that the geotextile layers installed reduced the horizontal displacements by as much as 40% in August 2018 (three years after the end of construction).

The non-wicking geotextile was also used as an alternative option in the reinforced model and the results show that there is still a reduction in displacements by 30% in August 2018. The large displacements occurring during the summer following winter construction was reduced by 31% using wicking geotextiles and by 15% using non-wicking geotextiles.

3. Embankments with thickness less than 2 m will have the entire embankment fill thawed during the summer following construction where the original permafrost table adjusted to the natural ground surface. Embankments with thickness more than 4 m will have a frozen core that will eventually be the new permafrost zone after 2 years following construction (aggradation of permafrost). The models however showed that this frozen core will reduce in size as warmer air temperatures become more prevalent due to climate change. A slope inclination less than 3H:1V will reduce the horizontal displacements at the crest and midslope of the embankments investigated. The general consequence of increased thickness and larger embankment volume (decrease of slope inclination) to mitigate displacements is increase in project costs.

4. The near-term and long-term climate change models applied to the control section, and a near-term model on the reinforced section overestimated the horizontal displacements for both test sections during the same scale of the three-year monitoring period. Using the results derived from climate change models without calibration against available field data may be conservative with the large displacements they provide that can lead to embankment overdesign. Care should be exercised in applying regional near-term and long-term climate change conditions.

5. Results from parametric reinforced models indicate that reducing the slope inclination is the most plausible option in mitigating the development of large horizontal displacements for thawing slopes. With prohibitive project costs to accommodate gentler slopes, geotextiles can

be used as an alternative strategy to have steeper slopes yet reduce the displacements. The benefit of installing geotextile layers is realized as long as there is a region where the geotextiles are still embedded within a frozen core and designed using a tighter vertical spacing between layers for cold region applications. Once the frozen core thaws, including when the entire length of the geotextile is above 0°C, the displacements are almost the same as the unreinforced embankment unless stiffer geotextiles are used to mitigate this.

Table 6.1. Summary of thermal properties for the embankment fill and foundation soil.

Property	Units	Temperature (°C)	Foundation	Temperature (°C)	Fill
Thermal conductivity	J/days·m·°C	-0.5	120000	-1	163948
		0	45000	0	122500
Specific heat	J/kg·°C	-0.5	2756	-0.5	890
		0	5086	0	1160
Latent heat	J/kg	Solidus: -0.5 Liquidus: 1	334000	Solidus: -2 Liquidus: 0	21850
Density	kg/m^3	---	1039.8	---	1625.9

Table 6.2. Summary of mechanical properties for the embankment fill and foundation soil.

Property	Units	Temperature (°C)	Foundation	Temperature (°C)	Fill
Material cohesion (d)	Pa	-1	25000	-1	21764.4
		0	7294.1	0	7115.4
Angle of friction (β)	°	-1	51.2	-1	49.4
		0	39.5	0	37.3
Elastic modulus (E)	Pa	-1	100000000	-1	214000000
		0	130000	0	150000
Poisson's ratio (ν)	---	-1	0.25	-1	0.25
		0	0.3	0	0.3
Lambda (λ)	---	-1	0.006	-1	0.006
		0	1.6	0	0.9
Kappa (κ)	---	-1	0.0008	-1	0.0008
		0	0.2	0	0.02
Hydraulic conductivity (k)	m/day	-1	1E-8	-1	1E-8
		0	0.00226 (e_o = 5.0) 0.00076 (e_o = 0.1)	0	0.001 (e_o = 0.64) 0.005 (e_o = 0.72)
Density	kg/m^3	---	1039.8	---	1625.9

Table 6.3. Summary of mechanical and interface properties for wicking and non-wicking geotextiles.

Type of Geotextile	Elastic Modulus (Pa)	Interface Properties (°)		
		Both conditions	At 2% strain	At EOT
		Frozen (at -1°C)	Thawed (at 0°C)	Thawed (at 0°C)
Wicking	150000000	50 (1.1918)	5.8 (0.1016)	7.7 (0.1352)
Non-wicking	150000000	50 (1.1918)	4.3 (0.0752)	6.3 (0.1104)

Note: Numbers in parentheses are the equivalent values of the interface property as $\tan\phi$.

Table 6.4. Summary of thermal modifiers used on embankment and foundation surfaces.

Location	$n_{freezing}$	$n_{thawing}$
Top	0.95	1.00
Slope Top	0.92	1.00
Slope Middle	0.83	1.00
Slope Bottom	0.55	1.00
Toe	0.20	0.55
Prairie	0.20	0.45

Table 6.5. Summary of solid and staged models for the control and reinforced test sections.

Model Approach	Control Section		Reinforced Section
	Fully-coupled (CP)	Sequentially-coupled (SQ)	Sequentially-coupled (SQ)
Solid	CCP	CSQ	---
Staged	UCP	USQ	RSQ

Table 6.6. Models attributes analyzed for the control and reinforced test sections.

Boundary condition		Control Section		Reinforced section
		Solid (C)	Staged (U)	Staged (R)
Three-year data	Actual	-3yrAct	-3yrAct	-3yrAct
	Average	-3yrAve	---	---
Near-term conditions	d2005i1	-d05i1	---	---
	d2005i2	-d05i2	---	---
	d2015	-d15	-d15	-d15
Long-term conditions	RCP 2.6	-rcp26	---	---
	RCP 4.5	-rcp45	---	---
	RCP 8.5	-rcp85	---	---

Note: Heat transfer (CHT, UHT, RHT) models for both test sections, fully-coupled (CCP, UCP) for the control section, and sequentially-coupled (CSQ, USQ, RSQ) for both test sections were analyzed.

Table 6.7. Models analyzed for parametric studies on unreinforced embankments using CCP approach.

Embankment height	Slope inclination		
	2H:1V (S2)	3H:1V (S3)	4H:1V (S4)
2 m (H2)	H2S2	H2S2	H2S2
4 m (H4)	H4S2	H4S4	H4S4
6 m (H6)	H6S2	H6S6	H6S6

Note: Heat transfer (PHT) and fully-coupled (PCP) models were analyzed. Three-year actual temperature, near-term and long-term climate change conditions were analyzed for all heat transfer cases. Three-year actual temperature and d2015 conditions were analyzed for fully-coupled cases.

Table 6.8. Models analyzed for parametric studies on reinforced embankments using RSQ approach.

Slope inclination	Reinforcement length	Reinforcement spacing	Wicking geotextile
2H:1V (S2)	6 m	0.60 m	S2L6Sp6-W
		0.90 m	S2L6Sp9-W
	8 m	0.60 m	S2L8Sp6-W
		0.90 m	S2L8Sp9-W
3H:1V (S3)	6 m	0.60 m	S3L6Sp6-W
		0.90 m	S3L6Sp9-W
	8 m	0.60 m	S3L8Sp6-W
		0.90 m	S3L8Sp9-W

Note: Heat transfer (PRHT) and sequentially-coupled (PRSQ) models were analyzed. Three-year actual temperature and d2015 conditions were analyzed for sequentially-coupled cases.

Table 6.9. Models analyzed for parametric studies on unreinforced embankments using USQ approach.

Slope inclination	Fill layer spacing	Staged (U)
2H:1V (S2)	0.60 m	S2Sp6
	0.90 m	S2Sp9
3H:1V (S3)	0.60 m	S3Sp6
	0.90 m	S3Sp9

Note: Heat transfer (PUHT) and sequentially-coupled (PUSQ) models were analyzed. Three-year actual temperature conditions were analyzed for sequentially-coupled cases.

Table 6.10. Change in thaw distances at different locations in the embankment between August 2015 and August 2018.

Slope Inclination	Embankment Height	With respect to vertical (m)		With respect to horizontal (m)
		Crest	Midslope	Midheight
2H:1V (S2)	2 m	0.5	0.3	Completely thawed
	4 m	0.6	0.5	2.2
	6 m	0.6	1.2	1.2
3H:1V (S3)	2 m	0.5	0.3	Completely thawed
	4 m	0.6	0.5	2.4
	6 m	0.6	1.2	1.8
4H:1V (S4)	2 m	0.5	0.3	Completely thawed
	4 m	0.6	0.5	2.9
	6 m	0.3	0.9	1.9

Table 6.11. Horizontal displacements at the embankment crest for varying embankment heights and slope configurations.

Slope Inclination	Embankment Height	Horizontal displacements (mm)		Δ_{max} (mm)	% reduction
		August 2015	August 2018		
2H:1V (S2)	2 m*	59.7	155.3	95.6	---
	4 m	102.9	478.2	375.3	---
	6 m	98.4	346.7	248.3	---
3H:1V (S3)	2 m*	43.5	120.7	77.2	19.3
	4 m	61.2	228.4	167.2	55.4
	6 m	59.3	138	78.7	68.3
4H:1V (S4)	2 m*	35.6	101.5	65.9	31.1
	4 m	43.9	130.3	86.4	77.0
	6 m	38.3	76.9	38.6	84.5

* Maximum displacements observed at midheight of the embankment.

Table 6.12. Horizontal displacements at the embankment midslope for varying embankment heights and slope configurations.

Slope Inclination	Embankment Height	Horizontal displacements (mm)		Δ_{max} (mm)	% reduction
		August 2015	August 2018		
2H:1V (S2)	2 m	71.3	178.4	107.1	---
	4 m	125.6	410.6	285.0	---
	6 m	150.1	546.2	396.1	---
3H:1V (S3)	2 m	54.7	133.7	79.0	26.3
	4 m	95.6	242.8	147.2	48.4
	6 m	115.1	360.3	245.2	38.1
4H:1V (S4)	2 m	43.0	84.8	41.8	61.0
	4 m	79.2	166.4	87.2	69.4
	6 m	85.7	253.6	167.9	57.6

Table 6.13. Vertical displacements along embankment midheight for varying embankment heights and slope configurations.

Slope Inclination	Embankment Height	Vertical displacements at outermost node (mm)		Δ_{max} (mm)	Vertical displacements underneath crest (mm)		Δ_{max} (mm)
		August 2015	August 2018		August 2015	August 2018	
2H:1V (S2)	2 m	41.6	65.6	24.0	56.0	244.1	188.1
	4 m	118.2	476	357.8		Still frozen	
	6 m	122.0	447.1	325.1		Still frozen	
3H:1V (S3)	2 m	37.4	61.2	23.8	48.6	229.6	181.0
	4 m	98.4	285.5	187.1		Still frozen	
	6 m	87.9	306.5	218.6		Still frozen	
4H:1V (S4)	2 m	38.7	65.8	27.1	44.8	224.6	179.8
	4 m	78.4	348.4	270.0		Still frozen	
	6 m	67.5	244.1	176.6		Still frozen	

Fig. 6.1. Model cross-section for solid section.

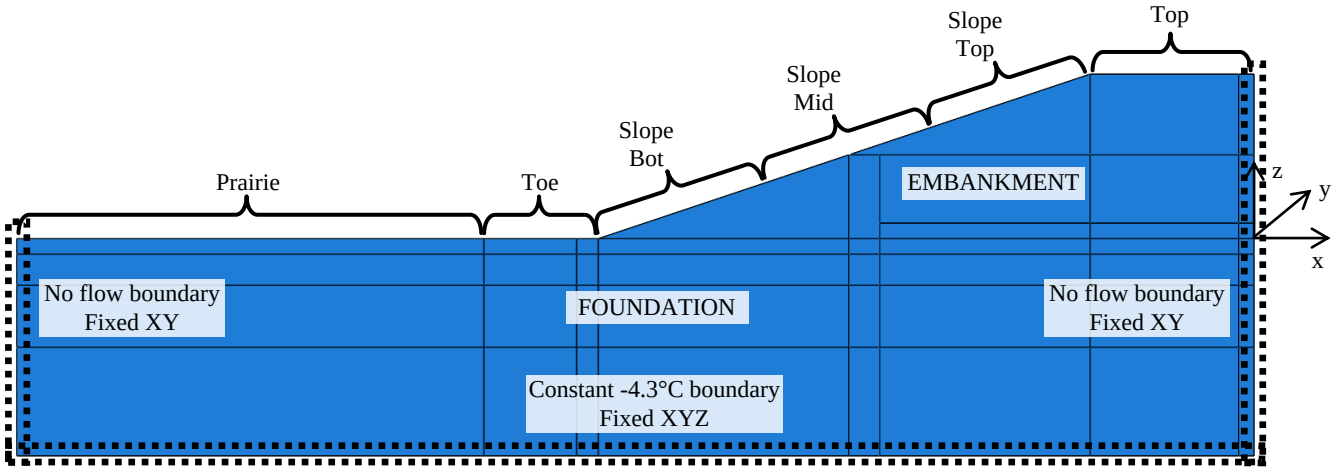

Fig. 6.2. Model cross-section for staged section.

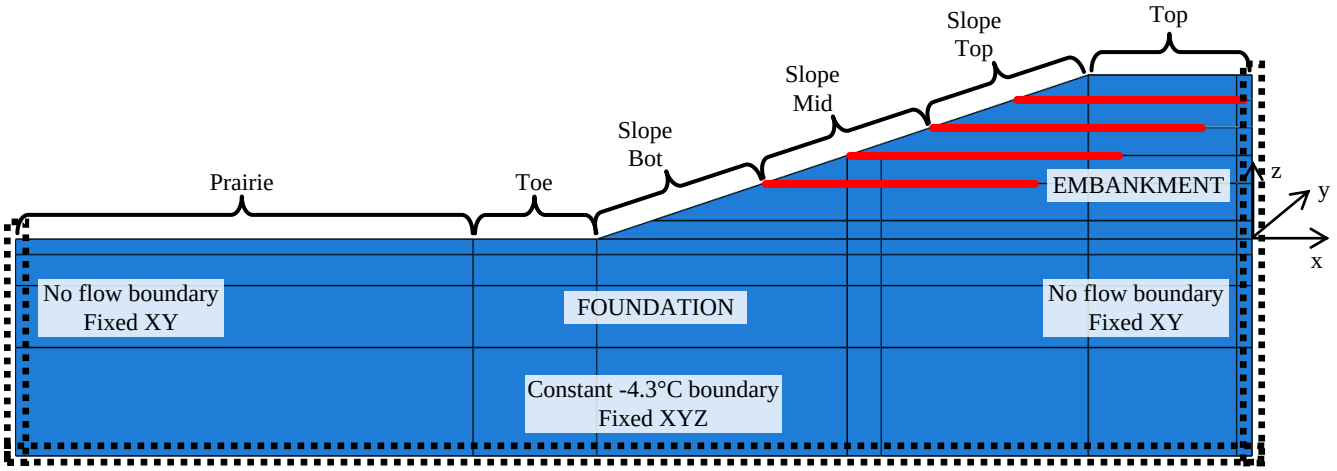

Fig. 6.3. Comparison of actual and average sinusoidal air temperatures at the research site.

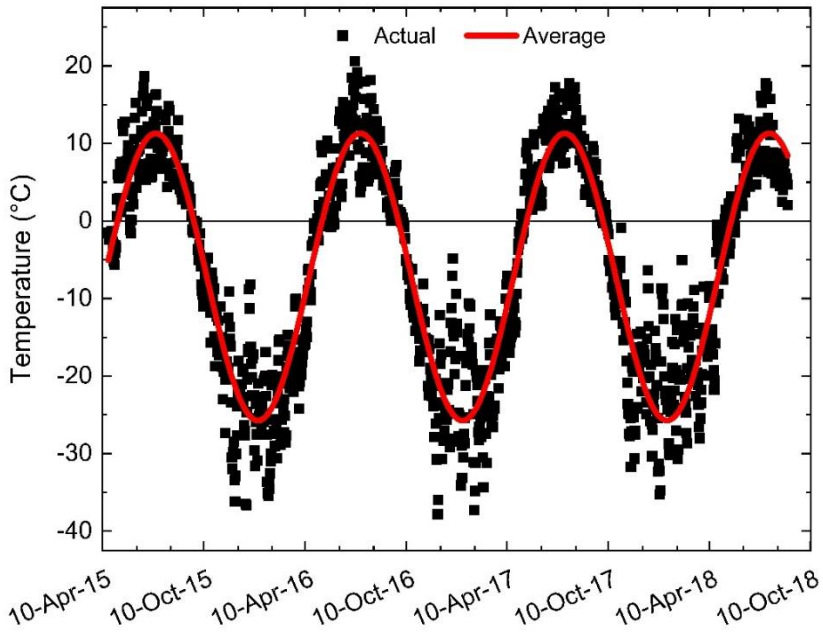

Fig. 6.4. Select observation locations for temperature and displacement comparisons in the control section (CHT, CCP, CSQ).

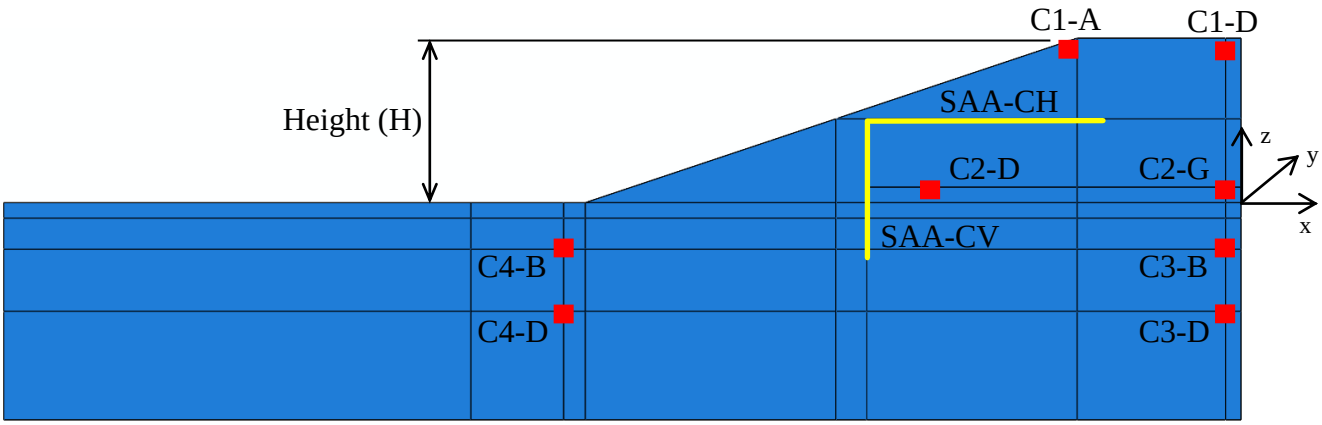

Fig. 6.5. Select observation locations for displacement comparisons in the reinforced and staged sections (UCP, USQ, RSQ).

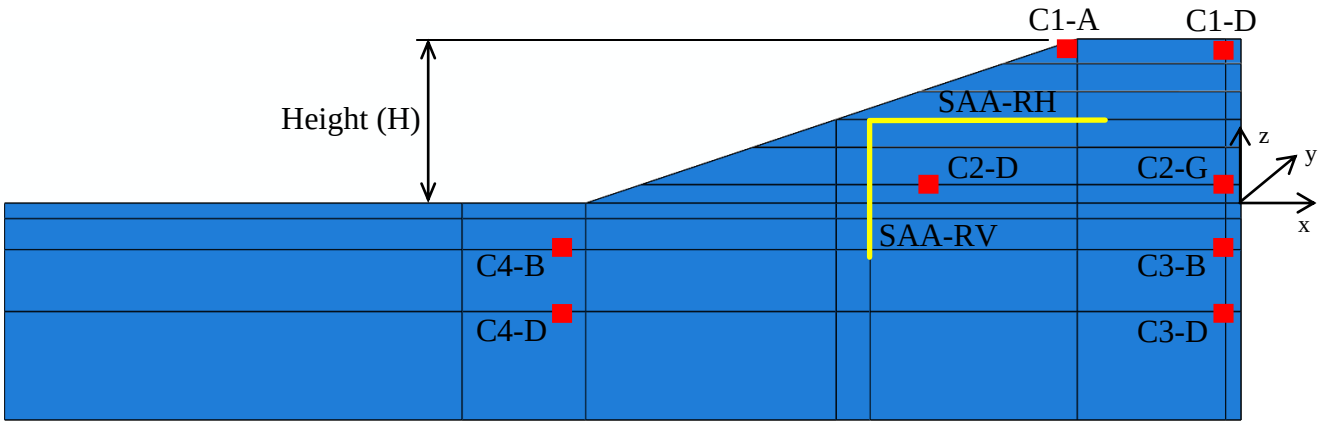

Fig. 6.6. Comparison of model temperatures between average sinusoidal (-3yrAve) and actual (-3yrAct) temperature boundaries in CCP models with thermistor values at select nodal locations: (a) C1-A and C1-D, (b) C2-C and C2-G, (c) C3-B and C3-D, and (d) C4-B and C4-D.

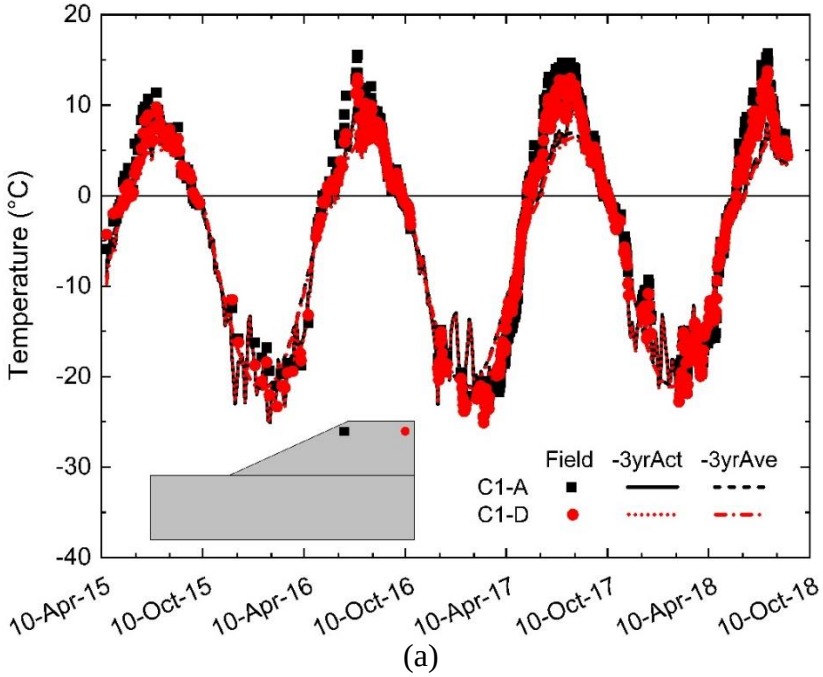

(a)

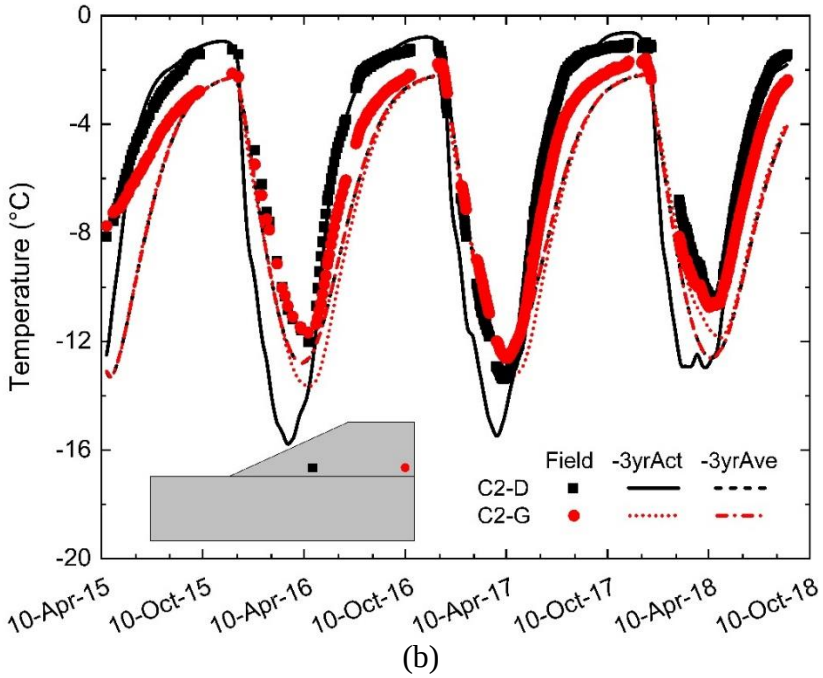

(b)

Fig. 6.6 (continued)

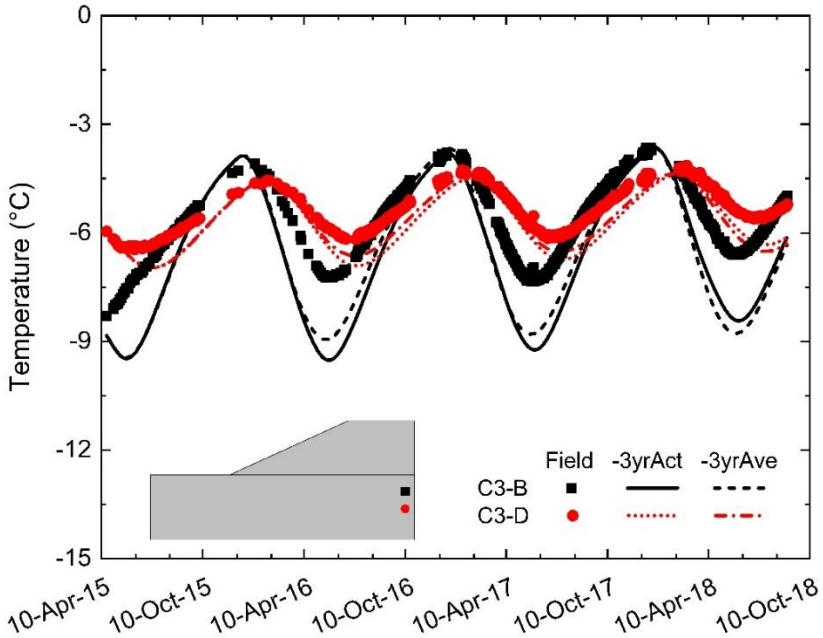

(c)

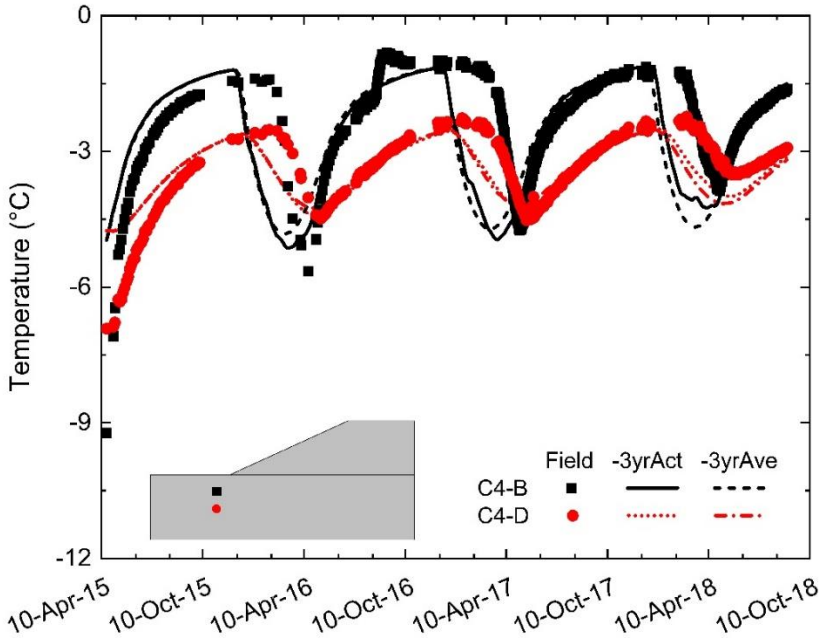

(d)

Fig. 6.7. Comparison of model temperatures between pure heat transfer (CHT) and fully-coupled (CCP) analyses with thermistor values at select nodal locations using -3yrAct: (a) C1-A and C1-D, (b) C2-C and C2-G, (c) C3-B and C3-D, and (d) C4-B and C4-D.

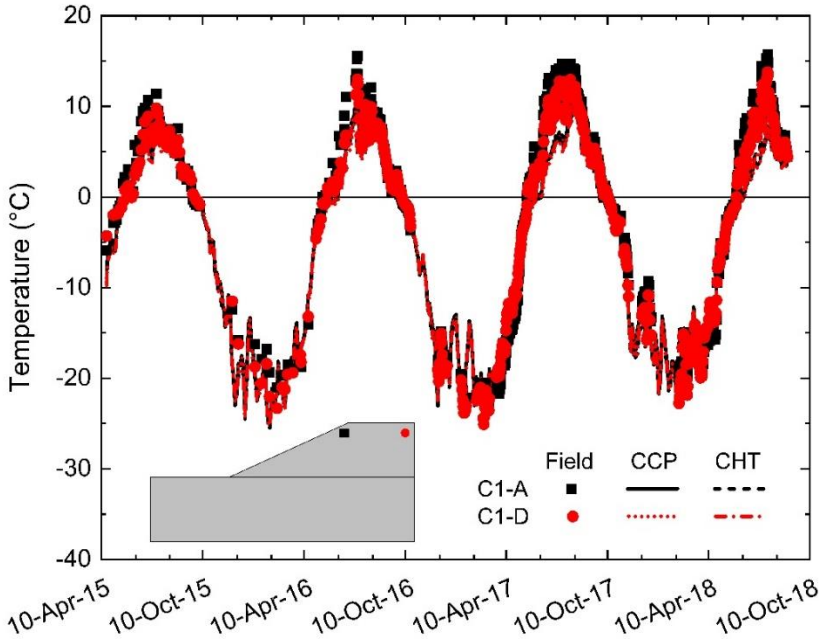

(a)

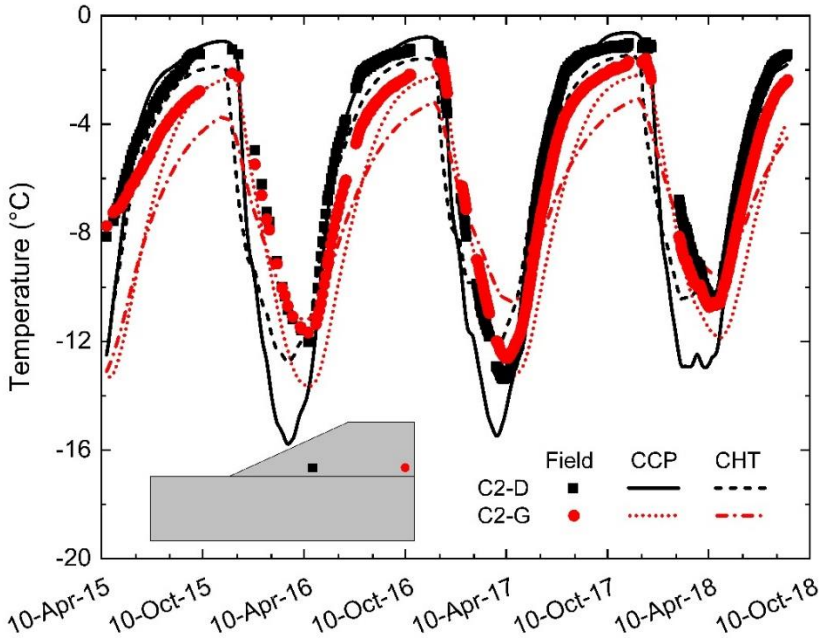

(b)

Fig. 6.7 (continued)

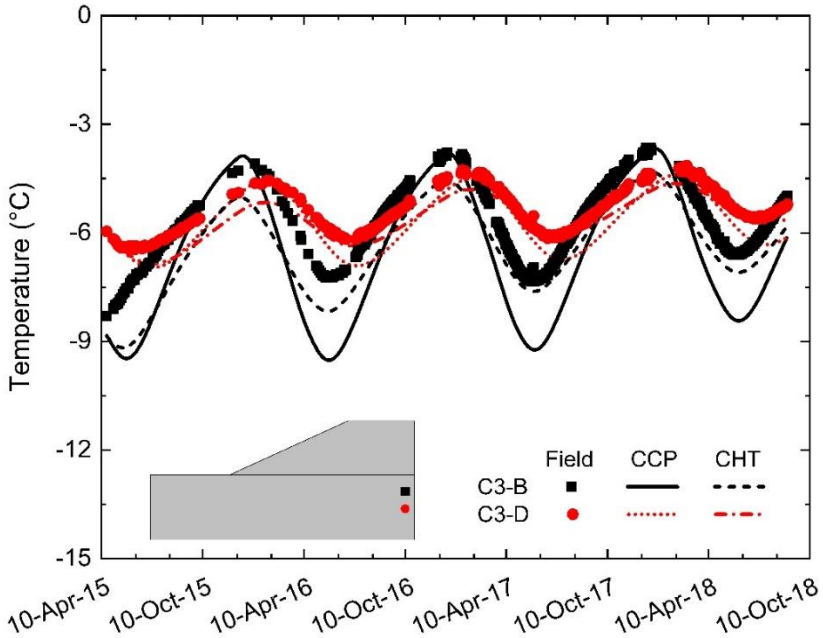

(c)

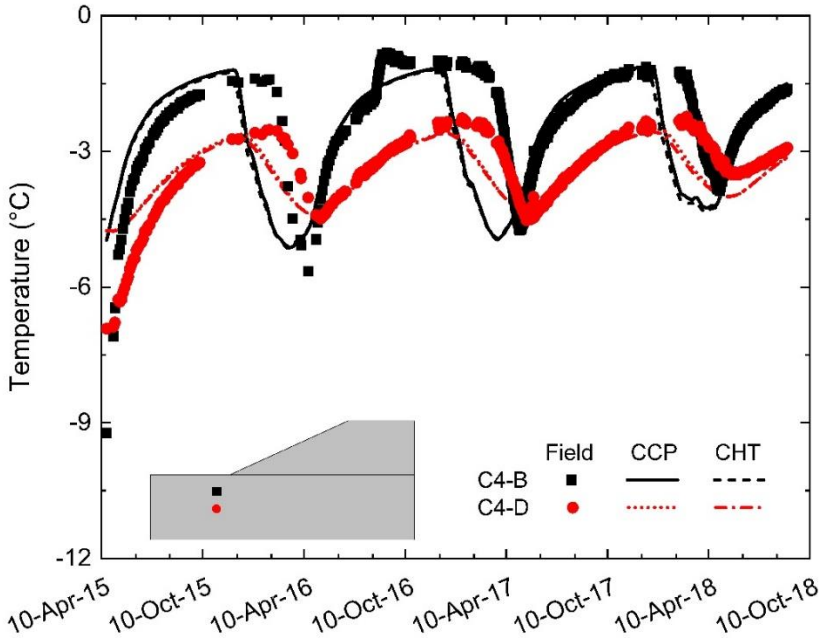

(d)

Fig. 6.8. Maximum extent of thawed state contours between (a) pure heat transfer (CHT) and (b) fully-coupled (CCP) analyses.

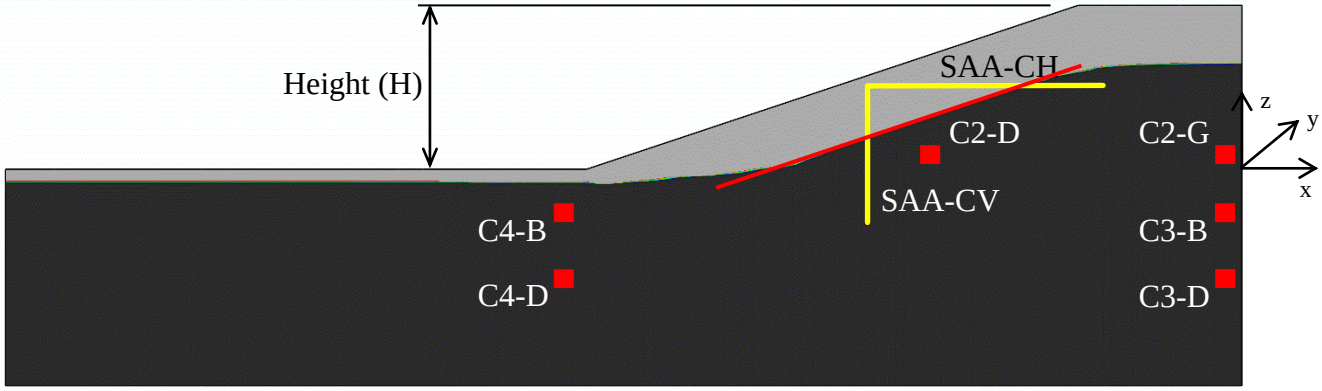

(a)

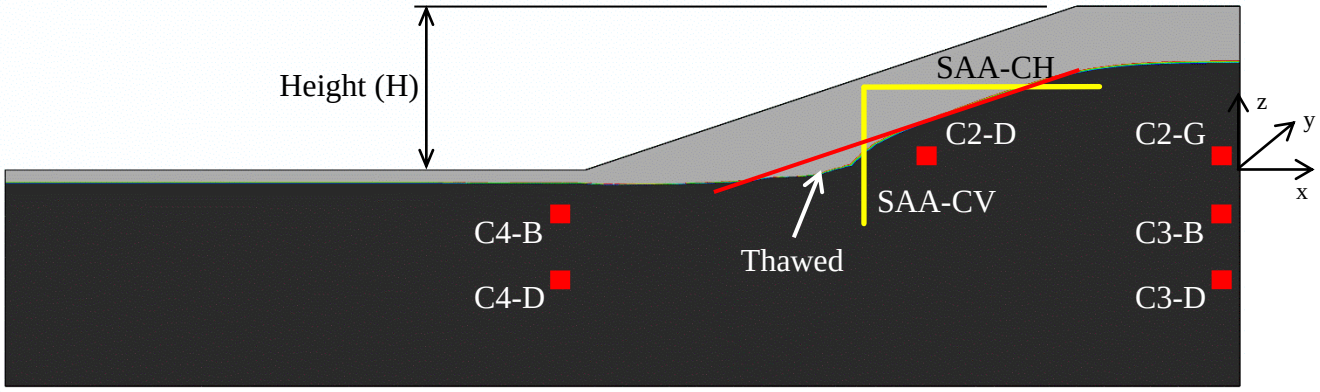

(b)

Fig. 6.9. Comparison of (a) horizontal and (b) vertical displacements between measured field values and model results for the control section using CP approach.

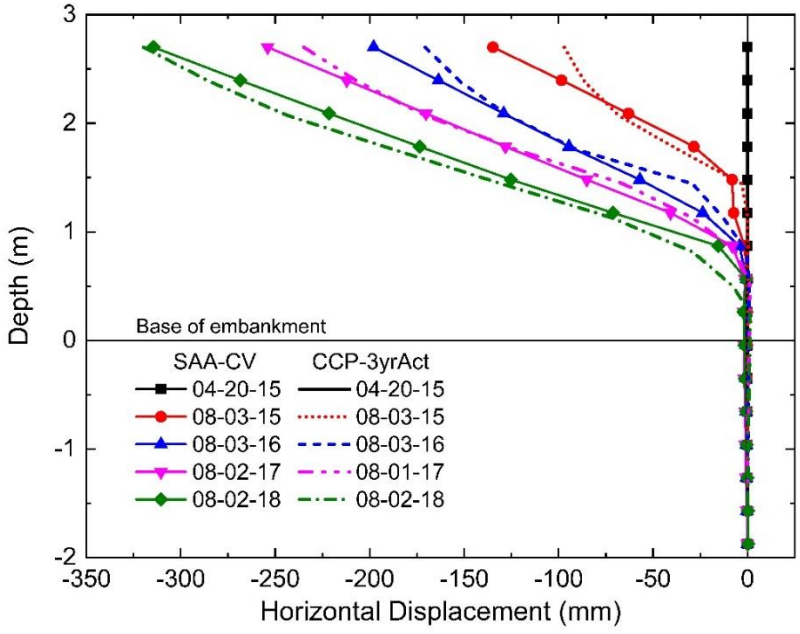

(a)

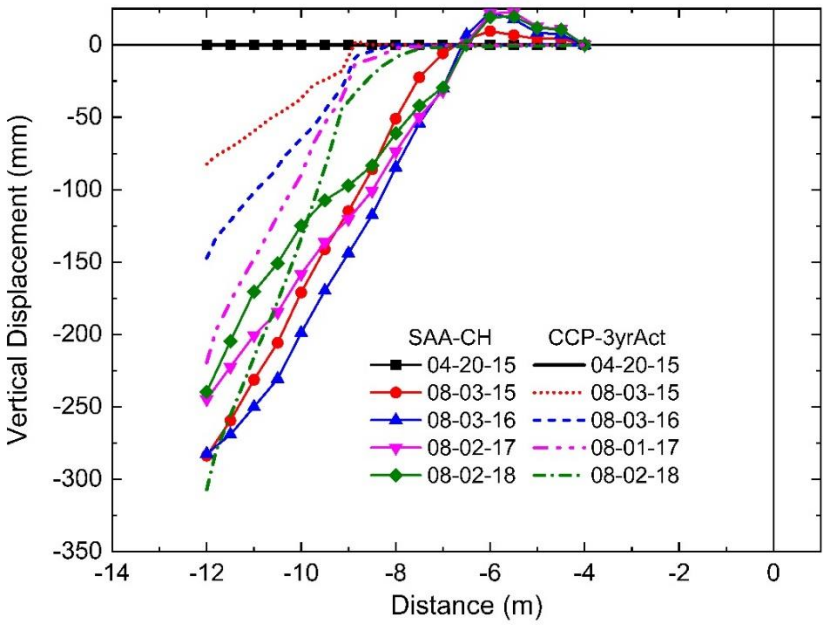

(b)

Fig. 6.10. Horizontal displacement with respect to time at the top of SAA-CV compared with CCP model result.

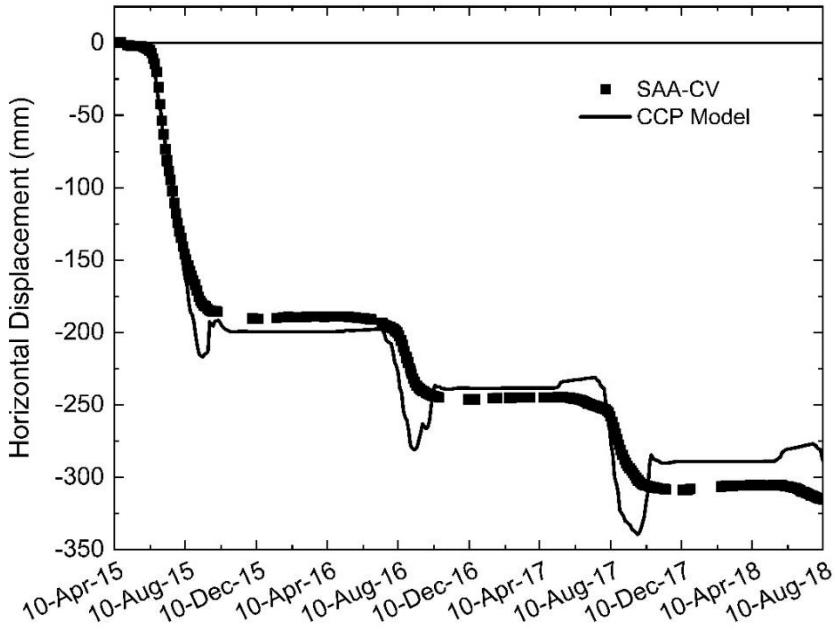

Fig. 6.11. Global displacement vectors for control test section in (a) August 2015 and (b) August 2018. Contour scale are in metres.

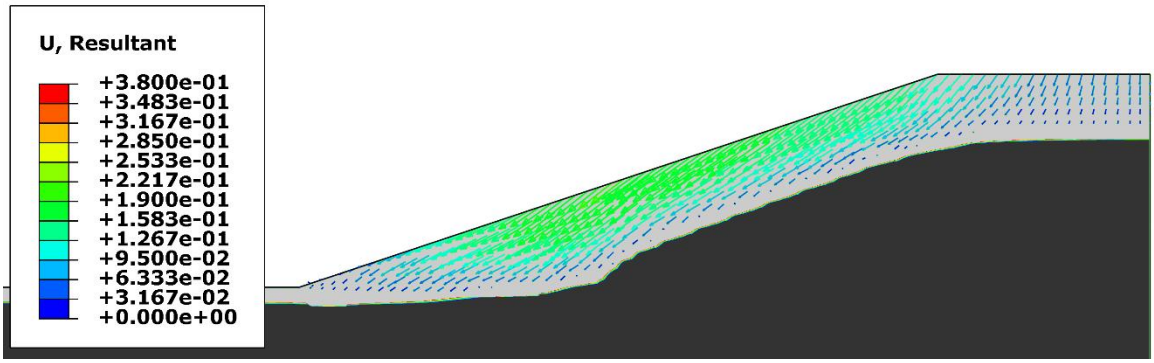

(a)

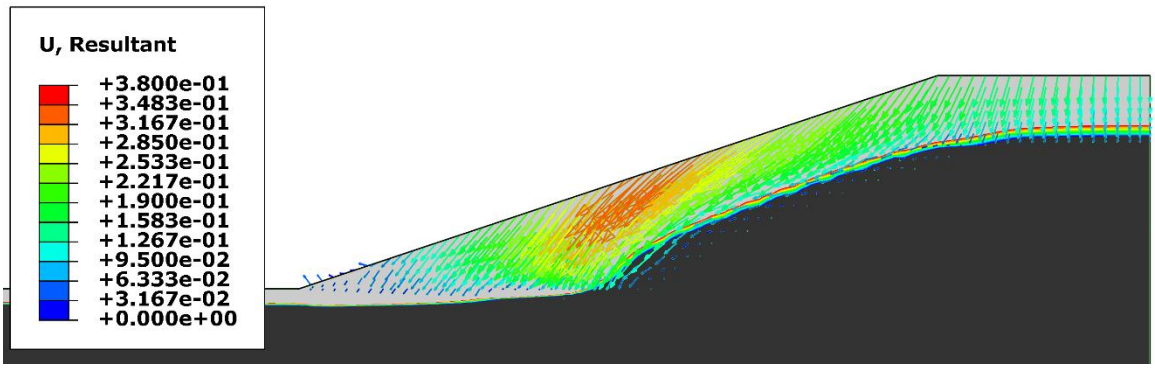

(b)

Fig. 6.12. Comparison of (a) horizontal and (b) vertical displacements between -3yrAct and -3yrAve boundary conditions for the control section using CP approach

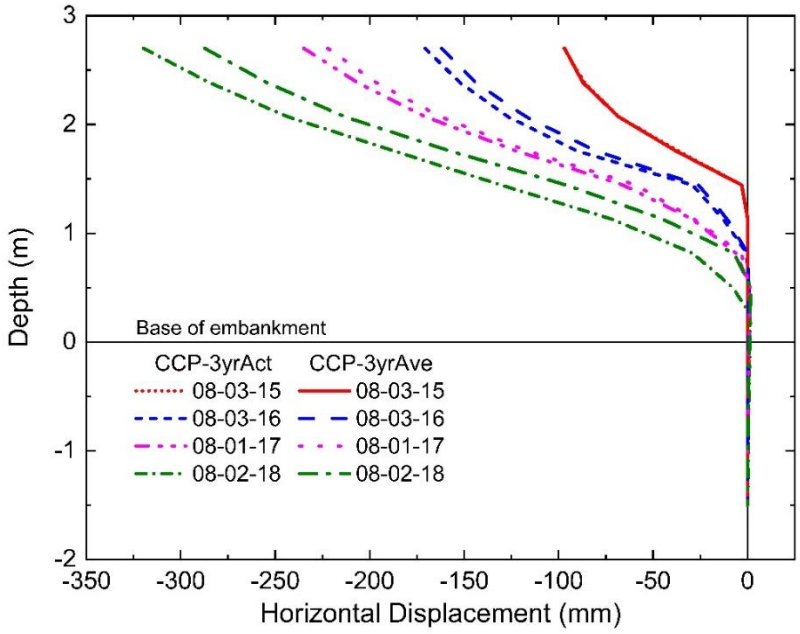

(a)

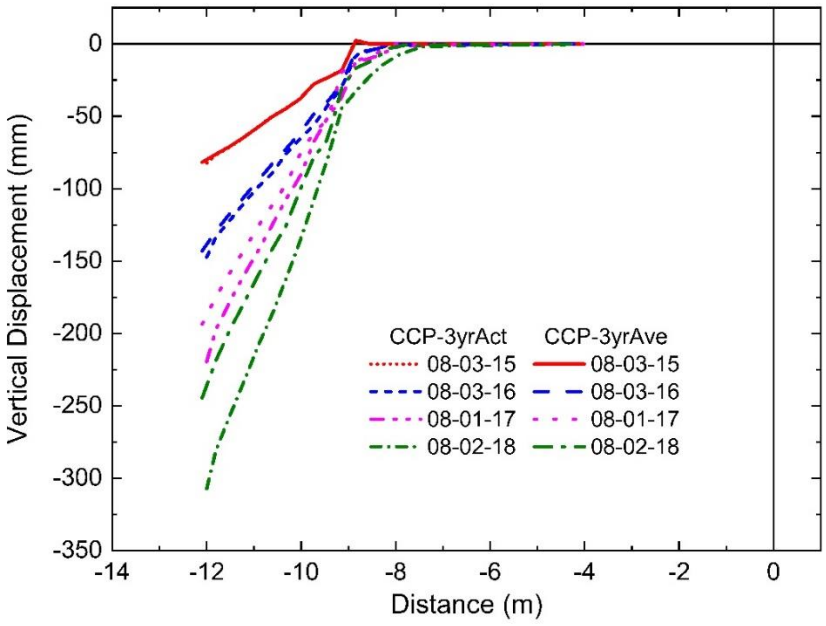

(b)

Fig. 6.13. Comparison of horizontal displacements for the control section between CCP, CSQ, UCP, and USQ: (a) Years 1 and 2 and (b) Years 3 and 4.

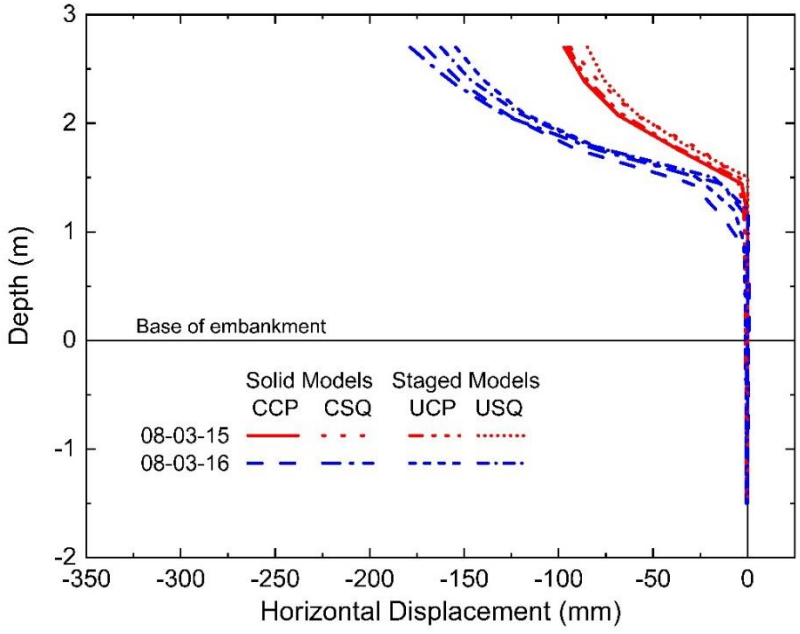

(a)

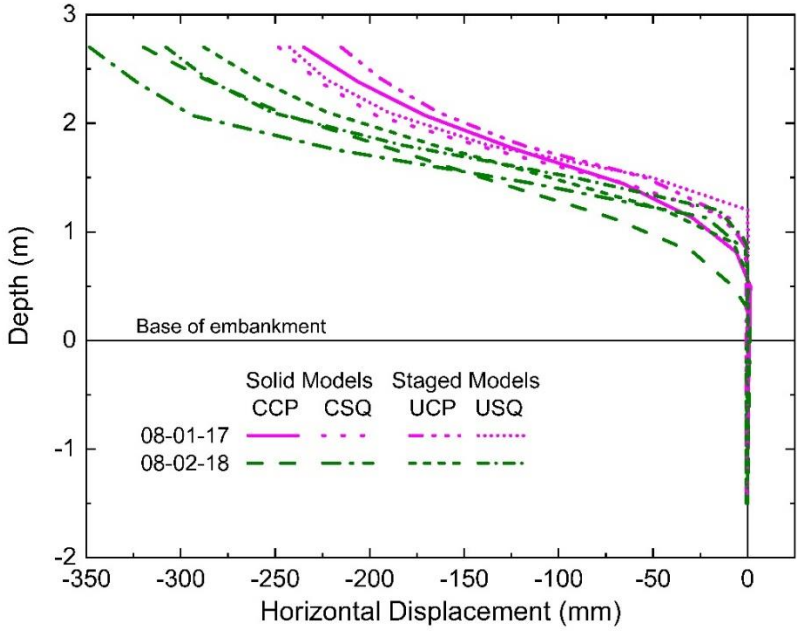

(b)

Fig. 6.14. Comparison of vertical displacements for the control section between CCP, CSQ, UCP, and USQ: (a) Years 1 and 2 and (b) Years 3 and 4.

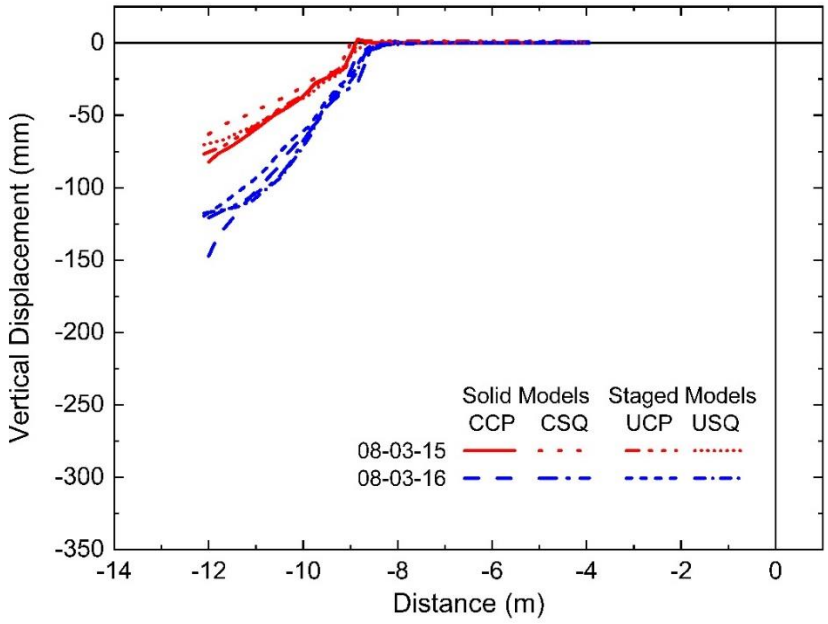

(a)

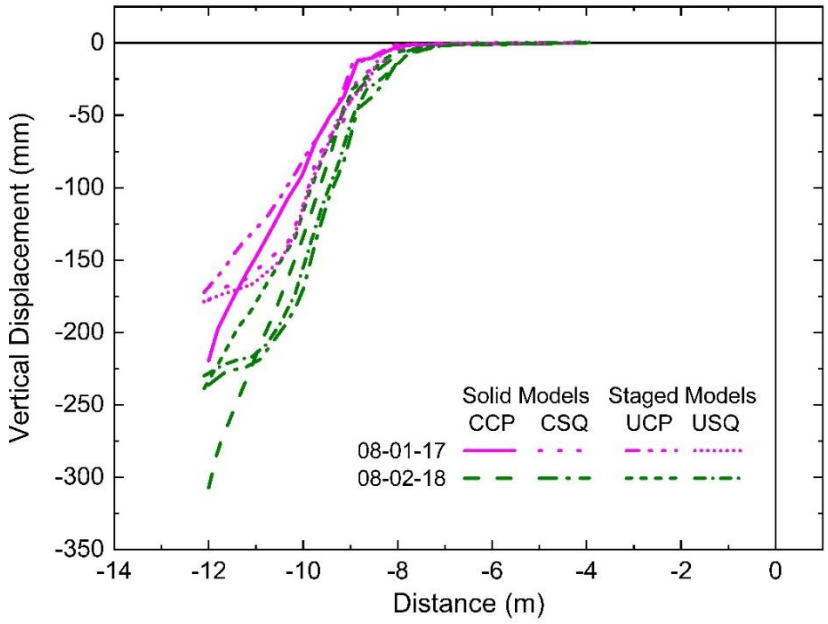

(b)

Fig. 6.15. Comparison of (a) horizontal and (b) vertical displacements between measured field values and model results for reinforced section using SQ approach.

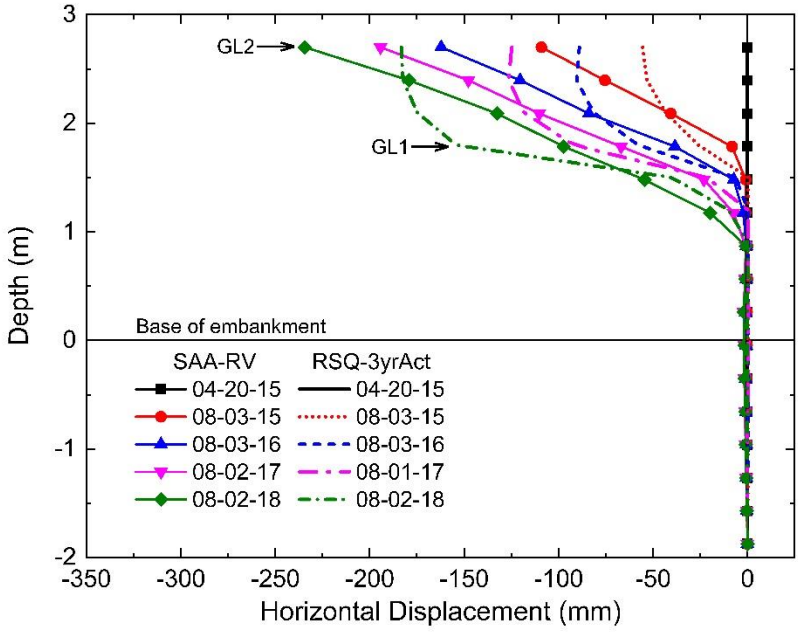

(a)

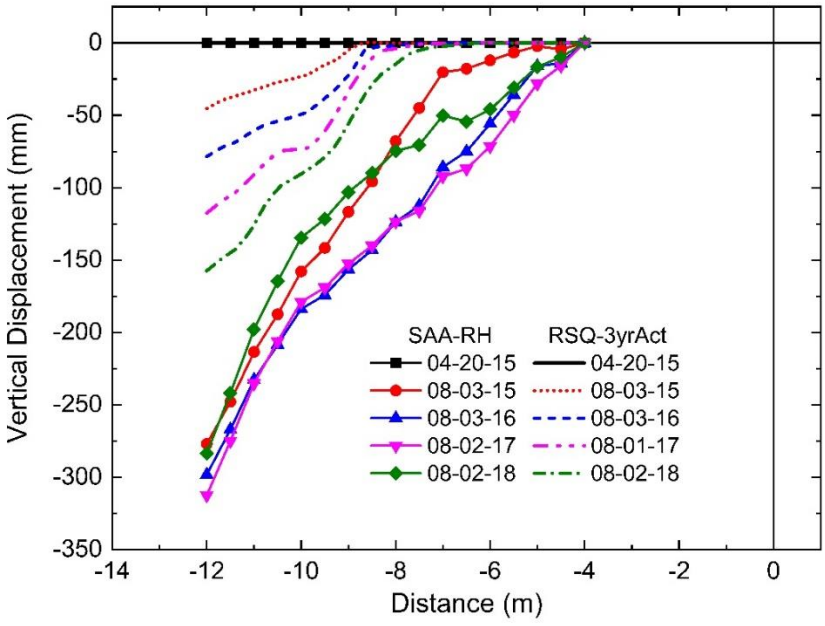

(b)

Fig. 6.16. Global displacement vectors for reinforced test section in (a) August 2015 and (b) August 2018. Contour scale are in metres.

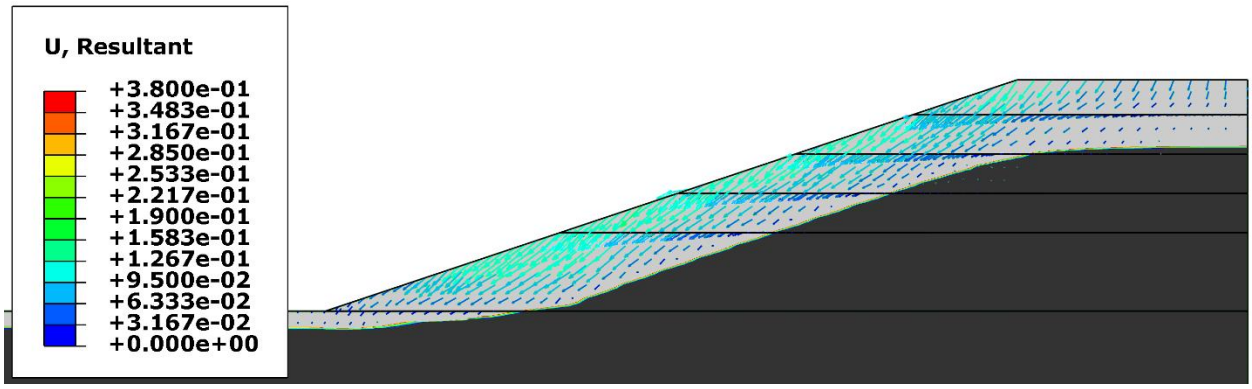

(a)

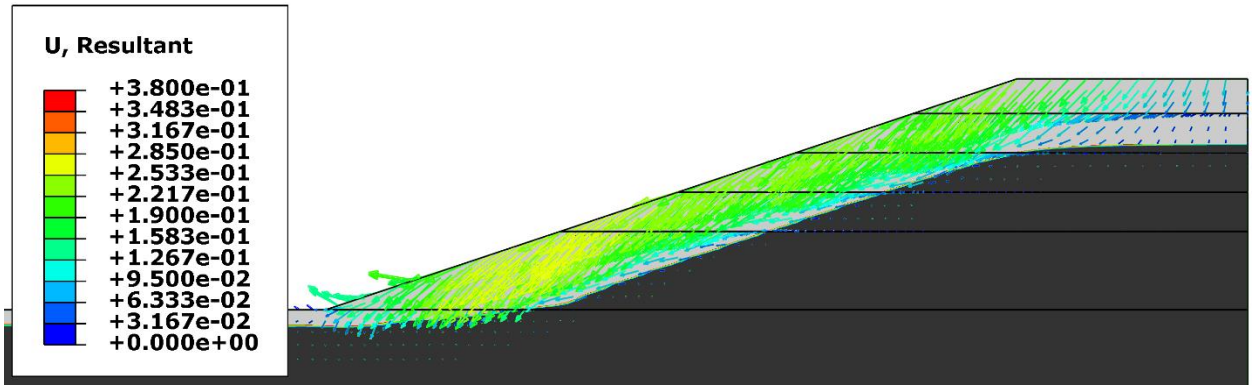

(b)

Fig. 6.17. Comparison of (a) horizontal and (b) vertical displacements between unreinforced (USQ) and reinforced (RSQ) results using sequential approach.

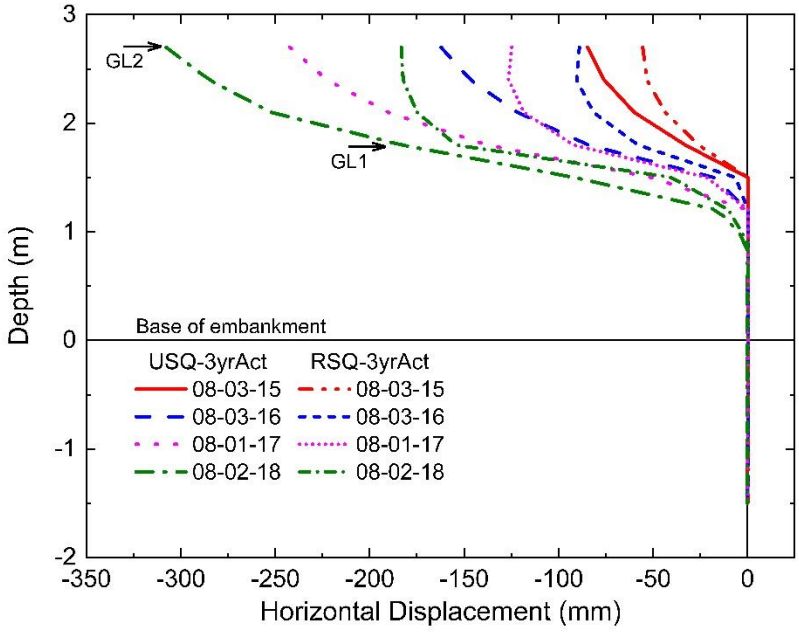

(a)

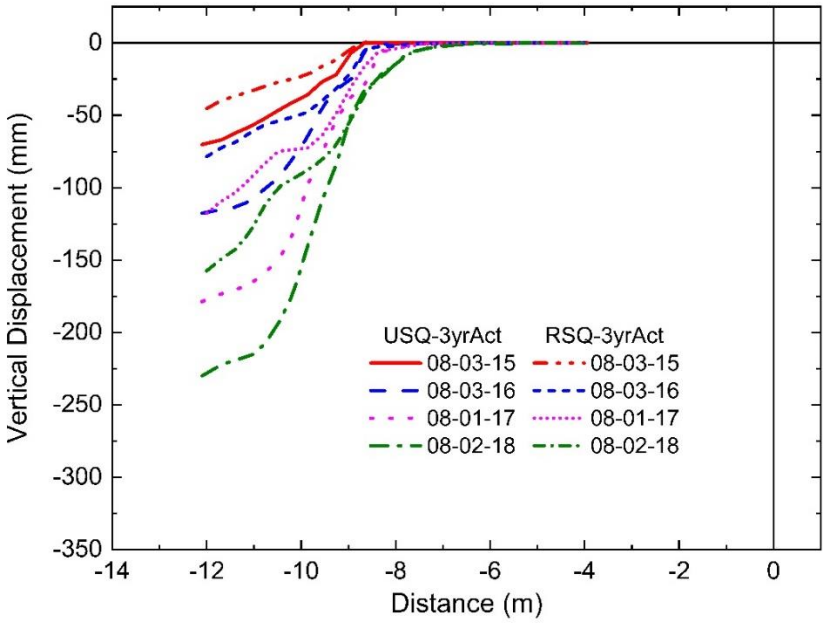

(b)

Fig. 6.18. Horizontal displacements along geotextile layers in RSQ model: (a) Layer 1 at 1.8 m, (b) Layer 2 at 2.7 m, (c) Layer 3 at 3.6 m, and (d) Layer 4 at 4.5 m.

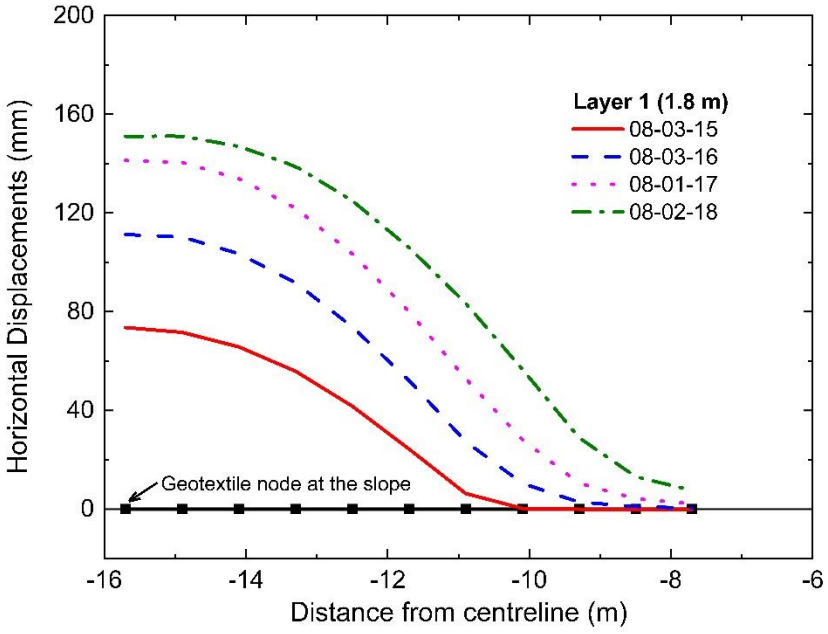

(a)

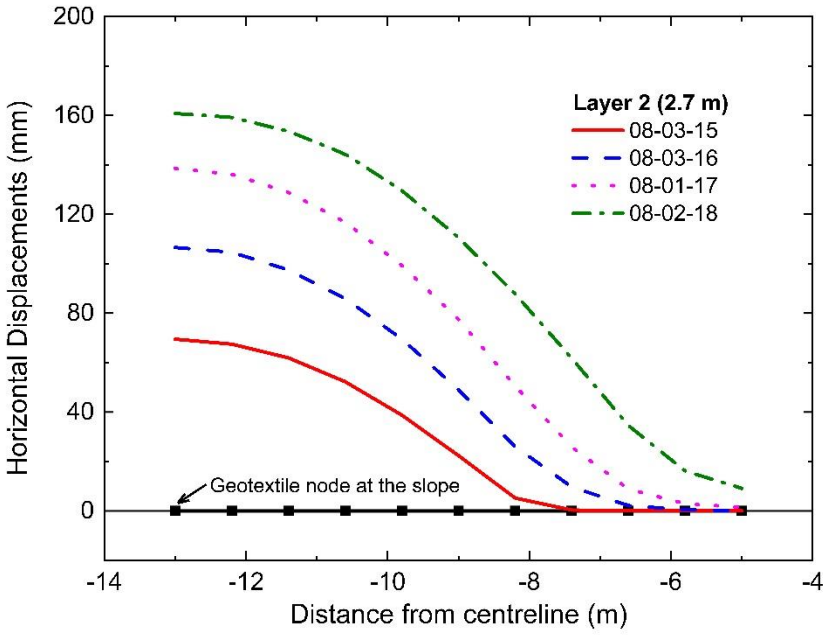

(b)

Fig. 6.18 (continued)

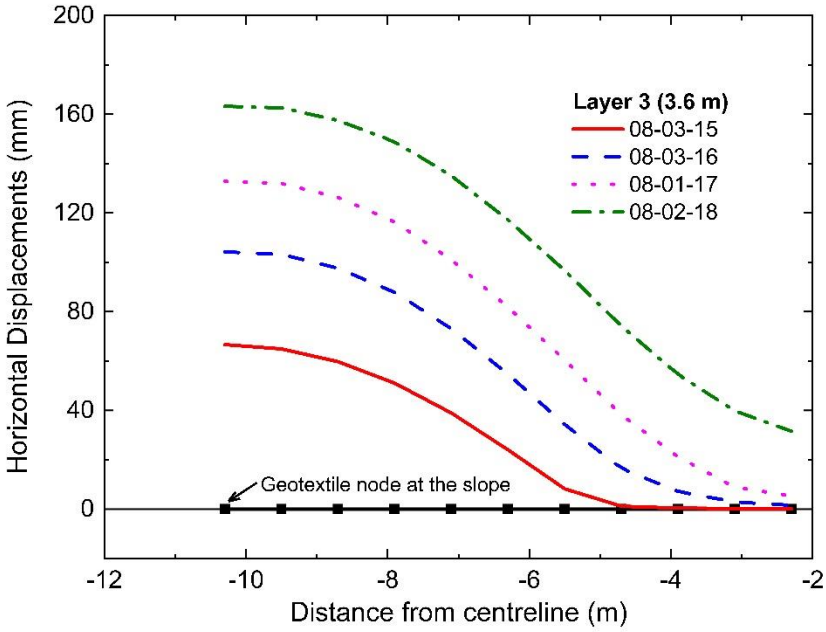

(c)

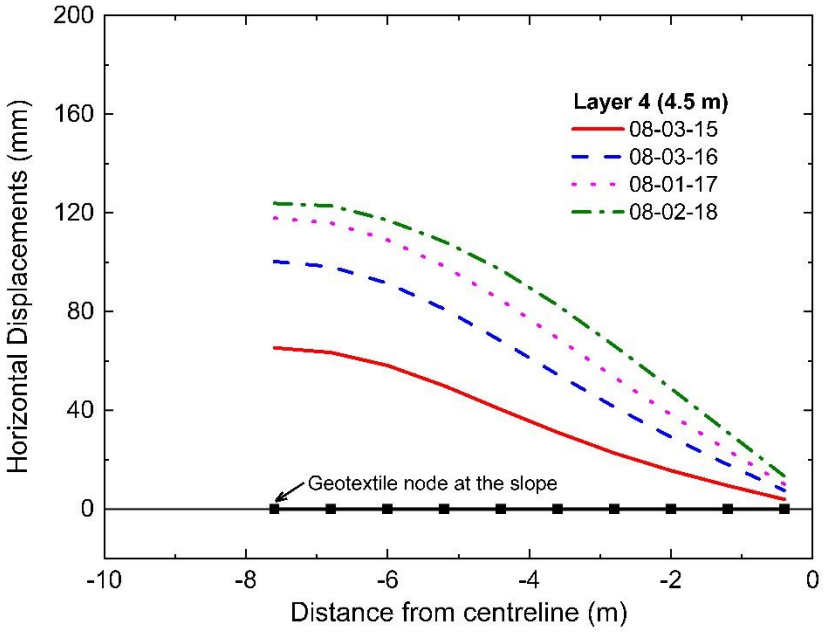

(d)

Fig. 6.19. Strains along geotextile layers in RSQ model: (a) Layer 1 at 1.8 m, (b) Layer 2 at 2.7 m, (c) Layer 3 at 3.6 m, and (d) Layer 4 at 4.5 m.

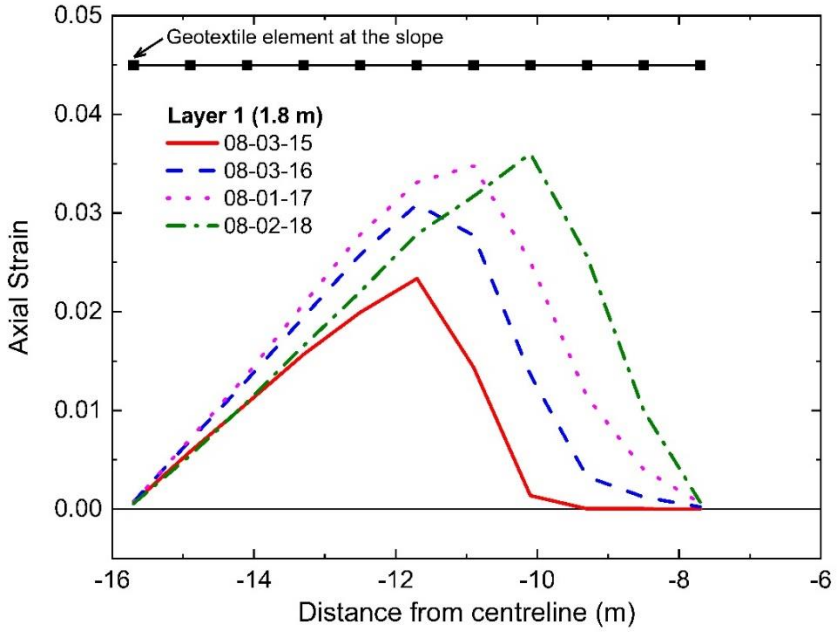

(a)

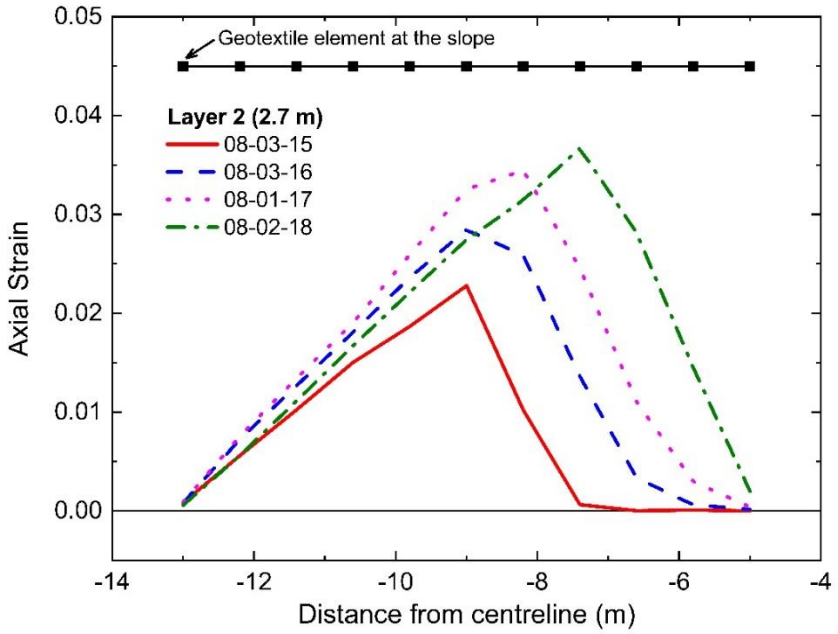

(b)

Fig. 6.19 (continued)

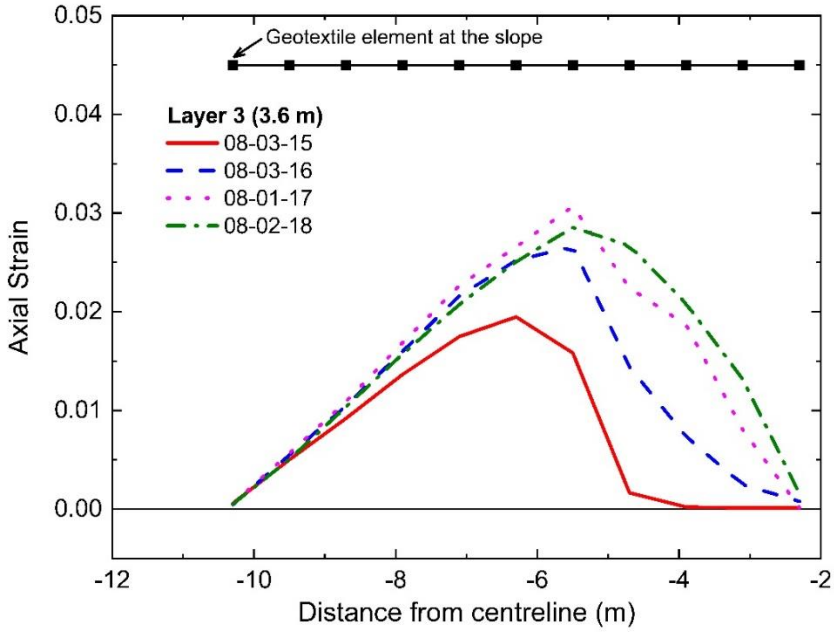

(c)

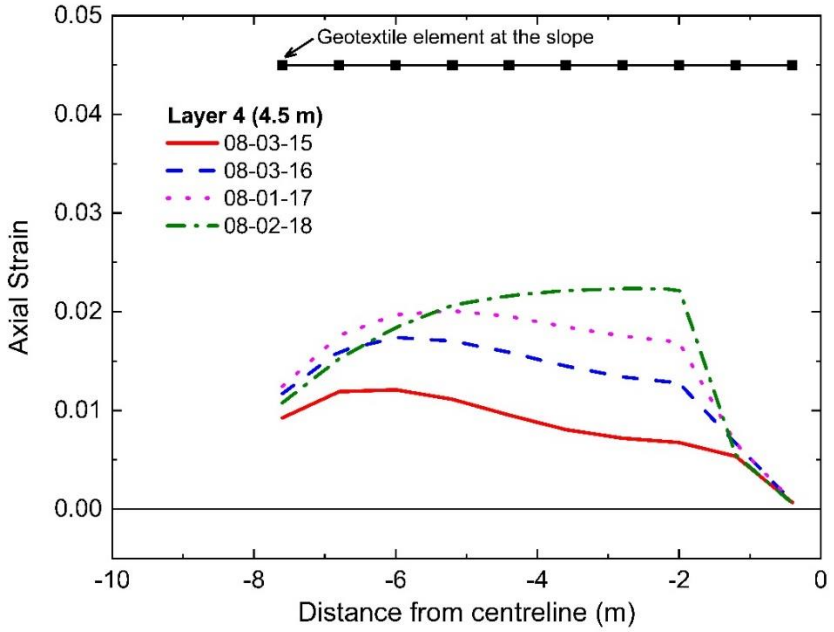

(d)

Fig. 6.20. Comparison of horizontal displacements at midslope of RSQ model between wicking and non-wicking geotextiles.

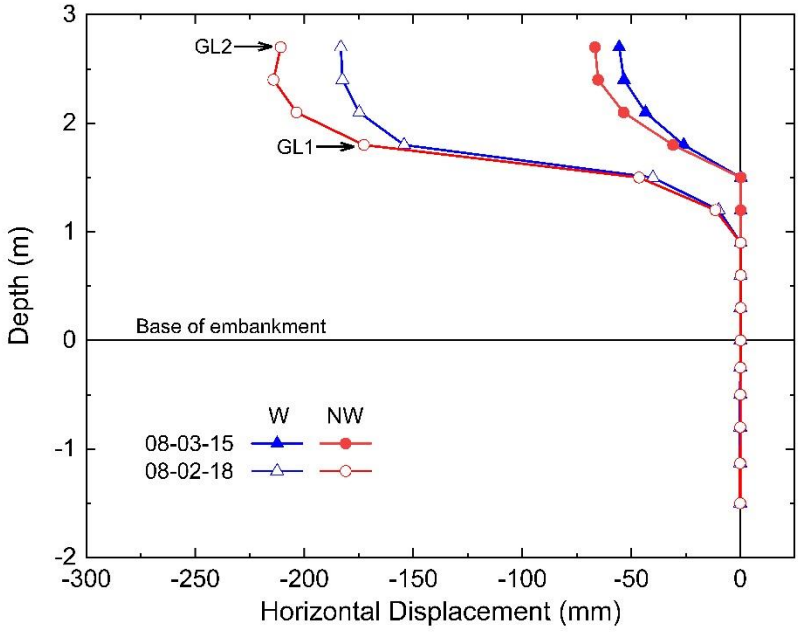

Fig. 6.21. Model cross-sections for parametric studies on reinforced embankments: (a) 2H:1V and s = 0.6 m, (b) 2H:1V and s = 0.9 m, (c) 3H:1V and s = 0.6 m, (d) 3H:1V and s = 0.9 m. Dashed line along midslope shows location of observation points. Reinforcement length simulated varies from 6 m and 8 m.

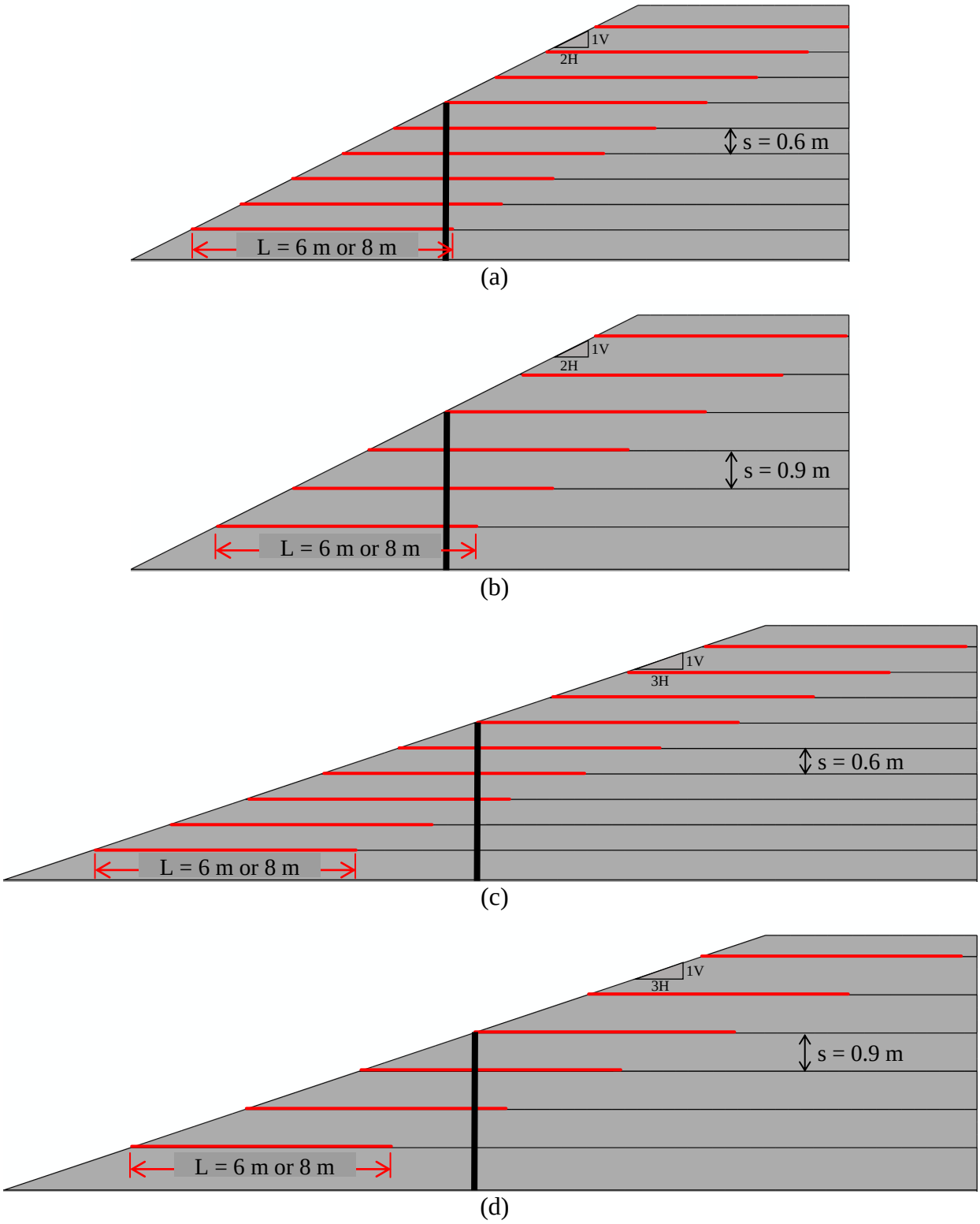

Fig. 6.22. Model horizontal displacements for 2 m embankments at (a) crest, (b) midslope, and (c) midheight for different slope configurations.

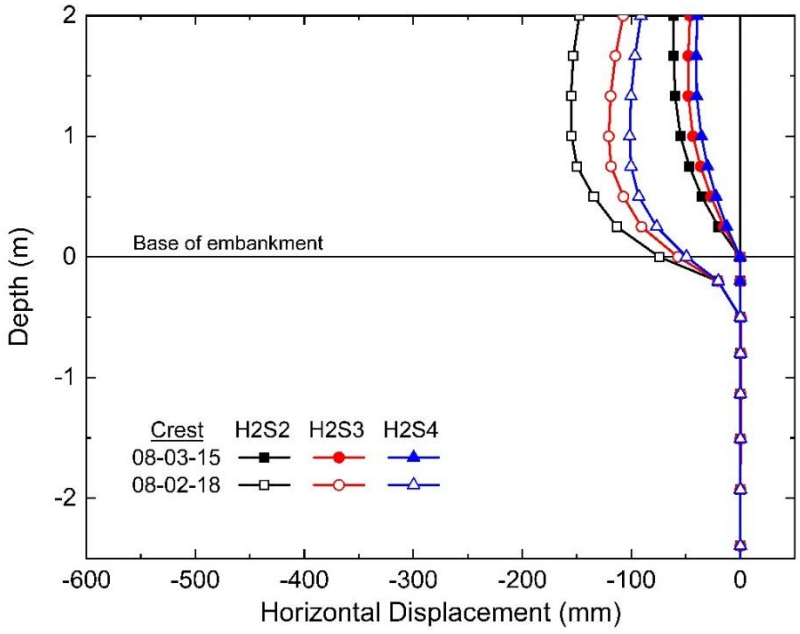

(a)

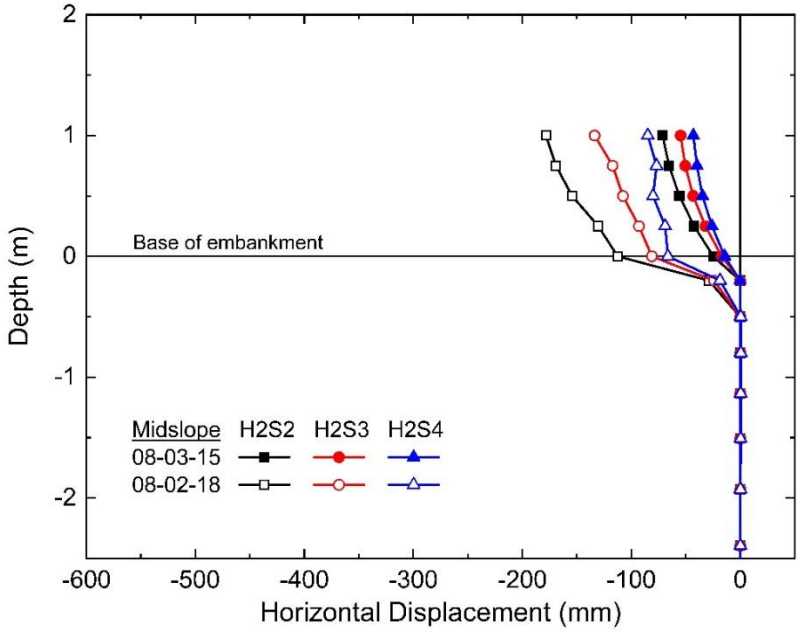

(b)

Fig. 6.22 (continued)

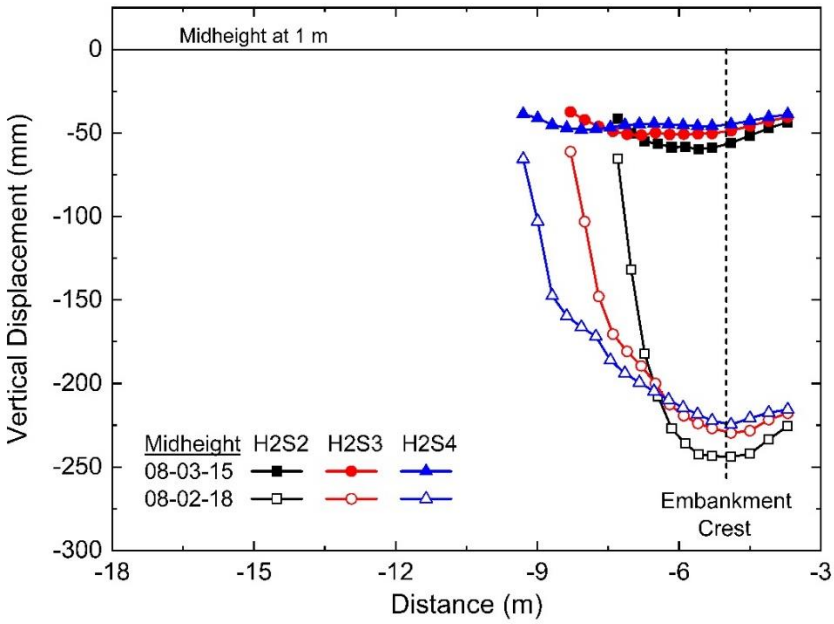

(c)

Fig. 6.23. Model horizontal displacements for 4 m embankments at (a) crest, (b) midslope, and (c) midheight for different slope configurations.

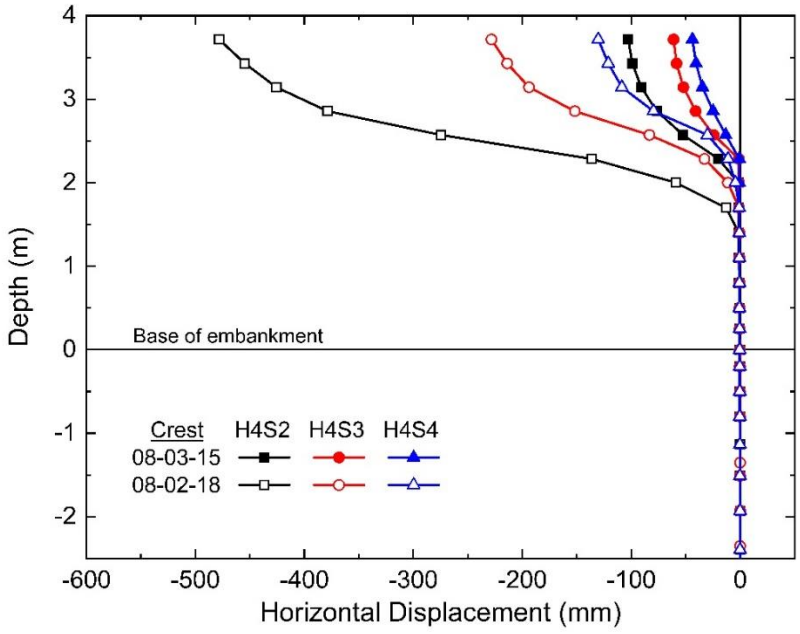

(a)

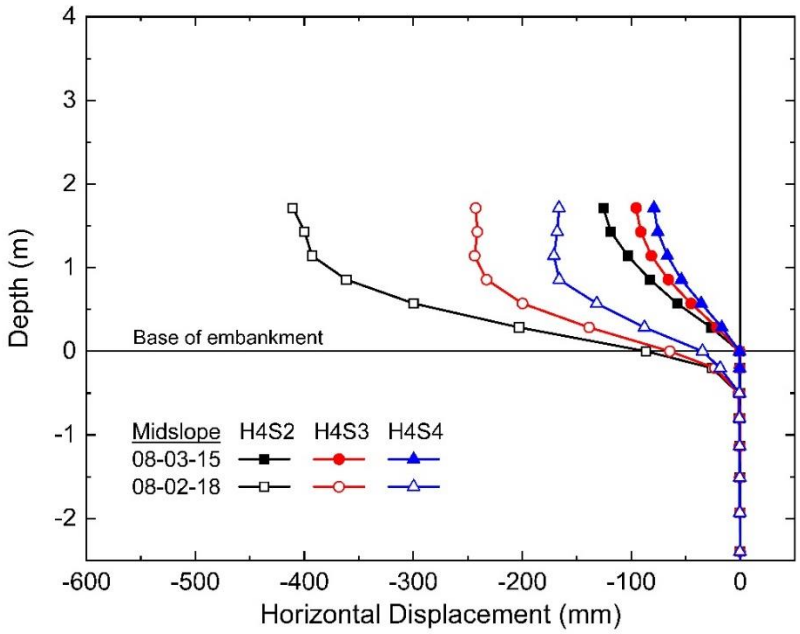

(b)

Fig. 6.23 (continued)

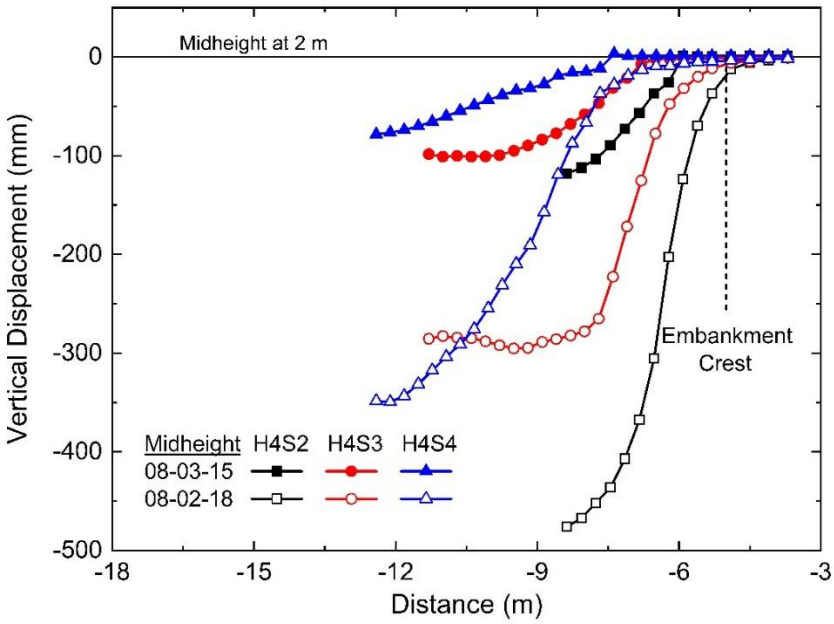

(c)

Fig. 6.24. Model vertical displacements for 6 m embankments at (a) crest, (b) midslope, and (c) midheight for different slope configurations.

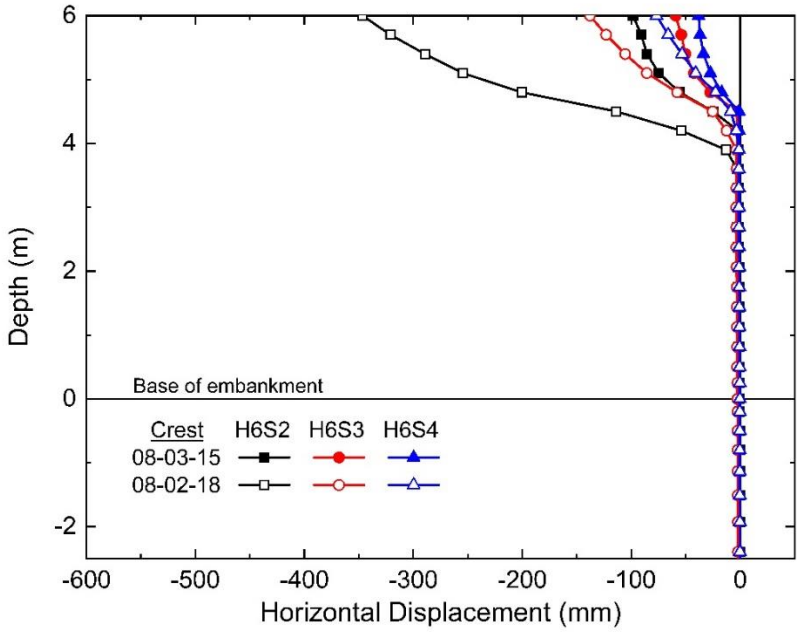

(a)

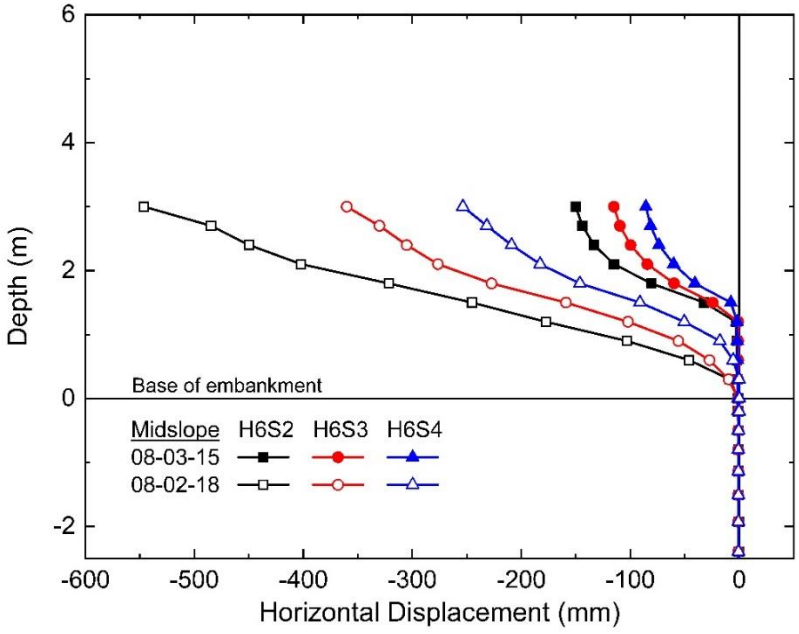

(b)

Fig. 6.24 (continued)

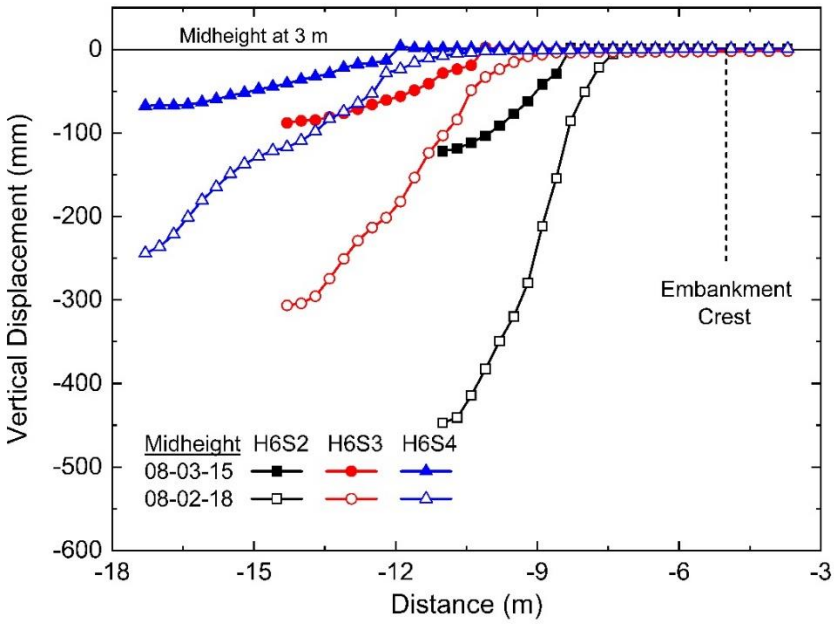

(c)

Fig. 6.25. Horizontal displacements for model embankments without the geotextile layers using varying slope inclination and vertical spacing.

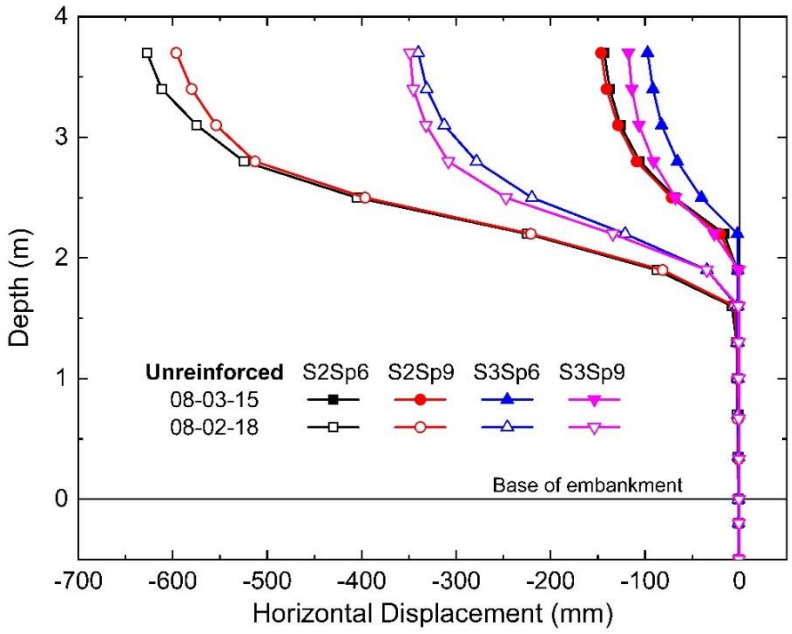

Fig. 6.26. Extent of thawed core where reinforcements were installed: (a) 2H:1V and (b) 3H:1V.

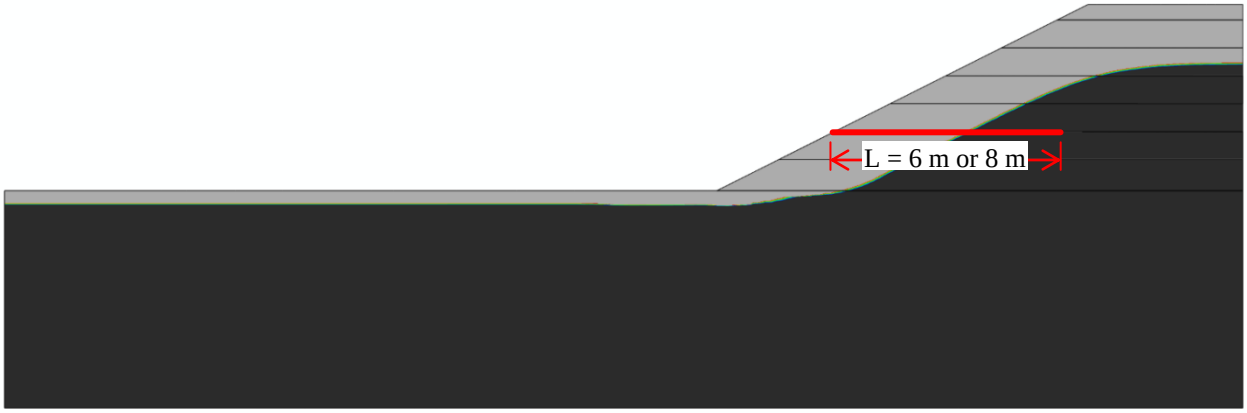

(a)

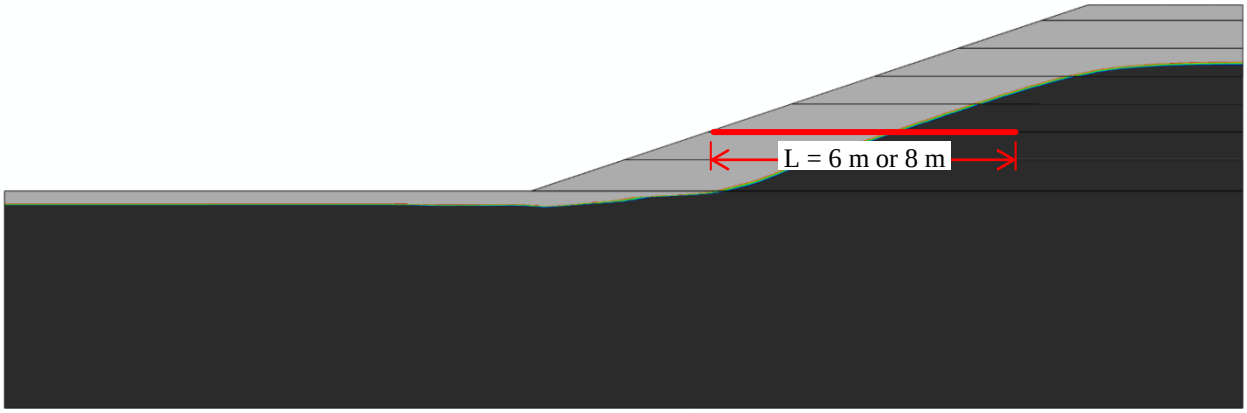

(b)

Fig. 6.27. Model horizontal displacements at midslope of embankment for (a) s = 0.6 m and (b) s = 0.9 m using two reinforcement lengths with 2H:1V slope configuration.

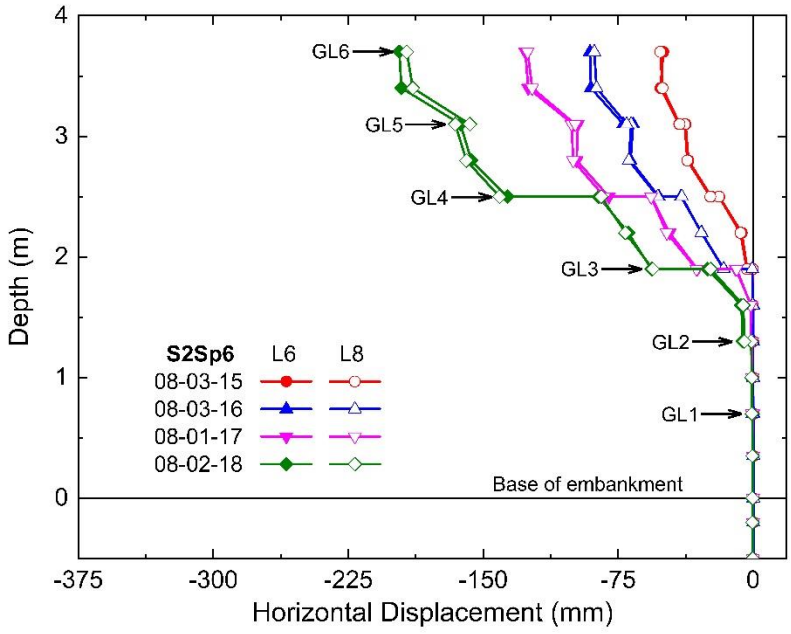

(a)

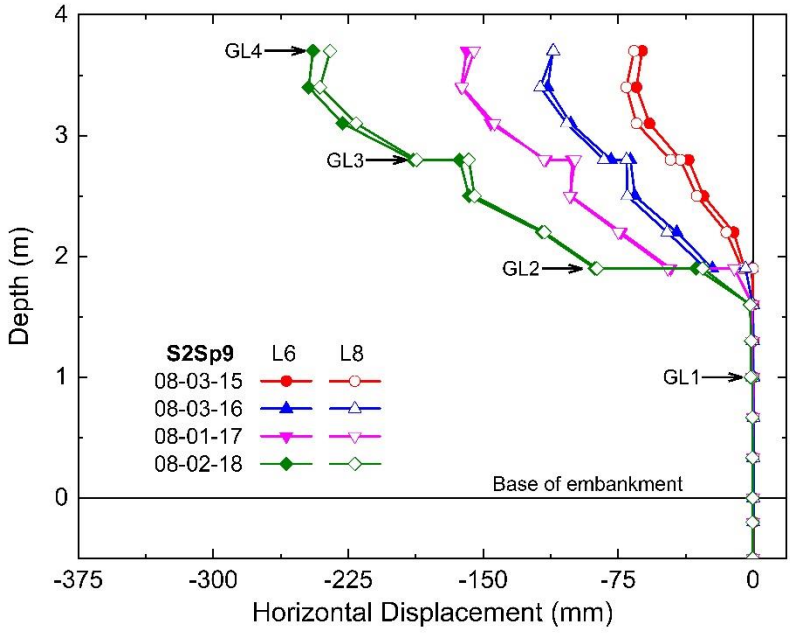

(b)

Fig. 6.28. Model horizontal displacements at midslope of embankment for (a) s = 0.6 m and (b) s = 0.9 m using two reinforcement lengths with 2H:1V slope configuration.

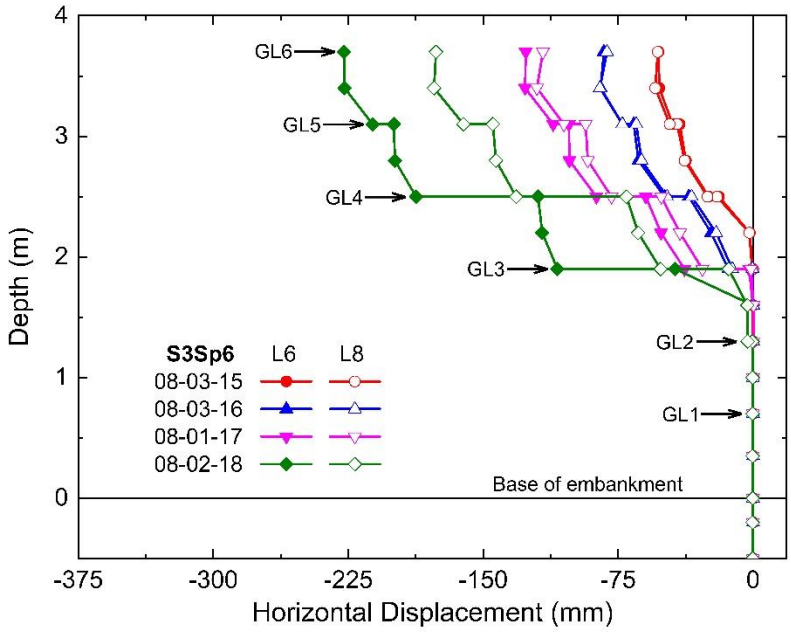

(a)

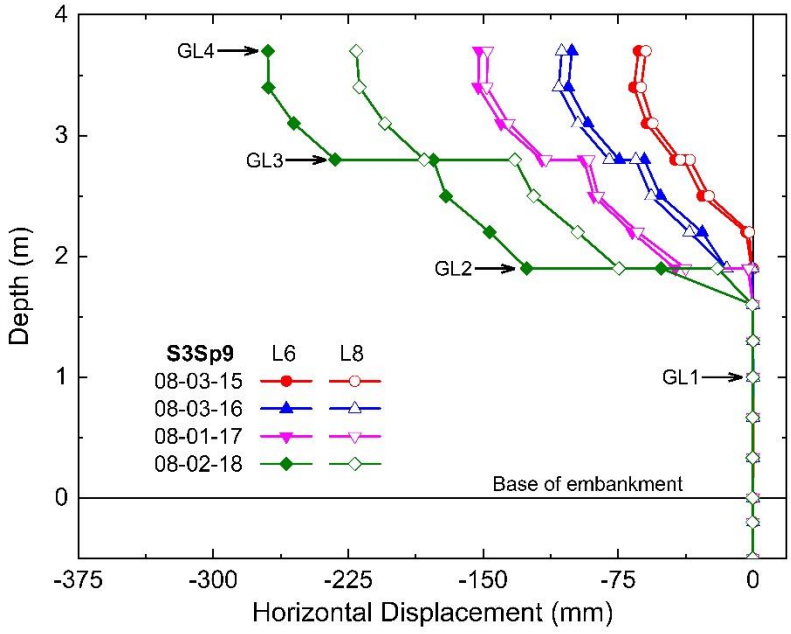

(b)

Fig. 6.29. Model horizontal displacements at midslope of embankment for 2H:1V slope configuration using (a) L = 6 m and (b) L = 8 m.

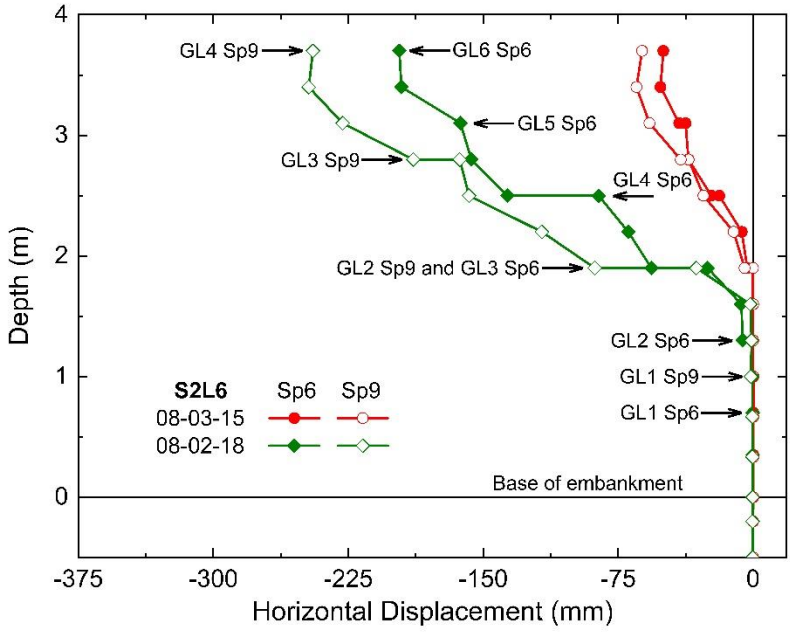

(a)

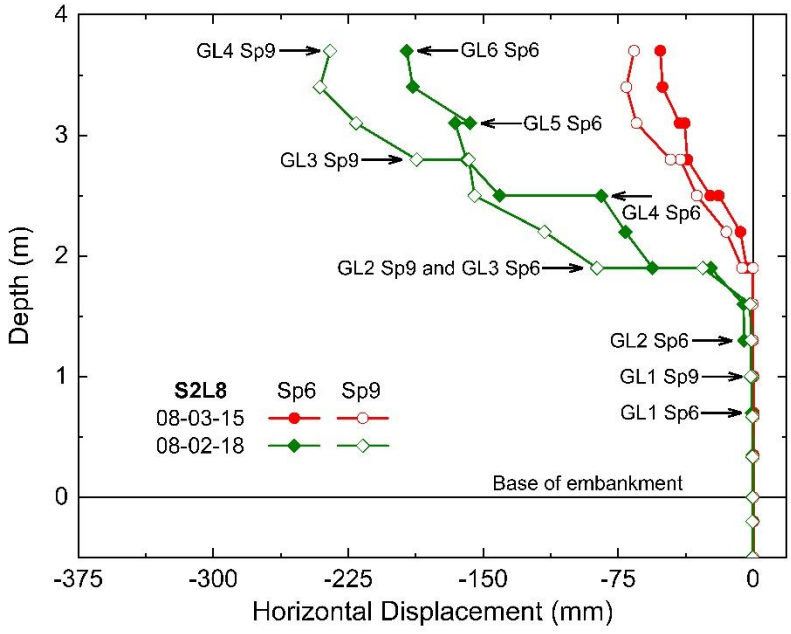

(b)

Fig. 6.30. Model horizontal displacements at midslope of embankment for 3H:1V slope configuration using (a) L = 6 m and (b) L = 8 m.

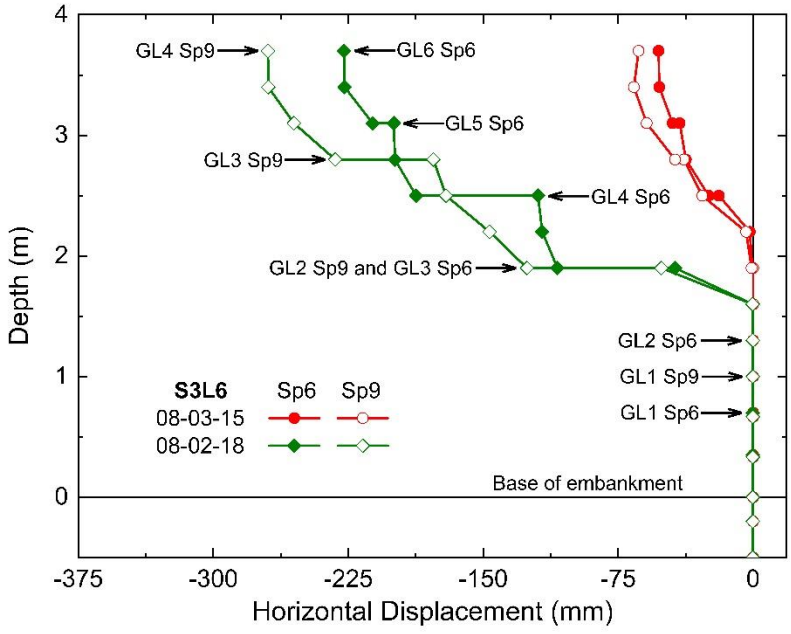

(a)

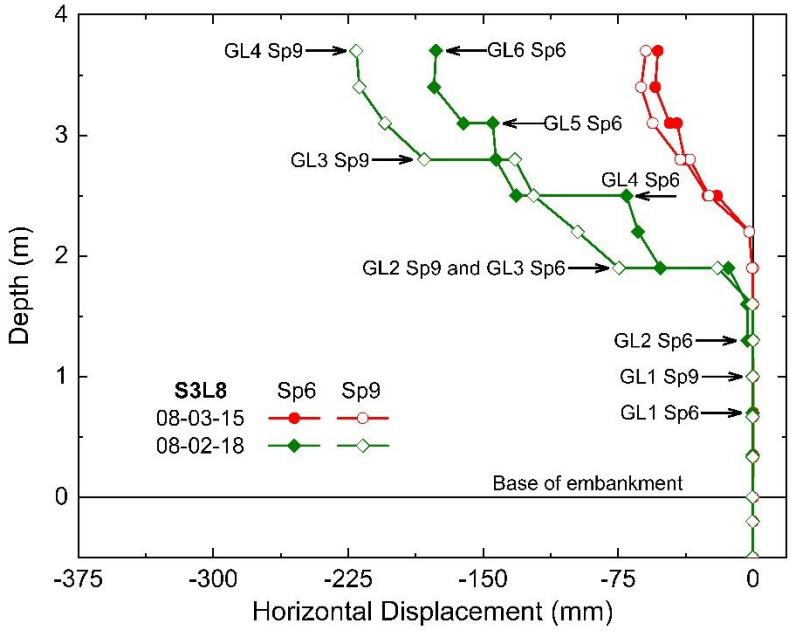

(b)

Fig. 6.31. Model horizontal displacements at midslope of control section using (a) d2015 and (b) RCP 8.5 temperature boundary conditions.

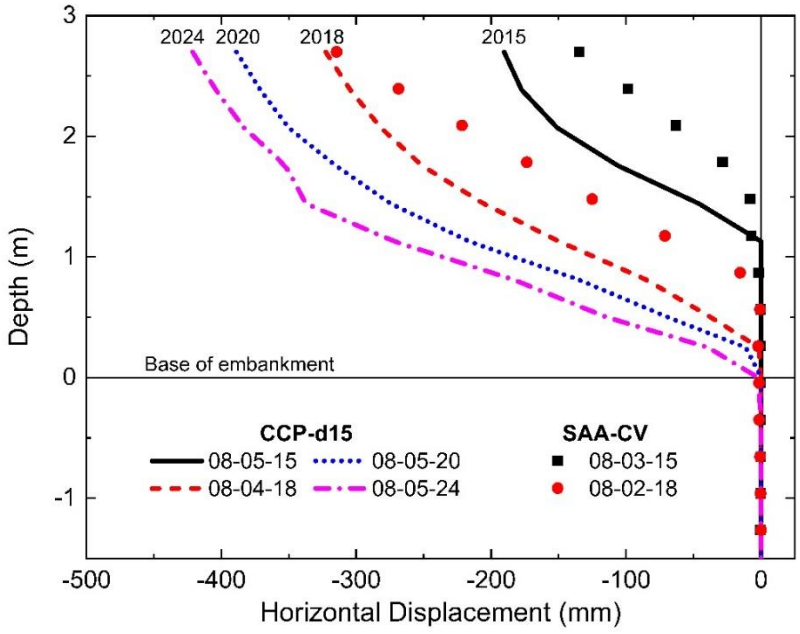

(a)

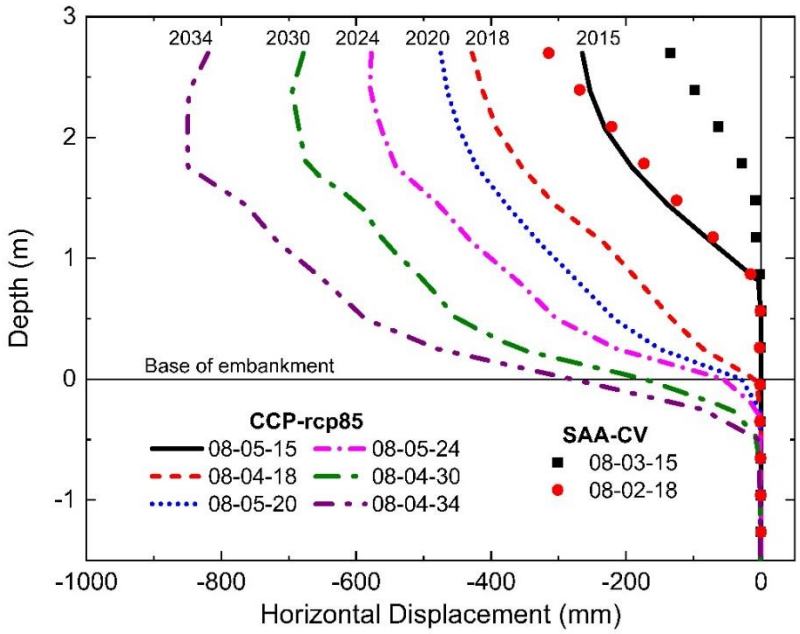

(b)

Fig. 6.32. Comparison of model horizontal displacements at midslope of control section in (a) 2020 and (b) 2024 using near-term and long-term climate change models.

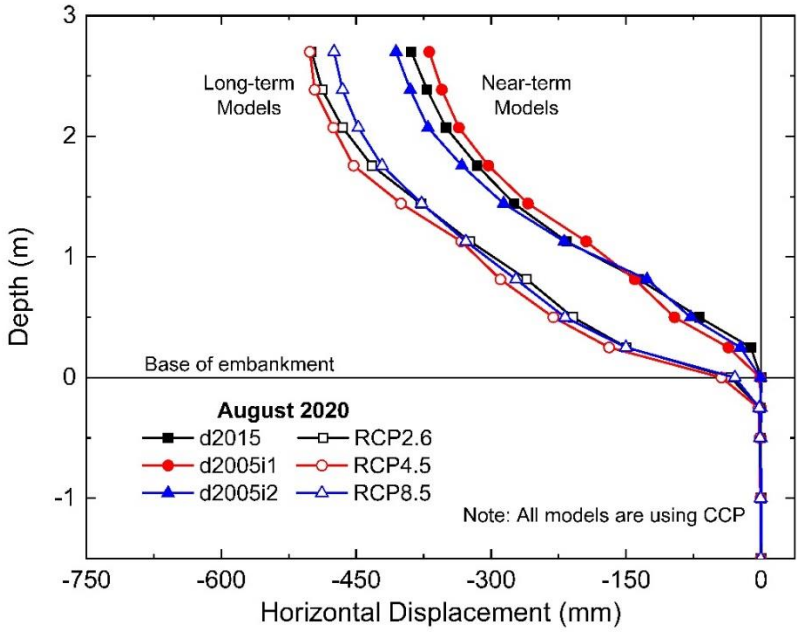

(a)

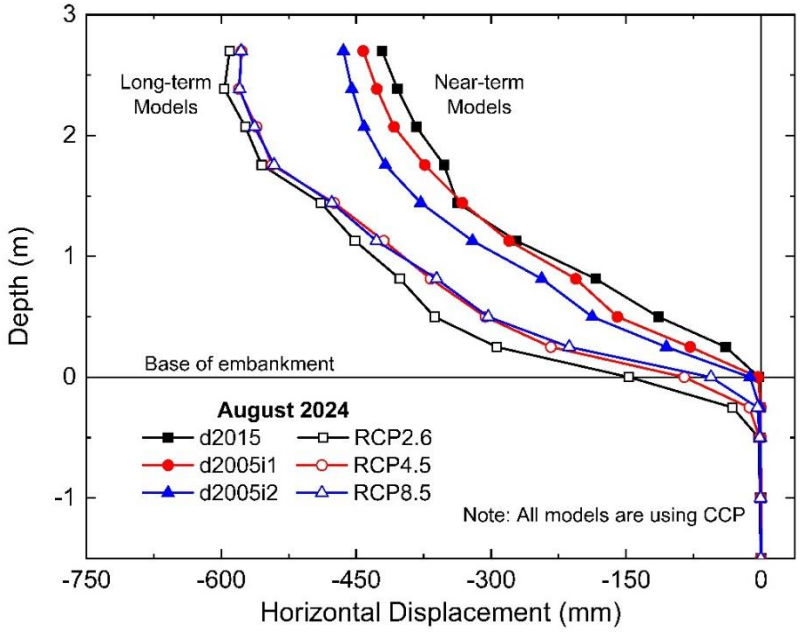

(b)

Fig. 6.33. Model horizontal displacements at midslope of (a) reinforced section using d2015 temperature boundary condition compared with (b) unreinforced (control) section.

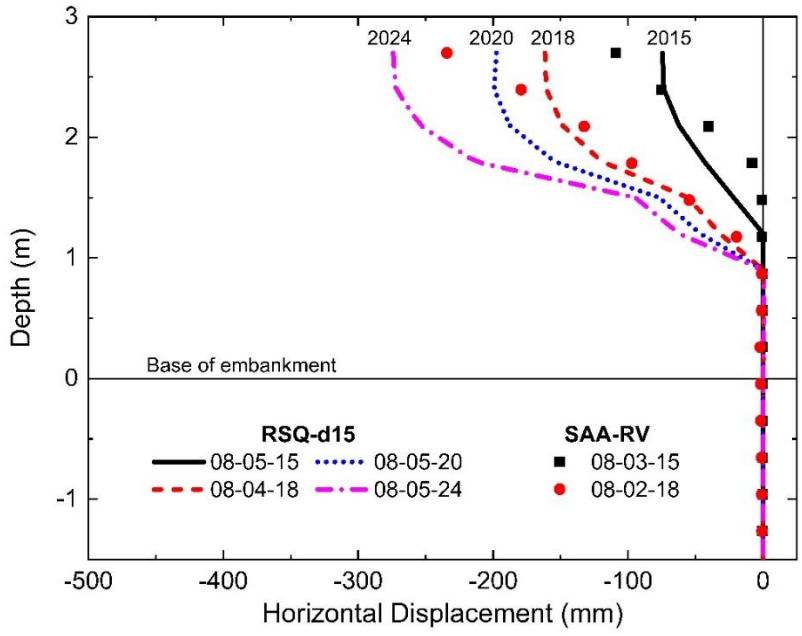

(a)

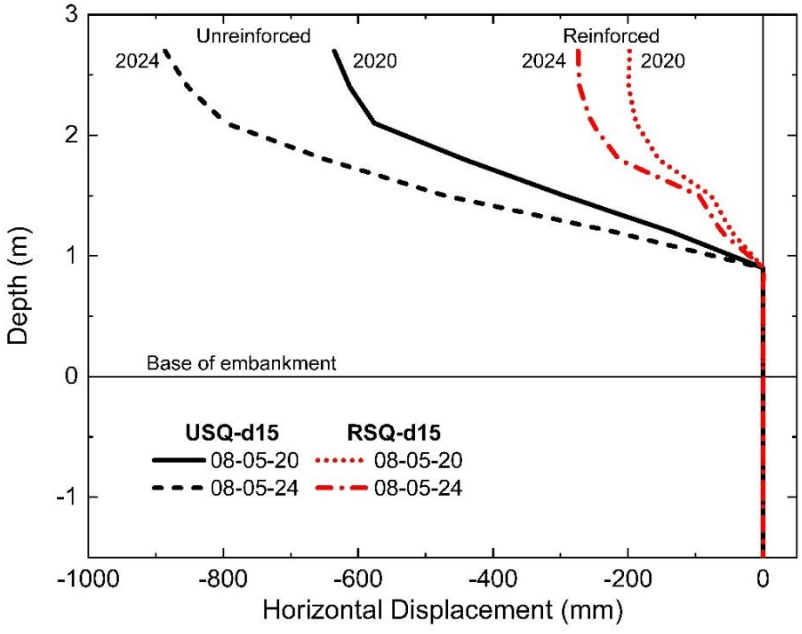

(b)

Fig. 6.34. Model horizontal displacements at midslope of control and reinforced test section models using FWC.

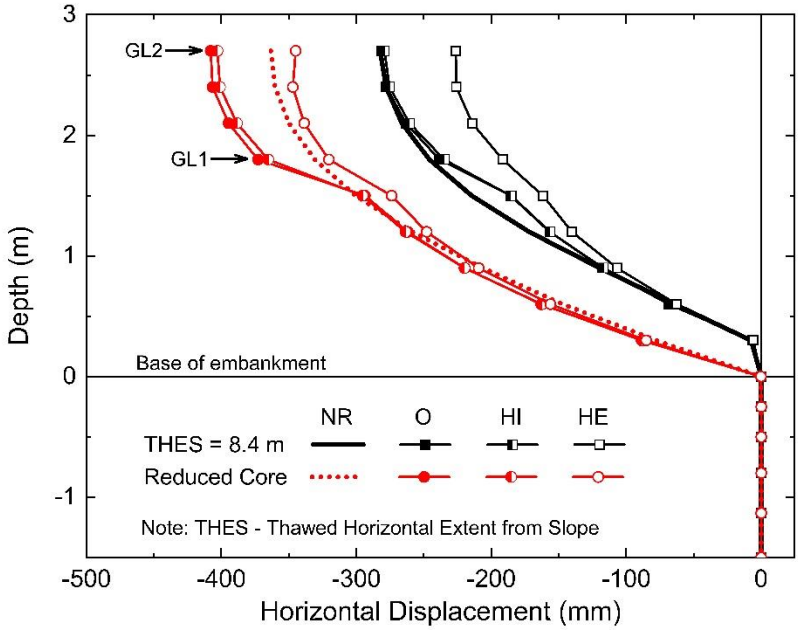

Fig. 6.35. Comparison of model horizontal displacements at midslope of reinforced embankment using different properties of geotextile reinforcement for 2H:1V slope configuration: (a) L = 6 m and (b) L = 8 m.

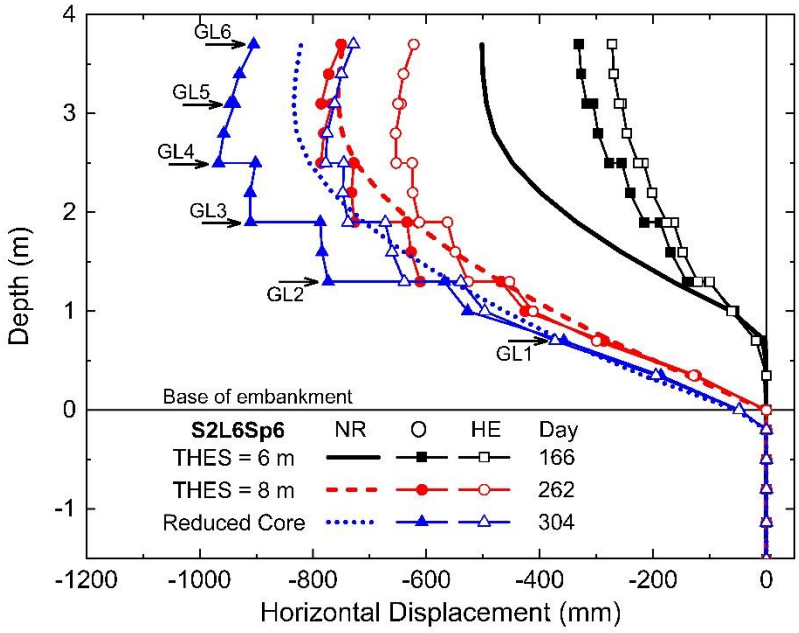

(a)

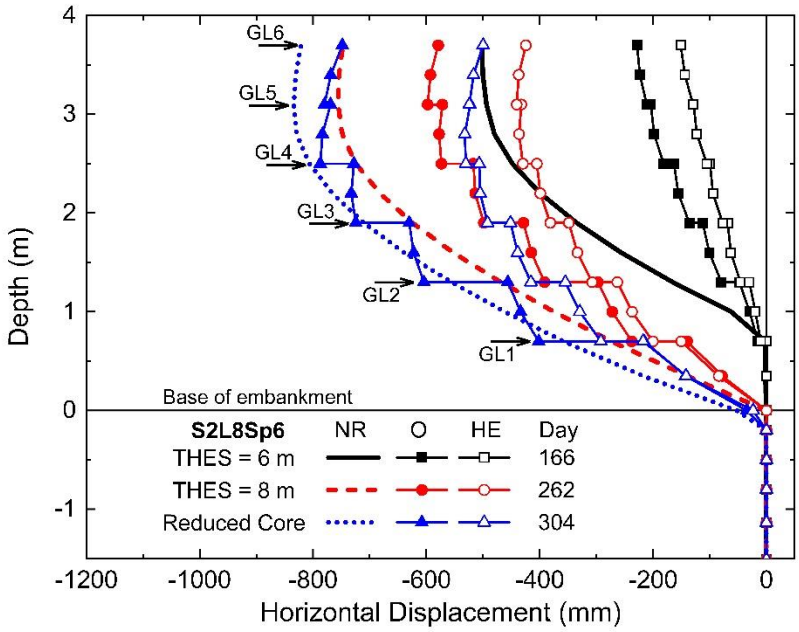

(b)

Fig. 6.36. Global displacement vectors for s = 0.6 m with 2H:1V slope configuration at THES = 8 m for the following models: (a) unreinforced, (b) L = 6 m, and (c) L = 8 m. Contour scale are in metres.

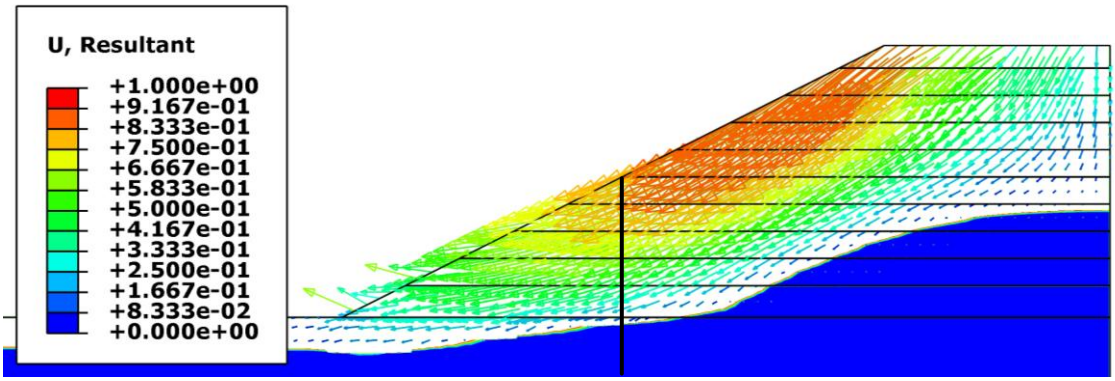

(a)

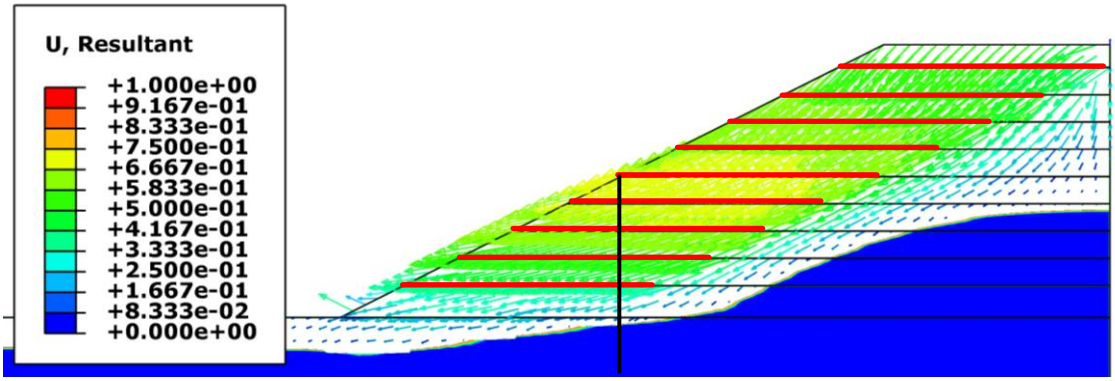

(b)

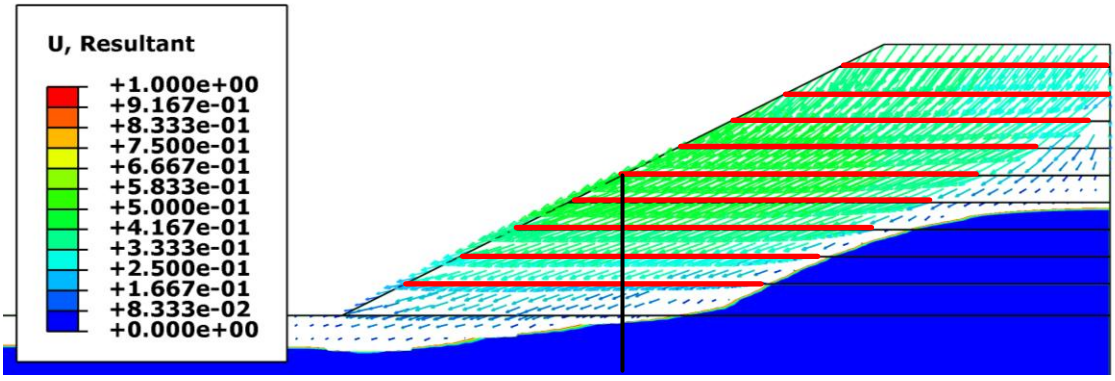

(c)

Fig. 6.37. Global displacement vectors for s = 0.6 m with 2H:1V slope configuration at reduced core size for the following models: (a) unreinforced, (b) L = 6 m, and (c) L = 8 m. Contour scale are in metres.

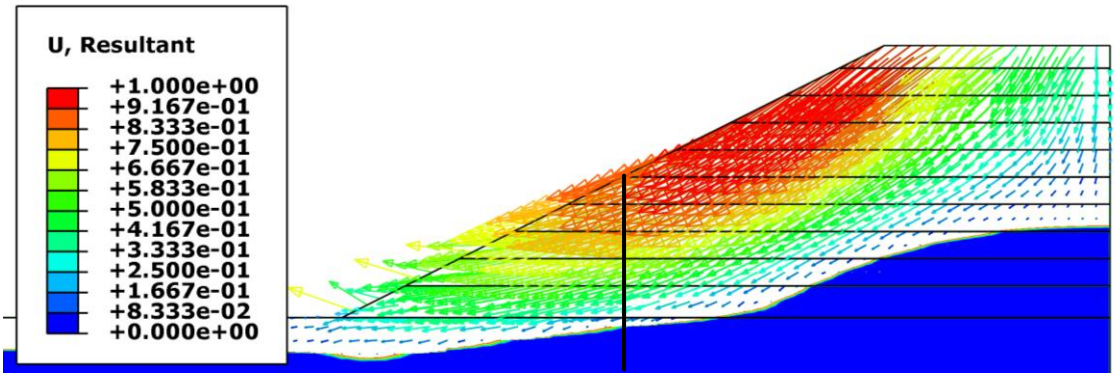

(a)

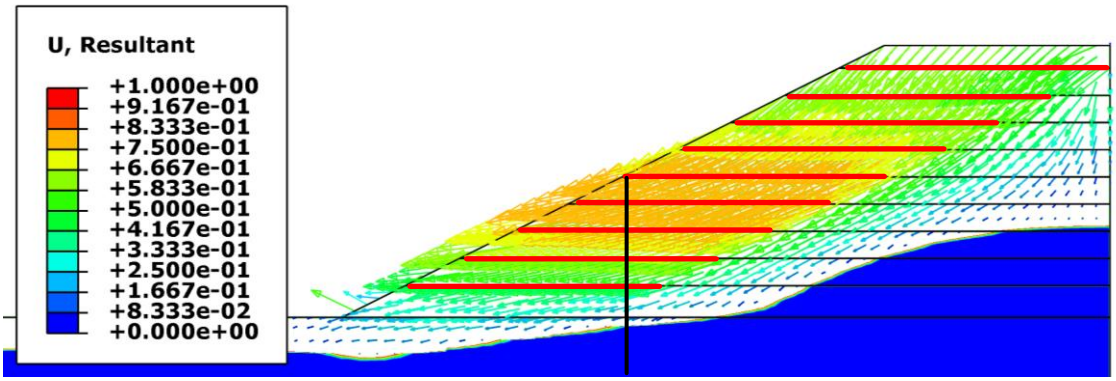

(b)

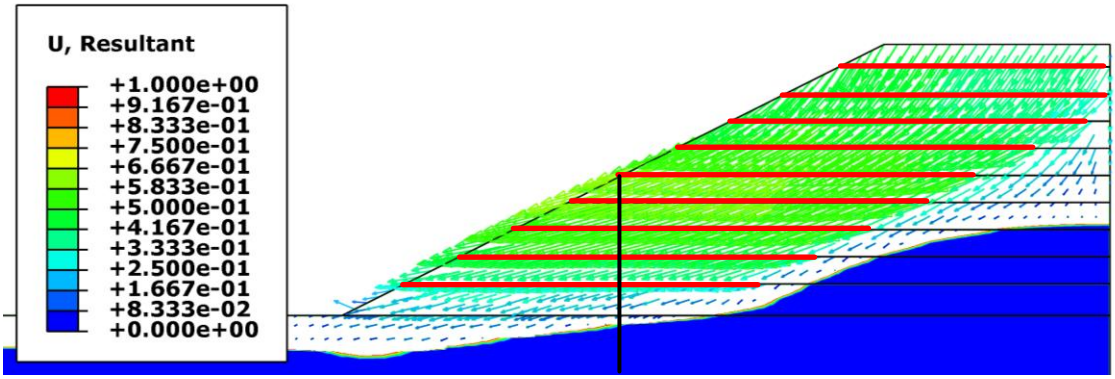

(c)

Fig. 6.38. Comparison of model horizontal displacements at midslope of reinforced embankment using different properties of geotextile reinforcement for 3H:1V slope configuration: (a) L = 6 m and (b) L = 8 m.

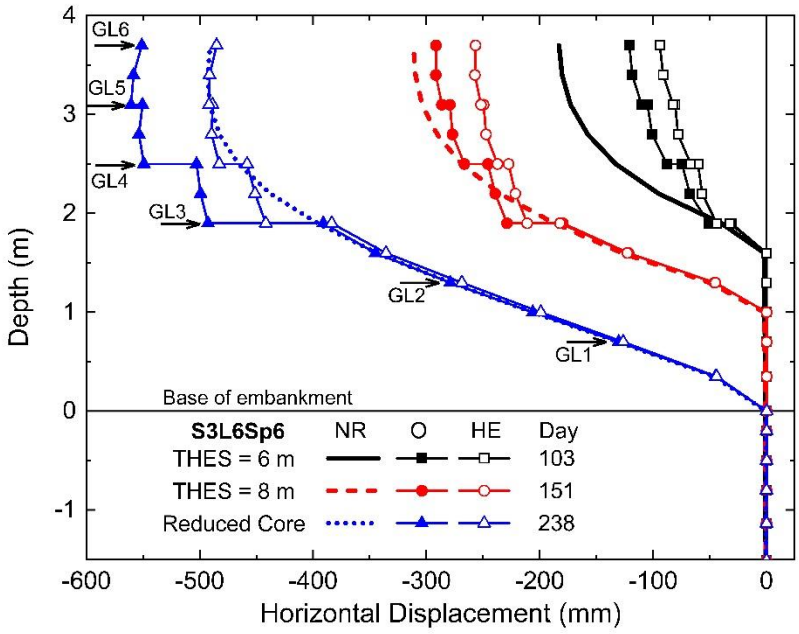

(a)

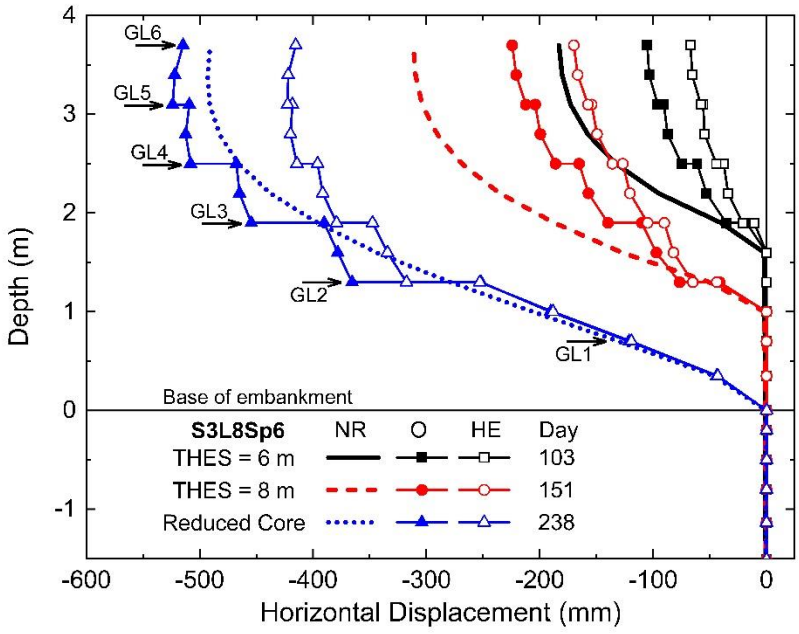

(b)

Fig. 6.39. Global displacement vectors for s = 0.6 m with 3H:1V slope configuration at THES = 8 m for the following models: (a) unreinforced, (b) L = 6 m, and (c) L = 8 m. Contour scale are in metres.

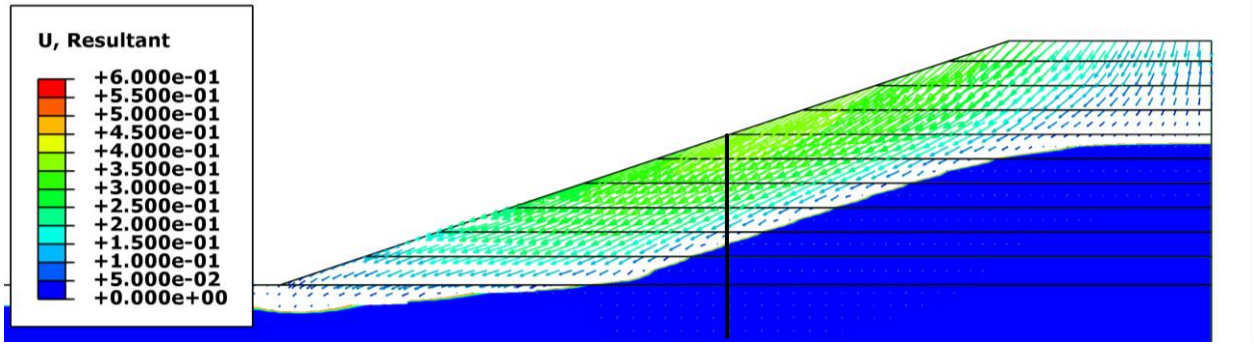

(a)

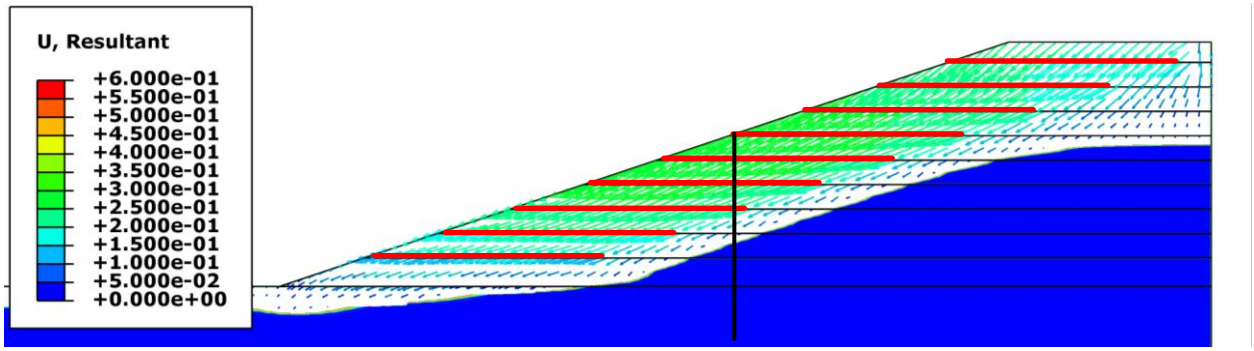

(b)

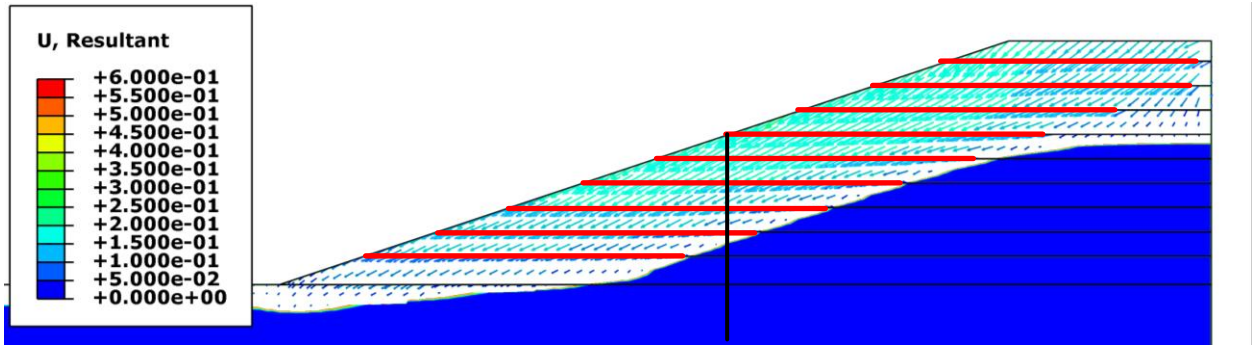

(c)

Fig. 6.40. Global displacement vectors for s = 0.6 m with 3H:1V slope configuration at reduced core size for the following models: (a) unreinforced, (b) L = 6 m, and (c) L = 8 m. Contour scale are in metres.

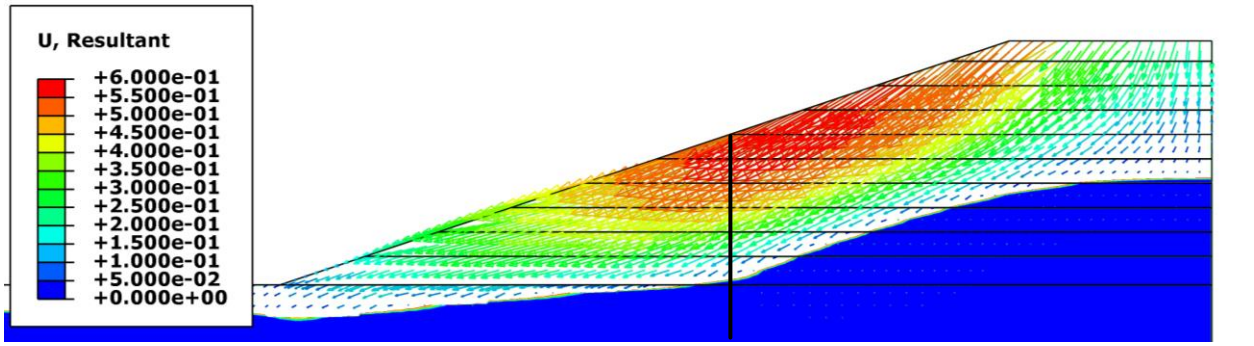

(a)

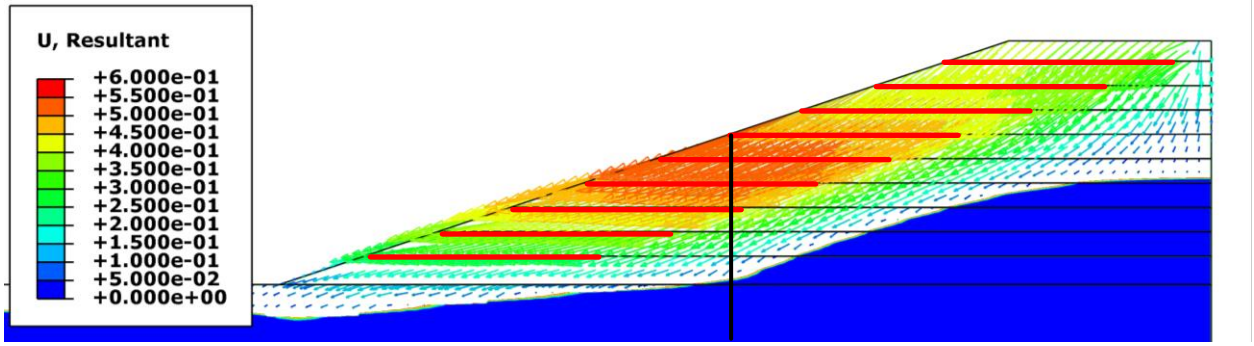

(b)

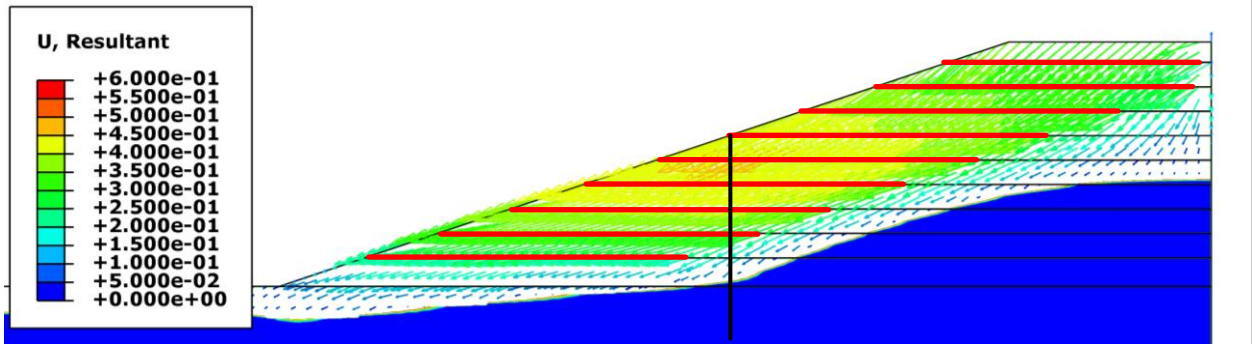

(c)

List of Notations and Acronyms in this Chapter

-3yrAct	Three-year actual air temperatures
-3yrAve	Three-year average sinusoidal air temperatures
-d05i1	Boundary condition using d2005i1 near-term climate change model
-d05i2	Boundary condition using d2005i2 near-term climate change model
-d15	Boundary condition using d2015 near-term climate change model
-O	Parametric reinforced models using original geotextile properties
-HE	Parametric reinforced models using higher elastic modulus for the geotextile
-HI	Parametric reinforced models using higher soil-geotextile interface properties
-rcp26	Boundary condition using RCP 2.6 long-term climate change model
-rcp45	Boundary condition using RCP 4.5 long-term climate change model
-rcp85	Boundary condition using RCP 8.5 long-term climate change model
A	sine function amplitude
CCCma	Canadian Centre for Climate Modelling and Analysis
CP	Fully-coupled approach for deformation analysis
CCP	Control test section model using CP
CHT	Control test section model for heat transfer analysis
CSQ	Control test section model using SQ
c	Cohesion (kPa)
d	Material cohesion for plasticity model in Abaqus
E	Elastic modulus (Pa)
E_f	Soil-geotextile interface efficiency factor
e_o	Void ratio
FWC	Forced warming conditions
GL#	Geotextile layer number
L	Length of geotextile (m)
$n_{freezing}$	Freezing n-factor
$n_{thawing}$	Thawing n-factor
p'	Mean effective stress (Pa)
p'_b	Hydrostatic compression yield stress (Pa)
RHT	Reinforced test section model for heat transfer analysis
RSQ	Reinforced test section model using SQ
SQ	Sequentially-coupled approach for deformation analysis
s	Vertical spacing between geotextile layers (m)
THES	Thawed horizontal extent from slope (m)
TM	Thermal modifier approach
UCP	Unreinforced model using CP

UHT	Unreinforced model for heat transfer analysis
USQ	Unreinforced model using SQ
u_x, u_y, u_z	displacement degrees of freedom
x_c	Sine function phase shift
y_o	Sine function offset
β	Angle of friction for plasticity model in Abaqus
Δ_{max}	Maximum displacement (mm)
ε_{vol}^{pl}	Plastic volumetric strain
θ	Friction angle of the soil (°)
κ	Kappa (recompression index)
λ	Lambda (compression index)
ν	Poisson's ratio
tan δ	Equivalent soil-geotextile interface friction angle
tan ϕ	Equivalent soil friction angle
ω	Sine function period

CHAPTER 7

SUMMARY, CONCLUSIONS, AND RECOMMENDATIONS FOR FUTURE RESEARCH

7.1. Summary

This research investigated the performance of fully-instrumented embankment test sections along the Inuvik-Tuktoyaktuk Highway (ITH) under winter construction conditions using frozen soil. One of the test sections was reinforced with wicking geotextiles at its side slopes to reduce the horizontal displacements once the frozen soil thaws. This is the first research that investigated the use of wicking geotextiles as slope reinforcement in Arctic regions. The temperature sensors have shown that there is a warming trend in the embankment fill and foundation soil, which is attributed to warmer air temperatures in the region and the heat trapped in the embankment during the winter months when the embankment slopes are covered in snow. The core of the embankment has remained frozen during the monitoring period but has reduced in size since end-of-construction. Largest lateral displacements were recorded in the summer following construction of the embankments due to thawing of the frozen soil at the slopes. Although lateral displacements which occurred on the second and third year of thawing were less than that at end-of-construction, the seasonal thaw depth at the slopes have gone deeper and led to additional displacements. The addition of the wicking geotextiles at the embankment slopes reduced the lateral displacements in the reinforced section.

To further understand the mechanisms involved in these embankments, laboratory tests were conducted on the frozen soil used as fill material and the wicking geotextiles. Large-scale direct

shear tests were conducted on remolded frozen soil samples obtained at the research site during embankment construction under different environmental conditions to determine its shear strength.

The interface strength properties of the wicking geotextiles were determined from a series of pullout tests under different moisture and compaction conditions. A comparable non-wicking geotextile was also tested under similar conditions to establish the contribution of the wicking function. The presence of the wicking function improved the soil-geotextile interface properties for all test conditions, especially when the soil was prepared and compacted at its optimum moisture condition.

The recorded field data, together with the results of the laboratory tests conducted on the soil and the geotextile, were used to calibrate numerical models to investigate the operating mechanisms contributing to the near-term and long-term performance of the embankment test sections. Thermal modelling (pure heat transfer) was developed for the embankment test sections using TEMP/W. The commonly used thermal modifier approach and surface energy balance approach were utilized to establish the thermal regime of the embankment fill and foundation soil during the monitoring period. The thermal modifier approach uses empirical values that lump all factors together to transform the air temperature to ground surface temperatures, while the surface energy balance approach uses the energy transfer between the ground surface and the atmosphere.

To account for the displacements occurring in the embankment, coupled thermal-mechanical modelling was developed for the embankment test sections using ABAQUS. The control test section was modelled using a fully-coupled approach in solid sections where both heat transfer and deformation occurring in the soil elements are solved simultaneously in a single analysis. The reinforced test section was modelled using a sequentially-coupled approach in staged sections where temperature fields for each time step in the heat transfer analysis is referenced in the

deformation analysis to invoke the corresponding material properties dependent on that temperature. Only the thermal modifier approach was used in these mechanical models. Reasonable agreement was achieved between the two approaches compared to the recorded field data when actual air temperatures during the monitoring period were used. Similar to the recorded field data, the largest displacements occurred during the summer following winter construction. With reasonable confidence on the results of these models, near-term and long-term climate change conditions were analyzed to evaluate future performance of these embankments. Parametric analyses of unreinforced and reinforced embankments were also analyzed to investigate the influence of slope inclination, embankment height, reinforcement length, and vertical spacing between reinforcements on embankment performance. Additionally, forced warming conditions were applied to examine the performance of reinforced slopes once the frozen core in the embankment is significantly reduced.

7.2. Conclusions

The results of this research will assist in the development of improved guidelines for the design, construction, and maintenance operations of highway embankments in Arctic regions constructed under winter conditions. The following conclusions are presented to address the research hypotheses:

Hypothesis 1: Short term stability is governed by thawing of frozen soil and corresponding decrease in shear strength at the slopes where significant lateral displacements and settlements occur during the subsequent summer after winter construction.

1. Compaction in the field during embankment construction plays an important role because there is no optimum condition as to which frozen soils should be compacted. The higher the moisture content of the frozen soil matrix the more challenging the compaction will be. Although fill

material for embankment construction is taken from locally-available sources and thus have high variability both in composition and moisture content, it is practical to keep the moisture content below 20% to benefit from higher compaction densities and to minimize thaw related displacements during the onset of the first thawing following winter construction.

2. The frozen soil samples exhibited significant shear strength as long as they remained frozen, but upon thawing close to phase change and upon freeze-thaw cycling the shear strength is reduced by up to 50%. The most critical condition, based on the tests conducted, is during the onset of the first thawing when the ice bonding in the soil matrix melts. This is consistent with the field data from vertical SAAs where the largest horizontal displacements were recorded in the summer following construction for both control and reinforced test sections.

3. The core of the embankment test sections has remained frozen in the monitoring period but has reduced in size since end-of-construction. This is attributed to warming air temperatures in the region and the heat trapped in the embankment during the winter months when the embankment slopes are covered in snow. Thawing of the previously compacted frozen soil over time is contributing to the incremental increase in lateral displacements and settlements.

4. The fully-coupled approach used in the control section resulted to reasonably accurate results when calibrated against the recorded field data on temperatures and displacements using the actual air temperatures during the monitoring period. The sequentially-coupled approach used to model the reinforced section slightly underestimated the horizontal displacements at the midslope. A comparable control section using the same approach showed that the geotextile layers reduced the horizontal displacements by as much as 40% for 3H:1V slope configuration.

5. The non-wicking geotextile was also used as an alternative option in the reinforced model. The large displacements occurring during the summer following winter construction for

unreinforced embankments were reduced by 31% using wicking geotextiles and by 15% using non-wicking geotextiles.

6. Parametric unreinforced embankments were subjected to the same air temperatures during the monitoring period. Embankments with thickness less than 2 m will have the entire embankment fill thawed during the summer following construction where the permafrost table remained close to the natural ground surface. Embankments with thickness 4 m or more will have a frozen core that will eventually be the new permafrost zone after 2 years. The numerical models however showed that this frozen core will reduce in size as warmer air temperatures become more prevalent due to climate change. Decreasing the slope inclination will significantly reduce the horizontal displacements at the crest and midslope of these embankments. The general consequence of increased thickness and larger embankment volume to mitigate displacements is increased project costs.

Hypothesis 2: Long-term stability is governed by climate change conditions where the depth of thaw penetration in the embankment fill and foundation soil increases over time contributing to additional displacements and the formation of taliks can lead to instabilities which may compromise performance.

1. The lateral displacements recorded in the second and third year of thawing were less than that at end-of-construction, but the seasonal thaw depth at the slopes have gone deeper due to warmer air temperatures in the region as recorded by the weather stations and satellite data that led to additional displacements. It is recognized that there is an overlapping influence of warming air temperatures and thermal disturbance on the permafrost underneath the embankment due to embankment construction. The idealized case where an average sinusoidal temperature function was used as a boundary condition still contributed to displacements with

displacements plateauing after several years (7 to 10 years) of cycling. It is expected that with climate change the frozen core will continuously shrink and exacerbate displacements.

2. The results of thermal modelling are highly dependent on the modelling approach selected. The thermal modifier approach uses empirical values that lump all factors together to transform the air temperature to ground surface temperatures, while the surface energy balance approach requires complex input parameters that require sophisticated and expensive instrumentations to obtain accurate values. The difference in soil temperatures between the two approaches is an inherent variable a designer should assess. The snow depth and albedo was assumed to be constant throughout the analyses for the surface energy balance approach which may not be accurate for future conditions. The snow depth and albedo available from satellite data are on a regional scale which do not account for existing infrastructure in the region. The numerical models showed that using an average sinusoidal air temperature as a boundary condition underestimates both the temperatures and displacements.

3. Embankment performance modelling considering the effects of climate change should account for the possibility of the formation of taliks. The thermal models showed that taliks will form in 2080 using RCP 8.5. However, the coupled thermal-mechanical models were not simulated beyond 2025 due to the excessive displacements encountered in the model using the available climate change models. The forced warming conditions show that displacements occur at the interface of the frozen and unfrozen soil respect to the shrinking of the frozen core. It is therefore reasonable to assume that the unfrozen soil bounded by the frozen core and the soil above this region below 0°C to be a possible failure surface.

4. The near-term and long-term climate change models applied to the control section, and a near-term model on the reinforced section overestimated the horizontal displacements for both test

sections during the same time scale of the three-year monitoring period. Using the results derived from climate change models without calibration against available field data may be conservative with the large displacements they provide but may lead to embankment overdesign.

5. Because climate models were derived on a regional scale, historical and present-day meteorological data from local weather stations and downscaling climate models to a local scale are still indispensable source of data in engineering design of new linear infrastructure. Even with this shortcoming, the results of the near-term and long-term climate models provided an insight when remediation can be employed to impede permafrost degradation and maintain embankment thermal stability.

Hypothesis 3: Geotextiles with wicking function when used as slope reinforcement reduce lateral displacements and improve the short-term and long-term stability of embankments.

1. The addition of the wicking geotextiles reduced the lateral displacements as the embankment slope experienced seasonal freezing and thawing. The control section remains stable even without slope reinforcement because of its designed slope configuration, but development of longitudinal cracks and settlements can eventually lead to serviceability problems (excessive movements) as the depth of thaw penetration increases due to climate change. Based on the recorded field data and numerical models developed, these displacements are reduced with the use of geotextiles.

2. The wicking function improved the soil-geotextile interface properties compared to a non-wicking geotextile based on the pullout tests for different moisture and compaction conditions. The optimum moisture conditions tests where unsaturated soil interacts with the wicking geotextile showed the largest increase in interface properties. Although this condition is

desirable in embankment construction, the high variability of moisture content from locally-available fill material and the compaction effort during winter construction will have a reduced interface strength once the embankment slopes undergo seasonal freezing and thawing cycles.

3. Results from parametric reinforced models indicate that reducing the slope inclination is the most plausible option in mitigating the development of large horizontal displacements for thawing slopes. With prohibitive project costs to accommodate gentler slopes, geotextiles can be used as an alternative strategy to have steeper slopes yet reduce the displacements.

4. The benefit of installing geotextile layers is realized as long as there is a region where the geotextiles are still embedded within a frozen core and designed using a tighter vertical spacing between layers for cold region applications. Once the frozen core thaws, including the soil along the entire length of the geotextile is above 0°C, the displacements are almost the same as the unreinforced embankment unless stiffer geotextiles are used.

7.3. Recommendations for Future Research

Significant work has been done in the field instrumentation and monitoring program, laboratory testing, and numerical modelling to improve embankment performance in Arctic regions. The following recommendations are provided to further advance this area of research:

1. The study presented focused on an average moisture content and soil gradation obtained from a pit site where fill material was obtained for the embankment test sections. It is recommended to determine the shear strength of fill material for varying soil gradation, compaction effort, moisture content, and testing temperatures. Limitations of the large scale direct shear tests were discussed in Chapter 3 but this type of testing still provides indispensable results in developing a material property matrix that can be utilized in preliminary design. Future shear strength tests

should account for different borrow sources (e.g. borrow sources with higher fines content) to obtain variability with the results where statistical tools can be applied on the shear strength, dilation angle, cohesion, and soil density that can be used in a limit states design approach.

2. Limited work has been done on the foundation soil due to the limited samples collected from the research site, the availability of testing equipment to quantify mechanical properties (e.g. deformation, shear strength, creep). It is recommended to characterize the physical properties (e.g. ice content, fibre/soil content and orientation) of frozen soil cores in the region at different depths to develop reconstituted frozen soil samples prepared under historical consolidation stresses. These reconstituted samples can then be used to conduct testing programs that can account for variability in mechanical properties of the foundation soil.

3. Although the traditional deterministic approach using known soil properties to determine a factor of safety for slopes is common, this does not account for several uncertainties and may not provide any meaningful value to embankments that continuously undergo freezing and thawing cycles. With the suggested testing programs (Recommendations 1 and 2) to account for variability in mechanical properties of the fill material and foundation soil, a probabilistic approach can be explored as part of long-term maintenance strategies particularly the climatic influences of freezing and thawing on embankment slopes and load capacity of the foundation. This will improve risk assessment strategies in a quantitative context where the probability of exceeding a prescribed limit state condition is used as an indicator of continuous functionality.

4. The study has shown the benefit of using geotextiles in thawing slopes under the three-year monitoring period and climate change conditions based on the pullout tests conducted in Chapter 4. However, long-term climate change modelling should incorporate the effects of freezing and thawing at the geotextile interface as well as creep of the geotextile reinforcement

under sustained loading. The effect of fines content on the wicking geotextile at different moisture conditions and temperature and its impact on long-term performance should also be examined. Soils with higher fines content can hold significant amount of water at its frozen state and upon thawing can keep the slopes saturated for a longer period of time due to its inherent low permeability. The probabilistic approach in Recommendation 3 should also be explored for reinforced slopes.

5. Based on the results of the reinforced embankment models, geogrids can be used an alternative to geotextiles because they inherently have a high elastic modulus. In addition, the interlocking and confining mechanisms between the geogrid and the soil provide additional resistance to slope movements which can significantly reduce lateral displacements. The use of geogrids with locally-available frozen fill material during winter construction and how geogrids interact with frozen soil and subsequent thawing warrants further investigation for cold regions applications.

6. Chapter 5 showed that under the current climate change models a talik will form in the control section in 2080. However, this was not achieved in the mechanical models in Chapter 6 due to the excessive deformations encountered in the numerical model before 2030. It is recommended to implement adaptive remeshing strategies to overcome this limitation. It should be noted that using the climate change models in the coupled thermal-mechanical models in Chapter 6 overestimated the midslope displacements. The formation of the talik may be due to the aggressive nature of the climate change model (e.g. RCP 8.5), but research on the influence of talik formation on overall embankment performance is warranted.

7. The coupled thermal-mechanical models in Chapter 6 showed the use of the fully-coupled approach for the control test section and parametric unreinforced embankments, and the use of

the sequentially-coupled approach for the reinforced test section and parametric reinforced embankments. It is recommended in future studies to investigate the geotextile as a solid element instead of an idealized shell element. The in-plane drainage of the wicking geotextile was not incorporated in the shell element but otherwise can be invoked for solid elements. The basic friction model available in the software was used, but it is recommended to examine sophisticated interface models (e.g. Duncan and Chang model) between the geotextile and the soil which may improve the numerical results presented.

8. Only the thermal modifier approach was used in coupled thermal-mechanical modelling because of its simplicity and the comparable results it provided with the recorded field data. It is recommended to investigate the use of the surface energy balance approach in these models to investigate how climatic factors (wind speed, relative humidity, solar radiation, etc.) other than air temperatures influence embankment behaviour.

9. The numerical models developed only investigated the deformations occurring in the embankment slopes due to thawing of frozen slopes. Excitation loads due to truck traffic for different embankment heights and its influence on deformations, especially at the interface between the frozen and unfrozen soil at the extent of the frozen core, should be explored in future studies. Dynamic and cyclic properties of the fill material at the research site, as well as varying soil gradation, compaction effort, moisture content, and testing temperatures close to 0°C should be determined.

10. Ice wedges and polygonal ground are avoided during highway planning studies because of the possibility of void development underneath the embankment when they thaw. It is recognized that they are prevalent in northern environments and it may be more costly to avoid them instead of mitigating their influence on embankment performance. A series of laboratory tests

were conducted by the author to study the mechanical and thermal properties of a composite geofoam-geogrid material as a possible reinforcement strategy to improve embankment performance underlain by these voids. The geofoam provides insulation to the polygonal ground while the geogrid provides reinforcement to the geofoam once the voids develop. Preliminary numerical studies have been conducted with promising results and future research on this type application is warranted.

11. Remedial measures for maintenance considerations under climate change conditions were not fully investigated in this study. It is recommended to consider how methods such as berm placement, snow clearing operations, and additional placement of fill material to maintain road elevation influences the preservation or degradation of the permafrost and overall embankment stability.

12. The instrumentation installed at the research site provided insights on how to establish embankment performance which provided calibration for the numerical models. For sites where instrumentation are installed (e.g. thermistor strings, ShapeAccelArrays), it is recommended to create a database to develop predictors for failures by correlating air temperatures, soil temperatures, and recorded displacements.

REFERENCES

Abu-Farsakh, M., Coronel, J., and Tao, M. 2007. Effect of Soil Moisture Content and Dry Density on Cohesive Soil–Geosynthetic Interactions Using Large Direct Shear Tests. Journal of Materials in Civil Engineering, **19**: 540–549.

Alfaro, M., Miura, N., and Bergado, D.T. 1995a. Soil-Geogrid Reinforcement Interaction by Pullout and Direct Shear Tests. Geotechnical Testing Journal, **18**: 157–167.

Alfaro, M.C., Hayashi, S., Miura, N., and Watanabe, K. 1995b. Pullout Interaction Mechanism of Geogrid Strip Reinforcement. Geosynthetics International, **2**(4): 679–698.

Alkire, B.D., Haas, W.M., and Botz, J.J. 1976. Winter earthwork: embankment construction using frozen soil. Canadian Geotechnical Journal, **13**(4): 364–371.

Andersland, O.B., and Ladanyi, B. 2004. Frozen Ground Engineering. John Wiley & Sons. Inc.

Arenson, L.U., and Springman, S.M. 2005. Mathematical descriptions for the behaviour of ice-rich frozen soils at temperatures close to 0°C. Canadian Geotechnical Journal, **42**(2): 431–442.

Argue, G.H., Fullerton, J.A., Johnston, G.H., and Peckover, F.L. 1981. Roads, railways and airfields. *In* Permafrost Engineering and Construction. *Edited by* G.H. Johnston. Wiley, New York. pp. 345–391.

Barker, J., and Thomas, H. 2013. Geotechnical Engineering in Cold Regions. *In* 10th International Symposium on Cold Regions Development. *Edited by* J.E. Zufelt. American Society of Civil Engineers, Anchorage, Alaska, United States. pp. 204–214.

Batenipour, H., Alfaro, M., Kurz, D., and Graham, J. 2014. Deformations and ground temperatures at a road embankment in northern Canada. Canadian Geotechnical Journal, **51**(3): 260–271.

Berg, R.L., and Esch, D.C. 1983. Effect of color and texture on the surface temperature of asphalt concrete pavements. *In* 4th International Conference on Permafrost. National Academy Press, Fairbanks, Alaska. pp. 57–61.

Biskaborn, B.K., Smith, S.L., Noetzli, J., Matthes, H., Vieira, G., Streletskiy, D.A., Schoeneich, P., Romanovsky, V.E., Lewkowicz, A.G., Abramov, A., Allard, M., Boike, J., Cable, W.L., Christiansen, H.H., Delaloye, R., Diekmann, B., Drozdov, D., Etzelmüller, B., Grosse, G., Guglielmin, M., Ingeman-Nielsen, T., Isaksen, K., Ishikawa, M., Johansson, M., Johannsson, H., Joo, A., Kaverin, D., Kholodov, A., Konstantinov, P., Kröger, T., Lambiel, C., Lanckman, J.P., Luo, D., Malkova, G., Meiklejohn, I., Moskalenko, N., Oliva, M., Phillips, M., Ramos, M., Sannel, A.B.K., Sergeev, D., Seybold, C., Skryabin, P., Vasiliev, A., Wu, Q., Yoshikawa, K., Zheleznyak, M., and Lantuit, H. 2019. Permafrost is warming at a global scale. Nature Communications, **10**(264): 1–11.

Budhu, M. 2011. Soil Mechanics and Foundations (3rd Ed.). John Wiley & Sons, Inc.

Burwash, W.J., and Clark, J.I. 1981. Compaction of Soils in Freezing Conditions. *In* 34th Canadian Geotechnical Conference. Fredericton, NB, Canada.

Davis, R.O., and Selvadurai, A.P.S. 1996. The elastic constants. *In* Elasticity and Geomechanics. pp. 60–61.

De Guzman, E.M.B., and Alfaro, M.C. 2016. Performance of Road Embankments on Seasonally-Frozen Peat Foundations with and without Corduroy Bases. ASCE Journal of Performance of Constructed Facilities, **30**(6): 1-9. doi:10.1061/(ASCE)CF.1943-5509.0000906.

De Guzman, E.M.B., and Alfaro, M.C. 2018. Geotechnical Properties of Fibrous and Amorphous Peats for the Construction of Road Embankments. ASCE Journal of Materials in Civil Engineering, **30**(7): 1–9. doi:10.1061/(ASCE)MT.1943-5533.0002325.

De Guzman, E.M.B., Stafford, D., Alfaro, M.C., Doré, G., and Arenson, L.U. 2018. Large-scale direct shear testing of compacted frozen soil under freezing and thawing conditions. Cold Regions Science and Technology, **151**: 138–147. doi:10.1016/j.coldregions.2018.03.011.

Dounias, G.T., and Potts, D.M. 1993. Numerical analysis of drained direct and simple shear tests. Journal of Geotechnical Engineering, **119**(12): 1870–1891.

Esch, D. 1988. Roadway embankments on warm permafrost problems and remedial treatments. *In* 5th International Conference on Permafrost. *Edited by* K. Senneset. Tapir Publishers, Trondheim, Norway. pp. 1223–1228.

Esch, D.C. 1983. Evaluation of Experimental Design Features for Roadway Construction over Permafrost. *In* 4th International Conference on Permafrost. pp. 283–288.

Esmaili, D., Hatami, K., and Miller, G.A. 2014. Influence of matric suction on geotextile reinforcement-marginal soil interface strength. Geotextiles and Geomembranes, **42**: 139–153.

Farouki, O.T. 1981. Thermal Properties of Soils CRREL Monograph 81-1. Hanover, MH.

Farrag, K., and Morvant, M. 2000. Effect of Clamping Mechanism on Pullout and Confined Extension Tests. *In* Grips, Clamps, Clamping Techniques, and Strain Measurement for Testing of Geosynthetics ASTM STP 1379. *Edited by* P.E. Stevenson. American Society for Testing and Materials, West Conshohocken, PA. pp. 89–96.

Flynn, D., Alfaro, M., Kurz, D., Graham, J., and Arenson, L.U. 2016. Forecasting Ground Temperatures under a Highway Embankment on Degrading Permafrost. Journal of Cold Regions Engineering, **30**(4).

Fortier, R., LeBlanc, A.-M., and Yu, W. 2011. Impacts on permafrost degradation on a road embankment at Umiujaq in Nunavik (Quebec), Canada. Canadian Geotechnical Journal, **48**(5): 720–740.

Geo-slope International, 2018. Heat and Mass Transfer Modeling with GeoStudio 2018 2nd Ed. Calgary, Alberta, Canada.

Ghionna, V.N., Moraci, N., and Rimoldi, P. 2001. Experimental Evaluation of the Factors Affecting Pull-out Test Results on Geogrids. *In* International Symposium: Earth Reinforcement. Fukuoka, Kyushu, Japan.

Han, J., Zhang, X., Guo, J., and Wang, F. 2016. Laboratory evaluation of wickability of wicking fabrics under controlled temperature and relative humidity. *In* 3rd Pan-American Conference on Geosynthetics. pp. 1–7.

Hatami, K., and Esmaili, D. 2015. Unsaturated soil–woven geotextile interface strength properties from small-scale pullout and interface tests. Geosynthetics International, **22**(2): 161–172.

Hatami, K., Garcia, L.M., and Miller, G.A. 2011. A Moisture Reduction Factor for Pullout Resistance of Geotextile Reinforcement in Marginal Soils. *In* Geo-Frontiers Congress 2011. Dallas, Texas, United States. pp. 3576–3586.

Hayashi, S., Alfaro, M.C., and Watanabe, K. 1996. Dilatancy effects of granular soil on the pullout resistance of strip reinforcement. *In* International Symposium: Earth Reinforcement. Fukuoka, Kyushu, Japan. pp. 39–44.

Helwany, S. 2007. Applied Soil Mechanics with ABAQUS Applications. John Wiley & Sons. Inc.

IPCC, 2013. Climate Change 2013: The Physical Science Basis. Contribution of Working Group I to the Fifth Assessment Report of the Intergovernmental Panel on Climate Change. Stocker, T.F., D. Qin, G.-K. Plattner, M. Tignor, S.K. Allen, J. Boschung, A. Nauels, Y. Xia, V. Bex and P.M. Midgley (eds.). Cambridge University Press, Cambridge, United Kingdom and New York, NY, USA, 1535 pp.

IPCC, 2014. Climate Change 2014: Impacts, Adaptation, and Vulnerability. Part B: Regional Aspects. Contribution of Working Group II to the Fifth Assessment Report of the Intergovernmental Panel on Climate Change. Barros, V.R., C.B. Field, D.J. Dokken, M.D. Mastrandrea, K.J. Mach, T.E. Bilir, M. Chatterjee, K.L. Ebi, Y.O. Estrada, R.C. Genova, B. Girma, E.S. Kissel, A.N. Levy, S. MacCracken, P.R. Mastrandrea, and L.L. White (eds.). Cambridge University Press, Cambridge, United Kingdom and New York, NY, USA, 688 pp.

James, M., Lewkowicz, A.G., Smith, S.L., and Miceli, C.M. 2013. Multi-decadal degradation and persistence of permafrost in the Alaska Highway corridor, northwest Canada. Environmental Research Letters, **8**. doi:10.1088/1748-9326/8/4/045013.

Jewell, R.A. 1996. Soil reinforcement with geotextiles. CIRIA, London.

Johnson, A.W., and Sallberg, J.R. 1962. Factors Influencing Compaction Test Results. Highway Research Record Bulletin No. 319,: 148.

Khoury, C.N., Miller, G.A., and Hatami, K. 2011. Unsaturated soil-geotextile interface behavior. Geotextiles and Geomembranes, **29**: 17–28.

Kim, C.-S. 2007. Evaluating Shear Mobilization in Rockfill Columns Used for Riverbank Stabilization. University of Manitoba.

Kinney, T.C., and Connor, B. 1990. Geosynthetic reinforcement of paved road embankments on polygonal ground. Journal of Cold Regions Engineering, **4**(2): 102–112.

Kinney, T.C., and Connor, B. 1987. Geosynthetic supporting embankments over voids. Journal of Cold Regions Engineering, **1**(4): 158–170.

Kong, X., Doré, G., and Calmels, F. 2019. Thermal modeling of heat balance through embankments in permafrost regions. Cold Regions Science and Technology, **158**: 117–127. doi:10.1016/j.coldregions.2018.11.013.

Lee, H.-S., and Bobet, A. 2005. Laboratory Evaluation of Pullout Capacity of Reinforced Silty Sands in Drained and Undrained Conditions. Geotechnical Testing Journal, **28**(4): 1–10.

Leshchinsky, D., and Marcozzi, G.F. 1990. Bearing capacity of shallow foundations: Rigid versus flexible models. Journal of Geotechnical Engineering, **116**(11): 1750–1756. doi:10.1061/(ASCE)0733-9410(1990)116:11(1750).

Lopes, M.L. 2002. Soil-Geosynthetic Interaction. *In* Geosynthetics and Their Application. *Edited by* S. Shukla. Thomas Telford Ltd., London. pp. 57–78.

Loria, A.F., Frigo, B., and Chiaia, B. 2017. A non-linear constitutive model for describing the mechanical behaviour of frozen ground and permafrost. Cold Regions Science and Technology, **133**: 63–69.

Ma, W., Qi, J., and Wu, Q. 2008. Analysis of the Deformations of Embankments on the Qinghai-Tibet Railway. Journal of Geotechnical and Geoenviromental Engineering, **134**(11): 1645–1654.

Ma, W., Sheng, Y., Wu, Q., Wang, D., and Feng, W. 2012. Remedying embankment thaw settlement in a warm permafrost region with thermosyphons and crushed rock revetment. Canadian Geotechnical Journal, **49**(9): 1005–1014.

McGregor, R., Hayley, D., Wilkins, G., Hoeve, E., Grozic, E., Roujanski, V., Jansen, A., and Doré, G. 2010. Guidelines for Development and Management of Transportation Infrastructure in Permafrost Regions. Transportation Association of Canada, Ottawa, ON, Canada.

McHattie, R.L., and Esch, D.C. 1983. Benefits of peat underlay used in road construction on permafrost. 4th International Conference on Permafrost,: 826–831. National Academy Press, Fairbanks, Alaska.

Mosallanezhad, M., Taghavi, S.H.S., Hataf, N., and Alfaro, M.C. 2016. Experimental and numerical studies of the performance of the new reinforcement system under pull-out conditions. Geotextiles and Geomembranes, **44**: 70–80.

Pathak, Y.P., and Alfaro, M.C. 2010. Wetting-drying behaviour of geogrid-reinforced clay under working load conditions. Geosynthetics International, **17**(3): 144–156.

Qi, J., Sheng, Y., Zhang, J., and Wen, Z. 2007. Settlement of embankments in permafrost regions in the Qinghai-Tibet Plateau. Norwegian Journal of Geography, **61**: 49–55.

Qin, Y., Li, G., and Qu, G. 2009. A Formula for the Unfrozen Water Content and Temperature of Frozen Soils. *In* 14th Conference on Cold Regions Engineering. pp. 155–161.

Rahmaninezhad, S.M., Han, J., Weldu, M., Kakrasul, J.I., and Razeghi, H.R. 2016. Effect of methods of applying normal stresses in pullout tests on pressure distributions and pullout resistance. *In* 3rd Pan-American Conference on Geosynthetics. pp. 1308–1315.

Romanovsky, V.E., Smith, S.L., and Christiansen, H.H. 2010. Permafrost thermal state in the polar northern hemisphere during the international polar year 2007-2009: A synthesis. Permafrost and Periglacial Processes, **21**: 106–116. doi:10.1002/ppp.689.

Saboundjian, S. 2008. Evaluation of Alternative Embankment Construction Methods. Fairbanks, Alaska.

Savage, J.E. 1965. Location and construction of roads in the discontinuous permafrost zone, Mackenzie District, Northwest Territories. *In* Canadian Regional Permafrost Conference. National Research Council of Canada, Ottawa. pp. 119–131.

Sengupta, M., Johansen, N.I., and Sinha, A.K. 1991. Slope Stability in Arctic Surface Mines. Journal of Cold Regions Engineering, **4**(3): 154–158.

Sikkema, M., and Carpita, J. 2016. Pioneer Scenic Byway Frost Heave Prevention and Results. *In* 3rd Pan-American Conference on Geosynthetics. pp. 1871–1879.

Smith, S.L., Romanovsky, V.E., Lewkowicz, A.G., Burn, C.R., Allard, M., Clow, G.D., Yoshikawa, K., and Throop, J. 2010. Thermal State of Permafrost in North America: A Contribution to the International Polar Year. Permafrost and Periglacial Processes, **21**: 117–135.

Smith, M. 2014. ABAQUS/Standard User's Manual, Version 6.14. Dassault Systèmes Simulia Corp, Providence, RI.

Sturm, M., Holmgren, J., König, M., and Morris, K. 1997. The thermal conductivity of seasonal snow. Journal of Glaciology, **43**: 26–41. doi:10.1017/S0022143000002781.

Sun, Z., Ma, W., and Li, D. 2005. In Situ Test on Cooling Effectiveness of Air Convection Embankment with Crushed Rock Slope Protection in Permafrost Regions. Journal of Cold Regions Engineering, **19**(2): 38–51.

Swiderski, R.E. 1976. The effects of angularity on the compaction and shear strength of a cohesionless material. New Jersey Institute of Technology.

Wang, F., Han, J., Zhang, X., and Guo, J. 2017. Laboratory tests to evaluate effectiveness of wicking geotextile in soil moisture reduction. Geotextiles and Geomembranes, **45**: 8–13.

Warren, K.A., Christopher, B., and Howard, I.L. 2010. Geosynthetic strain gage installation procedures and alternative strain measurement methods for roadway applications. Geosynthetics International, **17**(6): 403–430.

Weerasekara, L., and Wijewickreme, D. 2010. An analytical method to predict the pullout response of geotextiles. Geosynthetics International, **17**(4): 193–206.

Wu, Q., and Niu, F. 2013. Permafrost changes and engineering stability in Qinghai-Xizang Plateau. Chinese Science Bulletin, **58**(10): 1079–1094.

Wu, Q., Zhang, Z., and Liu, Y. 2010. Long-term thermal effect of asphalt pavement on permafrost under an embankment. Cold Regions Science and Technology, **60**: 221–229.

Yang, Z., Still, B., and Ge, X. 2015. Mechanical properties of seasonally frozen and permafrost soils at high strain rate. Cold Regions Science and Technology, **113**: 12–19.

Yasufuku, N., Springman, S.M., Arenson, L.U., and Ramholt, T. 2003. Stress-dilatancy behaviour of frozen sand in direct shear. *In* 8th International Conference on Permafrost. *Edited by* M. Phillips, S.M. Springman, and L.U. Arenson. Swets & Zeitlinger, Zurich, Switzerland. pp. 1253–1258.

Yi, S., Woo, M.-K., and Altaf Arain, M. 2007. Impact of peat and vegetation on permafrost degradation under climate warming. Geophysical Research Letters, **34**: L16504. doi:10.1029/2007GL030550.

Yu, F., Qi, J., Yao, X., and Liu, Y. 2013. In-situ monitoring of settlement at different layers under embankments in permafrost regions on the Qinghai-Tibet Plateau. Engineering Geology, **160**: 44–53.

Yu, W., Che, F., Feng, W., Guo, M., and Zhou, G. 2012. Properties of subgrade and construction techniques of Mobei expressway. *In* GeoCongress 2012: State of the Art and Practice in Geotechnical Engineering. *Edited by* R.D. Hryciw, A. Athanasopoulos-Zekkos, and N. Yesiller. American Society of Civil Engineers, Oakland, California. pp. 1410–1417.

Zhang, L., and Thornton, C. 2007. A numerical examination of the direct shear test. Géotechnique, **57**(4): 343–354.

Zhang, X., Presler, W., Li, L., Jones, D., and Odgers, B. 2014. Use of Wicking Fabric to Help Prevent Frost Boils in Alaskan Pavements. Journal of Materials in Civil Engineering, **26**(4): 728–740.

APPENDICES

Appendix A Reinforced Test Section Thermistor and ShapeAccelArray Temperatures

Appendix B Pullout test results for room OMC, thawed HMC, and thawed OMC tests, and horizontal displacements and average pullout loads for thawed HMC and thawed OMC tests

Fig. A1. Temperature readings at different time steps at different locations in the reinforced embankment section: (a) top, (b) base, (c) centreline, (d) toe, and (e) offset. EOC: end-of-construction and EOY: end-of-year

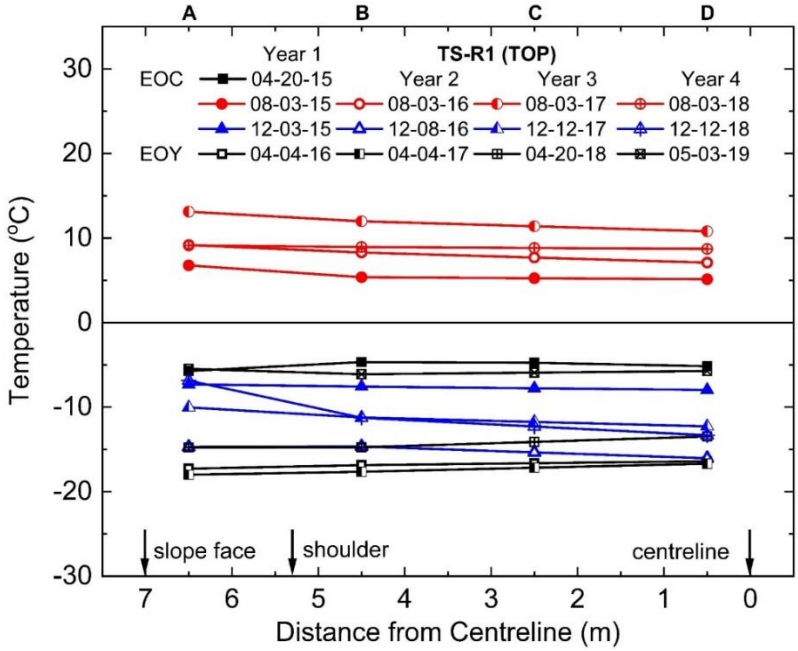

(a)

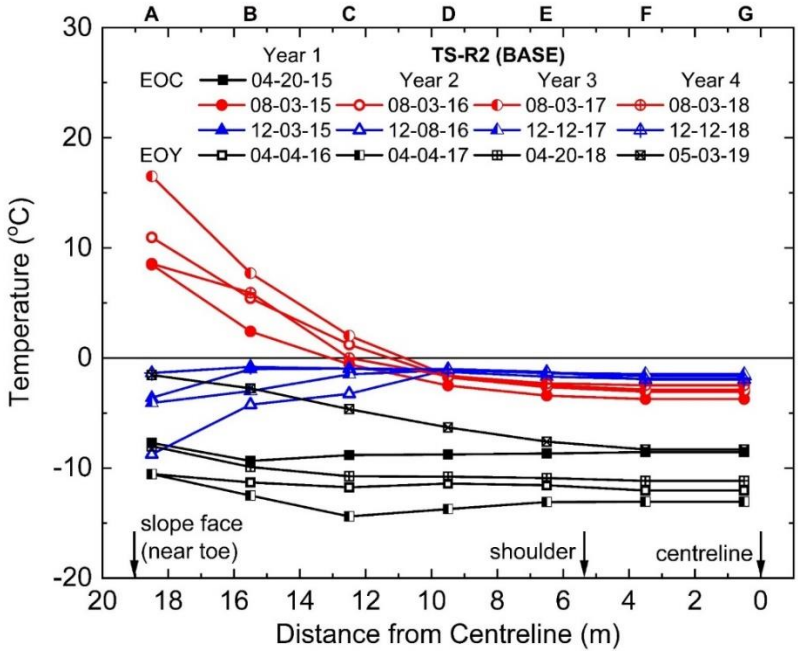

(b)

Fig. A1 (continued)

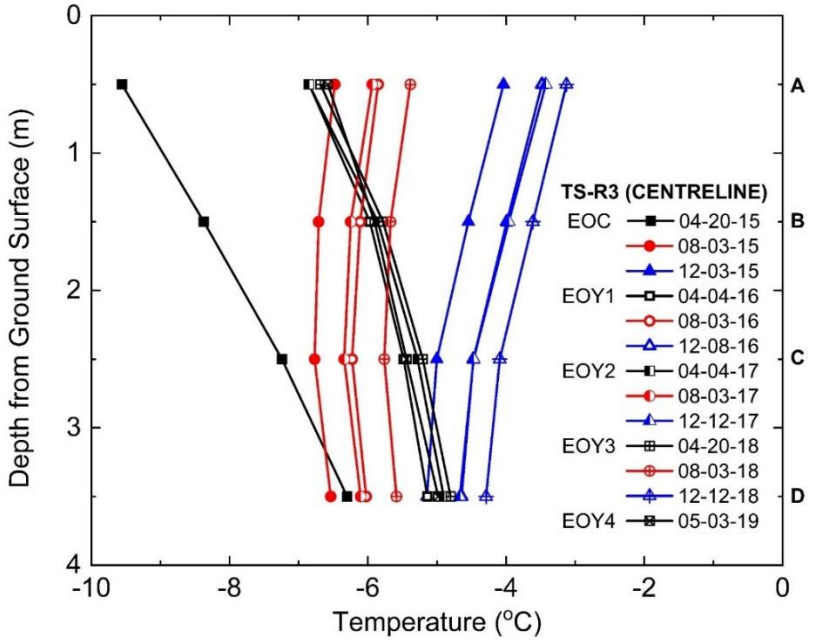

(c)

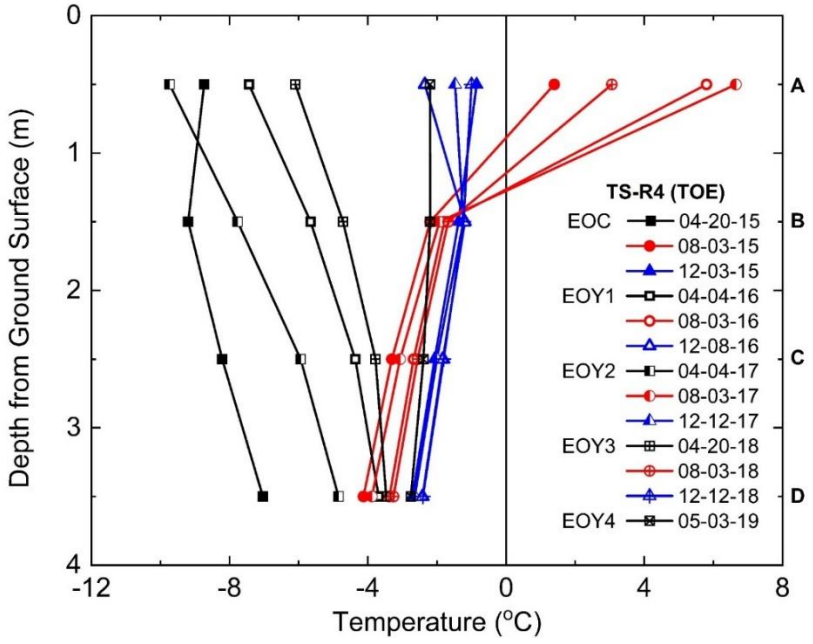

(d)

Fig. A1 (continued)

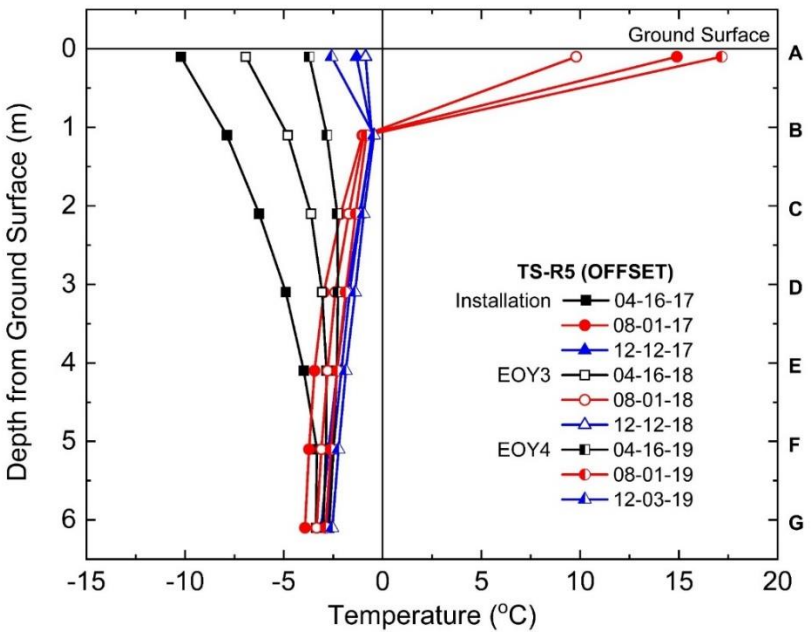

(e)

Fig. A2. Temperature readings from (a) vertical and (b) horizontal ShapeAccelArrays at different time steps at different locations in the reinforced embankment section. EOC: end-of-construction and EOY: end-of-year

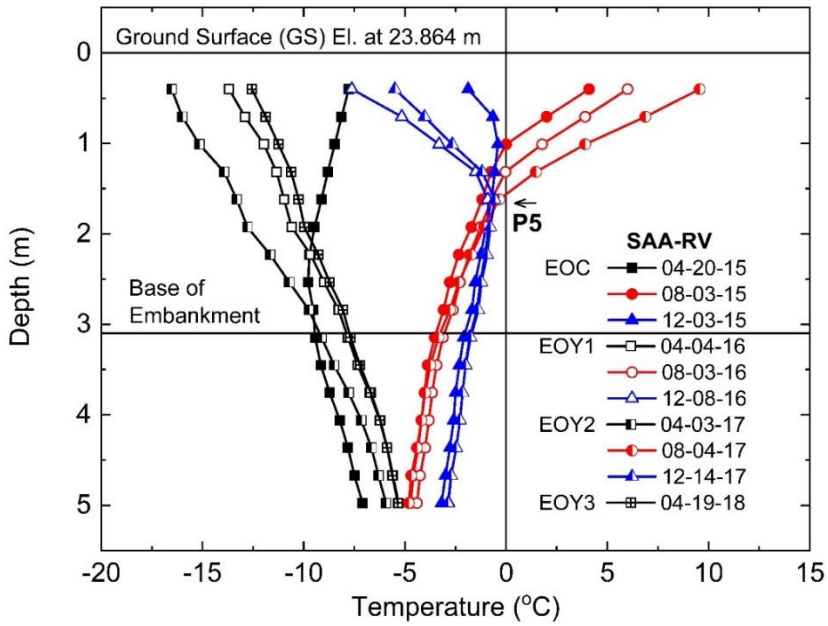

(a)

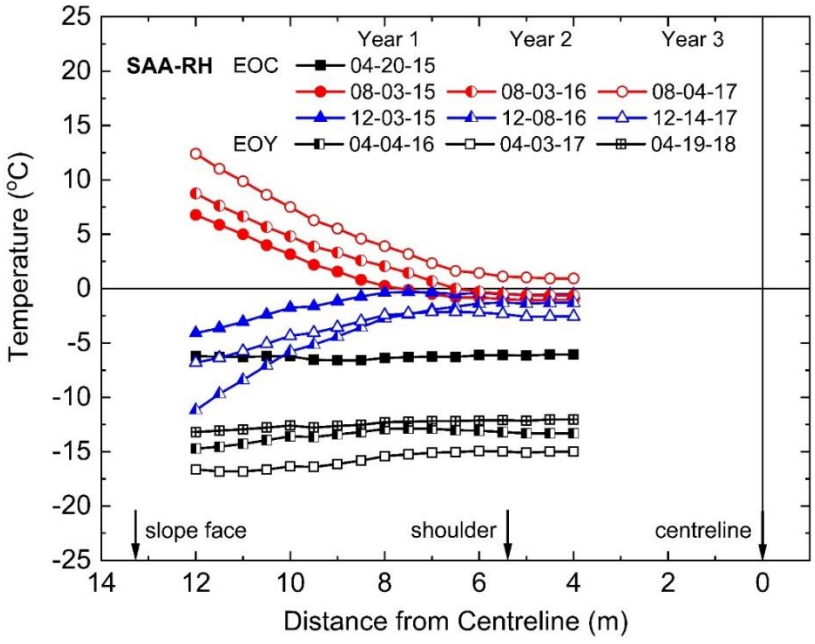

(b)

Fig. B1. Pullout test results from room OMC tests for wicking and non-wicking geotextiles: (a) gross pullout load and (b) calibration pullout load.

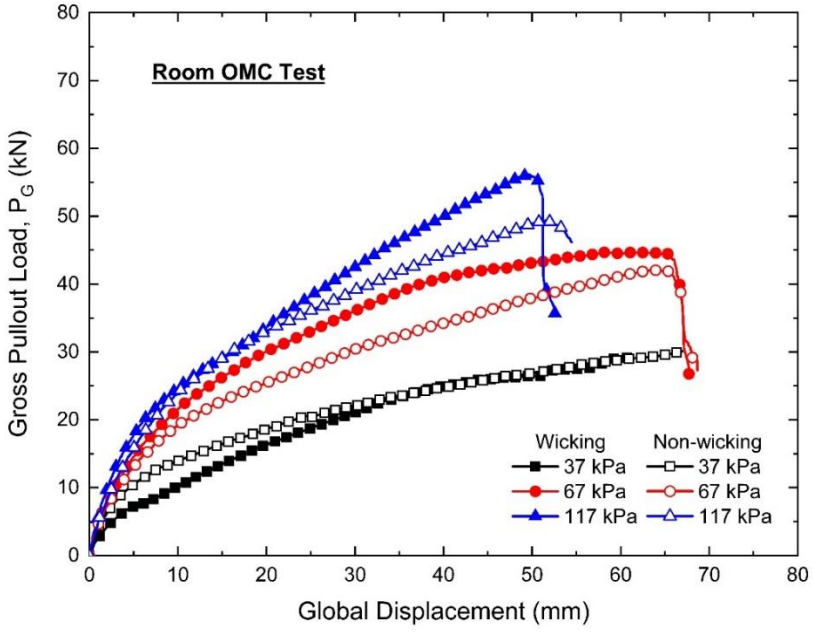

(a)

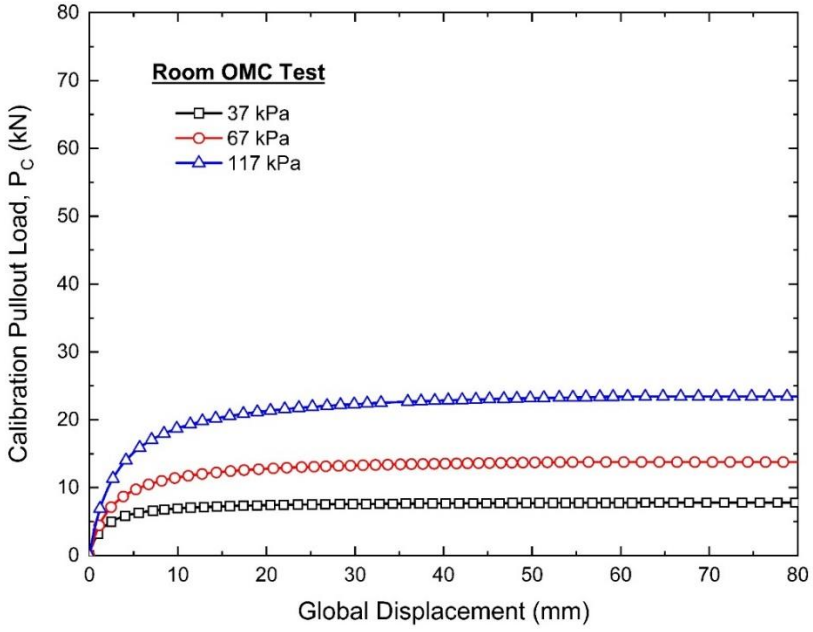

(b)

Fig. B2. Pullout test results from thawed HMC tests for wicking and non-wicking geotextiles: (a) gross pullout load and (b) calibration pullout load.

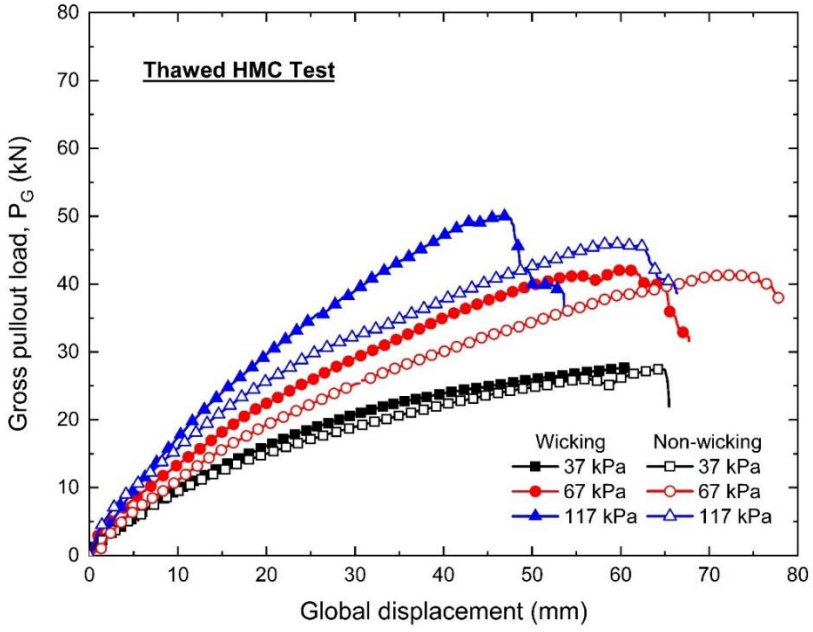

(a)

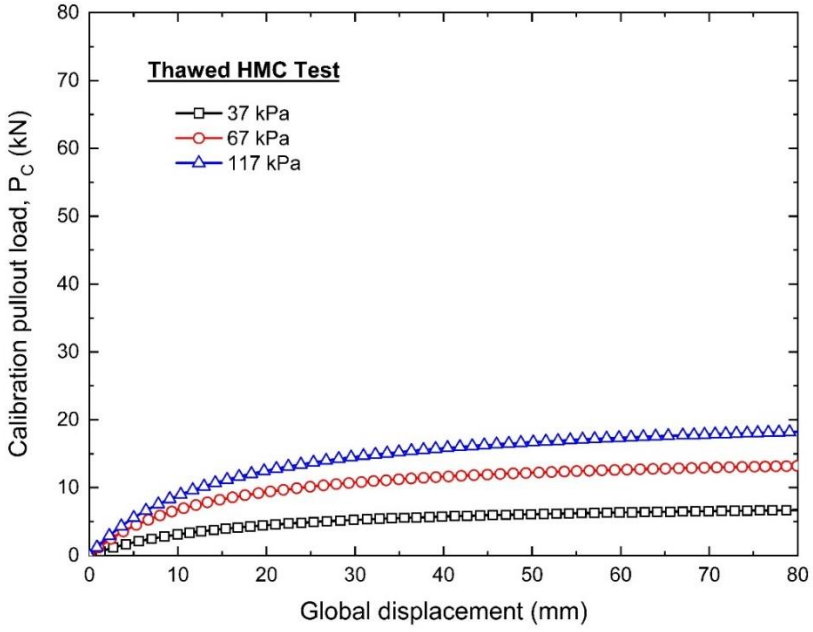

(b)

Fig. B3. Pullout test results from thawed OMC tests for wicking and non-wicking geotextiles: (a) gross pullout load and (b) calibration pullout load.

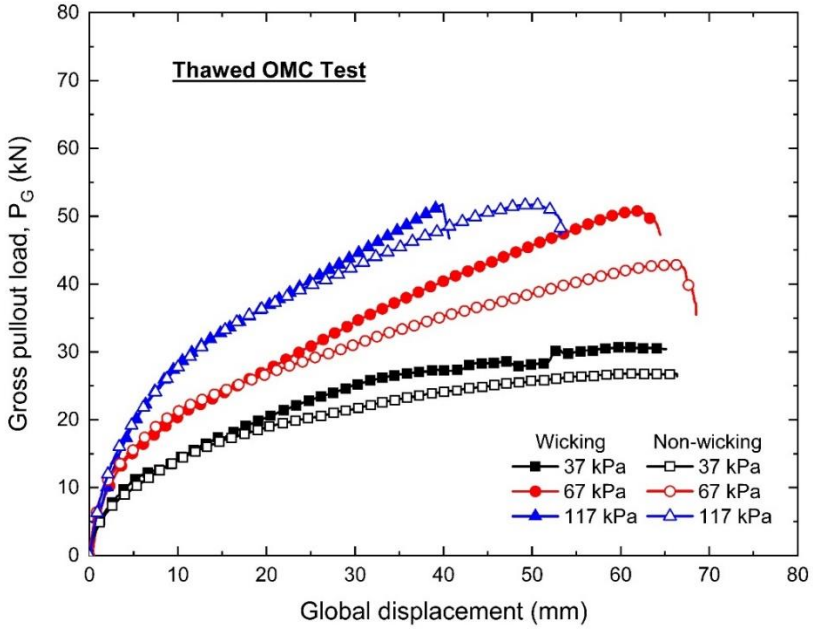

(a)

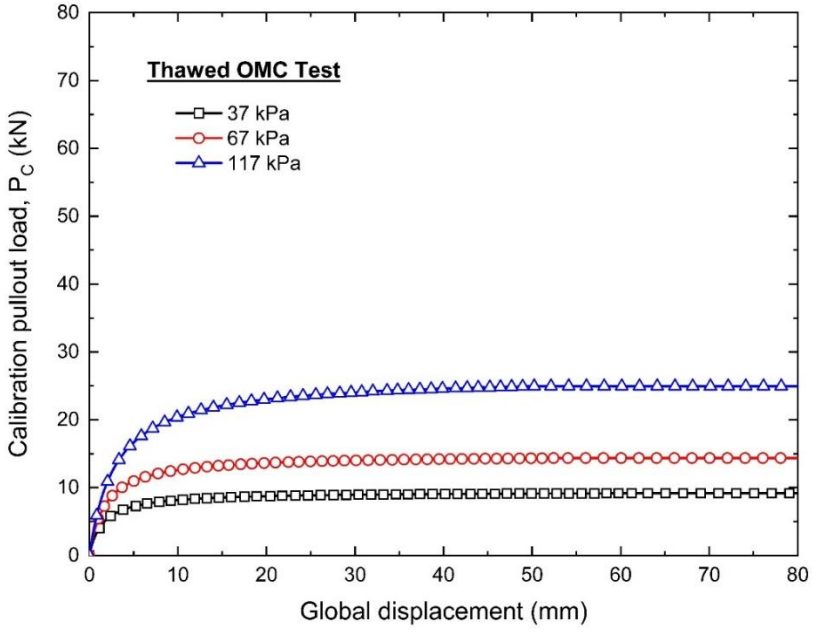

(b)

Fig. B4. Horizontal displacements along the geotextile from thawed HMC tests at 2% and EOT strains under different normal stresses: (a) wicking geotextile and (b) non-wicking geotextile.

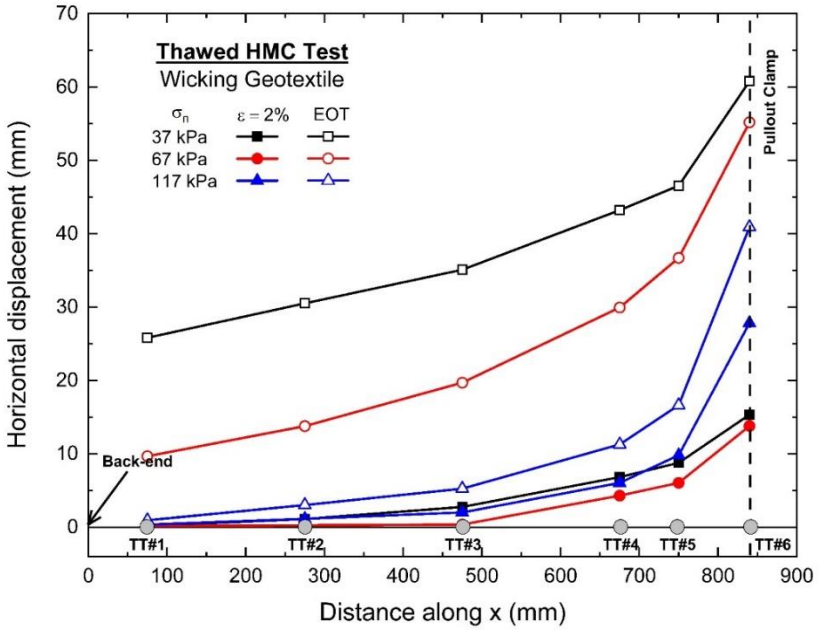

(a)

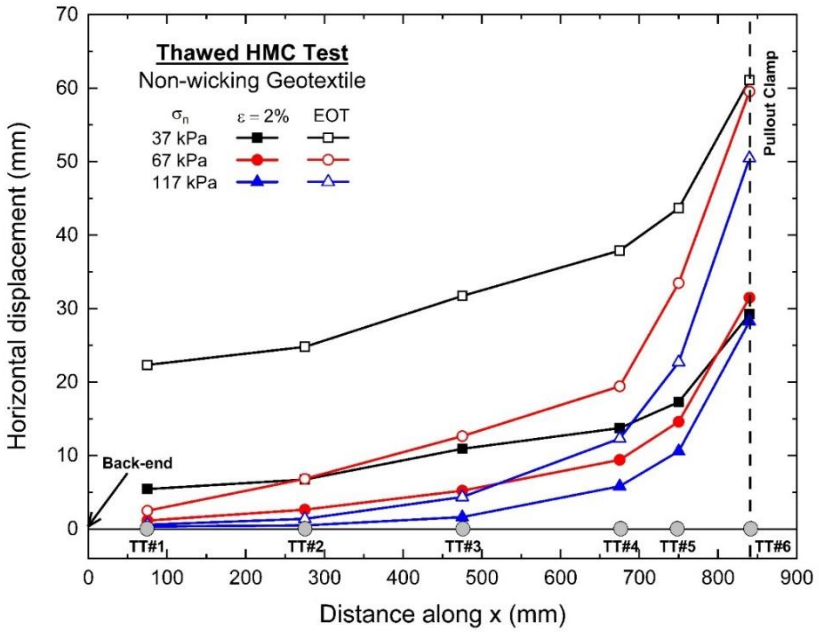

(b)

Fig. B5. Horizontal displacements along the geotextile from thawed OMC tests at 2% and EOT strains under different normal stresses: (a) wicking geotextile and (b) non-wicking geotextile.

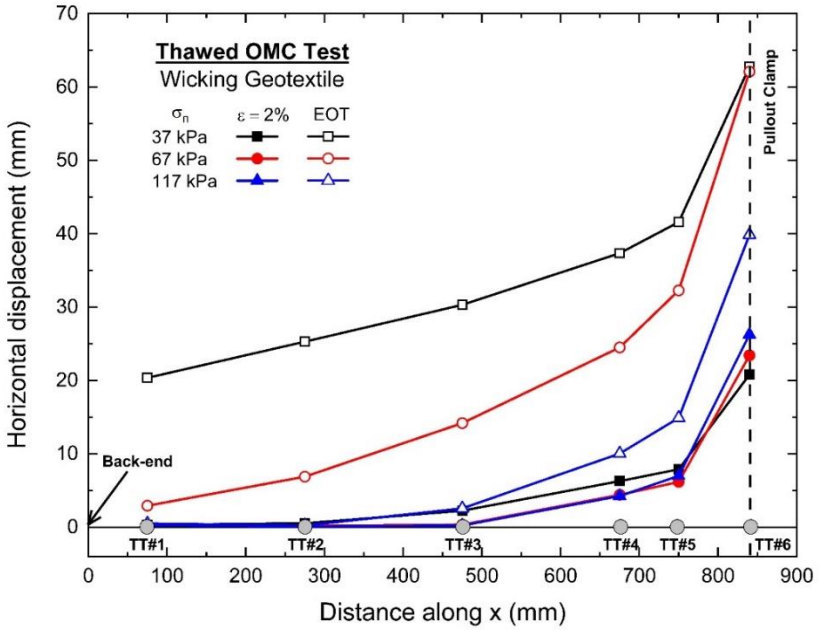

(a)

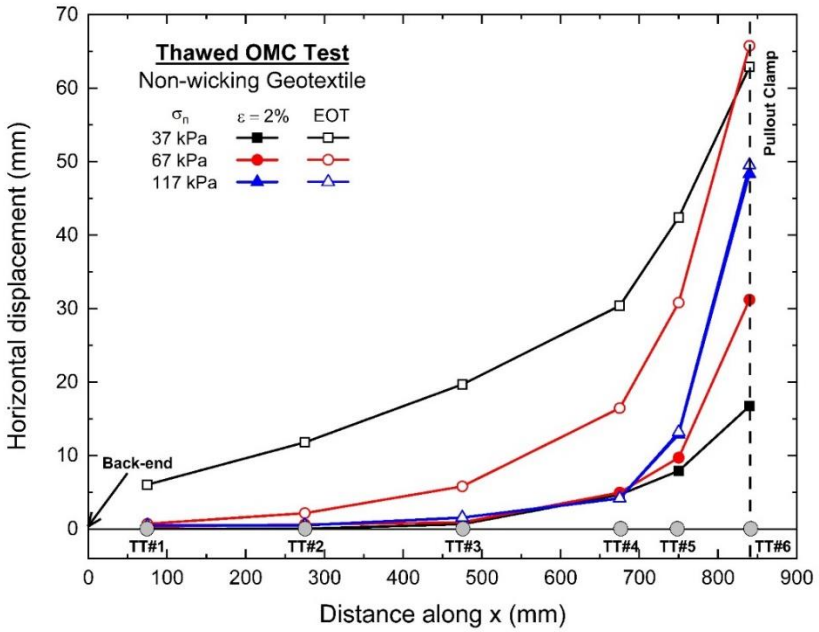

(b)

Fig. B6. Average pullout load along the geotextile from thawed HMC tests at 2% and EOT strains under different normal stresses: (a) wicking geotextile and (b) non-wicking geotextile.

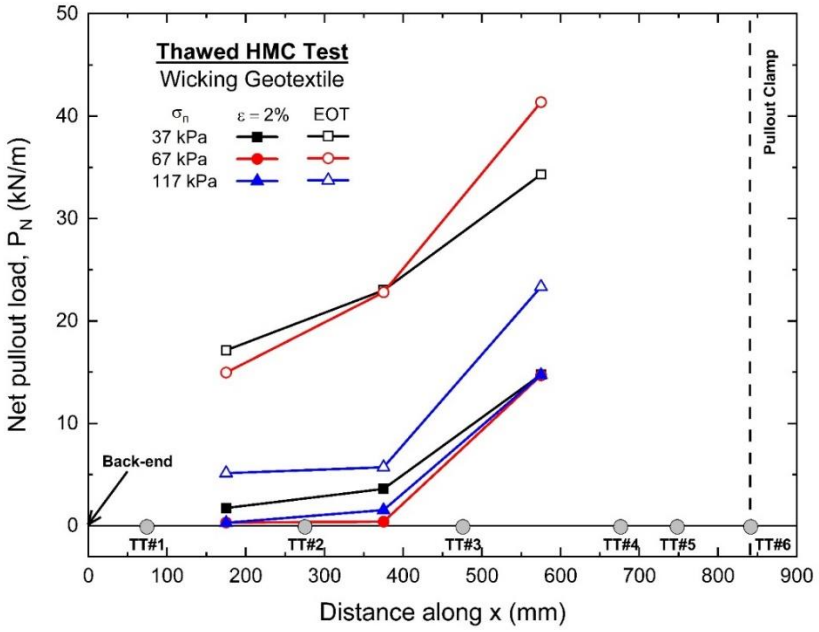

(a)

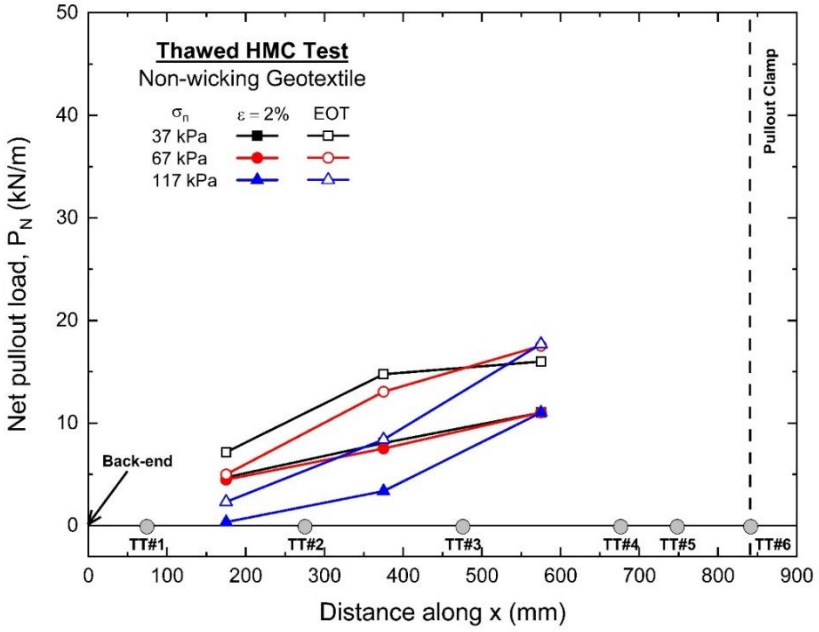

(b)

Fig. B7. Average pullout load along the geotextile from thawed OMC tests at 2% and EOT strains under different normal stresses: (a) wicking geotextile and (b) non-wicking geotextile.

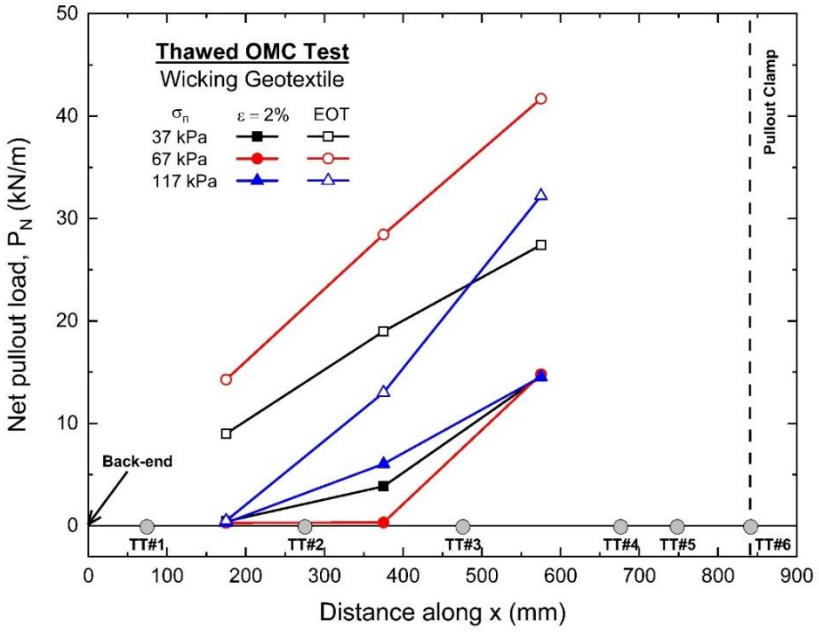

(a)

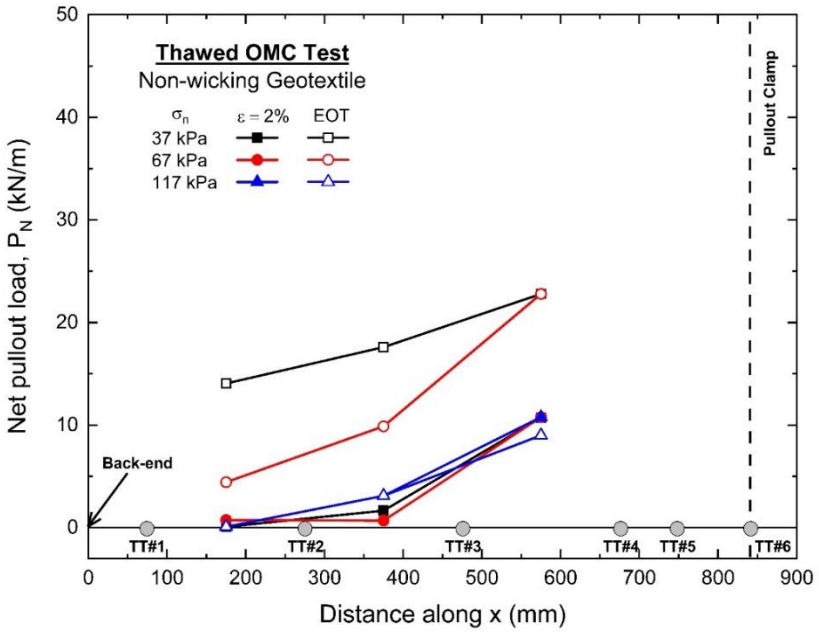

(b)